

# Fluid-Driven Fracture in Poroelastic Medium

A DISSERTATION

SUBMITTED TO THE FACULTY OF THE GRADUATE SCHOOL  
OF THE UNIVERSITY OF MINNESOTA

BY

Yevhen Kovalyshen

IN PARTIAL FULFILLMENT OF THE REQUIREMENTS  
FOR THE DEGREE OF  
Doctor Of Philosophy

February, 2010

© Yevhen Kovalyshen 2010  
ALL RIGHTS RESERVED

## ACKNOWLEDGMENTS

I would like to express my gratitude to my adviser Emmanuel Detournay. During this 3.5 years he was for me rather a senior mate than just an adviser. I would like to thank him for supporting me in different difficult situations of my life, for helping me to merge into civilized world. As in any close relationship we went through some conflicts and misunderstandings... I would like to thank to Emmanuel's wife, Christine, for supporting both of us during these 3.5 years.

I would like to express my gratitude to my family for their unconditional support, their unwavering believe, and their limitless understanding.

The main part of this research was born under fruitful sun of Australia. I would like to thank the CSIRO drilling group for a warm welcome. Special thanks goes to Thomas and Luiz who ensured my survival on this "dangerous" continent.

I would like to express my appreciation to Lisa for keen discussions as well as for friendly support.

Also I would like to thank all my friends, especially Luc and Catalina, who were an essential part of my life during these 3.5 years.

Yevhen Kovalyshen

Minneapolis, February 2010.

## ABSTRACT

This research deals with an analysis of the problem of a fluid-driven fracture propagating through a poroelastic medium. Formulation of such model of an hydraulic fracture is at the cross-road of four classical disciplines of engineering mechanics: lubrication theory, filtration theory, fracture mechanics, and poroelasticity, which includes both elasticity and diffusion. The resulting mathematical model consists of a set of non-linear integro-differential history-dependent equations with singular behaviour at the moving fracture front.

The main contribution of this research is a detailed study of the large-scale 3D diffusion around the fracture and its associated poroelastic effects on fracture propagation. The study hinges on scaling and asymptotic analyses. To understand the behavior of the solution in the tip region, we study a semi-infinite fracture propagating at a constant velocity. We show that, in contrast to the classical case of the Carter's leak-off model (1D diffusion), the tip region of a finite fracture cannot, in general, be modeled by a semi-infinite fracture when 3D diffusion takes place. Moreover, 3D diffusion does not permit separation of the problem into two regions: the tip and the global fracture.

We restrict our study of the fracture propagation to an investigation of two limiting cases: zero viscosity and zero toughness. We show that large-scale 3D diffusion and its associated poroelastic effects can significantly affect the fracture evolution. In particular, we observe a significant increase of the net fracturing fluid pressure compared to the case of 1D diffusion due to the porous medium dilation. Another consequence of 3D diffusion is the possibility of fracture arrest. Indeed, the fracture stops propagating at large time, when the fracturing fluid injection rate is balanced by the leak-off rate at pressure below the critical propagation pressure.

# Contents

<b>Acknowledgements</b>	<b>i</b>
<b>Abstract</b>	<b>ii</b>
<b>List of Tables</b>	<b>ix</b>
<b>List of Figures</b>	<b>x</b>
<b>1 Introduction</b>	<b>1</b>
1.1 Context . . . . .	1
1.2 Models . . . . .	5
1.3 First glance at a “simple” mathematical model . . . . .	7
1.4 On different approaches in hydraulic fracturing studies . . . . .	11
1.5 Objectives and organization of the research . . . . .	18
<b>2 Mathematical formulation</b>	<b>21</b>
2.1 Lubrication theory . . . . .	21
2.2 Elasticity equation . . . . .	23
2.3 Propagation criterion . . . . .	24
2.4 Poroelasticity equations . . . . .	25
2.5 Low permeability cake build-up . . . . .	27

<b>3</b>	<b>Semi-infinite fracture</b>	<b>28</b>
3.1	Introduction . . . . .	28
3.2	Review of present knowledge . . . . .	30
3.3	Mathematical model . . . . .	33
3.3.1	Lubrication equations . . . . .	34
3.3.2	Elasticity equation . . . . .	35
3.3.3	Linear elastic fracture mechanics . . . . .	35
3.3.4	Diffusion equations . . . . .	35
3.3.5	Low permeability cake build-up . . . . .	36
3.4	Scaling . . . . .	37
3.4.1	Diffusion scaling . . . . .	41
3.5	Structure of solution . . . . .	43
3.5.1	Previous works in reference to our model . . . . .	45
3.5.1.1	Impermeable cake build-up . . . . .	45
3.5.1.2	Zero lag . . . . .	47
3.5.2	Case of storage domination . . . . .	49
3.5.2.1	Cake build-up domination . . . . .	51
3.5.2.2	Negligible cake build-up . . . . .	53
3.5.3	Case of leak-off domination . . . . .	54
3.5.3.1	Cake build-up domination . . . . .	55
3.5.3.2	Negligible cake build-up . . . . .	56
3.6	Near- and far-field asymptotes . . . . .	57
3.6.1	Near-field asymptote, $\xi \ll 1$ . . . . .	57
3.6.1.1	Toughness-dominated region with small lag $\Lambda \ll 1$ . . . .	58
3.6.2	Far-field asymptote, $\xi \gg 1$ . . . . .	59
3.6.2.1	Toughness region . . . . .	60

3.6.2.2	Storage-viscosity region . . . . .	62
3.6.2.3	Leak-off-viscosity region . . . . .	64
3.7	Transient solution . . . . .	66
3.8	Discussion . . . . .	70
3.8.1	Diffusion . . . . .	70
3.8.2	Carter's leak-off model . . . . .	71
3.8.3	Backstress . . . . .	72
3.9	Summary of the chapter results . . . . .	73
<b>4</b>	<b>Auxiliary problem</b>	<b>80</b>
4.1	Introduction . . . . .	80
4.2	Problem formulation . . . . .	83
4.2.1	Starting equations . . . . .	83
4.2.2	Scaling . . . . .	84
4.3	Small-time asymptote, $\tau \ll 1$ . . . . .	85
4.3.1	Tip region, $ 1 - \xi  \ll 1$ . . . . .	86
4.3.1.1	Near-field asymptote, $ \zeta  \ll 1$ . . . . .	87
4.3.1.2	Far-field asymptotes, $2\sqrt{s} \gg  \zeta  \gg 1$ . . . . .	88
4.3.1.3	Transient solution . . . . .	88
4.3.2	Global solution . . . . .	90
4.4	Large-time asymptote, $\tau \gg 1$ . . . . .	92
4.4.1	$O(1)$ solutions . . . . .	94
4.4.2	$O(\sqrt{s})$ solutions . . . . .	95
4.4.2.1	Back to time domain . . . . .	96
4.5	Transient solution . . . . .	97
4.6	Summary of the chapter results . . . . .	98

<b>5</b>	<b>Fracture propagation: zero viscosity</b>	<b>101</b>
5.1	Preamble . . . . .	101
5.2	Mathematical model . . . . .	103
5.2.1	Dimensional formulation . . . . .	103
5.2.2	Dimensionless formulation . . . . .	105
5.3	Methodology . . . . .	107
5.4	Propagation regimes . . . . .	110
5.4.1	$K_0\tilde{K}_{\kappa 0}\tilde{K}_{\sigma 0}$ -face: 1D diffusion, $\mathcal{G}_d \ll 1$ . . . . .	113
5.4.2	$K_\infty\tilde{K}_{\kappa \infty}\tilde{K}_{\sigma \infty}$ -face: pseudo steady-state diffusion, $\mathcal{G}_d \gg 1$ . . . . .	115
5.5	Transient solution . . . . .	117
5.6	Discussion . . . . .	123
<b>6</b>	<b>Fracture propagation: zero toughness</b>	<b>128</b>
6.1	Preamble . . . . .	128
6.2	Mathematical model . . . . .	129
6.2.1	Dimensional formulation . . . . .	129
6.2.2	Dimensionless formulation . . . . .	131
6.3	Propagation regimes . . . . .	133
6.3.1	$M$ -vertex: storage-dominated regime . . . . .	135
6.3.2	$\tilde{M}_0$ -vertex: leak-off-dominated regime with 1D diffusion, $\mathcal{G}_d \ll 1$ . . . . .	137
6.3.3	$\tilde{M}_\infty$ -vertex: leak-off-dominated regime with pseudo steady-state (3D) diffusion, $\mathcal{G}_d \gg 1$ . . . . .	139
6.4	Transient solution . . . . .	140
6.5	Summary of the chapter results . . . . .	146
<b>7</b>	<b>Conclusions</b>	<b>153</b>
7.1	Main results . . . . .	153



7.2	Practical applications . . . . .	155
7.3	Further development . . . . .	158
<b>Bibliography</b>		<b>160</b>
<b>Appendix A. Semi-infinite fracture</b>		<b>167</b>
A.1	Approach of Entov et al. (2007) . . . . .	167
A.2	Uniform pressure . . . . .	169
A.3	Far-field asymptote . . . . .	170
A.4	Numerical scheme . . . . .	172
A.4.1	Elasticity equation . . . . .	172
A.4.2	Leak-off equation . . . . .	174
A.4.3	Backstress equation . . . . .	175
A.4.4	Lubrication equation . . . . .	176
A.4.5	Closing remarks . . . . .	176
<b>Appendix B. Auxiliary problem</b>		<b>178</b>
B.1	Small-time and tip asymptotes . . . . .	178
B.2	Numerical solution of the tip region problem (4.19), (4.21) . . . . .	179
B.3	Numerical algorithm for the transient solution . . . . .	181
B.4	On numerical inversion of the Laplace transform . . . . .	184
<b>Appendix C. Zero viscosity case: numerical scheme</b>		<b>186</b>
C.1	Temporal integration . . . . .	186
C.2	Spatial integration . . . . .	189
C.3	The end of the story . . . . .	190
<b>Appendix D. Zero toughness case: numerical scheme</b>		<b>192</b>
D.1	Elasticity equation . . . . .	192

D.2	Lubrication equation . . . . .	193
D.2.1	Channel . . . . .	193
D.2.2	Tip . . . . .	194
D.3	Tip solution . . . . .	194
D.4	Evaluation of leak-off displacement function (6.44) . . . . .	195
D.4.1	Temporal integration . . . . .	195
D.4.2	Spatial integration . . . . .	196
D.5	The end of the story . . . . .	197

# List of Tables

3.1	Scalings for different limiting cases . . . . .	44
5.1	Propagation regimes and corresponding scalings . . . . .	112
6.1	Propagation regimes and corresponding scalings . . . . .	135
7.1	Characteristic parameters during production water re-injection (Longue- mare et al., 2001) . . . . .	155
7.2	Crack propagation . . . . .	156

# List of Figures

1.1	Hydraulic fracturing vs waterflooding [after Adachi (2001)] . . . . .	2
1.2	Diffusion patterns . . . . .	4
1.3	Different hydraulic fracturing models [after Adachi (2001)] . . . . .	6
1.4	Sketch of the problem . . . . .	8
1.5	Examples of parametric spaces . . . . .	17
3.1	Parametric space and few solution “trajectories” parametrized by number $\chi$ : $0 < \chi_1 < \chi_2$ . . . . .	32
3.2	Semi-infinite fracture . . . . .	34
3.3	Fracture opening profile $\Omega(\xi)$ , $\mathcal{K} = \mathcal{M} = \mathcal{X} = \mathcal{S} = 1$ . . . . .	61
3.4	Fluid displacement function profile $\Upsilon(\xi)$ , $\mathcal{K} = \mathcal{M} = \mathcal{X} = \mathcal{S} = 1$ . . . . .	62
3.5	Fluid displacement function profile $\Upsilon(\xi)$ , $\mathcal{K} = \mathcal{M} = \mathcal{X} = \mathcal{S} = 1$ : the fracturing-pore fluids boundary region . . . . .	63
3.6	Fluid pressure profile $\Pi(\xi)$ , $\mathcal{K} = \mathcal{M} = \mathcal{X} = \mathcal{S} = 1$ . Here $\Pi_{\eta=0}(0) =$ $-1.068$ and $\Pi_{\eta=0.5}(0) = -1.098$ . . . . .	64
3.7	Backstress profile $\Sigma(\xi)$ , $\mathcal{K} = \mathcal{M} = \mathcal{X} = \mathcal{S} = 1$ . Here $\Sigma(0) = 0.1815$ . . .	65
3.8	Backstress profile $\Sigma(\xi)$ , $\mathcal{K} = 4$ , $\mathcal{M} = 1$ , $\mathcal{X} = 10^{13}$ , $\mathcal{S} = 0.01$ , and $\eta = 0.5$ . Here $\Sigma(0) = 0.054$ . . . . .	66
3.9	Backstress profile $\Sigma(\xi)$ , $\mathcal{K} = 4$ , $\mathcal{M} = 1$ , $\mathcal{X} = 10^{13}$ , $\mathcal{S} = 0.01$ , and $\eta = 0.5$	67
3.10	Backstress profile $\Sigma(\xi)$ , $\mathcal{K} = 4$ , $\mathcal{M} = 1$ , $\mathcal{X} = 10^{13}$ , $\mathcal{S} = 0.01$ , and $\eta = 0.5$	68

3.11	Constant pressure region solution + toughness dominance: fluid displacement function profile $\Upsilon(\xi)$ , $\mathcal{K} = 0.4$ , $\mathcal{M} = 0.01$ , $\mathcal{X} = 100$ , and $\mathcal{S} = 1$ . . .	69
3.12	Constant pressure region solution + toughness dominance: fluid displacement function profile $\Upsilon(\xi)$ (enlarged behind the lag region), $\mathcal{K} = 0.4$ , $\mathcal{M} = 0.01$ , $\mathcal{X} = 100$ , and $\mathcal{S} = 1$ . . . . .	70
3.13	Constant pressure region solution + toughness dominance: fluid pressure profile $\Pi(\xi)$ , $\mathcal{K} = 0.4$ , $\mathcal{M} = 0.01$ , $\mathcal{X} = 100$ , and $\mathcal{S} = 1$ . . . . .	71
3.14	Comparison with analytical solution found by Detournay and Garagash (2003): fluid displacement function profile $\Upsilon(\xi)$ for the case of $v_{DG} \ll 1$ . The simulations were performed for $\mathcal{K} = 4$ , $\mathcal{M} = 1$ , $\mathcal{X}/\mathcal{S} = 10^{12}$ , and 1) $\mathcal{S} = 100$ , $\Lambda = 1.86 \times 10^{-6}$ ; 2) $\mathcal{S} = 1.0$ , $\Lambda = 2.0 \times 10^{-6}$ ; 3) $\mathcal{S} = 0.2$ , $\Lambda = 2.25 \times 10^{-6}$ ; 4) $\mathcal{S} = 0.01$ , $\Lambda = 4.4 \times 10^{-6}$ . . . . .	72
3.15	Comparison with analytical solution found by Detournay and Garagash (2003): fluid pressure profile $\Pi(\xi)$ for the case of $v_{DG} \ll 1$ . The simulations were performed for $\mathcal{K} = 4$ , $\mathcal{M} = 1$ , $\mathcal{X}/\mathcal{S} = 10^{12}$ , and 1) $\mathcal{S} = 100$ , $\Lambda = 1.86 \times 10^{-6}$ ; 2) $\mathcal{S} = 1.0$ , $\Lambda = 2.0 \times 10^{-6}$ ; 3) $\mathcal{S} = 0.2$ , $\Lambda = 2.25 \times 10^{-6}$ ; 4) $\mathcal{S} = 0.01$ , $\Lambda = 4.4 \times 10^{-6}$ . . . . .	73
3.16	Comparison with analytical solution found by Detournay and Garagash (2003): fluid displacement function profile $\Upsilon(\xi)$ for the case of $v_{DG} \gg 1$ . The simulations were performed for $\mathcal{K} = 4 \times 10^4$ , $\mathcal{M} = 10^8$ , $\mathcal{X}/\mathcal{S} = 10^{20}$ : 1) $\mathcal{S} = 10^9$ , $\Lambda = 187$ ; 2) $\mathcal{S} = 3.3 \times 10^6$ , $\Lambda = 207.5$ ; 3) $\mathcal{S} = 10^6$ , $\Lambda = 227$ ; 4) $\mathcal{S} = 3.3 \times 10^4$ , $\Lambda = 318$ . . . . .	74

3.17	Comparison with analytical solution found by Detournay and Garagash (2003): fluid pressure profile $\Pi(\xi)$ for the case of $v_{DG} \gg 1$ . The simulations were performed for $\mathcal{K} = 4 \times 10^4$ , $\mathcal{M} = 10^8$ , $\mathcal{X}/\mathcal{S} = 10^{20}$ : 1) $\mathcal{S} = 10^9$ , $\Lambda = 187$ ; 2) $\mathcal{S} = 3.3 \times 10^6$ , $\Lambda = 207.5$ ; 3) $\mathcal{S} = 10^6$ , $\Lambda = 227$ ; 4) $\mathcal{S} = 3.3 \times 10^4$ , $\Lambda = 318$ . . . . .	75
3.18	Illustration of diffusion length scale . . . . .	76
3.19	Pore pressure distribution $-1 + \Pi_d(\xi, z/\ell_d)$ , $\mathcal{K} = \mathcal{M} = \mathcal{X} = \mathcal{S} = 1$ , and $\eta = 0.5$ . . . . .	77
3.20	Pore pressure distribution $-1 + \Pi_d(\xi, z/\ell_d)$ (lag region), $\mathcal{K} = \mathcal{M} = \mathcal{X} = \mathcal{S} = 1$ , and $\eta = 0.5$ . . . . .	78
3.21	Pore pressure distribution $-1 + \Pi_d(\xi, z/\ell_d)$ (far-field), $\mathcal{K} = \mathcal{M} = \mathcal{X} = \mathcal{S} = 1$ , and $\eta = 0.5$ . . . . .	79
4.1	Sketch of auxiliary problem . . . . .	81
4.2	Stationary tip: flux distribution function $\phi \equiv \sqrt{s}\tilde{\psi}$ vs $\zeta$ . . . . .	89
4.3	Stationary tip: normal component of stress $\tilde{\Xi}_{zz}$ behind tip, $\zeta > 0$ . . . .	90
4.4	Stationary tip: pressure distribution $\tilde{\Pi}$ ahead of tip, $\zeta < 0$ . . . . .	91
4.5	Stationary tip: parallel component of stress $\tilde{\Xi}_{xx}$ ahead of tip, $\zeta < 0$ . . .	92
4.6	Stationary tip: backstress distribution $\tilde{\Xi}_{zz}$ vs $\zeta$ . . . . .	93
4.7	Normalized flux distribution function $\psi(\xi, \tau)/\psi(0, \tau)$ in time domain for different times: $\tau = 0.0004, 0.01, 0.04, 0.09, 0.25, 0.5, 1.0, 10.0$ . Solid lines for $\tau = 0.0004, 0.01, 0.04, 0.09$ were obtained from inverse Laplace transform of the tip solution; dashed thick lines are numerical solutions of the global problem; solid line $(1 - \xi^2)^{-1/2}$ is the large-time asymptote; and dashed thin lines mark diffusion length scale for $\tau = 0.0004, 0.01, 0.04, 0.09$ and located at $\xi = 1 - \sqrt{\tau}$ . . . . .	94
4.8	Total fluid displacement function $\Psi$ vs time $\tau$ . . . . .	97

4.9	Backstress $\Xi$ vs time $\tau$ for different spacial points: $\xi = 0, 0.95, 1.05, 1.95$	98
4.10	Spatial distribution of backstress $\Xi$ for small time, $\tau = 10^{-4}$	99
4.11	Spatial distribution of backstress $\Xi$ for large time, $\tau = 10^5$	100
4.12	Far-field spatial distribution of backstress $\Xi$ for different times: $\tau =$ 0.1, 1.0, 10	100
5.1	Parametric space	111
5.2	Physical interpretation of the difference between $K_0$ - and $K_\infty$ -vertices	116
5.3	Fracture radius $\rho$ vs time $\tau$ : general case $G_v = G_c = 1, \eta = 0.0, 0.25, 0.5$	117
5.4	Fracturing fluid pressure $\Pi$ vs time $\tau$ : general case $G_v = G_c = 1, \eta =$ 0.0, 0.25, 0.5	118
5.5	Hydraulic fracturing efficiency $\mathcal{E}$ vs time $\tau$ : general case $G_v = G_c = 1,$ $\eta = 0.0, 0.25, 0.5$	119
5.6	Fracture radius $\rho$ vs time $\tau$ : $G_v = 10^{-5}, G_c = 10, \eta = 0.0, 0.25, 0.5$ . Here fracture goes through $\tilde{K}_{\kappa 0}$ -vertex	120
5.7	Fracturing fluid pressure $\Pi$ vs time $\tau$ : $G_v = 10^{-5}, G_c = 10, \eta =$ 0.0, 0.25, 0.5. Here fracture goes through $\tilde{K}_{\kappa 0}$ -vertex	121
5.8	Hydraulic fracturing efficiency $\mathcal{E}$ vs time $\tau$ : $G_v = 10^{-5}, G_c = 10, \eta =$ 0.0, 0.25, 0.5. Here fracture goes through $\tilde{K}_{\kappa 0}$ -vertex	122
5.9	Fracture radius $\rho$ vs time $\tau$ : $G_v = 10^{-15}, G_c = 3 \times 10^{-11}, \eta = 0.0, 0.5$ . Here fracture goes through $\tilde{K}_{\sigma 0}$ -vertex	123
5.10	Fracturing fluid pressure $\Pi$ vs time $\tau$ : $G_v = 10^{-15}, G_c = 3 \times 10^{-11},$ $\eta = 0.0, 0.5$ . Here fracture goes through $\tilde{K}_{\sigma 0}$ -vertex	124
5.11	Hydraulic fracturing efficiency $\mathcal{E}$ vs time $\tau$ : $G_v = 10^{-15}, G_c = 3 \times 10^{-11},$ $\eta = 0.0, 0.5$ . Here fracture goes through $\tilde{K}_{\sigma 0}$ -vertex	125
5.12	Fracture radius $\rho$ vs time $\tau$ : $G_v = 10^{-30}, G_c = 10^{-10}, \eta = 0.0, 0.5$ . Here fracture goes through $\tilde{K}_{\kappa 0}$ - and $\tilde{K}_{\sigma 0}$ -vertices	126

5.13	Fracturing fluid pressure $\Pi$ vs time $\tau$ : $G_v = 10^{-30}$ , $G_c = 10^{-10}$ , $\eta = 0.0, 0.5$ . Here fracture goes through $\tilde{K}_{\kappa 0}$ - and $\tilde{K}_{\sigma 0}$ -vertices . . . . .	127
5.14	Hydraulic fracturing efficiency $\mathcal{E}$ vs time $\tau$ : $G_v = 10^{-30}$ , $G_c = 10^{-10}$ , $\eta = 0.0, 0.5$ . Here fracture goes through $\tilde{K}_{\kappa 0}$ - and $\tilde{K}_{\sigma 0}$ -vertices . . . . .	127
6.1	Parametric space . . . . .	134
6.2	Fracture radius $\gamma$ vs time $\tau$ : $G_v = 1$ . . . . .	140
6.3	Fracture opening at the injection point $\Omega(0)$ vs time $\tau$ : $G_v = 1$ . . . . .	141
6.4	Fracturing fluid displacement function at the injection point $\Upsilon(0)$ vs time $\tau$ : $G_v = 1$ . . . . .	142
6.5	Fracture radius $\gamma$ vs time $\tau$ : $G_v = 10^{-10}$ . . . . .	143
6.6	Fracture opening at the injection point $\Omega(0)$ vs time $\tau$ : $G_v = 10^{-10}$ . . . . .	144
6.7	Fracturing fluid displacement function at the injection point $\Upsilon(0)$ vs time $\tau$ : $G_v = 10^{-10}$ . . . . .	145
6.8	Fracture opening profile: $M$ -vertex, $G_v = 10^{-10}$ . . . . .	146
6.9	Fracturing fluid pressure profile: $M$ -vertex, $G_v = 10^{-10}$ . . . . .	147
6.10	Fracturing fluid displacement function profile: $M$ -vertex, 1D diffusion, $G_v = 10^{-10}$ . . . . .	147
6.11	Fracture opening profile: $\tilde{M}_0$ -vertex, $G_v = 10^{-10}$ . . . . .	148
6.12	Fracturing fluid pressure profile: $\tilde{M}_0$ -vertex, $G_v = 10^{-10}$ . . . . .	148
6.13	Fracturing fluid displacement function profile: $\tilde{M}_0$ -vertex, $G_v = 10^{-10}$ . . . . .	149
6.14	Fracture opening profile: $\tilde{M}_\infty$ -vertex, $G_v = 10^{-10}$ . . . . .	149
6.15	Fracturing fluid pressure profile: $\tilde{M}_\infty$ -vertex, $G_v = 10^{-10}$ . . . . .	150
6.16	Fracturing fluid displacement function profile: $\tilde{M}_\infty$ -vertex, $G_v = 10^{-10}$ . . . . .	150
6.17	Fracture radius $\gamma$ vs time $\tau$ : $G_v = 10^6$ . . . . .	151
6.18	Fracturing fluid displacement function at the injection point $\Upsilon(0)$ vs time $\tau$ : $G_v = 10^6$ . . . . .	151



6.19	Fracturing fluid displacement function profile: $M$ -vertex, 3D diffusion,	
	$G_v = 10^6$ . . . . .	152
B.1	Sketch of numerical integration . . . . .	183

# Chapter 1

## Introduction

### 1.1 Context

Hydraulic fracturing is a process by which a fracture is initiated and propagated in a rock mass by injection of a pressurized fluid from a borehole. A natural example of hydraulic fracturing is a magma-driven dike, which can reach kilometers in length (Lister and Kerr, 1991). Hydraulic fracturing is widely used in industry, for example, stimulation of hydrocarbons reservoirs, disposal of liquids (e.g. production water in the oil industry, supercritical CO<sub>2</sub>, and liquid waste), and preconditioning of rock masses in the mining industry.

Let us consider in more details an example of stimulation of an oil reservoir by hydraulic fracturing (HF) (Economides and Nolte, 2000). First, a fluid with low viscosity (the “pad”) is used to break down the rock and initiate propagation of a crack. Low viscosity is necessary to reduce frictional losses in the well. After propagation is established, special agents (such as high-density polymers and crosslinkers) are added in order to increase viscosity to up to 1000 times that water, and enhance the creation of a filter cake on the fracture walls to reduce fluid losses. The fracturing fluid is followed

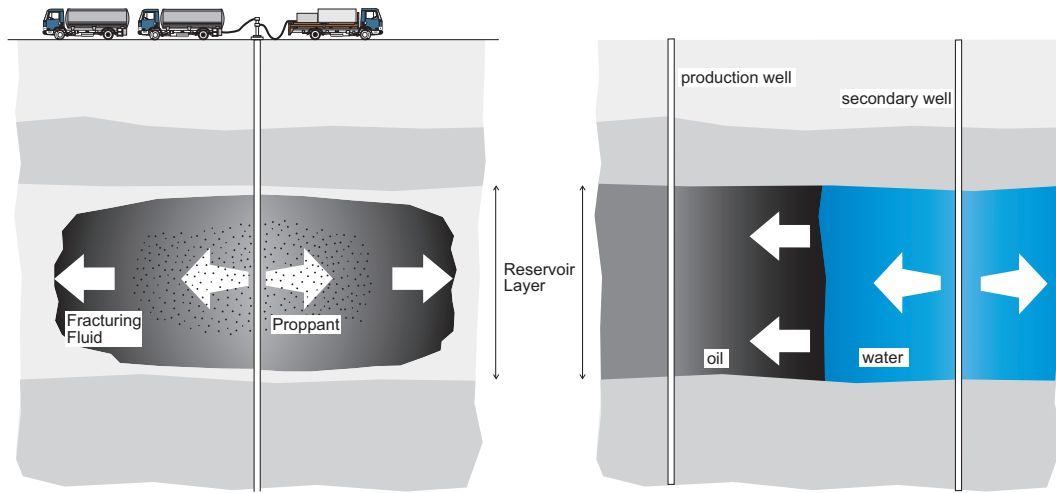


Figure 1.1: Hydraulic fracturing vs waterflooding [after Adachi (2001)]

by a slurry of fluid carrying propping materials (the “proppant”). The function of the proppant (e.g., coarse sand) is to hold the fracture open after the hydraulic fracturing treatment is completed in order to provide a high-permeability channel for the hydrocarbons (oil or gas). The last step of the treatment is the cleanup of the well. For this purpose, breaking agents are injected in order to break down the polymer chains. The resulting thin fluid is pumped out, leaving the proppant in place. This procedure can take up to one day. Obviously, one would like to create a fracture that is as long as possible using the least amount of fracturing fluid. At the same time, the fracture should be wide enough in order to place the proppant inside the fracture.

Another interesting example from the oil industry is a postprimary recovery method called waterflooding (WF) (Craig, 1971; Thakur et al., 2003). After the main recovery period, when the efficiency of a production well drops significantly, water is pumped into the reservoir through secondary wells which surround the production well. This water pushes the oil toward the production well, thus increasing its efficiency. The treatment can last for several months. The objective of this treatment is to inject into the reservoir

as much fluid as fast as possible. Some investigations indicate that the formation of a fracture improves the efficiency of the treatment (Craig, 1971; Thakur et al., 2003).

In both examples, a fluid-driven fracture propagates through a permeable medium and in both cases we have some fluid losses due to the infiltration of the fracturing fluid into the medium. This process is referred to as leak-off. Despite their apparent similarities, the two problems are different: the fracturing fluids have vastly different viscosities and treatment times differ significantly. Additionally, the leak-off phenomenon is evidently desirable in waterflooding recovery operations, while it is not in the hydraulic fracturing treatments. It is apparent that these two “similar” problems are in fact quite different from a physical point of view. Indeed, one can often assume [Adachi et al. (2007)] that during an HF treatment, viscous dissipation associated with the flow of the fracturing fluid dominates over the energy dissipation associated with the rock damage, whereas during a WF treatment the situation seems to be the opposite. Thus, for the modeling of HF, toughness – a measure of the energy required to crack the solid, can often be taken to be equal to zero, whereas for modeling of WF the fracturing fluid viscosity can be taken to be equal to zero. These two limits were studied in a series of papers where they were called the viscosity- and toughness-dominated regimes of fracture propagation [see Detournay (2004) for a summary]. In particular, it was shown that for a Newtonian fluid the viscosity-dominated regime is valid for short treatments, whereas the toughness-dominated regime is expected for long treatments.

The other significant difference between the HF and WF treatments is in the diffusion pattern. As illustrated in Fig.1.2, during an HF treatment when the fluid losses are minimized, the diffusion explores only a narrow neighborhood around the fracture, i.e., the pore fluid pressure changes only in the boundary layer adjacent to the fracture. If the width of this boundary layer is small enough compared to the fracture size, the diffusion pattern is one-dimensional, and the mathematical model can be simplified significantly.

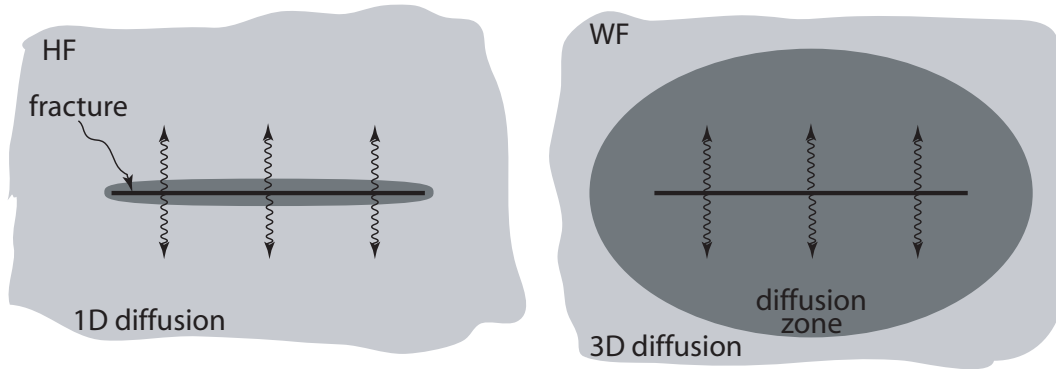


Figure 1.2: Diffusion patterns

In contrast to HF, a WF treatment can be characterized by a rather large diffusion zone, the size of which is at least of the order of the fracture size (see Fig.1.2). In this case we say that the diffusion is three-dimensional. An interesting consequence of such large-scale diffusion is the following: as the fracturing fluid infiltrates into the porous rock, the rock dilates and attempts to close the fracture. Mathematically, this means that additional confining stress is generated.

Most papers on hydraulic fracturing simulation assume the first, one-dimensional, diffusion pattern. The theoretical modeling of such a one-dimensional fluid leak-off was developed by Carter (1957). The Carter's leak-off model also takes into account formation of a low permeability cake build-up on the fracture walls, resulting from the fracturing fluid infiltration. This theory proved to be very efficient for modeling HF (Economides and Nolte, 2000). At the same time, it is obvious that the Carter's leak-off model is not applicable to three-dimensional cases like WF. Development of a theory describing the propagation of a fluid-driven fracture with large scale-diffusion is the *raison d'être* of the present research.

## 1.2 Models

Modeling a fluid-driven fracture propagation is a challenging problem. The mathematical formulation of the problem is represented by a set of nonlinear integro-differential equations. Also, the problem has a moving boundary where the governing equations degenerate and become singular. The complexity of the problem often restricts researchers to consider only simple fracture geometries. The most widely used ones are (see Fig.1.3): i) the plane strain or KGD model introduced by Khristianovic and Zheltov (1955) and Geertsma and de Klerk (1969), which assumes that crack deformation and propagation occurs under plane strain conditions; ii) the PKN model, introduced by Perkins and Kern (1961) and Nordgren (1972), which assumes an elliptically shaped cross-section fracture of constant height (plane strain deformation is assumed within a vertical cross-section), and localization of the elasticity equation, leading to a simple proportionality relationship between the fracture aperture and the fluid pressure; and iii) the penny-shaped or radial model, which assumes a crack propagating symmetrically with respect to the well perpendicular to it.

3D diffusion was first introduced into the modeling of a fluid-driven fracture by Hagoort et al. (1980). The authors studied a KGD fracture propagating through a porous medium by assuming a homogeneous pressure distribution inside the crack and by adopting Darcy's law to describe the fracturing fluid flow through the porous medium. As a result, the pore fluid pressure evolution is governed by a diffusion equation. The problem was solved numerically through the discretization of a relatively large domain around the fracture. Some further development of this model was carried out by several authors including Gordeyev (1993); Gordeyev and Entov (1997); Murdoch and Germanovich (2006), and Mathias and Reeuwijk (2009).

Gordeyev (1993) approached the problem analytically. Starting from the general

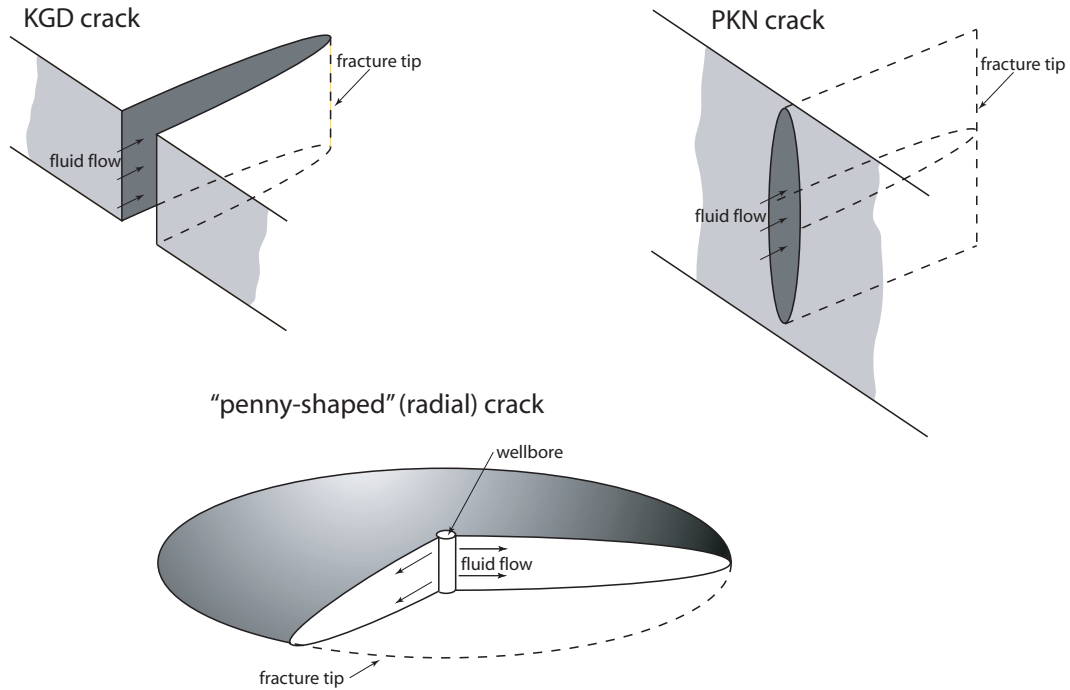


Figure 1.3: Different hydraulic fracturing models [after Adachi (2001)]

equations of poroelasticity introduced by Biot (1941), Gordeyev derived a set of equations governing the propagation of an axisymmetric/plane strain hydraulic fracture in a poroelastic medium. The set of governing equations was solved explicitly only in the case of the penny-shaped geometry and for large times, when the fracture propagation terminates. Gordeyev and Entov (1997) examined the propagation of penny-shaped and plane strain fractures as well. Instead of introducing a propagation criterion, the authors postulated that the fracture length evolves according to the square root of time. However, this time-dependence of the fracture length is not appropriate for the problem under consideration. An interesting work was published by Mathias and Reeuwijk (2009), who studied the case of a “stationary” 3D leak-off. These authors considered the case of very slow propagation of a fluid-driven fracture assuming the pore pressure around the fracture to be always in equilibrium. Of the papers mentioned here, only

Gordeyev (1993) has studied some poroelastic effects like the generation of an additional confining stress due to the dilation of the medium.

Some numerical simulations of KGD fracture propagation through a poroelastic medium were performed by Boone and Ingraffea (1990) and Boone et al. (1991). It was concluded there that the poroelastic effects can have a significant influence on a hydraulic fracture propagation. For example, it was shown that poroelastic mechanisms i) contribute to an increase of the breakdown pressure, ii) can cause the pressure at closure to be significantly greater than that of the minimum in situ stress, iii) affect the re-opening pressure, and iv) influence the process of fracture closure and reopening, in that the fracture was observed to close progressively from the tip back towards the borehole, whereas in the absence of the poroelastic effects it first pinches near the borehole.

It is also worthwhile to mention studies on non-hydraulic fractures in poroelastic/thermoelastic materials done by Atkinson and Craster (1991, 1992); Craster and Atkinson (1994, 1996) and other authors. These papers dealt either with stationary or semi-infinite fractures. In both cases the problem is linear and can be effectively solved using integral transforms.

### 1.3 First glance at a “simple” mathematical model

Models of hydraulic fracturing aim to predict the evolution of the fracturing fluid pressure at the inlet, the fracture length and the aperture field. In this research, we study the influence of 3D diffusion and the related poroelastic effects on the propagation of a fracture. Physically, one would expect to find the following effects: i) a decrease in the fracture opening and/or an increase of the fracturing fluid pressure due to the porous medium dilation and ii) an arrest of the fracture propagation at large times due to the balance between the fracturing fluid injection rate and the leak-off rate.

It is worth noting that in the case of 1D diffusion fracture arrest is impossible.



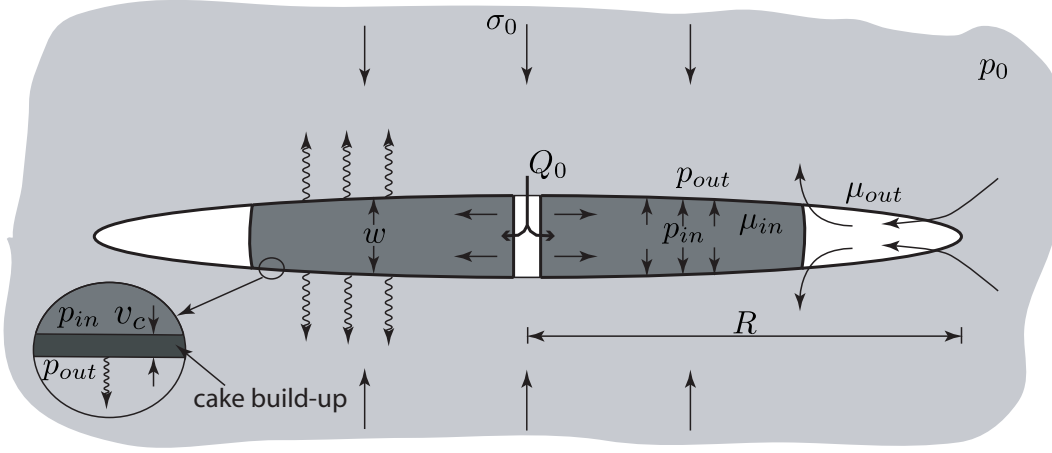


Figure 1.4: Sketch of the problem

Indeed, when diffusion is one-dimensional, the fluid leak-off rate at a given position of the fracture depends only on the fracturing fluid pressure history at this position and does not depend on the pressure in the adjacent regions. As time elapses, the leak-off rate at each position decreases proportionally to  $1/\sqrt{t}$ , where  $t$  is time; therefore, a balance between the fluid injection and leak-off is not possible.

In this research we aim to gain a physical understanding of the processes under investigation rather than to develop a numerical solution of the general case. For this reason we mainly concentrate on studying the particular propagation regimes in which certain physical processes overshadow other ones. For example, if the energy dissipation due to the fluid viscosity dominates over the energy dissipation due to the rock toughness we say that the fracture propagates in the viscosity-dominated regime. During its evolution, a fracture can go through different propagation regimes, and we would like to know what are the intrinsic parameters that govern fracture propagation, namely when a given propagation regime is valid, which parameters govern transitions between different regimes, and what are the characteristic times of these transitions.

From here on we consider a penny-shaped fracture driven by the injection of an incompressible Newtonian fluid with viscosity  $\mu_{\text{in}}$ , at a constant rate  $Q_0$  (see Fig.1.4). The fracturing fluid infiltrates into the porous medium and, as a result, a low permeability cake builds up on the walls of the fracture. The crack propagates through an infinite, homogeneous, brittle, poroelastic rock saturated by a fluid with the same viscosity  $\mu_{\text{out}}$  as the filtrate, i.e., these fluids are physically indistinguishable inside the medium. The medium is characterized by Young's modulus  $E$ , Poisson's ratio  $\nu$ , fracture toughness  $K_{Ic}$ , intrinsic permeability  $\kappa$ , storage coefficient  $S$ , Biot coefficient  $\alpha$ , a far-field (undisturbed) pore pressure  $p_0$ , and is subjected to a far-field stress  $\sigma_0$ , perpendicular to the fracture plane. We assume the existence of a cavity (lag) separating the fracture front and the fracturing fluid front. The cavity can be fully filled or partially filled (cavitation) with the pore fluid.

It was mentioned above that the diffusion process leads to the porous medium dilation. This dilation can be modeled by the introduction of the so-called backstress. By definition, the backstress would be the stress induced across the fracture plane if the fracture were closed. Studying this backstress is one more goal of this research.

The governing equations are summarized below (see Chapter 2 for details):

- **Lubrication equation**

$$\frac{\partial w}{\partial t} + g + \nabla \cdot \mathbf{q} = 0. \quad (1.1)$$

Here  $t$  is time,  $w(\mathbf{r}, t)$  is the fracture opening,  $g(\mathbf{r}, t)$  is the fluid leak-off rate, and  $\mathbf{q}(\mathbf{r}, t)$  is the “in-plane” fracturing fluid flux inside the fracture given by

$$\mathbf{q}(\mathbf{r}, t) = -\frac{w^3}{12\mu} \nabla p_{\text{in}}, \quad (1.2)$$

where  $p_{\text{in}}$  is the fluid pressure inside the fracture,  $\mu = \mu_{\text{in}}$  in the fracturing fluid filled region, and  $\mu = \mu_{\text{out}}$  in the cavity region. If the cavity is only partially filled with the pore fluid, the fluid pressure in the cavity is equal to zero:  $p_{\text{in}} = 0$ .

- **Elasticity equation**

$$w(\mathbf{r}, t) = \int_{\mathcal{S}(t)} [p_{\text{in}}(\bar{\mathbf{r}}, t) + \sigma_b(\bar{\mathbf{r}}, t) - \sigma_0] \mathcal{L}[\mathcal{S}(t), \mathbf{r}, \bar{\mathbf{r}}] d\bar{\mathbf{r}}. \quad (1.3)$$

Here  $\mathcal{S}(t)$  is the fracture surface,  $\sigma_b$  is the backstress, and  $\mathcal{L}(\mathcal{S}, \mathbf{r}, \bar{\mathbf{r}})$  is the elasticity kernel. In the case of the penny-shaped fracture  $\mathcal{S}(t) = \{r < R(t), z = 0\}$ , where  $\{r, \varphi, z\}$  is a cylindrical coordinate system with the origin at the fracture center and  $R(t)$  is the fracture radius.

- **Propagation criterion**

$$K_I = K_{Ic}, \quad (1.4)$$

where  $K_I$  is the stress intensity factor which can be related to the opening asymptote in the tip region by

$$w(\mathbf{r}, t) \rightarrow \frac{2^{5/2}}{\pi^{1/2}} \frac{K_I}{E'} x^{1/2}, \quad x \rightarrow 0, \quad (1.5)$$

where  $E' \equiv E/(1 - \nu^2)$  is the plane strain modulus and  $x$  is the distance from the fracture tip;

- **Poroelasticity equations**

$$p_{\text{out}}(\mathbf{r}, t) - p_0 = \int_0^t d\bar{t} \int_{\mathcal{S}(\bar{t})} g(\bar{\mathbf{r}}, \bar{t}) p^{\text{si}}(\mathbf{r} - \bar{\mathbf{r}}, t - \bar{t}) d\bar{\mathbf{r}}, \quad (1.6)$$

$$\sigma_b(\mathbf{r}, t) = \int_0^t d\bar{t} \int_{\mathcal{S}(\bar{t})} g(\bar{\mathbf{r}}, \bar{t}) \sigma_b^{\text{si}}(\mathbf{r} - \bar{\mathbf{r}}, t - \bar{t}) d\bar{\mathbf{r}}, \quad (1.7)$$

where  $p_{\text{out}}(\mathbf{r}, t)$  is the pore pressure outside the fracture,  $p^{\text{si}}(\mathbf{r}, t)$  and  $\sigma_b^{\text{si}}(\mathbf{r}, t)$  are the medium responses to an instantaneous point fluid source,  $g^{\text{si}}(\mathbf{r}, t) = \delta(t) \delta(\mathbf{r})$ , and  $\delta(x)$  is the Dirac delta function;

- **Low permeability cake build-up**

– *Fracturing fluid filled region*

$$p_{\text{in}} - p_{\text{out}}|_{\mathbf{r} \in \mathcal{S}(t)} = \frac{v_c}{\kappa_c} g, \quad (1.8)$$

where  $\kappa_c$  is the permeability of the cake,  $v_c$  is the thickness of the cake given by

$$v_c(\mathbf{r}, t) = \beta \int_0^t g(\mathbf{r}, \bar{t}) d\bar{t}, \quad (1.9)$$

$\beta$  is a dimensionless constant coefficient characterizing the rate of cake buildup relative to the leak-off rate

– *Cavity*

$$p_{\text{in}} - p_{\text{out}}|_{\mathbf{r} \in \mathcal{S}(t)} = 0. \quad (1.10)$$

Our eventual goal is to find the fracture opening profile  $w(\mathbf{r}, t)$ , the leak-off rate profile  $g(\mathbf{r}, t)$ , the fluid pressure distributions  $p_{\text{in}}(\mathbf{r}, t)$  and  $p_{\text{out}}(\mathbf{r}, t)$ , the backstress profile  $\sigma_b(\mathbf{r}, t)$ , and the fracture shape  $\mathcal{S}(t)$ .

## 1.4 On different approaches in hydraulic fracturing studies

One can see that the problem under consideration is highly non-linear and challenging even though we have predefined a simple penny-shaped fracture geometry. Part of the challenge comes from the integral equations (1.3), (1.6), and (1.7) and the time dependence of the integration domain (moving boundary); the other part of the challenge comes from the non-linear structure of the equation governing the fluid flux inside the fracture (1.2).

Papers dealing with theoretical modeling of fluid-driven fractures can conveniently be divided into two main groups. The first group can be characterized by ad-hoc conjectures in the construction of solutions. This group contains such classical works as Khris-tianovic and Zheltov (1955), Geertsma and de Klerk (1969), Perkins and Kern (1961)

and Nordgren (1972), which represent the historical cornerstone of hydraulic fracturing modeling. This group includes studies conducted by Abé et al. (1976); Advani et al. (1987); Biot et al. (1986), who further develop the classical models. Some of these works were built upon inconsistent assumptions, however. For example, Advani et al. (1987) adopted the incompatible assumptions of viscosity domination in energy dissipation and uniform fracturing pressure distribution along the crack (Detournay, 2004).

The second group contains papers mostly written from the early 1990's and which aim to construct a rigorous solution to the non-linear set of integro-differential equations representing the problem. The papers within this group are hinged on scaling and asymptotic analysis (Detournay, 2004), and they address the following features of the problem: i) the moving boundary and degeneration of the governing equations at this boundary, and ii) the strong dependence of the set of the physical processes involved into the propagation of the fracture on the problem parameters like viscosity, toughness, permeability of the hosting medium, treatment time etc. (see Section 1.1 ). The latter property is related to the multiple time scale nature of the problem (Detournay, 2004). Let us consider each of these features in more detail.

### **Tip region**

As already stated, the governing equations degenerate in the tip region, and the solution of these equations is singular. As a result, the question of appropriate boundary conditions arises. The problem of boundary conditions is especially important for numerical modeling of a fluid-driven fracture propagation. The original approach to tackle this problem consisted in adopting the square root tip asymptote ( $w \sim x^{1/2}$ , where  $x$  is the distance from the tip) that is predicted by linear elastic fracture mechanics. This tip asymptote, referred to as the toughness-dominated asymptote, depends only on the elastic modulus and on the toughness of the hosting medium. However, it is clear that this

tip asymptote is not appropriate in the limiting case of zero rock toughness. Spence and Sharp (1985) and later Lister (1990) observed that in this case the tip solution is of the form  $w \sim x^{2/3}$ , due to the coupling of lubrication theory and linear elasticity. This particular asymptotics was further studied by Desroches et al. (1994), who demonstrated that  $w \sim x^{2/3}$ , is also the solution of a semi-infinite hydraulic fracture propagating steadily in a zero toughness impermeable elastic solid. This stationary solution depends only on the fracturing fluid viscosity, the elastic modulus of the medium, and the tip velocity and it is called the viscosity-dominated asymptote. The authors suggested that the tip region of a finite fracture is equivalent to a steadily propagating semi-infinite fracture. A rigorous justification of this assumption in the case of an impermeable rock was provided by Garagash and Detournay (2005). In this research we will show that in the case of 3D diffusion, the tip region of a finite fracture cannot, in general, be modeled by a steadily propagating semi-infinite fracture.

In addition, Desroches et al. (1994) (and also Carbonell et al. (1999)) introduced a criterion based on the consideration of energy dissipation, that shows which asymptote (viscosity- or toughness-dominated) should be used. Namely, if energy dissipation is mainly associated with viscous flow, then the viscosity-dominated tip asymptote should be used, otherwise, when energy dissipation is mainly due to the creation of new surfaces in the solid material, the toughness-dominated tip asymptote is the proper choice.

In studying the propagation of a hydraulic fracture in a permeable medium (the Carter's leak-off) with zero toughness, Lenoach (1995) has found one more tip asymptote,  $w \sim x^{5/8}$ . A natural question arises: under which conditions should each asymptote be used? The first understanding of this problem came with the recognition of the multiscale nature of the tip region. Thus, Garagash and Detournay (2000) have shown that the solution of a semi-infinite fluid-driven fracture propagating through an impermeable medium can be characterized by a single length scale  $\ell_{mk}$ . This length scale is a function

of the fluid viscosity, the material toughness, the elastic modulus and the propagation velocity. If  $x \ll \ell_{mk}$ , then the solution is given by the toughness-dominated asymptote, whereas for  $x \gg \ell_{mk}$  the solution is given by the viscosity-dominated one. Moreover, the authors developed a numerical solution for the intermediate region,  $x \sim \ell_{mk}$ . Experimental validation of this result was reported by Bungier and Detournay (2008), who studied the propagation of a penny-shaped hydraulic fracture through an impermeable medium (polymethyl methacrylate (PMMA) and glass).

Applying the results of Garagash and Detournay (2000) one arrives at the following criterion of choosing a relevant asymptote: if the size of the fracture is small compared to the characteristic length scale  $\ell_{mk}$ , the toughness-dominated asymptote should be used, otherwise, if the size of the fracture is large compared to  $\ell_{mk}$ , the viscosity-dominated asymptote should be used. In the latter case the toughness-dominated region, which is small compared to  $\ell_{mk}$ , plays the role of a boundary layer near the tip of the fracture (Garagash and Detournay, 2005).

An important property of the tip solution is its dependence on the tip velocity. This dependence plays a key role during matching the tip solution to the global one (Adachi, 2001; Madyarova, 2003). Moreover, one can encounter a situation in which the tip solution changes its nature during the fracture propagation. For example, in the case of a penny-shaped fracture driven by a Newtonian fluid (Savitski and Detournay, 2002), the viscosity-dominated asymptote is applicable only at small times, whereas for large times the toughness-dominated asymptote is the correct one.

Further, Detournay et al. (2002) and Garagash et al. (2009) have shown that in the case of a permeable medium the 5/8 tip asymptote found by Lenoach (1995) can appear at a length scale, which is intermediate to the ones of the toughness- and viscosity-dominated asymptotes. In other words, the incorporation of new physical processes leads to the appearance of new length scales. In turn, the overlapping of different length

scales can lead to a complicated structure of the tip asymptote.

### Multiple time scales

In Section 1.1 we have illustrated that different hydraulic fracturing applications can involve different physical processes. Thus, for example, for short treatments the diffusion process has a 1D diffusion pattern, whereas for long treatments it has a 3D pattern (see Fig.1.2). To quantify the influence of a particular physical process, one can introduce a characteristic time or length scale. In the case of diffusion, the characteristic length scale is  $\ell_d \sim \sqrt{cT}$ , and the characteristic time scale is  $t_d \sim L^2/c$ , where  $c$  is the diffusion coefficient,  $T$  is the treatment time or another time scale of interest, and  $L$  is the fracture size. If  $\ell_d \ll L$  or  $t_d \ll T$  the diffusion pattern is 1D, otherwise if  $\ell_d \gtrsim L$  or  $t_d \gtrsim T$  it is 3D. The diffusion time scale  $t_d$  also can be called the characteristic time of the transition from 1D to 3D diffusion.

A transition time can also be introduced when two competitive processes are considered. For example, in the case of a penny-shaped fracture driven by a Newtonian fluid (Savitski and Detournay, 2002) there exists a competition between energy dissipation associated with the material toughness and energy dissipation associated with the fracturing fluid viscosity. The transition time scale  $t_{mk}$  is such that for times  $t \ll t_{mk}$  the viscosity is the main source of the energy dissipation, and for large times  $t \gg t_{mk}$  the toughness is the main source.

Another example of competitive processes is the storage of the injected fracturing fluid inside the fracture versus the fracturing fluid leak-off. Again, there is a time scale  $t_{m\tilde{m}}$  [KGD fracture, (Adachi, 2001)] such that for times which are small compared to this  $t_{m\tilde{m}}$ , the main part of the injected fluid is stored inside the fracture and the leak-off process can be neglected whereas for large times  $t \gg t_{m\tilde{m}}$  the situation is the opposite, i.e., the main part of the injected fluid leaks into the formation.



One can see that in the case of a simple geometry, propagation of a hydraulic fracture can be characterized by a set of transition times  $t_i$ . We define a propagation regime as a limiting case of the fracture propagation during which either  $t \ll t_i$  or  $t \gg t_i$  for each transition time  $t_i$  (Detournay, 2004). For example, in the case of a penny-shaped fracture propagating through an impermeable medium (Savitski and Detournay, 2002) we have only one transition time  $t_{mk}$  and two propagation regimes:  $t \ll t_{mk}$  called the viscosity-dominated regime, and  $t \gg t_{mk}$  – the toughness-dominated regime.

In the case of a penny-shaped fracture propagating through a permeable medium (the Carter’s leak-off model), we already have four propagation regimes and four characteristic transition times (Madyarova, 2003) (but only two transition times are independent). These regimes are  $M$ , the storage-viscosity-dominated regime;  $K$ , the storage-toughness-dominated regime;  $\tilde{M}$ , the leak-off-viscosity-dominated regime; and  $\tilde{K}$ , the leak-off-toughness-dominated regime. The corresponding transition times can be denoted by  $t_{mk}$ ,  $t_{m\tilde{m}}$ ,  $t_{k\tilde{k}}$ , and  $t_{\tilde{m}\tilde{k}}$ . Each of the propagation regimes introduced above can be characterized in terms of the transition times as follows:  $M$ ,  $t \ll t_{mk}$  and  $t \ll t_{m\tilde{m}}$ ;  $K$ ,  $t \gg t_{mk}$  and  $t \ll t_{k\tilde{k}}$ ;  $\tilde{M}$ ,  $t \ll t_{\tilde{m}\tilde{k}}$  and  $t \gg t_{m\tilde{m}}$ ; and  $\tilde{K}$ ,  $t \gg t_{\tilde{m}\tilde{k}}$  and  $t \gg t_{k\tilde{k}}$ . A nice property of a propagation regime is that in the case of a simple fracture geometry, such as the ones introduced in Section 1.2, and simple boundary conditions (for example fracturing at a constant injection rate), the solution of the problem is self-similar (Detournay, 2004).

It is convenient to represent the fracture propagation by a trajectory line lying inside a geometrical figure. Each vertex of this figure corresponds to a propagation regime. Along an edge connecting two different propagation regimes, the domination of one physical process is displaced by the domination of another one. In Fig.1.5 we show the parametric space for the case of a penny-shaped fracture propagating through a permeable medium, which we discussed above.

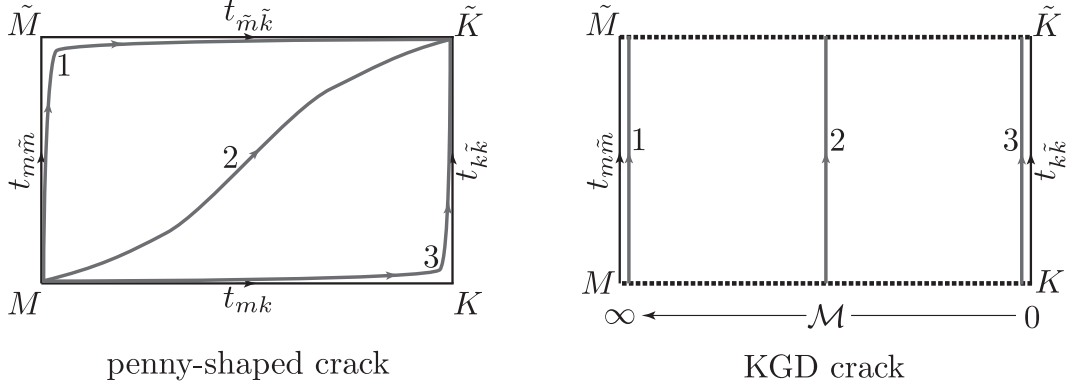


Figure 1.5: Examples of parametric spaces

All trajectories of the fracture propagation start at the  $M$ -vertex and end, for large enough times, at the  $\tilde{K}$ -vertex. If the different time scales are well separated, a trajectory can follow some of the edges of the parametric space. For instance, trajectory 1 illustrates the case  $t_{m\tilde{m}} \ll t_{mk}$ , whereas trajectory 3 demonstrates the opposite case  $t_{mk} \ll t_{k\tilde{k}}$ . Trajectory 2 shows the case when all the transition times are of the same order.

Here, a transition between two different propagation regimes is characterized by a transition time. Alternatively, one can introduce a transition parameter. For example, Savitski and Detournay (2002) used the dimensionless viscosity  $\mathcal{M}$  to describe the transition of a penny-shaped fracture propagation from the viscosity- to toughness-dominated regime. This dimensionless viscosity can be expressed in terms of the transition time  $t_{mk}$  by  $\mathcal{M} = (t/t_{mk})^{-2/5}$ . Thus, for the  $M$ -vertex  $\mathcal{M} = \infty$ , whereas for the  $K$ -vertex  $\mathcal{M} = 0$ . Mathematically, the notion of a transition parameter is more straightforward and more general. Usually transition parameters depend on time, but in some cases they can be time-independent. For instance, Fig.1.5 shows the parametric space of a KGD crack propagating through a permeable medium (the Carter's leak-off model) (Adachi et al., 2002). Here the dimensionless viscosity  $\mathcal{M}$  does not depend on time. As a result, the solution of the problem along the  $MK$ -edge is self-similar. Moreover, for the KGD

geometry, the edge  $\tilde{M}\tilde{K}$  is also self-similar. All trajectories start at the  $MK$ -edge, and end at the  $\tilde{M}\tilde{K}$ -edge. In Fig.1.5 we also trace trajectories 1-3, which are analogous to the ones we discussed in the case of the penny-shaped geometry.

In practice, the different times scales are often well separated. For example, in the case of an HF stimulation of an oil reservoir, the fracture propagates near the  $M$ -vertex,  $T \lesssim t_{m\tilde{m}} \ll t_{mk}$ , where  $T$  is the treatment time (Adachi et al., 2007). Therefore the fracture evolves along the  $M\tilde{M}$ -edge. Another situation takes place in laboratory experiments when  $t_{mk} \ll T \lesssim t_{k\tilde{k}}$  (Adachi et al., 2007). In this case the fracture spends most of its propagation time along the  $K\tilde{K}$ -vertex. In practice, studying of the parametric space and locating the domain of the fracture propagation can significantly simplify modeling the problem under consideration and improve the efficiency of numerical simulations. For example, if it is known that the fracture spends most of its propagation time at the  $K\tilde{K}$ -edge, then, during the numerical simulation it is not necessary to model the fracture propagation along the  $MK$ -edge. Therefore one can start the simulation from the  $K$ -vertex using the self-similar solution at this vertex to define the initial conditions.

## 1.5 Objectives and organization of the research

The main objective of this research is to study the 3D diffusion and the backstress effect. Throughout this study we will intensively use scaling and asymptotic analysis.

In Chapter 2 we formulate the problem mathematically for a penny-shaped geometry. We discuss the main assumptions built in the model, and the restrictions introduced by them.

In Chapter 3 we study a semi-infinite fracture propagating through a poroelastic medium at a constant velocity. We build a semi-analytical solution of the problem, in the sense that we construct the near- and far-field asymptotes, as well as some intermediate ones, and develop a numerical algorithm for the calculation of a transient solution

connecting the analytical asymptotes. We show that, due to the time-dependence of the diffusion length scale, the tip region of a finite fracture is not always equivalent to a steadily propagating semi-infinite fracture (see the details in Chapters 3 and 4).

Through the rest of the research we use the following simplifications: i) there is no cake build-up; and ii) from a diffusion point of view the fracturing fluid pressure distribution is uniform along the fracture. The former assumption means that  $p_{\text{in}} = p_{\text{out}}|_{\mathbf{r} \in \mathcal{S}(t)}$  (further, we simply omit the subscripts “in” and “out”). The latter assumption means that in the diffusion equation (1.6) the fluid pressure in the left-hand side is uniform along the fracture, whereas in the lubrication and elasticity equations it can be nonuniform. This is an appropriate assumption for the toughness-dominated regime, or when the confining stress  $\sigma_0$  is large compared to the far-field pore fluid pressure  $p_0$ . Indeed, the propagation of a hydraulic fracture is driven by the difference between the fracturing fluid pressure and the far-field confining stress,  $p - \sigma_0$ , whereas the diffusion is driven by the difference between the fracturing fluid pressure and the far-field pore pressure,  $p - p_0$ . Therefore if  $\sigma_0 \gg p_0$  then  $p - p_0 \gg p - \sigma_0$ , which means that from a diffusion point of view the fracturing fluid pressure is uniform and equal to the confining stress,  $p \approx \sigma_0$ . Using a uniform pressure distribution we can invert (1.6)

$$v(\mathbf{r}, t) \equiv \int_0^t g(\mathbf{r}, \bar{t}) d\bar{t} = \int_0^t u[\mathcal{S}(\bar{t}), \mathbf{r}, t - \bar{t}] [p(\bar{t}) - p_0] d\bar{t}, \quad (1.11)$$

where  $v(\mathbf{r}, t)$  is the fluid displacement function, the total amount of the fluid leaked-off at time  $t$  through a unit surface of the fracture. The function  $u(\mathcal{S}, \mathbf{r}, t)$  can be considered as the fluid displacement function normal to the surface  $\mathcal{S}$  generated by a uniform unit pulse of pore pressure applied along the surface  $\mathcal{S}$ ,  $p(\mathbf{r} \in \mathcal{S}, t) - p_0 = \delta(t)$ . We can write a similar equation for the backstress.

It is natural to break our “simple” problem into two even simpler ones: i) studying the poroelastic medium response to a uniform pressure pulse generated on a stationary

surface  $\mathcal{S}$  (we refer to this problem as the auxiliary problem); and ii) studying a hydraulic fracture propagation using convolution-type equations similar to (1.11).

Chapter 4 is devoted to the auxiliary problem. In Chapter 5 we study the propagation problem in the case of the toughness-dominated regime, whereas in Chapter 6 we study the viscosity-dominated regime. Finally we summarize the results in Chapter 7.

## Chapter 2

# Mathematical formulation

In this Chapter we introduce the mathematical model, which describes the propagation of a penny-shaped fracture through an infinite poroelastic medium.

### 2.1 Lubrication theory

We assume that there is a cavity (lag) separating the fracture edge and the fracturing fluid front. The cavity can be fully filled or partially filled (cavitation) with pore fluid. In the case of cavitation, the fluid pressure inside the cavity  $p_{\text{in}}$  is taken to be equal to zero,  $p_{\text{in}} = 0$ . Fluid transport in the fluid-filled part of the fracture is governed by the volume balance equation

$$\frac{\partial w}{\partial t} + \frac{\partial v}{\partial t} + \frac{1}{r} \frac{\partial}{\partial r} (rq) = 0, \quad (2.1)$$

and by Poiseuille's law

$$q(r, t) = -\frac{w^3}{12\mu} \frac{\partial p_{\text{in}}}{\partial r}. \quad (2.2)$$

In the above,  $r$  is the radial coordinate of the cylindrical system of coordinate  $\{r, \varphi, z\}$  with the origin at the fracture center,  $t$  is time,  $w(r, t)$  is the fracture opening,  $v(r, t)$  is the integrated fluid leak-off rate or the leak-off displacement function,  $q(r, t)$  is the

fracturing fluid flux inside the fracture,  $p_{\text{in}}(r, t)$  is the fluid pressure inside the fracture, and  $\mu$  is the fluid viscosity taken to be  $\mu = \mu_{\text{in}}$  in the fracturing fluid filled region, and  $\mu = \mu_{\text{out}}$  in the cavity region.

In writing the volume balance equation (2.1) we have neglected the compressibility of the fluid. Indeed, the compliance of the crack  $C_c$ ,  $C_c \sim R/E'$ , is large compared to the fracturing fluid compliance  $C_f$ ,  $C_f \sim w/K_f$ , where  $E' \equiv E/(1 - \nu^2)$  is the plane strain modulus,  $E$  is the Young's modulus,  $\nu$  is the Poisson's ration,  $K_f$  is the bulk modulus of the fracturing fluid, and  $R$  is the fracture radius. Therefore the fracturing fluid compressibility effect is as small as  $wE'/(RK_f) \sim (p_{\text{in}} - \sigma_0)/K_f \lesssim \sigma_0/K_f \ll 1$ , where  $\sigma_0$  is far-field confining stress. For example, for water  $K_f \approx 2.2$  GPa, and for hydraulic fracturing  $\sigma_0 \sim 10$  MPa; the compressibility effect correction is therefore of order of  $10^{-2}$ .

Poiseuille's law (2.2) is valid only for a stationary flow and it does not take into account the inertia effect. Garagash (2006) has shown that the inertia effect is important only at a time scale, which, in the case of hydraulic fracturing, is small compared to the treatment time. Therefore this effect can be dismissed.

The boundary conditions are given by

$$2\pi \lim_{r \rightarrow 0} r q(r, t) = Q_0, \quad w(R(t), t) = v(R(t), t) = q(R(t), t) = 0, \quad (2.3)$$

where  $Q_0$  is the fracturing fluid injection rate. Here we consider times at which the fracture radius  $R(t)$  is large compared to the wellbore radius, therefore we can model the injection by a point source in the center of the fracture [see first equation of (2.3)].

The initial conditions are given by

$$w(r, 0) = v(r, 0) = q(r, 0) = R(0) = 0. \quad (2.4)$$

Strictly speaking, these boundary conditions are only formal and not physical, in a sense that they are introduced from view point of mathematical convenience rather than

from the perspective of a physical problem. Here we would like to reiterate that we are considering only time scales at which the fracture radius  $R(t)$  is large compared to the well bore radius. At these times the exact form of the initial conditions is not important. The only requirement is that the total amount of injected fracturing fluid is correct. Moreover, we expect that a particular similarity solution could act as a small-time asymptote for the problem under consideration. Thus, in practice, this self-similar solution plays the role of initial conditions.

## 2.2 Elasticity equation

The fracture opening  $w$  and the pressure loading  $p_{\text{in}}$  applied to the fracture walls can be related using the linear theory of elasticity. If the response of the medium is purely elastic, then the opening  $w$  can be expressed in terms of the net pressure  $p_{\text{in}} - \sigma_0$ . In order to incorporate the backstress  $\sigma_b$ , we decompose the hydraulic loading and the confining stress as follows:  $\{p_{\text{in}}, \sigma_0 - \sigma_b\} = \{p_{\text{in}} + \sigma_b, \sigma_0\} + \{-\sigma_b, -\sigma_b\}$  (note that  $\sigma_b > 0$  for tensile backstress). Obviously, the second part of the loading,  $\{-\sigma_b, -\sigma_b\}$ , does not make any contribution to the opening. Therefore, the net pressure is equal to  $p_{\text{in}} + \sigma_b - \sigma_0$ .

The relation between the fracture opening and the net pressure can be written through superposition of dislocations (Arin and Erdogan, 1971; Cleary and Wong, 1985)

$$p_{\text{in}}(r, t) + \sigma_b(r, t) - \sigma_0 = -\frac{E'}{R(t)} \int_0^1 \frac{\partial w[sR(t), t]}{\partial s} M\left[\frac{r}{R(t)}, s\right] ds, \quad (2.5)$$

where  $E' \equiv E/(1 - \nu^2)$  is the plane strain modulus,  $E$  is the Young's modulus,  $\nu$  is the Poisson's ration,  $\sigma_b(r, t)$  is the backstress due to the leak-off, and  $M(\xi, s)$  is the elasticity kernel,

$$M(\xi, s) = \frac{1}{2\pi} \begin{cases} \frac{1}{\xi} K\left(\frac{s^2}{\xi^2}\right) + \frac{\xi}{s^2 - \xi^2} E\left(\frac{s^2}{\xi^2}\right), & \xi > s \\ \frac{s}{s^2 - \xi^2} E\left(\frac{\xi^2}{s^2}\right), & s > \xi \end{cases}, \quad (2.6)$$



$K(x)$  and  $E(x)$  are complete elliptic integrals of the first and second kinds (Abramowitz and Stegun, 1972).

Inversion of (2.5) was initially obtained by Sneddon and Lowengrub (1969) in the form of a double integration. Here we use a modified version of this inverse relation (Barr, 1991; Savitski and Detournay, 2002)

$$w(r, t) = \frac{8}{\pi} \frac{R(t)}{E'} \int_0^1 \{p_{\text{in}}[sR(t), t] + \sigma_b[sR(t), t] - \sigma_0\} G\left[\frac{r}{R(t)}, s\right] s ds, \quad (2.7)$$

where

$$G(\xi, s) = \begin{cases} \frac{1}{\xi} F\left(\arcsin \sqrt{\frac{1-\xi^2}{1-s^2}}, \frac{s^2}{\xi^2}\right), & \xi > s \\ \frac{1}{s} F\left(\arcsin \sqrt{\frac{1-s^2}{1-\xi^2}}, \frac{\xi^2}{s^2}\right), & \xi < s \end{cases}, \quad (2.8)$$

$F(\phi, m)$  is the incomplete elliptic integral of the first kind (Abramowitz and Stegun, 1972).

## 2.3 Propagation criterion

The propagation criterion is introduced within the context of linear elastic fracture mechanics (LEFM). The main assumption of LEFM is that the process zone, a region near the fracture tip where behavior of the material is not elastic (e.g. region of plastic deformation, microcracking, *etc.*), is small compared to the fracture size. According to LEFM a fracture can propagate only if the mode I stress intensity factor  $K_I$  exceeds the material toughness  $K_{Ic}$ . Thus in the case of quasi-static fracture propagation we can write the following criterion

$$K_I = K_{Ic}. \quad (2.9)$$

For a penny-shaped fracture, the stress intensity factor  $K_I$  is given by (Sneddon and Lowengrub, 1969)

$$K_I = \frac{2}{\sqrt{\pi}} R^{1/2}(t) \int_0^1 \frac{p_{\text{in}}[sR(t), t] + \sigma_b[sR(t), t] - \sigma_0}{\sqrt{1-s^2}} s ds. \quad (2.10)$$

By accounting for the propagation criterion (2.9), one arrives to the following tip asymptote (Rice, 1968)

$$w(r, t) \rightarrow \frac{2^{5/2}}{\pi^{1/2}} \frac{K_{Ic}}{E'} \sqrt{R(t) - r} \quad \text{as } r \rightarrow R(t). \quad (2.11)$$

## 2.4 Poroelasticity equations

The hosting medium is modelled according to the theory of linear poroelasticity (Biot, 1941). However, we neglect the solid-to-fluid coupling, i.e., we assume that mechanical deformations do not affect the fluid transport through the medium. This simplification was studied by Detournay and Cheng (1991), who have concluded that in the case of hydraulic boundary conditions when the pore pressure is prescribed, the fluid exchange between the fracture and the medium calculated via poroelastic theory is nearly identical to that computed by uncoupled diffusion equation. The assumptions allows us to uncouple pure elastic deformation due to hydraulic loading (introduced in Section 2.2) from the pore pressure diffusion leading to generation of the backstress.

From the hydraulic diffusion point of view the fracture is simply a distributed fluid source  $g(\mathbf{r}, t)$ . It is convenient to decompose this fluid source  $g(\mathbf{r}, t)$ , which is distributed in space and time, into a set of instantaneous point fluid sources  $g^{\text{si}}(\mathbf{r}, t) = \delta(t) \delta(\mathbf{r})$ , where  $\delta(t)$  is the Dirac delta function

$$g(\mathbf{r}, t) = \int_0^t d\bar{t} \int_{\bar{z}=0, \bar{r} < R(\bar{t})} g(\bar{\mathbf{r}}, \bar{t}) g^{\text{si}}(\mathbf{r} - \bar{\mathbf{r}}, t - \bar{t}) d\bar{\mathbf{r}}. \quad (2.12)$$

Due to the linearity of the diffusion equation, the pore pressure field outside the fracture  $p_{\text{out}}(\mathbf{r}, t)$  can be written as

$$p_{\text{out}}(\mathbf{r}, t) - p_0 = \int_0^t d\bar{t} \int_{\bar{z}=0, \bar{r} < R(\bar{t})} g(\bar{\mathbf{r}}, \bar{t}) p^{\text{si}}(\mathbf{r} - \bar{\mathbf{r}}, t - \bar{t}) d\bar{\mathbf{r}}, \quad (2.13)$$

where  $p^{\text{si}}(\mathbf{r}, t)$  is the pore pressure induced by an instantaneous point fluid source  $g^{\text{si}}(\mathbf{r}, t)$  (Cheng and Detournay, 1998). Integration by parts with respect to time yields

$$p_{\text{out}}(\mathbf{r}, t) - p_0 = \int_0^t d\bar{t} \int_{\bar{z}=0, \bar{r} < R(\bar{t})} v(\bar{\mathbf{r}}, \bar{t}) p^{\text{li}}(\mathbf{r} - \bar{\mathbf{r}}, t - \bar{t}) d\bar{\mathbf{r}}, \quad (2.14)$$

where  $v(\mathbf{r}, t) \equiv \int_0^t g(\mathbf{r}, \bar{t}) d\bar{t}$  is the fluid displacement, and  $p^{\text{li}}(\mathbf{r}, t) \equiv \partial p^{\text{si}}(\mathbf{r}, t) / \partial t$ .

Let us discuss the meaning of  $p^{\text{li}}(\mathbf{r}, t)$ . Comparing (2.13) and (2.14) one can see that  $p^{\text{li}}(\mathbf{r}, t)$  is the fluid pressure distribution generated by an instantaneous point fluid dilation  $v^{\text{li}}(\mathbf{r}, t) = \delta(t) \delta(\mathbf{r})$ . This instantaneous point dilation is actually equivalent to the time dipole of a fluid source  $g^{\text{li}}(\mathbf{r}, t) = \delta'(t) \delta(\mathbf{r})$ , where prime means derivative with respect to argument. In other words we have an instantaneous injection of fluid immediately followed by an instantaneous withdrawing of the same amount of fluid at the same point.

A similar equation can be written for the backstress  $\sigma_b(\mathbf{r}, t)$

$$\sigma_b(\mathbf{r}, t) = \int_0^t d\bar{t} \int_{\bar{z}=0, \bar{r} < R(\bar{t})} v(\bar{\mathbf{r}}, \bar{t}) \sigma_{zz}^{\text{li}}(\mathbf{r} - \bar{\mathbf{r}}, t - \bar{t}) d\bar{\mathbf{r}}. \quad (2.15)$$

The pore pressure field  $p^{\text{li}}(\mathbf{r}, t)$  and the stress field  $\sigma_{zz}^{\text{li}}(\mathbf{r}, t)$  induced by an instantaneous point fluid dilation  $v^{\text{li}}(\mathbf{r}, t)$  are given by (Cheng and Detournay, 1998)

$$p^{\text{li}}(\mathbf{r}, t) = \frac{2c^2}{\pi^{3/2}\kappa} \frac{1}{|\mathbf{r}|^5} \left( 2 \frac{|\mathbf{r}|^2}{4ct} - 3 \right) \left( \frac{|\mathbf{r}|}{\sqrt{4ct}} \right)^5 \exp \left( -\frac{|\mathbf{r}|^2}{4ct} \right), \quad (2.16)$$

$$\sigma_{zz}^{\text{li}}(\mathbf{r}, t) = \frac{\eta c}{2\pi\kappa} \frac{1}{|\mathbf{r}|^3} \left[ \delta(t) + \frac{16c}{\sqrt{\pi}} \frac{1}{|\mathbf{r}|^2} \left( 1 - \frac{|\mathbf{r}|^2}{4ct} \right) \left( \frac{|\mathbf{r}|}{\sqrt{4ct}} \right)^5 \exp \left( -\frac{|\mathbf{r}|^2}{4ct} \right) \right], \quad (2.17)$$

where  $c$  is the diffusion coefficient,  $\kappa$  is the permeability,  $\eta = \alpha(1 - 2\nu) / (2 - 2\nu)$ , and  $\alpha$  is the Biot coefficient (Biot, 1941). Substitution of these expressions into (2.14), (2.15) and integration over the angle  $\varphi$  yield

$$p_{\text{out}}(r, \varphi, z = 0; t) - p_0 = -\frac{1}{S} \frac{1}{\sqrt{\pi}} \int_0^t \frac{(4c)^{-3/2} d\bar{t}}{(t - \bar{t})^{5/2}} \int_0^{R(\bar{t})} \bar{r} v(\bar{r}, \bar{t}) \exp \left[ -\frac{r^2 + \bar{r}^2}{4c(t - \bar{t})} \right] \times$$

$$\left\{ 3I_0 \left( \frac{r\bar{r}}{2c(t-\bar{t})} \right) - \frac{1}{2c(t-\bar{t})} \left[ (r^2 + \bar{r}^2) I_0 \left( \frac{r\bar{r}}{2c(t-\bar{t})} \right) - 2r\bar{r}I_1 \left( \frac{r\bar{r}}{2c(t-\bar{t})} \right) \right] \right\} d\bar{r}, \quad (2.18)$$

$$\begin{aligned} \sigma_b(r, \varphi, z=0; t) = & \frac{\eta}{S} \frac{2}{\pi} \int_0^{R(t)} \bar{r} v(\bar{r}, \bar{t}) \frac{E \left[ \frac{4r\bar{r}}{(r+\bar{r})^2} \right]}{(r-\bar{r})^2 (r+\bar{r})} d\bar{r} + \\ & + \frac{\eta}{S} \frac{4}{\sqrt{\pi}} \int_0^t \frac{(4c)^{-3/2} d\bar{t}}{(t-\bar{t})^{5/2}} \int_0^{R(\bar{t})} \bar{r} v(\bar{r}, \bar{t}) \exp \left[ -\frac{r^2 + \bar{r}^2}{4c(t-\bar{t})} \right] \times \\ & \left\{ I_0 \left( \frac{r\bar{r}}{2c(t-\bar{t})} \right) - \frac{1}{4c(t-\bar{t})} \left[ (r^2 + \bar{r}^2) I_0 \left( \frac{r\bar{r}}{2c(t-\bar{t})} \right) - 2r\bar{r}I_1 \left( \frac{r\bar{r}}{2c(t-\bar{t})} \right) \right] \right\} d\bar{r}, \end{aligned} \quad (2.19)$$

where  $S = \kappa/c$  is the storage coefficient, and  $I_\nu(x)$  is the modified Bessel function of the first kind (Abramowitz and Stegun, 1972).

## 2.5 Low permeability cake build-up

As the fracturing fluid infiltrates into the medium, a low permeability cake of thickness  $v_c$  builds up on the fracture walls. We assume that the cake thickness  $v_c$  is small compared to the fracture opening  $w$ , and that the fluid flow across the cake is one dimensional in the direction normal to the fracture plane. Pressure drop across the cake can be found from Darcy's law

$$\frac{\partial v}{\partial t} = -\kappa_c \frac{p_{\text{out}}|_{z=0} - p_{\text{in}}}{v_c} \quad \Rightarrow \quad p_{\text{in}} - p_{\text{out}}|_{z=0} = \frac{v_c}{\kappa_c} \frac{\partial v}{\partial t}, \quad (2.20)$$

where  $\kappa_c$  is the cake permeability. We further postulate that the rate of the solid particles into the cake is proportional to the fluid leak-off rate, i.e.,

$$v_c(r, t) = \beta v(r, t), \quad (2.21)$$

$\beta$  is the proportionality coefficient.

In the cavity region we have only pore fluid which is not able to leave any deposit on the fracture walls,  $v_c = 0$ , therefore the pressure field is continuous

$$v_c = 0 \quad \Rightarrow \quad p_{\text{in}} - p_{\text{out}}|_{z=0} = 0. \quad (2.22)$$

## Chapter 3

# Semi-infinite fracture

### 3.1 Introduction

In this chapter we study the tip region of a fluid-driven fracture propagating through a poroelastic medium. Inspired by numerous works on the tip region, we model it by a semi-infinite fracture propagating at a constant speed (see Section 1.4). The main accent of our study is on investigating the influence of large-scale 3D diffusion on the propagation of a semi-infinite fracture. This large-scale diffusion, which engage a large volume of the poroelastic material into the fracture evolution process, can lead to the generation of an additional confining stress (backstress). Studying this stress is one more goal of this research. In this study, we also take into account the fluid lag and low permeability cake build-up. The only input parameters of our model are the tip velocity and the parameters describing the properties of the poroelastic medium and the properties of the fracturing and pore fluids. The main restrictive assumptions here is that the tip cavity is fully filled with the pore fluid. As a result our model fails to describe the near-lag region of a fracture propagating in a low permeability rock. Indeed, in this case, the pore fluid only partially fills the cavity and the fluid pressure in the

cavity is equal to zero whereas the model predicts negative fluid pressure. However, our model is still valid in the far-field region, the size of which is large compared to the fluid lag length,  $x \gg \lambda$ , where  $x$  is the distance from the fracture tip and  $\lambda$  is the length of the fluid lag. At the same time, the problems studied by Garagash et al. (2009) and Detournay and Garagash (2003) represent limiting cases of our more general consideration (see Section 3.2). Note finally that our problem is very similar to the one, studied by Entov et al. (2007). However, we use a different approach to model the tip region of a finite fracture (see discussion in Appendix A.1).

This chapter is organized as follows. In Section 3.2 we present the current understanding of the tip region. In Section 3.3 we introduce the mathematical model and discuss limits of its applicability.

In Section 3.4 we discuss general ideas of scaling analysis. We show that the problem depends only on five dimensionless parameters. In Subsection 3.4.1 we introduce a reference scaling. The main idea of this scaling is to simplify our governing equations and introduce explicitly the dependence of the problem on five dimensionless parameters.

Before solving the problem numerically, we perform detailed scaling and asymptotic analyses. Thus in Section 3.5 we study the behaviour of the solution for different limiting cases. In Subsection 3.5.1 we show how our model degenerates to the ones studied by Garagash and Detournay (2000); Garagash et al. (2009); Detournay and Garagash (2003). In Subsections 3.5.2 and 3.5.3 we investigate the cases of the storage and leak-off domination respectively. In Section 3.6 we find near- and far-field solutions.

In Section 3.7 we present a numerical transient solution which connects the near- and far-field asymptotes. We discuss the main outcomes of the study in Section 3.8. Finally we summarize the results in Section 3.9.

### 3.2 Review of present knowledge

Different aspects of a semi-infinite fracture propagation were studied by Garagash and Detournay (2000); Garagash et al. (2009); Detournay and Garagash (2003).

Garagash and Detournay (2000) have studied the case of an impermeable medium. The authors have shown that the solution is characterized by the existence of a lag between the fracturing fluid front and the fracture tip. This lag is filled with the vapour of the fracturing fluid. The pressure of this vapour is equal to zero. As a result the pressure distribution along the fracture is not singular anymore as it would be if the fracturing fluid were allowed to reach the fracture tip. Garagash and Detournay (2000) have found the following estimation for the maximum length of the lag  $\lambda$

$$\lambda \simeq \frac{4\mu_{\text{in}}E'^2V}{\sigma_0^3},$$

where  $V$  is the tip velocity.

The authors also have studied the intermediate distances from the tip, which are large compared to the lag length, yet small compared to the size of the finite fracture tip region of which is modeled by a semi-infinite crack. It was shown that if this intermediate region exists the fluid pressure and the fracture opening are given by an intermediate asymptote, which can be constructed assuming that the fluid reaches the tip of the fracture propagating through a medium of zero toughness. Therefore in the presence of such an intermediate region the details of the tip solution are not important for the solution of a finite fracture.

Garagash et al. (2009) have analyzed a semi-infinite fluid-driven fracture steadily propagating through a permeable medium. The fluid exchange between the fracture and medium was approximated by the Carter's leak-off model (Carter, 1957). The fracturing fluid was assumed to reach the tip of the fracture. The authors have shown that the solution is characterized by a multiscale singular behavior at the tip, and that the nature

of the dominant singularity depends both on the relative importance of the dissipative processes and on the scale of reference. In general the tip region can be divided into three regions: the near-field toughness region, the intermediate leak-off-viscosity region, and the far-field storage-viscosity region. The first region can be characterized by an uniform fluid pressure distribution and large energy dissipation due to the fracturing of the solid, while the last two regions can be described by large fluid pressure gradient and large dissipation of energy in the fluid. The difference between the last two regions, however, is in the fracturing fluid balance mechanism: in the leak-off-viscosity region the volume of the infiltrated into the rock formation fluid is large compared to the fracture volume, whereas in the storage-viscosity region the situation is the opposite, i.e., the volume of the filtrate is small compared to the fracture volume. In each of these three regions, the fracture aperture  $w$  is a power law function of the distance from the tip  $x$ . Thus,  $w \sim x^{1/2}$  in the near-field toughness region,  $w \sim x^{5/8}$  in the intermediate leak-off-viscosity region, and  $w \sim x^{2/3}$  in the far-field storage-viscosity region.

Mathematically this multiscale nature of the tip solution can be characterized by two independent length scales, which both depend on the tip velocity. For example one can define the following two length scales  $\ell_{mk}$  and  $\ell_{m\tilde{m}}$ , where  $\ell_{mk}$  is the length scale characterizing the transition from the toughness region to the viscosity region in the case of an impermeable medium and  $\ell_{m\tilde{m}}$  is the length scale characterizing the transition from the leak-off region to the storage region in the case of zero toughness. Furthermore, Garagash et al. (2009) have introduced a conceptual representation of this multiscale solution in the parametric  $m\tilde{m}k$ -space (see Fig.3.1). In this representation, the  $k$ -vertex corresponds to the near-field toughness region, the  $\tilde{m}$ -vertex corresponds to the intermediate leak-off-viscosity region, and  $m$ -vertex corresponds to the far-field storage-viscosity region. The spatial variation of the solution between the  $k$ - and  $m$ -vertices depends on the ratio of the length scales  $\chi^6 = \ell_{m\tilde{m}}/\ell_{mk}$ . If this ratio is small,



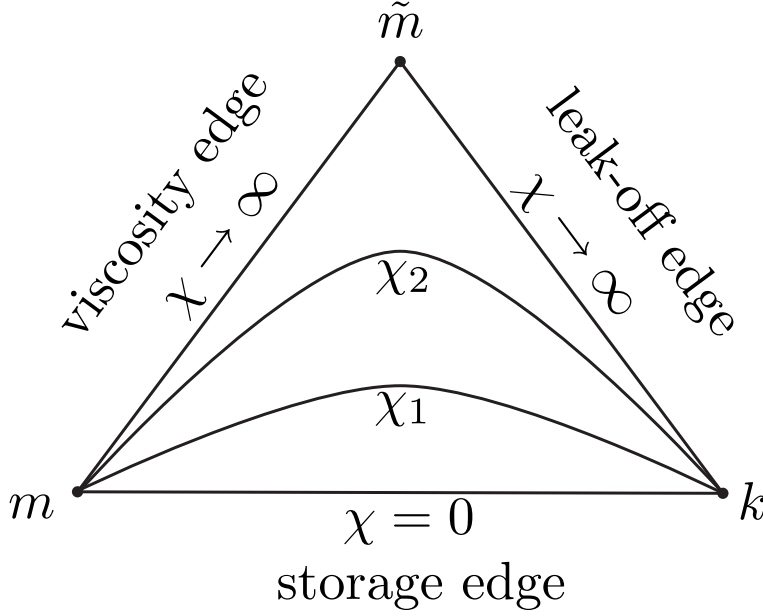


Figure 3.1: Parametric space and few solution “trajectories” parametrized by number  $\chi$ :  $0 < \chi_1 < \chi_2$

$\chi \ll 1$ , the solution has only two regions: the near-field toughness and the far-field storage-viscosity. With the increase of the ratio  $\chi$ , the intermediate leak-off-viscosity region emerges in between the near-field toughness region and far-field storage-viscosity region (see Fig.3.1).

Detournay and Garagash (2003) have carried out a detailed analysis of the fluid flow around the cavity (the region between the fracture edge and the fracturing fluid front) at the of a fluid-driven fracture propagating in a permeable saturated rock. They have carried out their analysis under the following assumptions: i) the problem is stationary, i.e., the tip velocity  $V$  and the cavity length  $\lambda$  are constant for the time scale of reference, ii) the cavity is fully filled with the pore fluid, iii) the fluid exchange is allowed only in the cavity region, i.e., the fracture walls behind the cavity are impermeable, iv) the cavity lies entirely within the toughness-dominated region, i.e.,  $w \sim x^{1/2}$ , v) the pore pressure field in the permeable rock is governed by the homogeneous 3D diffusion equation. Because of

their focus on the cavity region, Detournay and Garagash (2003) have taken the length of the cavity region as an input parameter (in other words, they do not solve the complete semi-infinite hydraulic fracture problem). The authors have shown that the fluid pressure is not singular, as in the case of impermeable rocks when the existence of a lag is accounted for. However, in contrast to impermeable rocks where the tip cavity is at zero pressure, the fluid pressure distribution in the cavity is now unknown and furthermore not uniform. This is a result of the fact that the flow of the pore fluid in the cavity region has rather complicated pattern: the pore fluid is drawn in, by suction, at the tip of the advancing fracture, and then is reinjected to the porous medium behind the tip, near the interface between the two fluids. Detournay and Garagash (2003) focused on the calculation of the fluid pressure in the tip cavity. In particular they have derived analytical expressions for the pressure and the fluid flux distributions in the two limiting cases:  $\lambda/\ell_d \ll 1$  and  $\lambda/\ell_d \gg 1$ , where  $\ell_d$  is the diffusion length scale. The authors also have discussed the inapplicability of their model for low permeability rocks. Indeed, in this case, the pore fluid only partially fills the cavity and the fluid pressure in the cavity is equal to zero. Instead, the model predicts negative fluid pressure.

### 3.3 Mathematical model

It is conventional to study the problem in a moving coordinate system  $\{x, y, z\}$  attached to the fracture tip and introduced by

$$x = -r + R(t) = -r + \int_0^t V(\tau) d\tau, \quad y = r\varphi, \quad z = z, \quad (3.1)$$

where  $V(t)$  is the tip velocity.

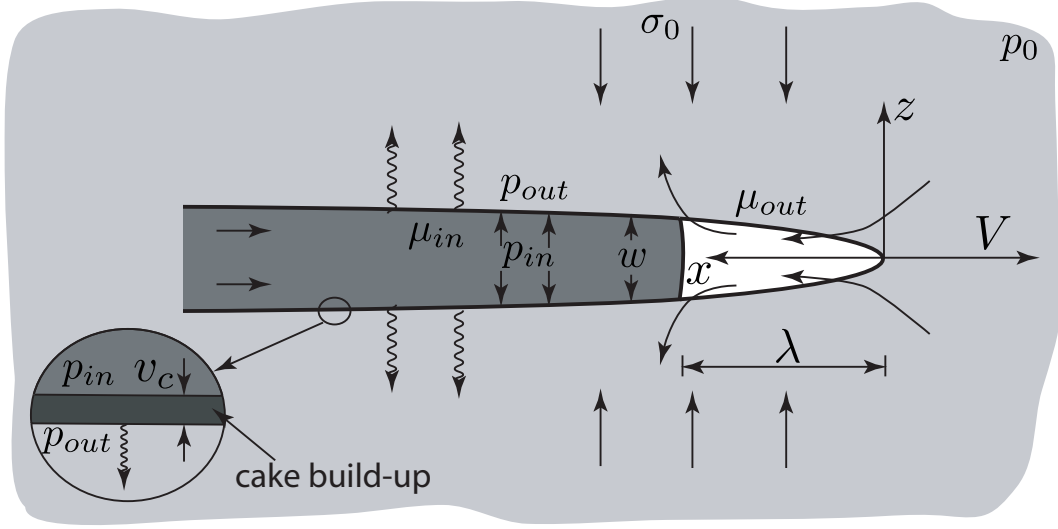


Figure 3.2: Semi-infinite fracture

### 3.3.1 Lubrication equations

In the moving coordinates system, the volume balance equation (2.1) reads

$$\frac{\partial w}{\partial t} + V \frac{\partial w}{\partial x} + \frac{\partial v}{\partial t} + V \frac{\partial v}{\partial x} - \frac{\partial q}{\partial x} = 0,$$

where we have used  $x \ll R$ . Assuming that in the tip region  $w \sim x^{a_w}$  and  $v \sim x^{a_v}$  with  $a_w, a_v < 1$  (to be verified a posteriori),  $V \partial/\partial x \gg \partial/\partial t$ . Therefore the volume balance equation can be rewritten as follows

$$V(w + v) = q, \quad (3.2)$$

where we have used the following boundary conditions derived from (2.3)

$$w|_{x=0} = v|_{x=0} = q|_{x=0} = 0. \quad (3.3)$$

Poiseuille's law(2.2) in the moving coordinate system transforms into

$$q = \frac{w^3}{12\mu} \frac{\partial p_{\text{in}}}{\partial x}, \quad \mu = \begin{cases} \mu_{\text{out}}, & x \in [0, \lambda) \\ \mu_{\text{in}}, & x \in [\lambda, \infty) \end{cases}, \quad (3.4)$$

where  $\lambda$  is the size of the cavity region.

### 3.3.2 Elasticity equation

Taking limit  $\xi, s \rightarrow 1$  in the kernel (2.6) and substituting the result into (2.5) we arrive to the following elasticity equation

$$p_{\text{in}} + \sigma_b - \sigma_0 = \frac{E'}{4\pi} \int_0^\infty \frac{\partial w}{\partial s} \frac{ds}{x-s}, \quad (3.5)$$

where we have used the fact that if  $x \ll X \sim R$ , then

$$\left( \int_0^\infty s^{a_w-1} \frac{ds}{x-s} \right) \bigg/ \left( \int_X^\infty s^{a_w-1} \frac{ds}{x-s} \right) = \mathcal{O} \left[ \left( \frac{x}{X} \right)^{a_w-1} \right].$$

### 3.3.3 Linear elastic fracture mechanics

The propagation criterion (2.11) transforms to

$$w \rightarrow \frac{2^{5/2}}{\pi^{1/2}} \frac{K_{Ic}}{E'} x^{1/2} \quad \text{as } x \rightarrow 0. \quad (3.6)$$

### 3.3.4 Diffusion equations

So far, assuming that  $x, y \ll R$ , we were able to transform our governing equations in the tip region to the ones that describe the propagation of a semi-infinite fracture. The situation becomes more complicated when we try to do the same with the poroelasticity equations (2.18) and (2.19). The problem here arises from the time dependence of the diffusion length scale  $\ell_d \sim \sqrt{ct}$ . It is obvious that in order to represent the tip region by a semi-infinite fracture, the finite fracture itself has to be large compared to the diffusion length scale, i.e.,  $R \gg \sqrt{ct}$ . After we have established this restriction, the procedure of transformation of the poroelastic equations (2.18) and (2.19) is straightforward. First, assuming  $R \gg \sqrt{ct}$ , one should replace the Bessel functions in these equations by their large-argument asymptotes and eliminate the curvature effects (Chapter 4 contains the details of the procedure for a fixed length fracture). Second, one should perform the change of coordinates (3.1) and, assuming  $R \gg \sqrt{ct}$ , move the upper limit of integration

to infinity. Third, assuming the fracture tip velocity  $V$  to be constant, one should perform integration over time [here some hints can be taken from the work by Cleary (1978)]. Alternatively, we can use the singular solution for a moving constant strength 2D source derived by Cleary (1978)

$$p^{(V)} = \frac{1}{2\pi\kappa} e^{\xi} K_0(|\xi|), \quad \xi = \frac{Vx}{2c}, \quad (3.7)$$

$$\begin{aligned} \begin{Bmatrix} \sigma_{xx}^{(V)} \\ \sigma_{zz}^{(V)} \end{Bmatrix} &= -\frac{\eta}{2\pi\kappa} \left\{ \mp \frac{1}{\xi} + e^{\xi} [K_0(|\xi|) \pm \text{sign}(\xi) K_1(|\xi|)] \right\} = \\ &= \pm \frac{\eta}{2\pi\kappa} \frac{1}{\xi} - \eta \begin{Bmatrix} 2p^{(V)} - dp^{(V)}/d\xi \\ dp^{(V)}/d\xi \end{Bmatrix}, \end{aligned} \quad (3.8)$$

where  $K_\nu(x)$  is the modified Bessel function of the second kind (Abramowitz and Stegun, 1972). Note that an equation for the temperature field, similar to (3.7), can be found in Carslaw and Jaeger (1950) for the equivalent problem in heat conduction.

The strength of the fluid source is given by

$$g(\mathbf{r}, t) \equiv \frac{\partial v(r, \varphi, z, t)}{\partial t} = V \frac{\partial v(x, y, z, t)}{\partial x}, \quad (3.9)$$

therefore the poroelastic equations (2.18) and (2.19) transform to

$$p_{\text{out}} - p_0 = V \int_0^\infty \frac{\partial v}{\partial s} p^{(V)}(x-s) ds, \quad (3.10)$$

$$\sigma_b = V \int_0^\infty \frac{\partial v}{\partial s} \sigma_{zz}^{(V)}(x-s) ds. \quad (3.11)$$

### 3.3.5 Low permeability cake build-up

The cake build-up equations (2.20), (2.21), and (2.22) yield

$$p_{\text{in}} - p_{\text{out}}|_{z=0} = \frac{1 + \text{sign}(v)}{2} \frac{\beta v}{\kappa_c} V \frac{\partial v}{\partial x}. \quad (3.12)$$

Here we have used the fact that the fluid displacement function  $v$  is negative in the lag region. To demonstrate this let us take a look at the expression for the fluid exchange

rate between the fracture and the medium given by (3.9). Together with the boundary conditions (3.3), it gives us another interpretation of the fluid displacement function, namely  $v(x) \sim \int_0^x g(s) ds$ . This means that the fluid displacement function is proportional to the total fluid volume exchange between the fracture and the medium on the interval  $s \in [0, x)$ . Moreover, the problem is stationary and depends only on the spatial coordinate  $x$ , therefore the total volume of the pore fluid in the lag region is constant, and the total fluid volume exchange rate between the fracture and the medium is equal to zero

$$v(\lambda) = 0. \quad (3.13)$$

This equation can be used to define the length of the lag region. Moreover, there is a region next to the fracture tip and inside the cavity where the pore fluid enters the cavity. Thus, the fluid displacement function  $v$  is negative there. Since there are no reasons for the fluid displacement function to be equal to zero at any other point, we conclude that this function is negative inside the cavity, whereas it is positive outside the cavity.

One more obvious restriction when modeling the tip region by a semi-infinite fracture is  $\lambda \ll R$ . Indeed, as in the case of the diffusion length scale, in order to model the tip region by a semi-infinite fracture, the fluid lag  $\lambda$ , being one more length scale of the problem, should be small compared to the fracture size  $R$ .

### 3.4 Scaling

The problem under consideration has three characteristic length scales

$$\ell_\mu = \epsilon^{-2} \frac{12\mu_{\text{in}} V}{\sigma_0 - p_0}, \quad \ell_k = \frac{8}{\pi} \left( \frac{K_{Ic}}{\sigma_0 - p_0} \right)^2, \quad \ell_d = \frac{2c}{V}, \quad \epsilon = \frac{\sigma_0 - p_0}{E'}. \quad (3.14)$$

Here  $\ell_\mu$  is the viscosity length scale,  $\ell_k$  is the toughness length scale,  $\ell_d$  is the diffusion length scale, and  $\epsilon$  is a small parameter.

To study the influence of different physical processes we use scaling analysis. We rewrite each physical quantity  $a$  in the form  $a = a_* A$ , where  $A$  is the dimensionless physical quantity which is usually of order 1, and the parameter  $a_*$  is of the same order as  $a$ ,  $a_* \sim a$ . In the case of our problem the general scaling is given by

$$x = \ell_* \xi, \quad w = w_* \Omega, \quad v = v_* \Upsilon, \quad \{p_{\text{in}} - \sigma_0, \sigma_b\} = p_* \{\Pi, \Sigma\}, \quad (3.15)$$

where  $\ell_*$  is the length scale of interest,  $w_*$ ,  $v_*$ , and  $p_*$  are characteristic values of the fracture opening  $w$ , fluid displacement function  $v$ , and net fluid pressure inside the fracture  $p - \sigma_0$  at the length scale of interest respectively, and  $\xi$ ,  $\Omega$ ,  $\Upsilon$ ,  $\Pi$ , and  $\Sigma$  are the dimensionless coordinate, fracture opening, fluid displacement function, fluid pressure inside the fracture, and backstress respectively.

In scaled form, the governing equations read as follows

- Lubrication equation (3.2), (3.4)

$$\mathcal{G}_v \Omega + \mathcal{G}_c \Upsilon = \Omega^3 \frac{d\Pi}{d\xi}, \quad m = \begin{cases} \mu_{\text{out}}/\mu_{\text{in}}, & \Upsilon(\xi) < 0 \\ 1, & \Upsilon(\xi) > 0 \end{cases}, \quad (3.16)$$

- Propagation criterion (3.6)

$$\Omega \rightarrow \Omega_0 \equiv \mathcal{G}_K \xi^{1/2} \quad \text{as} \quad \xi \rightarrow 0, \quad (3.17)$$

- Elasticity equation (3.5)

$$\Pi + \Sigma = \frac{\mathcal{G}_E}{4\pi} \int_0^\infty \frac{d\Omega}{d\bar{\xi}} \frac{d\bar{\xi}}{\xi - \bar{\xi}}, \quad (3.18)$$

- Leak-off equation (3.12), (3.10), and (3.7)

$$\mathcal{G}_p \Pi + 1 = \mathcal{G}_{cb} \frac{1 + \text{sign}(\Upsilon)}{2} \Upsilon \frac{d\Upsilon}{d\xi} + \Pi_d, \quad \Pi_d \equiv \frac{\mathcal{G}_S}{2\pi} \int_0^\infty \frac{d\Upsilon}{d\bar{\xi}} e^{\mathcal{G}_d(\xi - \bar{\xi})} K_0(\mathcal{G}_d |\xi - \bar{\xi}|) d\bar{\xi}, \quad (3.19)$$

- Backstress equation (3.11), (3.8)

$$\Sigma = -\frac{\eta}{2\pi} \frac{\mathcal{G}_S}{\mathcal{G}_d} \int_0^\infty \frac{d\Upsilon}{d\xi} \frac{d\bar{\xi}}{\xi - \bar{\xi}} - \frac{\eta}{\mathcal{G}_d} \frac{d\Pi_d}{d\xi}. \quad (3.20)$$

Here  $\mathcal{G}_i$  are the dimensionless groups defined by

$$\begin{aligned} \mathcal{G}_v &= \frac{\sigma_0 - p_0}{p_*} \frac{\epsilon^2 \ell_\mu \ell_*}{w_*^2}, & \mathcal{G}_c &= \frac{\sigma_0 - p_0}{p_*} \frac{\epsilon^2 \ell_\mu \ell_* v_*}{w_*^3}, & \mathcal{G}_E &= \frac{p_*}{\sigma_0 - p_0} \frac{w_*}{\epsilon \ell_*}, & \mathcal{G}_K &= \frac{2\epsilon \sqrt{\ell_k \ell_*}}{w_*}, \\ \mathcal{G}_p &= \frac{p_*}{\sigma_0 - p_0}, & \mathcal{G}_{cb} &= \epsilon \beta \frac{\kappa}{\kappa_c} \frac{v_*^2}{\epsilon^2 \ell_d \ell_*} \frac{2}{SE'}, & \mathcal{G}_S &= \frac{v_*}{\epsilon \ell_d} \frac{2}{SE'}, & \mathcal{G}_d &= \frac{\ell_*}{\ell_d}. \end{aligned} \quad (3.21)$$

Each of these dimensionless groups can be associated with a certain physical process. Thus  $\mathcal{G}_v$  and  $\mathcal{G}_c$  describe the distribution of the fracturing fluid between the fracture and the poroelastic medium, respectively. Indeed,  $\mathcal{G}_v$  is proportional to the amount of fluid stored inside the fracture, whereas  $\mathcal{G}_c$  is proportional to the amount of fluid which has leaked into the medium. The group  $\mathcal{G}_E$  is the elasticity group, the group  $\mathcal{G}_K$  is referred to as the dimensionless material toughness. The last four groups describe the fluid leak-off. Namely the group  $\mathcal{G}_p \sim (p_{\text{in}} - \sigma_0) / (\sigma_0 - p_0)$  and if it is small, then from a diffusion point of view the fluid pressure inside the fracture  $p_{\text{in}}$  is uniform and equal to the confining stress  $\sigma_0$ ,  $p_{\text{in}} \approx \sigma_0$ . The groups  $\mathcal{G}_{cb}$  and  $\mathcal{G}_S$  describe the fluid pressure drop from  $p_{\text{in}}$  inside the fracture to  $p_0$  in the far-field. Thus  $\mathcal{G}_{cb}$  is proportional to the pressure drop across the cake,  $\mathcal{G}_{cb} \sim p_{\text{in}} - p_{\text{out}}|_{z=0}$ , whereas  $\mathcal{G}_S$  is proportional to the pressure drop in the poroelastic medium  $\mathcal{G}_S \sim p_{\text{out}}|_{z=0} - p_0$ . Finally  $\mathcal{G}_d$  is the diffusion group. If it is large then the scale of reference  $\ell_*$  is large compared to the diffusion length scale  $\ell_d$  and the diffusion process is one dimensional, otherwise the diffusion process is three dimensional.

To understand the influence of different physical processes on the fracture propagation we study different limiting cases. In each limiting case some processes are dominating whereas the other ones could be neglected. Here we obtain a limiting case by contrasting



- energy dissipation associated with the viscous flow of the fracturing fluid versus energy dissipation associated with the cracking of the rock material
- volume of the fracture versus volume of the fluid which has leaked into the poroelastic medium
- pressure drop in the cake  $p_{\text{in}} - p_{\text{out}}|_{z=0}$  versus pressure drop in the porous medium  $p_{\text{out}}|_{z=0} - p_0$
- 1D diffusion versus 3D diffusion
- $(p_{\text{in}} - \sigma_0) / (\sigma_0 - p_0) \ll 1$  vs  $(p_{\text{in}} - \sigma_0) / (\sigma_0 - p_0) \gg 1$

It is convenient to study each limiting case in an inherent scaling. To finish introduction of the scaling (3.15) one has to define the parameters  $\ell_*$ ,  $w_*$ ,  $v_*$ , and  $p_*$ . Usually a scaling is introduced in such a way that the groups representing the dominating physical processes are either finite, e.g., equal to 1, or large compared to 1. The rest of the groups are usually small compared to 1. Thus, for example, if we want to study region where the fluid leak-off is negligible we introduce a scaling such that  $\mathcal{G}_v = 1$  and  $\mathcal{G}_c \ll 1$ , whereas if we want to study a general case when the volume of the fracture and the volume of the leaked-off fluid are of the same order we can introduce a scaling such that  $\mathcal{G}_v = \mathcal{G}_c$ . Therefore in order to define the dimensional parameters  $\ell_*$ ,  $w_*$ ,  $v_*$ , and  $p_*$  one can simply define four equations which define/relate the values of the dimensionless groups, and then solve the set of these equations with respect to  $\ell_*$ ,  $w_*$ ,  $v_*$ , and  $p_*$ .

A general result of the scaling procedure introduced in this section is that the dimensionless formulation of our problem depends only on six dimensionless parameters:  $m$ ,  $\eta$ , and four other dimensionless parameters which depend on a particular scaling. Indeed, we have eight dimensionless groups (3.21) and four equations binding the values of these groups, therefore only four of these groups are independent.

### 3.4.1 Diffusion scaling

Here we introduce a “reference” scaling that will be used throughout this chapter. All the other scaling introduced in this charter, will be eventually expressed in terms of this reference scaling. The motivation for introducing a reference scaling stems from the dependence of problem on on six dimensionless parameters, four of which hinge on the scaling. Therefore, by introducing the reference scaling, we fix these four parameters. At the same time, if we need for some reason to rescale the problem (for example when we are interested in a particular limiting case) we can express the new set of governing parameters in terms of those from the reference scaling. This significantly simplifies writing and analyzing of the governing equations in different scalings.

Since the main goal of this research is to study 3D diffusion we introduce a scaling, that highlights the role of diffusion, i.e.,  $\mathcal{G}_d = \mathcal{G}_p = \mathcal{G}_E = 1$  and  $\mathcal{G}_v = \mathcal{G}_c$ . Thus

$$\ell_* = \ell_d, \quad w_* = v_* = \epsilon \ell_d, \quad p_* = \sigma_0 - p_0. \quad (3.22)$$

The governing equations (3.16)-(3.20) read as follows

- Lubrication equation (3.16)

$$\Omega + \Upsilon = \frac{1}{m\mathcal{M}}\Omega^3 \frac{d\Pi}{d\xi}, \quad m = \begin{cases} \mu_{out}/\mu_{in}, & \Upsilon(\xi) < 0 \\ 1, & \Upsilon(\xi) > 0 \end{cases}, \quad (3.23)$$

- Propagation criterion (3.17)

$$\Omega \rightarrow \Omega_0 \equiv \mathcal{K}\xi^{1/2} \quad \text{as} \quad \xi \rightarrow 0, \quad (3.24)$$

- Elasticity equation (3.18)

$$\Pi + \Sigma = \frac{1}{4\pi} \int_0^\infty \frac{d\Omega}{d\bar{\xi}} \frac{d\bar{\xi}}{\xi - \bar{\xi}}, \quad (3.25)$$

- Leak-off equation (3.19)

$$\Pi + 1 = \frac{\mathcal{X}}{\mathcal{S}} \frac{1 + \text{sign}(\Upsilon)}{2} \Upsilon \frac{d\Upsilon}{d\xi} + \Pi_d, \quad \Pi_d \equiv \frac{1}{2\pi\mathcal{S}} \int_0^\infty \frac{d\Upsilon}{d\xi} e^{\xi - \bar{\xi}} K_0(|\xi - \bar{\xi}|) d\bar{\xi}, \quad (3.26)$$

- Backstress equation (3.20)

$$\Sigma = -\frac{\eta}{2\pi\mathcal{S}} \int_0^\infty \frac{d\Upsilon}{d\xi} \frac{d\bar{\xi}}{\xi - \bar{\xi}} - \eta \frac{d\Pi_d}{d\xi}. \quad (3.27)$$

Here the dimensionless parameters are given by

$$\mathcal{K} = 2\sqrt{\frac{\ell_k}{\ell_d}}, \quad \mathcal{M} = \frac{\ell_\mu}{\ell_d}, \quad \mathcal{X} = \epsilon\beta \frac{\kappa}{\kappa_c}, \quad \mathcal{S} = \frac{1}{2}SE', \quad (3.28)$$

where  $\mathcal{K}$  is the dimensionless material toughness,  $\mathcal{M}$  is the dimensionless fluid viscosity,  $\mathcal{X}$  describes the cake build-up, and  $\mathcal{S}$  describes fluid transport through the poroelastic medium. Physical understanding of the structure of the parameter  $\mathcal{S}$  can be gained from the following chain of simple transformations. We start with Darcy's law, which provides us with the estimation of the fluid flux through the poroelastic medium:  $g = -\kappa \nabla p_{\text{out}}$ , where  $\nabla p_{\text{out}} \sim (\sigma_0 - p_0)/\tilde{\ell}_d$  and  $\tilde{\ell}_d \sim \sqrt{ct}$ . Then integrating the fluid flux  $g$  over time we obtain the following estimation for the fluid displacement function  $v$ :  $v \sim S(\sigma_0 - p_0)\tilde{\ell}_d$ . Therefore the fluid displacement function  $v$  is equal to the volume of the fracturing fluid which has leaked into the rock formation and has been stored inside the region of size  $\tilde{\ell}_d$ . There are two mechanisms of the fluid storage in the medium: compressibility of the fluid and deformation of pores. To finish the chain of transformations we recall that the reference scaling was introduced under the assumption that  $\tilde{\ell}_d \sim \ell_d \sim x$ , thus  $v \sim \mathcal{S}v_*$ . Therefore in the case when diffusion is the only leak-off mechanism (no cake build-up), the parameter  $\mathcal{S}$  provides us with an estimation of the fluid displacement function  $\Upsilon$ ,  $\Upsilon \sim \mathcal{S}$ . Hereafter, we refer to the parameter  $\mathcal{S}$  as the dimensionless storage coefficient.

The advantage of the formulation (3.23)-(3.28) compared to the ones introduced by Garagash and Detournay (2000) and Detournay and Garagash (2003) is that this

formulation does not include the fluid lag length explicitly. However, once the fluid displacement function  $\Upsilon$  is known, the dimensionless lag length  $\Lambda = \lambda/\ell_d$  can be found from

$$\Upsilon(\Lambda) = 0. \quad (3.29)$$

### 3.5 Structure of solution

We see that our problem depends on six dimensionless parameters: the material toughness  $\mathcal{K}$ , the fracturing fluid viscosity  $\mathcal{M}$ , the cake build-up parameter  $\mathcal{X}$ , the storage coefficient  $\mathcal{S}$ , the ratio of the pore fluid viscosity to that of the fracturing fluid  $m$ , and the poroelastic stress modulus  $\eta$ . Throughout this section, we assume that  $m = 1$  and  $\eta = 0$ . In order to understand the dependence of the solution on the other four parameters we study different limiting cases. Our study is mainly based on simple scaling considerations rather than on explicit solutions.

One general statement can be done about the dependence of the fluid lag on the cake build-up parameter, namely the length of the fluid lag decreases with  $\mathcal{X}$ . To illustrate this fact let us imagine a fracture propagating with a certain cake permeability. Now, let us reduce the permeability of the cake by a small amount. If we assume that the distribution of the fluid flux and pore pressure in the medium are still the same, the pressure of the fracturing fluid should increase. Moreover since the thickness of the cake is not uniform, the pressure gradient of the fracturing fluid should also increase. Therefore in order to reach a new equilibrium the fracturing fluid should move a bit toward the fracture tip. This leads to a decrease of the length of the fluid lag.

	Previous works			Storage		Leak-off	
	“GD”	“DG”	“G”	cake build-up	diffusion	cake build-up	diffusion
$\mathcal{G}_v$	1	1	1	1		$\ll 1$	
$\mathcal{G}_c$	$\ll 1$	1		$\ll 1$		1	
$\mathcal{G}_E$	1		1	1		1	
$\mathcal{G}_K$		1	1	1		$\ll 1$	
$\mathcal{G}_p$	1		$\ll 1$			1	
$\mathcal{G}_{cb}$	$\gg 1$	$\gg 1$		1	$\ll 1$	1	$\ll 1$
$\mathcal{G}_S$	$\ll 1$			$\ll 1$	1	$\ll 1$	1
$\mathcal{G}_d$						$\gg 1$	
$\frac{\ell_*}{\ell_d}$	$\mathcal{M}$	$\Lambda$	$\frac{\kappa^6}{\mathcal{M}^2}$	$\frac{\kappa^6}{\mathcal{M}^2}$		$\mathcal{M}^{2/3} \left(\frac{\mathcal{S}}{\chi}\right)^{1/3}$	$(\mathcal{M}\mathcal{S})^{2/3}$
$\frac{w_*}{\epsilon \ell_d}$	$\mathcal{M}$	$\mathcal{M}\Lambda^{1/2}$	$\frac{\kappa^4}{\mathcal{M}}$	$\frac{\kappa^4}{\mathcal{M}}$		$\mathcal{M}^{2/3} \left(\frac{\mathcal{S}}{\chi}\right)^{1/3}$	$(\mathcal{M}\mathcal{S})^{2/3}$
$\frac{v_*}{\epsilon \ell_d}$		$\mathcal{M}\Lambda^{1/2}$		$\frac{\kappa^3}{\mathcal{M}} \sqrt{\frac{\mathcal{S}}{\chi}}$	$\mathcal{S}_{\max} \left[1, \frac{\kappa^3}{\mathcal{M}}\right]$	$\mathcal{M}^{1/3} \left(\frac{\mathcal{S}}{\chi}\right)^{2/3}$	$\mathcal{M}^{1/3} \mathcal{S}^{4/3}$
$\frac{p_*}{\sigma_0 - p_0}$	1	$\frac{\Pi_{-1}}{\Pi_{DG}} = \frac{\mathcal{M}}{\mathcal{K}^2}$	$\frac{\mathcal{M}}{\mathcal{K}^2}$	$\frac{\mathcal{M}}{\mathcal{K}^2}$		1	

Table 3.1: Scalings for different limiting cases

### 3.5.1 Previous works in reference to our model

In this subsection we illustrate how our model degenerates to the ones which were studied by Garagash and Detournay (2000); Garagash et al. (2009); and Detournay and Garagash (2003).

#### 3.5.1.1 Impermeable cake build-up

Mathematically, the impermeability of the cake build-up is equivalent to taking  $\mathcal{X}/\mathcal{S} \rightarrow \infty$ . Physically this means that the fracturing fluid is not allowed to infiltrate into the hosting rock. In other words

$$\Upsilon(\xi) = 0, \quad \xi \geq \Lambda. \quad (3.30)$$

Thus the leak-off equation (3.26) transforms to

$$\Pi(\xi) + 1 = \frac{1}{2\pi\mathcal{S}} \int_0^\Lambda \frac{d\Upsilon}{d\xi} e^{\xi-\bar{\xi}} K_0(|\xi-\bar{\xi}|) d\bar{\xi}, \quad 0 \leq \xi \leq \Lambda. \quad (3.31)$$

#### Case of large storage coefficient, $\mathcal{S} \gg 1$

Here we assume that the dimensionless storage coefficient  $\mathcal{S}$  is very large. Thus the fluid pressure distribution  $p_{\text{in}}$  is uniform along the fluid lag and equal to the far-field pore pressure  $p_0$ ,

$$\Pi(\xi) = -1, \quad 0 \leq \xi \leq \Lambda. \quad (3.32)$$

One can also obtain this solution directly from the leak-off equation (3.31) assuming that  $\mathcal{S} \rightarrow \infty$ .

Substitution of the uniform pressure distribution into the lubrication equation (3.23) yields

$$\Upsilon(\xi) = -\Omega(\xi), \quad 0 \leq \xi \leq \Lambda. \quad (3.33)$$

Now it is easy to show that mathematically this problem is similar to the one, studied by Garagash and Detournay (2000). To illustrate this fact we introduce the following scaling

$$\{\xi, \Omega\} = \mathcal{M} \{\xi_{GD}, \Omega_{GD}\}, \quad \Pi = \Pi_{GD},$$

where “GD” stands for the authors names. In terms of our dimensionless groups (3.21) this scaling is defined by  $\mathcal{G}_p = \mathcal{G}_E = \mathcal{G}_v = 1$ .

In this scaling, the lubrication equation (3.23), propagation criterion (3.24), and elasticity equation (3.25) read

$$1 = \Omega_{GD}^2 \frac{d\Pi_{GD}}{d\xi_{GD}}, \quad \xi_{GD} \geq \Lambda_{GD}, \quad (3.34)$$

$$\Omega_{GD} \rightarrow \kappa_{GD} \xi_{GD}^{1/2} \quad \text{as} \quad \xi_{GD} \rightarrow 0, \quad (3.35)$$

$$\Pi_{GD} = \frac{1}{4\pi} \int_0^\infty \frac{d\Omega_{GD}}{d\bar{\xi}} \frac{d\bar{\xi}}{\xi_{GD} - \bar{\xi}}, \quad (3.36)$$

where  $\Lambda_{GD} = \mathcal{M}^{-1}\Lambda$  and  $\kappa_{GD} = \mathcal{M}^{-1/2}\mathcal{K}$ .

One can see that this set of equation is exactly the same as the one derived by Garagash and Detournay (2000). The only difference is that Garagash and Detournay (2000) assumed that the fluid lag is filled with the vapor of the fracturing fluid. The pressure of this vapor was assumed to be equal to zero. In our case the fluid lag is filled with the pore fluid. The pressure of this fluid is equal to the undisturbed far-field pore pressure  $p_0$ .

Garagash and Detournay (2000) have derived the following expression for the size of the fluid lag region

$$\begin{aligned} \Lambda_{GD} &\approx 4.36 \cdot 10^{-3} \kappa_{GD}^6 e^{-\kappa_{GD}^2}, \quad \kappa_{GD} \gg 1 \\ \Lambda_{GD} &\sim 1, \quad \kappa_{GD} \ll 1 \end{aligned} \quad (3.37)$$

### Case of toughness domination

Here we assume that the fracture opening in the lag region is governed by the square root LEFM asymptote (3.24). This case was studied by Detournay and Garagash (2003). To illustrate how our model degenerates to the one, introduced by Detournay and Garagash (2003) we use the following scaling

$$\xi = \Lambda \xi_{DG}, \quad \{\Omega, \Upsilon\} = \mathcal{K} \Lambda^{1/2} \{\Omega_{DG}, \Upsilon_{DG}\}, \quad \Pi + 1 = \mathcal{M} \mathcal{K}^{-2} \Pi_{DG}. \quad (3.38)$$

Therefore the lubrication equation (3.23), propagation criterion (3.24), elasticity equation (3.25), and leak-off equation (3.31) transform to

$$\Omega_{DG} + \Upsilon_{DG} = \Omega_{DG}^3 \frac{d\Pi_{DG}}{d\xi_{DG}}, \quad (3.39)$$

$$\Omega_{DG} \rightarrow \xi_{DG}^{1/2} \quad \text{as} \quad \xi_{DG} \rightarrow 0, \quad (3.40)$$

$$\frac{\mathcal{M}}{\mathcal{K}^2} \Pi_{DG} - 1 = \frac{1}{4\pi} \frac{\mathcal{K}}{\Lambda^{1/2}} \int_0^\infty \frac{d\Omega_{DG}}{d\bar{\xi}} \frac{d\bar{\xi}}{\xi_{DG} - \bar{\xi}}, \quad (3.41)$$

$$\Pi_{DG}(\xi_{DG}) = \frac{1}{2\pi\rho_{DG}} \int_0^1 \frac{d\Upsilon_{DG}}{d\bar{\xi}} \exp\left[\frac{\eta_{DG}}{2}(\xi_{DG} - \bar{\xi})\right] K_0\left(\frac{\eta_{DG}}{2}|\xi_{DG} - \bar{\xi}|\right) d\bar{\xi}. \quad (3.42)$$

Here  $\eta_{DG} = 2\Lambda$  and  $\rho_{DG} = \mathcal{SM}/(\mathcal{K}^3\Lambda^{1/2})$  are the dimensionless parameters introduced by Detournay and Garagash (2003).

One can see that in the case of the toughness domination when  $\mathcal{K}^2/\mathcal{M} \gg 1$ , the elasticity equation (3.41) degenerates, and the problem in the lag region depends only on two dimensionless parameters  $\eta_{DG}$  and  $\rho_{DG}$ . Note that within this degenerated model it is impossible to define the size of the lag region.

#### 3.5.1.2 Zero lag

##### Leak-off equation

Here we assume that the dimensionless fluid pressure  $\Pi$  is small compared to 1,  $\Pi \ll 1$ . Therefore from a diffusion point of view the fluid pressure inside the fracture is uniform



and equal to the confining stress  $\sigma_0$ ,  $p_{\text{in}} \approx \sigma_0$ . Below we solve the leak-off equation (3.26) under slightly more general assumption. Namely we assume that  $\Pi + 1 \approx \text{const}$  along the fracture. Under this assumption, the solution of the leak-off equation (3.26) is of the form

$$\Upsilon = A_{\Upsilon}^{\text{const}} \xi^{1/2}. \quad (3.43)$$

Note that the structure of this solution is similar to the one of the Carter's leak-off model.

In Appendix A.2 we calculate the diffusion part  $\Pi_d$  of the pressure [see def. (3.26)] and show that it is indeed uniform

$$\Pi_d = \frac{\pi^{1/2}}{2^{5/2}} \frac{A_{\Upsilon}^{\text{const}}}{\mathcal{S}}. \quad (3.44)$$

Substitution of this expression and (3.43) into the leak-off equation (3.26) yields

$$A_{\Upsilon}^{\text{const}} = -\frac{\pi^{1/2}}{2^{5/2} \mathcal{X}} + \sqrt{\frac{\pi}{2^5 \mathcal{X}^2} + 2 \frac{\Pi + 1}{\mathcal{X}} \mathcal{S}}. \quad (3.45)$$

After substitution of (3.43) and (3.44) into the backstress equation (3.27) we get

$$\Sigma = 0. \quad (3.46)$$

Note that this result is valid for any  $\eta$ .

We see that in the case when  $\Pi + 1 \approx \text{const}$  along the fracture, in particular when the far-field confining stress  $\sigma_0$  is large compared to the far-field pore pressure  $p_0$  which means that  $\Pi + 1 \approx 1$ , the fluid lag is negligible and the fluid leak-off is similar to the one predicted by the Carter's model. We would like to stress here that expressions (3.43), (3.45) give the exact solution of the leak-off equation (3.26) which takes into account 3D diffusion whereas the Carter's leak-off model considers only 1D diffusion. Therefore similarity between our solution (3.43), (3.45) and the Carter's leak-off model is just an interesting fact, not a retrieve of the 1D case.

### Degenerated model

One can see that the problem has been reduced to the one studied by Garagash et al. (2009). It is convenient to analyze this case in the following scaling

$$\xi = \frac{\mathcal{K}^6}{\mathcal{M}^2} \xi_G, \quad \Omega = \frac{\mathcal{K}^4}{\mathcal{M}} \Omega_G, \quad \Pi = \frac{\mathcal{M}}{\mathcal{K}^2} \Pi_G, \quad (3.47)$$

In terms of the dimensionless groups (3.21) this scaling is defined by  $\mathcal{G}_K = \mathcal{G}_E = \mathcal{G}_v = 1$ .

In this scaling, the lubrication equation (3.23), propagation criterion (3.24), elasticity equation (3.25), and leak-off equation (3.26) transform to

$$\Omega_G + \chi_G \xi_G^{1/2} = \Omega_G^3 \frac{d\Pi_G}{d\xi_G}, \quad (3.48)$$

$$\Omega_G \rightarrow \xi_G^{1/2} \quad \text{as} \quad \xi_G \rightarrow 0, \quad (3.49)$$

$$\Pi_G = \frac{1}{4\pi} \int_0^\infty \frac{d\Omega_G}{d\bar{\xi}} \frac{d\bar{\xi}}{\xi_G - \bar{\xi}}, \quad (3.50)$$

where  $\chi_G = A_\Upsilon^{const}/\mathcal{K}$  is a dimensionless parameter, similar to  $\chi$  introduced by Garagash et al. (2009) (see also Section 3.2).

We see that in this case the structure of the solution depends only on one dimensionless parameter  $\chi_G$ . Thus, if  $\chi_G = 0$  then the solution has only two regions: the near-field toughness region  $\xi_G \ll 1$ , and the far-field viscosity region  $\xi_G \gg 1$ . Note that in the former region the fracture opening is governed by the square root LEFM asymptote (3.49), whereas in the latter one the opening is given by  $\Omega_G \sim \xi_G^{2/3}$ . As the parameter  $\chi_G$  increases, the intermediate leak-off-viscosity region emerges in between the near-field toughness region and far-field storage-viscosity region (see Fig. 3.1). In this region  $\Omega_G \ll \chi_G \xi_G^{1/2}$  and  $\Omega_G \sim \chi_G^{1/4} \xi_G^{5/8}$ .

#### 3.5.2 Case of storage domination

Here we consider the case when the fluid displacement function  $\Upsilon$  is small compared to the fracture opening  $\Omega$ ,  $|\Upsilon| \ll \Omega$ . It is clear that in this case our model is not

applicable in the cavity region. Indeed, if the fluid exchange between the fracture and medium is slow, the pore fluid can not entirely fill the cavity, therefore the pressure in the cavity should be equal to zero. Instead, our model predicts negative fluid pressure. Nevertheless it is interesting to investigate the behavior of the solution in this limiting case.

To study this case we introduce the following scaling

$$\xi = \frac{\mathcal{K}^6}{\mathcal{M}^2} \tilde{\xi}, \quad \Omega = \frac{\mathcal{K}^4}{\mathcal{M}} \tilde{\Omega}, \quad \Upsilon = v \tilde{\Upsilon}, \quad \Pi = \frac{\mathcal{M}}{\mathcal{K}^2} \tilde{\Pi}, \quad (3.51)$$

where  $v$  is a small positive parameter which we will define later. In terms of the dimensionless groups (3.21), this scaling corresponds to  $\mathcal{G}_K = \mathcal{G}_E = \mathcal{G}_v = 1$ .

In this scaling, the lubrication equation (3.23), propagation criterion (3.24), elasticity equation (3.25), and leak-off equation (3.26) transform to

$$\tilde{\Omega} + \frac{v\mathcal{M}}{\mathcal{K}^4} \tilde{\Upsilon} = \tilde{\Omega}^3 \frac{d\tilde{\Pi}}{d\tilde{\xi}}, \quad (3.52)$$

$$\tilde{\Omega} \rightarrow \tilde{\xi}^{1/2} \quad \text{as} \quad \tilde{\xi} \rightarrow 0, \quad (3.53)$$

$$\tilde{\Pi} = \frac{1}{4\pi} \int_0^\infty \frac{d\tilde{\Omega}}{d\tilde{\xi}} \frac{d\tilde{\xi}}{\tilde{\xi} - \tilde{\xi}}, \quad (3.54)$$

$$\begin{aligned} \frac{\mathcal{M}}{\mathcal{K}^2} \tilde{\Pi} + 1 &= \frac{\mathcal{X} v^2 \mathcal{M}^2}{\mathcal{S} \mathcal{K}^6} \frac{1 + \text{sign}(\tilde{\Upsilon})}{2} \tilde{\Upsilon} \frac{d\tilde{\Upsilon}}{d\tilde{\xi}} + \\ &+ \frac{v}{2\pi\mathcal{S}} \int_0^\infty \frac{d\tilde{\Upsilon}}{d\tilde{\xi}} \exp \left[ \frac{\mathcal{K}^6}{\mathcal{M}^2} (\tilde{\xi} - \tilde{\xi}) \right] K_0 \left( \frac{\mathcal{K}^6}{\mathcal{M}^2} |\tilde{\xi} - \tilde{\xi}| \right) d\tilde{\xi}. \end{aligned} \quad (3.55)$$

If  $v\mathcal{M}/\mathcal{K}^4 \ll 1$ , the set of equations (3.52), (3.53), and (3.54) gives a unique solution for the fracture opening  $\tilde{\Omega}$  and fluid pressure  $\tilde{\Pi}$ , which do not depend on any parameters. In order to find the fluid displacement distribution  $\tilde{\Upsilon}$ , one has to solve the leak-off equation (3.55) where the only unknown is  $\tilde{\Upsilon}(\tilde{\xi})$ .

### 3.5.2.1 Cake build-up domination

He we assume that  $p_{\text{in}} - p_{\text{out}}|_{z=0} \gg p_{\text{out}}|_{z=0} - p_0$ . In other words the pressure drop in the cake is large compared to the pressure drop in the porous medium. In this case the parameter  $v$  can be defined by

$$v = \frac{\mathcal{K}^3}{\mathcal{M}} \sqrt{\frac{\mathcal{S}}{\mathcal{X}}}. \quad (3.56)$$

In terms of the dimensionless groups (3.21) this is equivalent to  $\mathcal{G}_{cb} = 1$ .

The leak-off equation (3.55) reads

$$\begin{aligned} \frac{\mathcal{M}}{\mathcal{K}^2} \tilde{\Pi} + 1 &= \frac{1 + \text{sign}(\tilde{\Upsilon})}{2} \tilde{\Upsilon} \frac{d\tilde{\Upsilon}}{d\tilde{\xi}} + \\ &+ \frac{1}{2\pi} \frac{\mathcal{K}^3}{\mathcal{M}\sqrt{\mathcal{X}\mathcal{S}}} \int_0^\infty \frac{d\tilde{\Upsilon}}{d\tilde{\xi}} \exp\left[\frac{\mathcal{K}^6}{\mathcal{M}^2}(\tilde{\xi} - \tilde{\xi})\right] K_0\left(\frac{\mathcal{K}^6}{\mathcal{M}^2}|\tilde{\xi} - \tilde{\xi}|\right) d\tilde{\xi}. \end{aligned} \quad (3.57)$$

where we assume that the term with the integral is small compared to 1.

The solution of this equation is given by

$$\begin{aligned} \tilde{\Upsilon}(\tilde{\xi}) &= \sqrt{2 \int_{\tilde{\Lambda}}^{\tilde{\xi}} \left( \frac{\mathcal{M}}{\mathcal{K}^2} \tilde{\Pi}(\tilde{\xi}) + 1 \right) d\tilde{\xi}}, \quad \tilde{\xi} > \tilde{\Lambda}, \\ \tilde{\Upsilon}(\tilde{\xi}) &= \mathcal{O}\left(\frac{1}{\sqrt{\mathcal{X}\mathcal{S}}} \min\left[1, \frac{\mathcal{K}^3}{\mathcal{M}}\right]\right), \quad 0 < \tilde{\xi} < \tilde{\Lambda}, \end{aligned} \quad (3.58)$$

where  $\tilde{\Lambda} = (\mathcal{M}^2/\mathcal{K}^6) \Lambda$ . Here we have used the fact that if  $\mathcal{K}^6/\mathcal{M}^2 \gg 1$  then the diffusion kernel  $e^x K_0(|x|)$  can be replaced by its large argument asymptote  $\sqrt{\pi/(2x)}$  (see Subsection 3.6.2), therefore the integral in (3.57) is of order  $\mathcal{M}/\mathcal{K}^3$ .

Since the integral in (3.58) has to be positive, the function which is under the integral also has to be positive. Therefore we have the following implicit equation for the fluid lag length

$$\frac{\mathcal{M}}{\mathcal{K}^2} \tilde{\Pi}(\tilde{\Lambda}) + 1 = 0. \quad (3.59)$$

The assumption  $p_{\text{in}} - p_{\text{out}}|_{z=0} \gg p_{\text{out}}|_{z=0} - p_0$  is thus valid if  $(\mathcal{X}\mathcal{S})^{-1/2} \min[1, \mathcal{K}^3/\mathcal{M}] \ll 1$ . At the same time the assumption  $|\Upsilon| \ll \Omega$  is valid only if  $v\mathcal{M}/\mathcal{K}^4 = \mathcal{K}^{-1}\sqrt{\mathcal{S}/\mathcal{X}} \ll 1$ .

### Case $\mathcal{K}^2/\mathcal{M} \gg 1$

This is the case of the toughness domination. Therefore the fracture aperture is given by the square root LEFM asymptote (3.53), and the fluid pressure distribution can be found from the lubrication equation (3.52)

$$\tilde{\Pi} = \ln \tilde{\xi} + \text{const}, \quad (3.60)$$

where *const* is the integration constant. Substitution of this solution into the equation for the lag gives

$$\tilde{\Lambda} = \exp(-\mathcal{K}^2/\mathcal{M}), \quad (3.61)$$

where we have used  $\mathcal{K}^2/\mathcal{M} \gg 1$ . Note, that this solution is similar to the one obtained by Garagash and Detournay (2000), who used different dimensionless variables, namely  $\kappa_{GD} \equiv \mathcal{K}/\mathcal{M}^{1/2}$  and  $\Lambda_{GD} = \mathcal{M}\Lambda$ . Therefore our solution can be rewritten as  $\Lambda_{GD} = \kappa_{GD}^6 \exp(-\kappa_{GD}^2)$ .

### Case $\mathcal{K}^2/\mathcal{M} \ll 1$

This is the case of the viscosity domination, therefore the fluid pressure distribution is given by  $\tilde{\Pi} = -6^{-2/3}\tilde{\xi}^{-1/3}$  (see Subsection 3.6.2.2). Thus we have the following expression for the fluid lag

$$\tilde{\Lambda} = \frac{\mathcal{M}^3}{36\mathcal{K}^6}, \quad (3.62)$$

or in terms of “GD”:  $\Lambda_{GD} = 1/36$ .

### 3.5.2.2 Negligible cake build-up

Here we assume that  $p_{\text{in}} - p_{\text{out}}|_{z=0} \ll p_{\text{out}}|_{z=0} - p_0$ , i.e., the pressure drop in the cake is small compared to the pressure drop in the porous medium. The parameter  $v$  can be defined by ( $\mathcal{G}_S = 1$ )

$$v = \mathcal{S} \begin{cases} 1, & \mathcal{K}^6/\mathcal{M}^2 \lesssim 1 \\ \mathcal{K}^3/\mathcal{M}, & \mathcal{K}^6/\mathcal{M}^2 \gg 1 \end{cases}, \quad (3.63)$$

whereas the leak-off equation (3.55) transforms to

$$\begin{aligned} \frac{\mathcal{M}}{\mathcal{K}^2} \tilde{\Pi} + 1 = \mathcal{X} \mathcal{S} \frac{1 + \text{sign}(\tilde{\Upsilon})}{2} \tilde{\Upsilon} \frac{d\tilde{\Upsilon}}{d\tilde{\xi}} \begin{cases} \mathcal{M}^2/\mathcal{K}^6, & \mathcal{K}^6/\mathcal{M}^2 \lesssim 1 \\ 1, & \mathcal{K}^6/\mathcal{M}^2 \gg 1 \end{cases} + \\ + \frac{1}{2\pi} \begin{cases} \int_0^\infty \frac{d\tilde{\Upsilon}}{d\tilde{\xi}} \exp\left[\frac{\mathcal{K}^6}{\mathcal{M}^2}(\tilde{\xi} - \tilde{\xi}^-)\right] K_0\left(\frac{\mathcal{K}^6}{\mathcal{M}^2}|\tilde{\xi} - \tilde{\xi}^-|\right) d\tilde{\xi}, & \mathcal{K}^6/\mathcal{M}^2 \lesssim 1 \\ \sqrt{\frac{\pi}{2}} \int_0^{\tilde{\xi}} \frac{d\tilde{\Upsilon}}{d\tilde{\xi}} \frac{d\tilde{\xi}}{\sqrt{\tilde{\xi} - \tilde{\xi}^-}}, & \mathcal{K}^6/\mathcal{M}^2 \gg 1 \end{cases}. \end{aligned} \quad (3.64)$$

Here we have used the fact that if  $\mathcal{K}^6/\mathcal{M}^2 \gg 1$  then the diffusion kernel  $e^x K_0(|x|)$  can be replaced by its large argument asymptote  $\sqrt{\pi/(2x)}$  (see Subsection 3.6.2)

Note that there is always a region  $\tilde{\xi} > \tilde{\Xi}$  where  $(\mathcal{M}/\mathcal{K}^2) \tilde{\Pi} + 1 \approx 1$ . It can be show that in this region the solution of the leak-off equation is given by  $\tilde{\Upsilon} = 2^{5/2} \pi^{-1/2} \mathcal{K}^3 \mathcal{M}^{-1} \tilde{\xi}^{1/2} > 0$  (see, Subsection 3.5.1.2). It is obvious that the size of the lag region is of the same order as the size of the region where the assumption  $(\mathcal{M}/\mathcal{K}^2) \tilde{\Pi} + 1 \approx 1$  is not valid anymore, therefore

$$\frac{\mathcal{M}}{\mathcal{K}^2} \tilde{\Pi}(\tilde{\Lambda}) \sim -1. \quad (3.65)$$

This criterion is similar to the one governing the fluid lag in the case of the cake build-up domination [see (3.59)]. Therefore all calculation of the previous subsection are also applicable to our case of zero cake build-up.

One can see that the assumption  $p_{\text{in}} - p_{\text{out}}|_{z=0} \ll p_{\text{out}}|_{z=0} - p_0$  is valid if  $\mathcal{X} \mathcal{S} \max[1, \mathcal{M}^2/\mathcal{K}^6] \ll 1$ . At the same time the assumption  $|\Upsilon| \ll \Omega$  is valid only if

$v\mathcal{M}/\mathcal{K}^4 = \mathcal{S}\mathcal{K}^{-1}\max[1, \mathcal{M}/\mathcal{K}^3] \ll 1$ . These two assumption can be easily satisfied in the case of a small storage coefficient,  $\mathcal{S} \ll 1$ .

### 3.5.3 Case of leak-off domination

Here we consider the case when the fluid displacement function behind the cavity is large compared to the fracture opening,  $\Upsilon \gg \Omega$ .

To study this case we introduce the following scaling

$$\{\xi, \Omega\} = \sqrt{\mathcal{M}v} \left\{ \tilde{\xi}, \tilde{\Omega} \right\}, \quad \Upsilon = v\tilde{\Upsilon}, \quad \Pi = \tilde{\Pi}, \quad (3.66)$$

where  $v$  is a large positive parameter which we will define later. Note that in terms of the dimensionless groups (3.21) this scaling means that  $\mathcal{G}_p = \mathcal{G}_E = \mathcal{G}_c = 1$ .

In this scaling the lubrication equation (3.23), propagation criterion (3.24), elasticity equation (3.25), and leak-off equation (3.26) transform to

$$\sqrt{\frac{\mathcal{M}}{v}}\tilde{\Omega} + \tilde{\Upsilon} = \tilde{\Omega}^3 \frac{d\tilde{\Pi}}{d\tilde{\xi}}, \quad (3.67)$$

$$\tilde{\Omega} \rightarrow \frac{\mathcal{K}}{(\mathcal{M}v)^{1/4}}\tilde{\xi}^{1/2} \quad \text{as} \quad \tilde{\xi} \rightarrow 0, \quad (3.68)$$

$$\tilde{\Pi} = \frac{1}{4\pi} \int_0^\infty \frac{d\tilde{\Omega}}{d\tilde{\xi}} \frac{d\tilde{\xi}}{\tilde{\xi} - \tilde{\xi}}, \quad (3.69)$$

$$\tilde{\Pi} + 1 = \frac{\mathcal{X}v^{3/2}}{\mathcal{S}\mathcal{M}^{1/2}} \frac{1 + \text{sign}(\tilde{\Upsilon})}{2} \tilde{\Upsilon} \frac{d\tilde{\Upsilon}}{d\tilde{\xi}} + \frac{1}{2^{3/2}\pi^{1/2}} \frac{v^{3/4}}{\mathcal{S}\mathcal{M}^{1/4}} \int_0^{\tilde{\xi}} \frac{d\tilde{\Upsilon}}{d\tilde{\xi}} \frac{d\tilde{\xi}}{\sqrt{\tilde{\xi} - \tilde{\xi}}}. \quad (3.70)$$

Here we have used the fact that  $\sqrt{\mathcal{M}v} \gg 1$  (recall that  $v$  is a large parameter) and replaced the diffusion kernel  $e^x K_0(|x|)$  by its large argument asymptote  $\sqrt{\pi/(2x)}$  (see Subsection 3.6.2). Hence the diffusion is one dimensional, i.e., the leak-off rate at any position depends only on the pressure history at this position and does not depend on any processes happening in the adjacent regions. Also we assume here that the fluid exchange between the fracture and the medium is very fast. As a result, the fluid pressure

in the lag region is uniform and equal to the far-field pore pressure  $p_0$ . Moreover, the assumption that the fluid lag is entirely filled with the pore fluid means that the absolute value of the fluid displacement function  $\Upsilon$  in the cavity is exactly equal to the aperture of the fracture  $\Omega$ ,  $\Upsilon = -\Omega$ . Therefore in our scaling (3.66) the fluid pressure  $\tilde{\Pi}$  and fluid displacement function  $\tilde{\Upsilon}$  in the lag region are given by

$$\tilde{\Pi}(\tilde{\xi}) = -1, \quad \tilde{\xi} < \tilde{\Lambda}, \quad (3.71)$$

$$\tilde{\Upsilon}(\tilde{\xi}) = -\sqrt{\frac{\mathcal{M}}{v}}\tilde{\Omega}(\tilde{\xi}) \approx 0, \quad \tilde{\xi} < \tilde{\Lambda}, \quad (3.72)$$

where we have used the fact that the parameter  $v$  is large, therefore  $\sqrt{\mathcal{M}/v}$  is small. Note that these two equations can be derived directly from the lubrication equation (3.67) and leak-off equation (3.70).

One can see that in our scaling (3.66) the dimensionless material toughness  $\mathcal{K}(\mathcal{M}v)^{-1/4}$  is small [see (3.69)]. Therefore, hereafter in this subsection we assume that the material toughness is equal to zero.

### 3.5.3.1 Cake build-up domination

Here we assume that  $p_{\text{in}} - p_{\text{out}}|_{z=0} \gg p_{\text{out}}|_{z=0} - p_0$ . In other words, the pressure drop in the cake is large compared to the pressure drop in the porous medium. In this case the parameter  $v$  can be defined by

$$v = \mathcal{M}^{1/3} \left( \frac{\mathcal{S}}{\mathcal{X}} \right)^{2/3}. \quad (3.73)$$

In terms of the dimensionless groups (3.21) this is equivalent to  $\mathcal{G}_{cb} = 1$ .

The leak-off equation (3.70) reads

$$\tilde{\Pi} + 1 = \frac{1 + \text{sign}(\tilde{\Upsilon})}{2} \tilde{\Upsilon} \frac{d\tilde{\Upsilon}}{d\tilde{\xi}} + \frac{(\mathcal{X}\mathcal{S})^{-1/2}}{2^{3/2}\pi^{1/2}} \int_0^{\tilde{\xi}} \frac{d\tilde{\Upsilon}}{d\tilde{\xi}} \frac{d\tilde{\xi}}{\sqrt{\tilde{\xi} - \tilde{\xi}}}. \quad (3.74)$$



One can see that the assumption  $p_{\text{in}} - p_{\text{out}}|_{z=0} \gg p_{\text{out}}|_{z=0} - p_0$  is valid if  $\sqrt{\mathcal{X}\mathcal{S}} \gg 1$ . At the same time the assumption  $\Omega \ll \Upsilon$  is valid only if  $\sqrt{\mathcal{M}/v} = \mathcal{M}^{1/3}(\mathcal{X}/\mathcal{S})^{1/3} \ll 1$ . One more assumption we have made here is that the material toughness is equal to zero,  $\mathcal{K}(\mathcal{M}v)^{-1/4} = \mathcal{K}/\mathcal{M}^{-1/3}(\mathcal{X}/\mathcal{S})^{1/6} \ll 1$ . These assumptions can be easily satisfied in the case of large storage coefficient,  $\mathcal{S} \gg 1$ . Moreover, under these assumptions, our set of governing equation (3.67), (3.69), and (3.74) does not depend on any parameters. As a result the length of the fluid lag  $\tilde{\Lambda}$  is a constant. In the original scaling this leads to the following dependence of the fluid lag  $\Lambda$  on our governing parameters

$$\Lambda = \mathcal{M}^{2/3} \left( \frac{\mathcal{S}}{\mathcal{X}} \right)^{1/3} \tilde{\Lambda}, \quad \tilde{\Lambda} = \text{const.} \quad (3.75)$$

Our leak-off equation (3.74) is similar to the leak-off equation (3.57) which describe the case of low permeability rock. Thus we can define the length of the fluid lag  $\tilde{\Lambda}$  using the following implicit equation [cf. (3.59)]

$$\tilde{\Pi}(\tilde{\Lambda}) + 1 = 0. \quad (3.76)$$

To estimate the upper limit of  $\tilde{\Lambda}$  we solve the leak-off equation (3.74) assuming  $|\tilde{\Pi}| \ll 1$ . As a result, we have  $\tilde{\Upsilon} = \sqrt{2\tilde{\xi}}$ . Then using this solution we solve the set the lubrication equation (3.67) and elasticity equation (3.69). Thus  $\tilde{\Pi} \approx -0.15\tilde{\xi}^{-3/8}$  (see Subsection 3.6.2.3). Now we substitute this solution into (3.76) and find the following estimation for the length of the fluid lag

$$\tilde{\Lambda} \lesssim 6.39 \cdot 10^{-3}. \quad (3.77)$$

### 3.5.3.2 Negligible cake build-up

Here we assume that  $p_{\text{in}} - p_{\text{out}}|_{z=0} \ll p_{\text{out}}|_{z=0} - p_0$ , i.e., the pressure drop in the cake is small compared to the pressure drop in the porous medium. In this case the parameter  $v$  can be defined by ( $\mathcal{G}_S = 1$ )

$$v = \mathcal{M}^{1/3} \mathcal{S}^{4/3}. \quad (3.78)$$

The leak-off equation (3.70) reads

$$\tilde{\Pi} + 1 = \mathcal{X} \mathcal{S} \frac{1 + \text{sign}(\tilde{\Upsilon})}{2} \tilde{\Upsilon} \frac{d\tilde{\Upsilon}}{d\tilde{\xi}} + \frac{1}{2^{3/2} \pi^{1/2}} \int_0^{\tilde{\xi}} \frac{d\tilde{\Upsilon}}{d\tilde{\xi}} \frac{d\tilde{\xi}}{\sqrt{\tilde{\xi} - \tilde{\xi}}}. \quad (3.79)$$

The assumptions  $p_{\text{in}} - p_{\text{out}}|_{z=0} \gg p_{\text{out}}|_{z=0} - p_0$  and  $\Omega \ll \Upsilon$  are valid if  $\mathcal{X} \mathcal{S} \ll 1$  and  $\sqrt{\mathcal{M}/v} = \mathcal{M}^{1/3} / \mathcal{S}^{2/3} \ll 1$  respectively. Also the material toughness is taken to be equal to zero,  $\mathcal{K} (\mathcal{M} v)^{-1/4} = \mathcal{K} / (\mathcal{M} \mathcal{S})^{1/3} \ll 1$ . Under these assumptions, the set of governing equation (3.67), (3.69), and (3.79) does not depend on any parameters. In particular

$$\Lambda = (\mathcal{M} \mathcal{S})^{2/3} \tilde{\Lambda}, \quad \tilde{\Lambda} = \text{const}. \quad (3.80)$$

To estimate the length of the fluid lag we use the following equation (see Subsection 3.5.2.2)

$$\tilde{\Pi}(\tilde{\Lambda}) \sim -1. \quad (3.81)$$

To solve this equation we follow the procedure of the previous subsection. Namely we solve the leak-off equation (3.79) assuming  $|\tilde{\Pi}| \ll 1$ . Hence  $\tilde{\Upsilon} = 2^{5/2} \pi^{-1/2} \tilde{\xi}^{1/2}$ . Then using this solution we solve the set the lubrication equation (3.67) and elasticity equation (3.69). Thus  $\tilde{\Pi} \approx -0.184 \tilde{\xi}^{-3/8}$  (see Subsection 3.6.2.3). Now we substitute this solution into (3.80) and find the following estimation for the length of the fluid lag

$$\tilde{\Lambda} \lesssim 1.1 \cdot 10^{-2}. \quad (3.82)$$

## 3.6 Near- and far-field asymptotes

### 3.6.1 Near-field asymptote, $\xi \ll 1$

Here we consider scales which are small compared to the diffusion length scale,  $\xi \ll 1$ .

At these scales the pore pressure  $\Pi_d$  is uniform, i.e.,  $\Pi_d(\bar{\xi} \in \{|\xi - \bar{\xi}| \ll 1\}) \approx \Pi_d(\xi)$ .

Now, let us consider the region inside the cavity and near the very tip. The fluid pressure is uniform there

$$\Pi_0 = \text{const.} \quad (3.83)$$

The fracture opening  $\Omega$  is given by the toughness-dominated asymptote  $\Omega_0$  [see (3.24)], and the fluid displacement function  $\Upsilon$  can be found from the lubrication equation (3.23)

$$\Upsilon_0 = -\Omega_0 = -\mathcal{K}\xi^{1/2}. \quad (3.84)$$

Substitution of these solutions (3.83) and (3.84) into the backstress equation (3.27) leads to

$$\Sigma_0 = \text{const.} \quad (3.85)$$

### 3.6.1.1 Toughness-dominated region with small lag $\Lambda \ll 1$

If we assume that the whole cavity is inside the quasi steady-state region,  $\Lambda \ll 1$ , then the lubrication equation yields

$$\Upsilon = -\Omega, \quad \xi \in [0, \Lambda]. \quad (3.86)$$

If we also assume that we are in the toughness-dominated region,  $\Omega = \Omega_0$ , and if we recall that the pore pressure is uniform,  $\Pi_0 = \text{const}$ , we can get the following solution of the lubrication equation (3.23) in the neighborhood of  $\xi = \Lambda$  [cf. Garagash and Detournay (2000)]

$$\Pi_\Lambda = \Pi_0 + \frac{\mathcal{M}}{\mathcal{K}^2} \ln \left( \frac{\xi}{\Lambda} \right), \quad \xi \geq \Lambda. \quad (3.87)$$

Here we have used the fact that  $\Upsilon(\Lambda) = 0$ , therefore in the neighborhood of  $\xi = \Lambda$  one can assume that  $\Upsilon \ll \Omega$ .

Substitution of this solution into the leak-off equation (3.26) yields

$$\Upsilon_\Lambda = \sqrt{\frac{2\mathcal{M}\mathcal{S}}{\mathcal{K}^2\mathcal{X}} \left[ \xi \ln \left( \frac{\xi}{\Lambda} \right) - \xi + \Lambda \right]}, \quad \xi \geq \Lambda. \quad (3.88)$$

Recall that the solution (3.87), (3.88) is valid only if  $\Omega_0 \gg \Upsilon_\Lambda$ , which leads us to the following criterion

$$\Lambda < \xi \ll \Lambda \exp\left(\frac{\mathcal{K}^4 \mathcal{X}}{2\mathcal{MS}}\right).$$

### 3.6.2 Far-field asymptote, $\xi \gg 1$

In this subsection we look for a solution of the problem of the following asymptotic form

$$\Omega_\infty = A_\Omega^\infty \xi^{a_\Omega}, \quad \Upsilon_\infty = A_\Upsilon^\infty \xi^{a_\Upsilon}, \quad \xi \rightarrow \infty, \quad (3.89)$$

where  $A_i^\infty$  and  $0 < a_i < 1$  are constants. Substitution of these expressions into the elasticity equation (3.25) yields

$$\Pi_\infty + \Sigma_\infty = \frac{A_\Omega^\infty a_\Omega}{4} \cot(\pi a_\Omega) \xi^{a_\Omega-1}. \quad (3.90)$$

Here we have used the “localization” property of the elasticity kernel. [see (3.5) and following explanation, and Garagash and Detournay (2000)]. The term “localization” means, that the kernel “sees” only a finite region around the point of its singularity. That is why we can assume that  $\Omega \sim \xi^{a_\Omega}$  and dismiss the fact that away from the singularity this assumption is not correct.

In contrast, in the case of the diffusion kernel  $e^{\xi-\bar{\xi}} K_0(|\xi-\bar{\xi}|)$  localisation is taking place only at large  $\xi$  [see the leak-off equation (3.26)]. The small and large argument asymptotes of the diffusion kernel are given by (Abramowitz and Stegun, 1972)

$$e^x K_0(|x|) \rightarrow \begin{cases} e^{2x} \sqrt{-\pi/(2x)}, & x \rightarrow -\infty \\ -\ln(|x|), & x \rightarrow 0 \\ \sqrt{\pi/(2x)}, & x \rightarrow \infty \end{cases}, \quad (3.91)$$

therefore at large  $\xi$  the main influence in the integral in (3.26) is due to the  $\sqrt{\pi/(2x)}$  asymptote on the interval  $\bar{\xi} \in [0, \xi]$ . We prove this result carefully in Appendix A.3

where we also evaluate the integral. As a result, the leak-off equation (3.26) transforms into

$$\Pi_\infty + 1 = \frac{\mathcal{X}}{\mathcal{S}} A_\Upsilon^{\infty 2} a_\Upsilon \xi^{2a_\Upsilon - 1} + \frac{A_\Upsilon^\infty a_\Upsilon}{2^{3/2} \mathcal{S}} \frac{\Gamma(a_\Upsilon)}{\Gamma(a_\Upsilon + 1/2)} \xi^{a_\Upsilon - 1/2}. \quad (3.92)$$

Now, for large  $\xi$  the fluid pressure  $\Pi_\infty$  in the left-hand side is small (as proved later) and can be omitted. The resultant equation has the following solution

$$a_\Upsilon = \frac{1}{2}, \quad A_\Upsilon^\infty = -\frac{\pi^{1/2}}{2^{5/2} \mathcal{X}} + \sqrt{\frac{\pi}{2^5 \mathcal{X}^2} + \frac{2\mathcal{S}}{\mathcal{X}}}. \quad (3.93)$$

Substitution of this solution into the backstress equation (3.27) yields

$$\Sigma_\infty = 0, \quad \text{as } \xi \rightarrow \infty. \quad (3.94)$$

Here we have retrieved the case of one dimensional diffusion which is embedded into the Carter's leak-off model. One see that the problem has been degenerated to the one studied by Garagash et al. (2009). In the next subsections, we go briefly through the process of solution of this problem.

### 3.6.2.1 Toughness region

In this region energy dissipation associated with the cracking of the rock material dominates over energy dissipation associated with the flow of the viscous fluids. Thus the fracture aperture is governed by the square root asymptote of linear elastic fracture mechanics (3.24)

$$\Omega_\infty^k = \mathcal{K} \xi^{1/2}. \quad (3.95)$$

Substitution of this solution and the solution for the fluid displacement function (3.89), (3.93) leads to the following solution for the fluid pressure distribution

$$\Pi_\infty^k = \mathcal{M} \frac{\mathcal{K} + A_\Upsilon^\infty}{\mathcal{K}^3} \ln \xi + \text{const}, \quad (3.96)$$

where *const* is the integration constant.

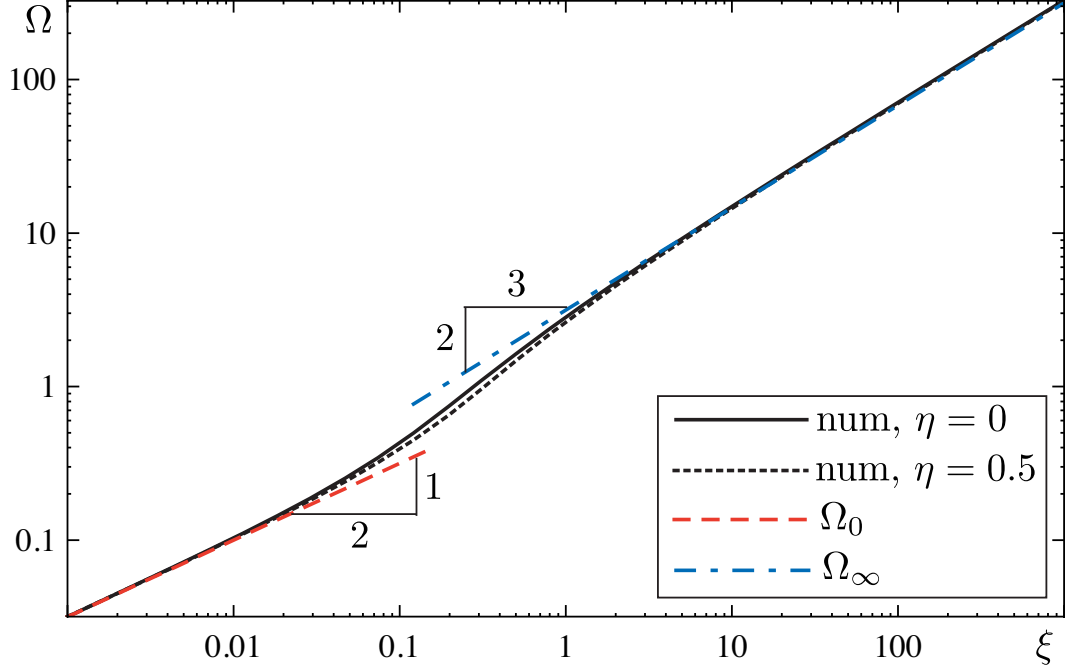


Figure 3.3: Fracture opening profile  $\Omega(\xi)$ ,  $\mathcal{K} = \mathcal{M} = \mathcal{X} = \mathcal{S} = 1$

This solution is valid only if  $\xi \gg 1$  and  $\Pi_\infty^k \ll 1$ . Therefore the toughness region is defined by

$$1 \ll \xi \ll \min \left\{ \exp \left( \frac{1 - \text{const}}{\mathcal{M}} \frac{\mathcal{K}^3}{\mathcal{K} + A_\Gamma^\infty} \right), \xi_{km}, \xi_{k\tilde{m}} \right\}. \quad (3.97)$$

Here  $\xi_{km}$  and  $\xi_{k\tilde{m}}$  are the transition length scales from the toughness region to the storage- and leak-off-viscosity regions respectively (see the next two subsections). These transition length scales can be defined from  $\Omega_\infty^k(\xi_{km}) = \Omega_\infty(\xi_{km})$  and  $\Omega_\infty^k(\xi_{k\tilde{m}}) = \Omega_\infty^{\text{leak-off}}(\xi_{k\tilde{m}})$ , thus

$$\xi_{km} = \frac{\mathcal{K}^6}{2^2 3^5 \mathcal{M}^2}, \quad \xi_{k\tilde{m}} = 5.89 \cdot 10^{-4} \frac{\mathcal{K}^8}{\mathcal{M}^2 A_\Gamma^{\infty 2}}. \quad (3.98)$$

Note that this far-field toughness region emerges in the solution of a semi-infinite fracture propagation only under certain conditions which are defined by (3.97).

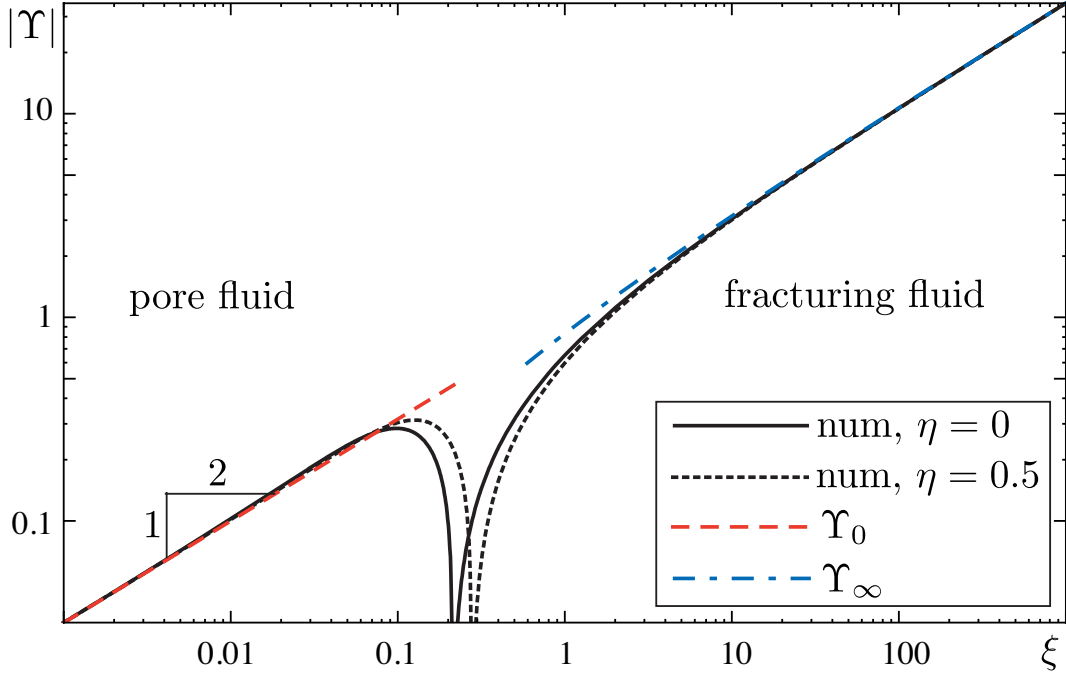


Figure 3.4: Fluid displacement function profile  $\Upsilon(\xi)$ ,  $\mathcal{K} = \mathcal{M} = \mathcal{X} = \mathcal{S} = 1$

### 3.6.2.2 Storage-viscosity region

This region can be characterized by large energy dissipation in the fracturing fluid and negligible fluid losses. The solution of (3.23), (3.89), (3.90), (3.93), and (3.94) is given by

$$\Omega_\infty = 2^{1/3} 3^{5/6} \mathcal{M}^{1/3} \xi^{2/3} + 2^{-1} A_\Upsilon^\infty \xi^{1/2}, \quad (3.99)$$

$$\Pi_\infty = -6^{-2/3} \mathcal{M}^{1/3} \xi^{-1/3}, \quad (3.100)$$

where the second term in the right-hand side of (3.99) is the leak-off correction. Thus one can neglect the leak-off only if  $\xi \gg \xi_{m\tilde{m}}$ , where  $\xi_{m\tilde{m}}$  is the transition length scale from the storage- to leak-off-viscosity region

$$\xi_{m\tilde{m}} = 2^{-8} 3^{-5} \mathcal{M}^{-2} A_\Upsilon^\infty{}^6. \quad (3.101)$$

Substitution of the pressure solution (3.100) into the leak-off equation (3.92) adds

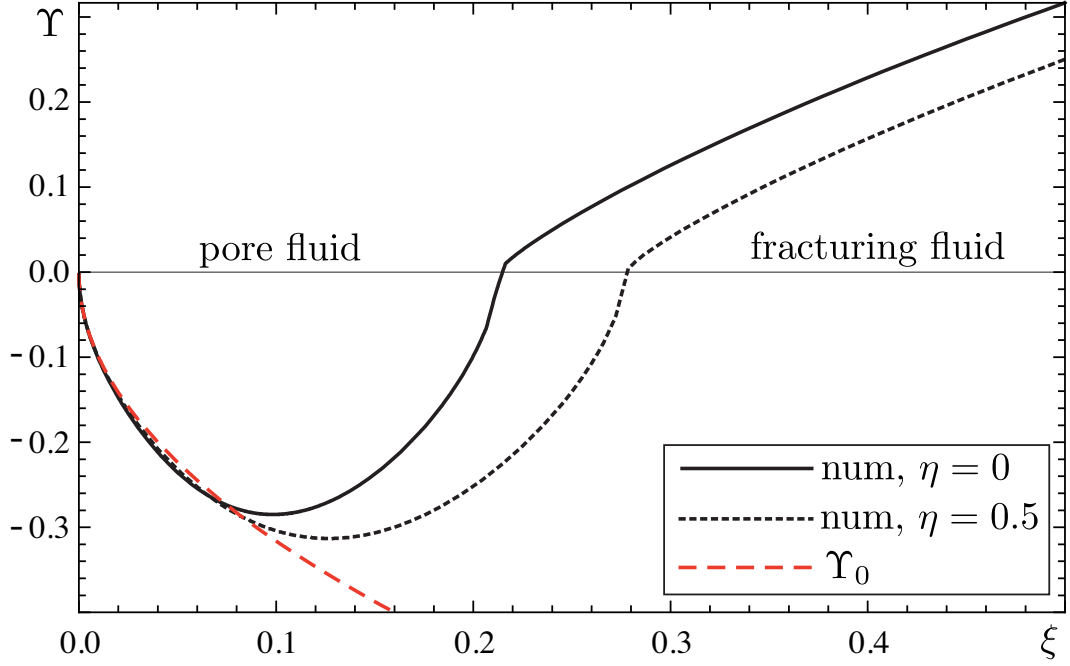


Figure 3.5: Fluid displacement function profile  $\Upsilon(\xi)$ ,  $\mathcal{K} = \mathcal{M} = \mathcal{X} = \mathcal{S} = 1$ : the fracturing-pore fluids boundary region

the next order term into the solution for the fluid displacement function  $\Upsilon_\infty$

$$\Upsilon_\infty = A_\Upsilon^\infty \xi^{1/2} - \frac{6^{1/3} \mathcal{M}^{1/3} \mathcal{S} \xi^{1/6}}{4\mathcal{X}A_\Upsilon^\infty + 1.45337}. \quad (3.102)$$

Thus the assumption  $\Pi_\infty \ll 1$  is valid only if  $\xi \gg 6\mathcal{M}\mathcal{S}^3[A_\Upsilon^\infty(4\mathcal{X}A_\Upsilon^\infty + 1.45337)]^{-3}$ .

Finally substitution of (3.102) into the backstress equation (3.27) yields

$$\Sigma_\infty = \frac{6^{-2/3} \mathcal{M}^{1/3} \eta}{4\mathcal{X}A_\Upsilon^\infty + 1.45337} \left[ \frac{\sqrt{3}}{2} \xi^{-5/6} - 0.484446 \xi^{-4/3} \right]. \quad (3.103)$$

Here we have used (3.90) to evaluate the first term in the right-hand side of the backstress equation (3.27) that is similar to the right-hand side of the elasticity equation (3.25). We also have used the result of Appendix A.3 to evaluate the second term of the right-hand side of (3.27).



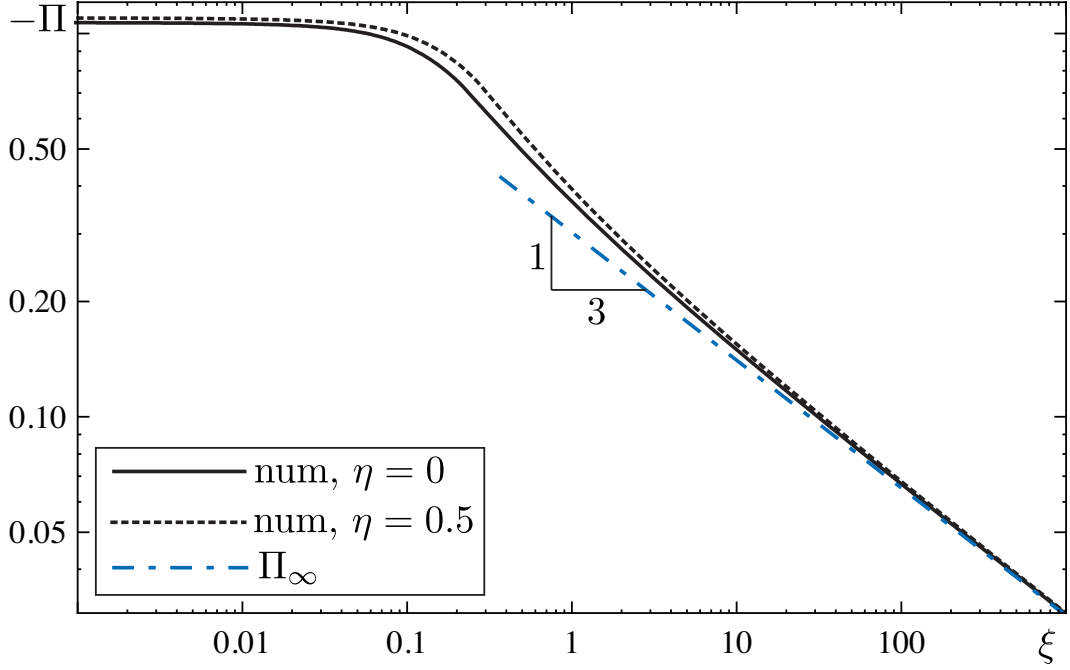


Figure 3.6: Fluid pressure profile  $\Pi(\xi)$ ,  $\mathcal{K} = \mathcal{M} = \mathcal{X} = \mathcal{S} = 1$ . Here  $\Pi_{\eta=0}(0) = -1.068$  and  $\Pi_{\eta=0.5}(0) = -1.098$

In summary, this far-field storage-viscosity region is defined by

$$\xi \gg \max \left\{ 1, \xi_{km}, \xi_{m\tilde{m}}, \frac{6\mathcal{M}\mathcal{S}^3}{A_{\Upsilon}^{\infty 3} (4\mathcal{X}A_{\Upsilon}^{\infty} + 1.45337)^3} \right\}. \quad (3.104)$$

One can see that this region is always a part of the solution of a semi-infinite fracture propagation.

### 3.6.2.3 Leak-off-viscosity region

This region can be characterized by large energy dissipation in the fracturing fluid and large fluid losses. Therefore the fracture volume effect in the lubrication equation (3.23) can be neglected. The solution of (3.23), (3.89), (3.90), (3.93), and (3.94) is given by

$$\Omega_{\infty}^{\text{leak-off}} = 2.53356\mathcal{M}^{1/4} A_{\Upsilon}^{\infty 1/4} \xi^{5/8} + 1.30165\mathcal{M}^{1/2} A_{\Upsilon}^{\infty -1/2} \xi^{3/4} \quad (3.105)$$

$$\Pi_{\infty}^{\text{leak-off}} = -0.163974\mathcal{M}^{1/4} A_{\Upsilon}^{\infty 1/4} \xi^{-3/8} - 0.244059\mathcal{M}^{1/2} A_{\Upsilon}^{\infty -1/2} \xi^{-1/4} \quad (3.106)$$

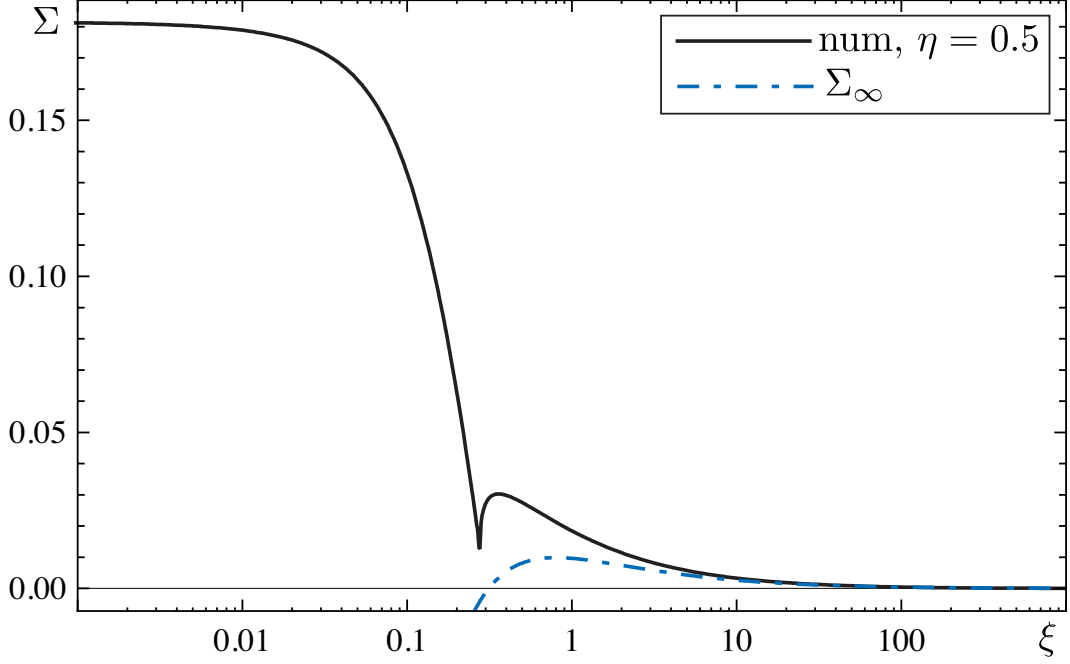


Figure 3.7: Backstress profile  $\Sigma(\xi)$ ,  $\mathcal{K} = \mathcal{M} = \mathcal{X} = \mathcal{S} = 1$ . Here  $\Sigma(0) = 0.1815$

$$\Upsilon_{\infty}^{\text{leak-off}} = A_{\Upsilon}^{\infty} \xi^{1/2} - \frac{0.779996 \mathcal{M}^{1/4} \xi^{1/8} \mathcal{S}}{5 \mathcal{X} A_{\Upsilon}^{\infty} + 2.66365}. \quad (3.107)$$

$$\Sigma_{\infty}^{\text{leak-off}} = \frac{0.0974995 \mathcal{M}^{1/4} \eta}{5 \mathcal{X} A_{\Upsilon}^{\infty} + 2.66365} \left[ 1.20711 \xi^{-7/8} - 0.696309 \xi^{-11/8} \right]. \quad (3.108)$$

This far-field leak-off-viscosity region is defined by

$$\max \left\{ 1, \xi_{k\tilde{m}}, \frac{\mathcal{M}^{2/3} \mathcal{S}^{8/3}}{A_{\Upsilon}^{\infty 8/3} (5 \mathcal{X} A_{\Upsilon}^{\infty} + 2.66365)^{8/3}} \right\} \ll \xi \ll \xi_{\tilde{m}m}, \quad (3.109)$$

where

$$\xi_{\tilde{m}m} = 206 \mathcal{M}^{-2} A_{\Upsilon}^{\infty 6} \quad (3.110)$$

is the transition length scale from the leak-off- to storage-viscosity region which we have defined assuming that the storage correction in the solution for the fracture aperture (3.105) is small.

One can see that similarly to the far-field toughness region this region emerges into a real solution only for some restricted sets of parameters.

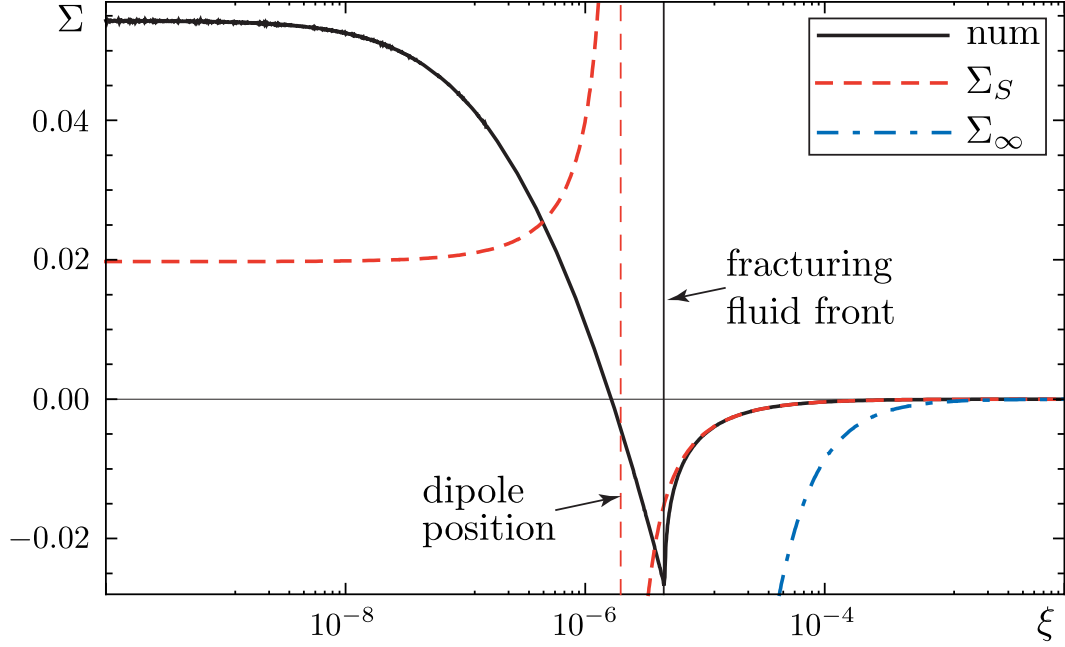


Figure 3.8: Backstress profile  $\Sigma(\xi)$ ,  $\mathcal{K} = 4$ ,  $\mathcal{M} = 1$ ,  $\mathcal{X} = 10^{13}$ ,  $\mathcal{S} = 0.01$ , and  $\eta = 0.5$ . Here  $\Sigma(0) = 0.054$

### 3.7 Transient solution

A transient solution which connects the above near- and far-field asymptotes, can be computed only numerically. We describe the numerical algorithm in Appendix A.4. In the rest of this section we test our numerical scheme against different asymptotic solutions.

Figs 3.3-3.7 illustrate a general case. In particular one can see that the transient solution matches the analytical near- and far-field asymptotes very well. The length of the fluid lag region can be easily defined from Figs 3.4 and 3.5, where we show the profile of the fluid displacement function  $\Upsilon$ . Recall that the fluid displacement function changes its sign at the boundary between the fracturing and pore fluids,  $\Upsilon(\Lambda) = 0$ , therefore in our case  $\Lambda_{\eta=0} \approx 0.2$  and  $\Lambda_{\eta=0.5} \approx 0.28$ .

Looking at the backstress profile (see Fig. 3.7) one can observe the following features:

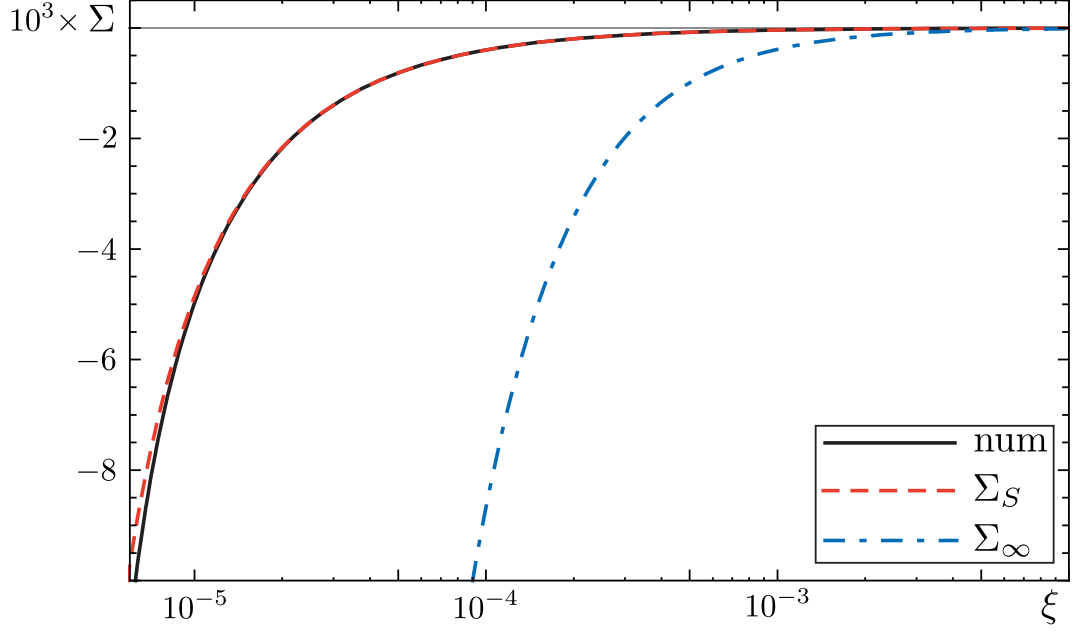


Figure 3.9: Backstress profile  $\Sigma(\xi)$ ,  $\mathcal{K} = 4$ ,  $\mathcal{M} = 1$ ,  $\mathcal{X} = 10^{13}$ ,  $\mathcal{S} = 0.01$ , and  $\eta = 0.5$

the backstress along the fracture is tensile,  $\Sigma > 0$ , and it is singular near  $\xi \approx \Lambda$ . The first feature will be discussed in details in the next section. As for the second feature one would wonder whether it is just a bug of the algorithm or it is a feature of the solution. To check this we simulate the propagation of a fracture with small fluid lag and impermeable cake build-up. Since the fluid exchange between the fracture and the medium is allowed only in the lag region where the net fluid exchange is equal to zero, the problem in the far-field  $\xi \gg \Lambda$  can be modeled by a fluid source dipole propagating at a constant speed. To derive the solution for a dipole we perform an integration by parts in the backstress equation (3.27)

$$\Sigma = \frac{\eta}{\mathcal{S}} \int_0^\Lambda \Upsilon(\bar{\xi}) \Sigma^{\text{li}}(\xi - \bar{\xi}) d\bar{\xi},$$

where

$$\Sigma^{\text{li}}(\xi) = \frac{1}{\xi^2} - \frac{1}{2} e^\xi [3K_0(|\xi|) - 4\text{sign}(\xi) K_1(|\xi|) + K_2(|\xi|)].$$

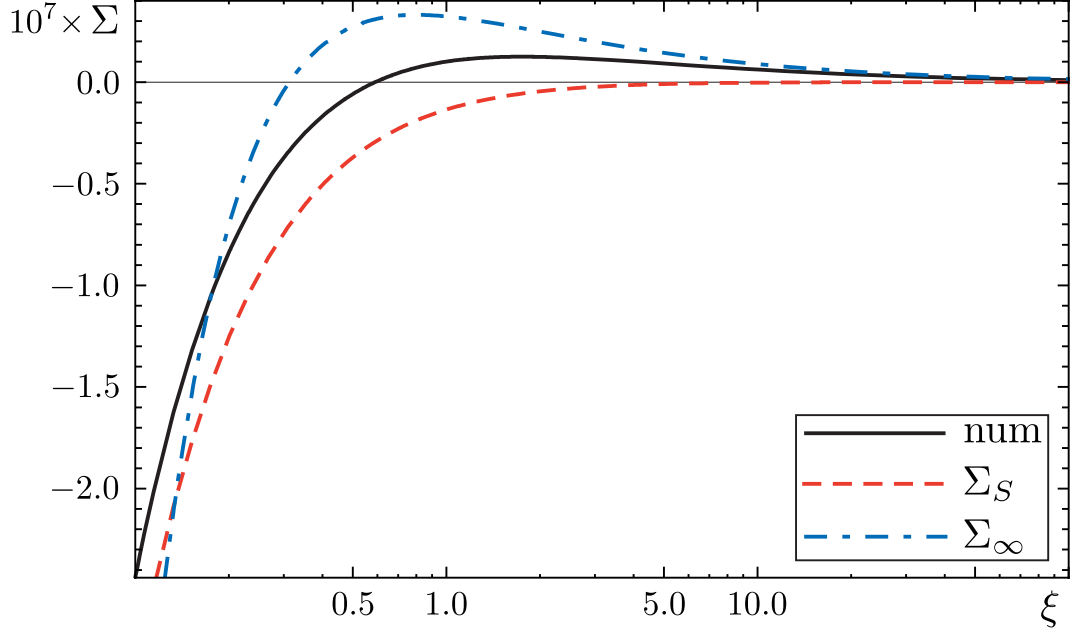


Figure 3.10: Backstress profile  $\Sigma(\xi)$ ,  $\mathcal{K} = 4$ ,  $\mathcal{M} = 1$ ,  $\mathcal{X} = 10^{13}$ ,  $\mathcal{S} = 0.01$ , and  $\eta = 0.5$

The length scale of the variation of the fluid displacement function is of order  $\Lambda$  whereas for  $\Sigma^{\text{li}}$  it is of order 1, therefore if  $\Lambda \ll 1$  then

$$\Sigma_S(\xi) \approx \frac{\eta}{\mathcal{S}} \Upsilon_S \Sigma^{\text{li}}(\xi - \xi_S), \quad \Upsilon_S = \int_0^\Lambda \Upsilon(\bar{\xi}) d\bar{\xi}, \quad \xi_S = \frac{1}{\Upsilon_S} \int_0^\Lambda \bar{\xi} \Upsilon(\bar{\xi}) d\bar{\xi}. \quad (3.111)$$

Here  $\Upsilon_S$  is the strength of the dipole and  $\xi_S$  is the position of the dipole.

To model such a dipole we set  $\mathcal{K} = 4$ ,  $\mathcal{M} = 1$ ,  $\mathcal{X} = 10^{13}$ ,  $\mathcal{S} = 0.01$ , and  $\eta = 0.5$ . In this case  $\Lambda \approx 4.52 \times 10^{-6} \ll 1$ ,  $\xi_S \approx 1.98 \times 10^{-6}$ , and  $\Upsilon_S = -4.9 \times 10^{-9}$ . The results are shown in Figs 3.8-3.10. One can observe very good agreement between the numerical and analytical solutions (see Fig. 3.9). Although the backstress is compressive behind the lag, it is still tensile in the far-field  $\xi \gtrsim 1$  where the system feels the finiteness of the cake build-up permeability (see Fig. 3.10).

Figs 3.11-3.13 compares our numerical solution with the toughness-dominated uniform pressure region asymptotes (3.87) and (3.88).

Interesting results are shown in Figs 3.14-3.17, where we compare our numerical

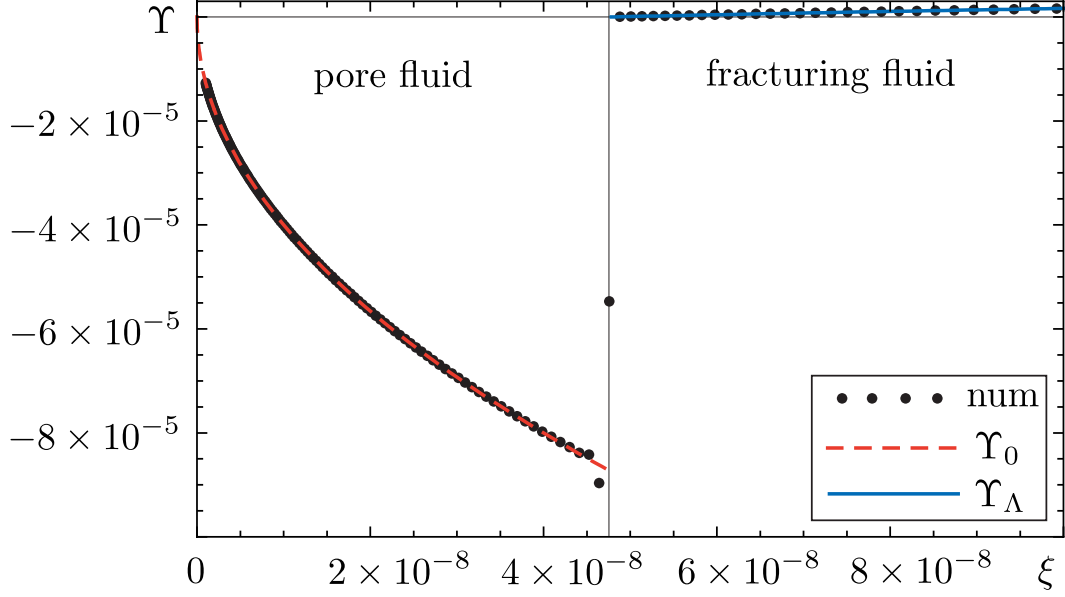


Figure 3.11: Constant pressure region solution + toughness dominance: fluid displacement function profile  $\Upsilon(\xi)$ ,  $\mathcal{K} = 0.4$ ,  $\mathcal{M} = 0.01$ ,  $\mathcal{X} = 100$ , and  $\mathcal{S} = 1$

simulations with the analytical solutions, found by Detournay and Garagash (2003) (see also Subsection 3.5.1.1). Recall that this work studied the case of impermeable cake build-up assuming that the fracture aperture along the fluid lag is governed by the square root LEFM asymptote (3.24). The authors have shown that in this case the solution depends only on two parameters

$$v_{DG} = 2\Lambda, \quad \rho_{DG} = \frac{\mathcal{M}\mathcal{S}}{\mathcal{K}^3\Lambda^{1/2}}.$$

Also they have found analytical asymptotes for the following limiting cases:  $v_{DG} \ll 1$  and  $v_{DG} \gg 1$ . To model the build-up of an impermeable cake, we set parameter  $\mathcal{X}\mathcal{M}/\mathcal{S}$  to be very large ( $\mathcal{X}\mathcal{M}/\mathcal{S} = 10^{12}$ ). Figs 3.14 and 3.15 illustrate the comparison with the asymptote  $v_{DG} \ll 1$ , whereas Figs 3.16 and 3.17 the comparison with the asymptote  $v_{DG} \gg 1$ .

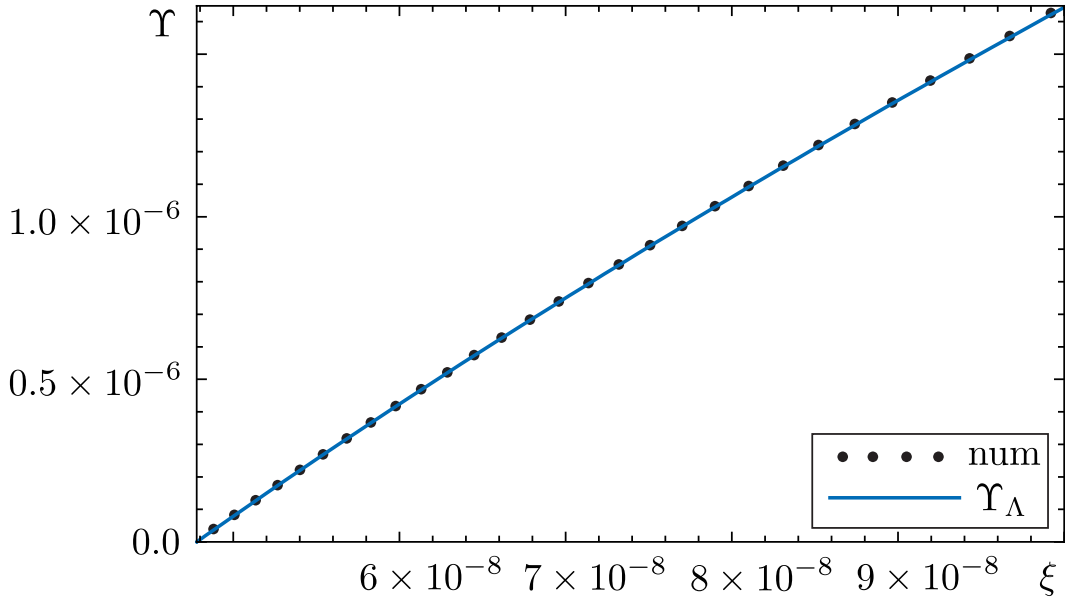


Figure 3.12: Constant pressure region solution + toughness dominance: fluid displacement function profile  $\Upsilon(\xi)$  (enlarged behind the lag region),  $\mathcal{K} = 0.4$ ,  $\mathcal{M} = 0.01$ ,  $\mathcal{X} = 100$ , and  $\mathcal{S} = 1$

## 3.8 Discussion

### 3.8.1 Diffusion

Above we have shown that the diffusion process is three dimensional only in the near-field region  $\xi \lesssim 1$ , whereas in the far-field region  $\xi \gg 1$  it is one dimensional (see Subsection (3.6.2)). A nice illustration of this fact is presented in Fig. 3.18. Thus, the fracture front propagates according to the linear law  $x = Vt$ , whereas diffusion spreads out according to the square root law  $x = \sqrt{ct}$ . One can see that diffusion covers small distances faster than the fracture front. At larger distances the fracture front catches up with diffusion and then passes it leaving behind (see Fig. 3.18). As the result the near-field region of the fracture is under the cover of 3D diffusion. At the same time the far-field region is governed by 1D diffusion.

Additional insight into the diffusion process can be grasped from the contours plot

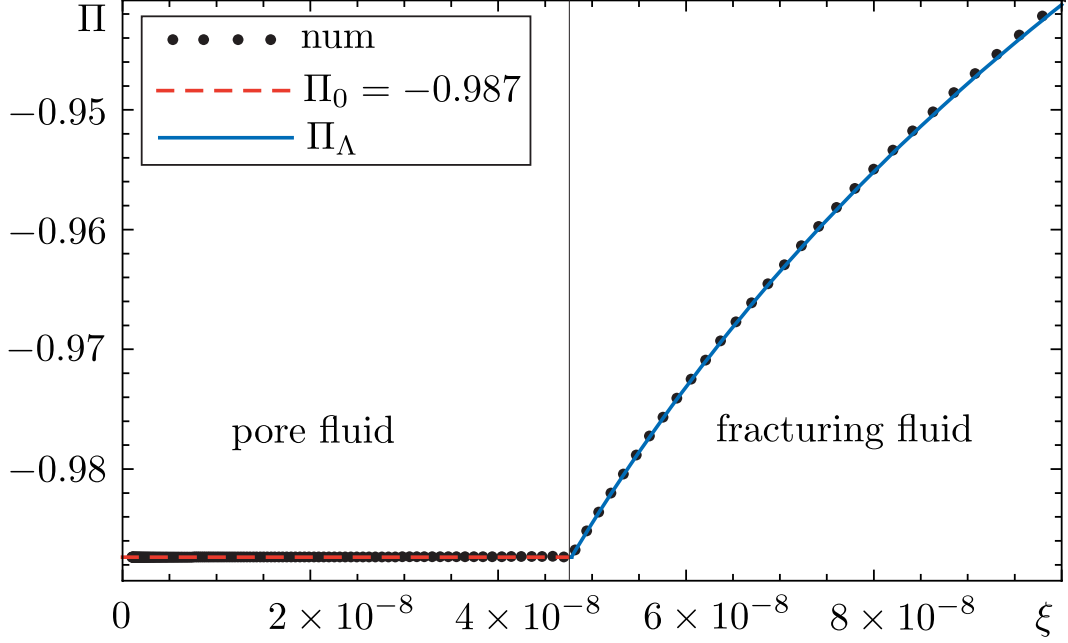


Figure 3.13: Constant pressure region solution + toughness dominance: fluid pressure profile  $\Pi(\xi)$ ,  $\mathcal{K} = 0.4$ ,  $\mathcal{M} = 0.01$ ,  $\mathcal{X} = 100$ , and  $\mathcal{S} = 1$

of the pore pressure distribution around the fracture (see Figs 3.19-3.21). Fig. 3.20 illustrates presence of a fluid source dipole in the lag region. At the same time in the far-field the pore pressure levels are almost parallel to the fracture plane (see Fig. 3.21). This supports the fact that diffusion in the far-field is one dimensional.

### 3.8.2 Carter's leak-off model

Recall the main simplifying assumptions of the Carter's leak-off model: i) the diffusion process is one dimensional and ii) the fluid pressure inside the fracture is equal to the far-field confining stress. In this chapter we have shown that for a propagating fracture the assumption of 1D diffusion is not necessary. Indeed, in Subsection 3.5.1.2 we have demonstrated that a Carter-like leak-off model is valid under less restrictive assumption, namely  $p_{\text{in}} - \sigma_0 \ll \sigma_0 - p_0$ , which means that from a diffusion point of view the fluid



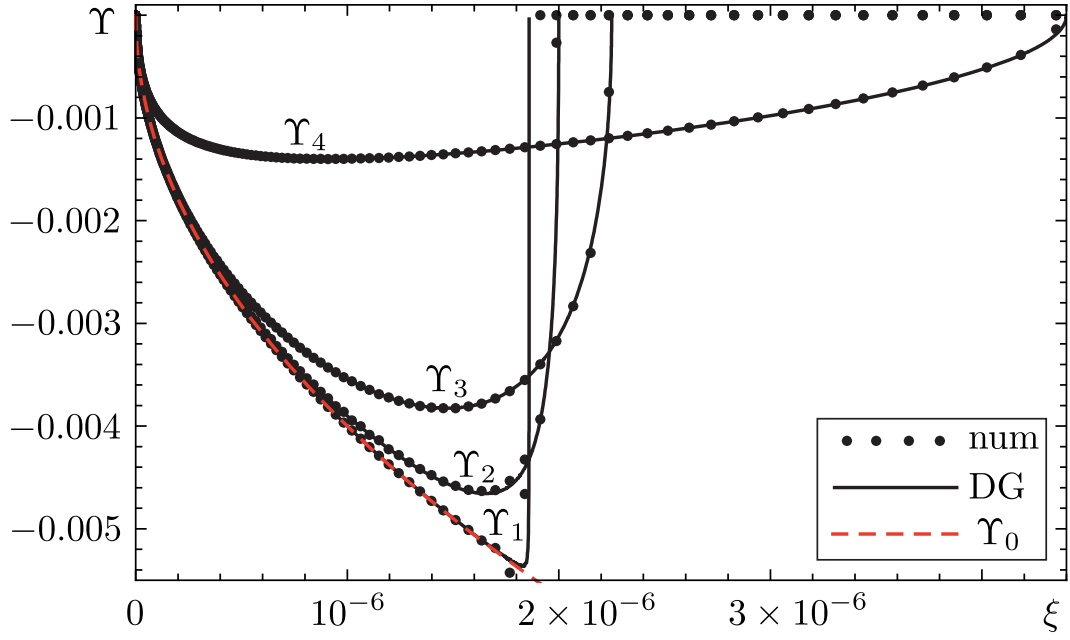


Figure 3.14: Comparison with analytical solution found by Detournay and Garagash (2003): fluid displacement function profile  $\Upsilon(\xi)$  for the case of  $v_{DG} \ll 1$ . The simulations were performed for  $\mathcal{K} = 4$ ,  $\mathcal{M} = 1$ ,  $\mathcal{X}/\mathcal{S} = 10^{12}$ , and 1)  $\mathcal{S} = 100$ ,  $\Lambda = 1.86 \times 10^{-6}$ ; 2)  $\mathcal{S} = 1.0$ ,  $\Lambda = 2.0 \times 10^{-6}$ ; 3)  $\mathcal{S} = 0.2$ ,  $\Lambda = 2.25 \times 10^{-6}$ ; 4)  $\mathcal{S} = 0.01$ ,  $\Lambda = 4.4 \times 10^{-6}$

pressure inside the fracture  $p_{\text{in}}$  is uniform and equal to the far-field confining stress  $\sigma_0$ .

In particular this assumption is valid in the far-field.

### 3.8.3 Backstress

Studying the general solution of the problem shown in Figs 3.3-3.7 one can observe that i) the backstress effect does not have any significant influence on the solution, and ii) the back stress is tensile along the fracture. Simulation of different cases shows that indeed the backstress effect is not so important in the tip region.

The fact that the backstress is tensile can be easily explained in the case of zero cake build-up. Indeed, the loading pressure  $p_{\text{in}}$  can be decomposed into  $p_{\text{in}}(x) = \sigma_0 + p(x)$ , where  $p$  is the net pressure which, in the case of a semi-infinite fracture, is negative,

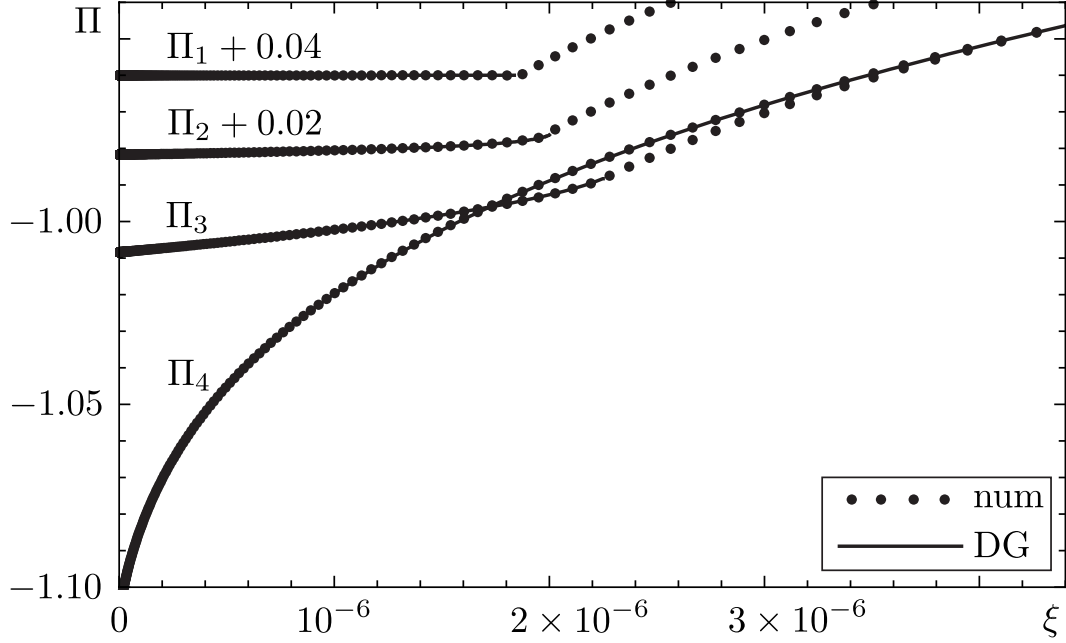


Figure 3.15: Comparison with analytical solution found by Detournay and Garagash (2003): fluid pressure profile  $\Pi(\xi)$  for the case of  $v_{DG} \ll 1$ . The simulations were performed for  $\mathcal{K} = 4$ ,  $\mathcal{M} = 1$ ,  $\mathcal{X}/\mathcal{S} = 10^{12}$ , and 1)  $\mathcal{S} = 100$ ,  $\Lambda = 1.86 \times 10^{-6}$ ; 2)  $\mathcal{S} = 1.0$ ,  $\Lambda = 2.0 \times 10^{-6}$ ; 3)  $\mathcal{S} = 0.2$ ,  $\Lambda = 2.25 \times 10^{-6}$ ; 4)  $\mathcal{S} = 0.01$ ,  $\Lambda = 4.4 \times 10^{-6}$

$p(x) < 0$ . The uniform part  $\sigma_0$  of the loading pressure results in a square root source distribution which does not lead to any backstress generation (see Subsection 3.5.1.2). At the same time the negative part  $p$  leads to the generation of a negative source distribution, and, as a result, to a tensile backstress.

### 3.9 Summary of the chapter results

In this Chapter we have studied propagation of a semi-infinite fracture through a poroelastic medium. Namely, we have performed a detailed scaling analysis and found the near- and far-field asymptotes, as well as some intermediate ones. In particular, we have shown that the far-field fluid leak-off can be modeled as Carter's leak-off. Also we

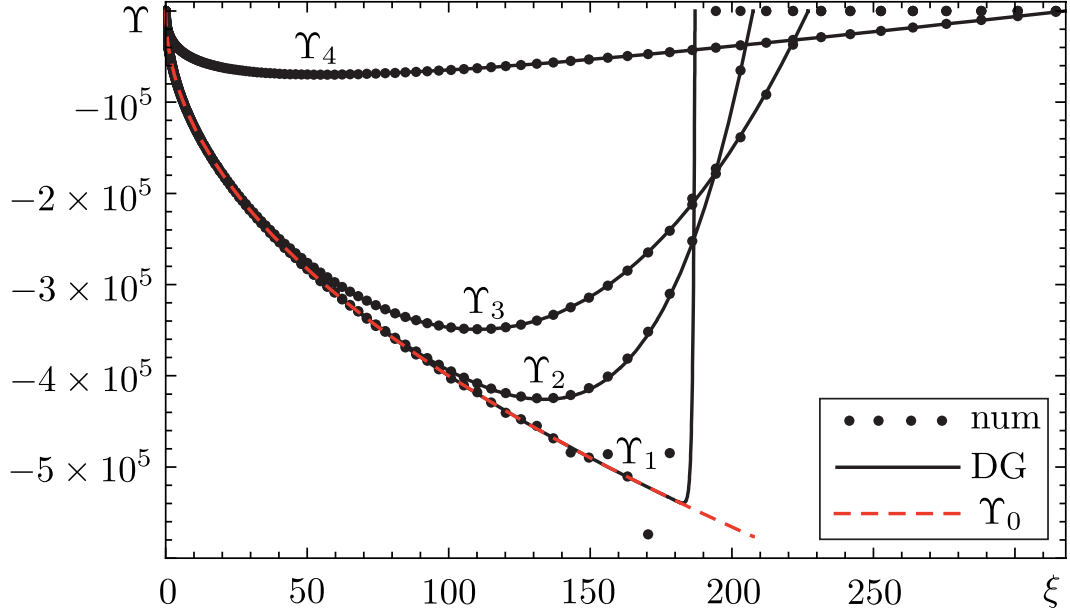


Figure 3.16: Comparison with analytical solution found by Detournay and Garagash (2003): fluid displacement function profile  $\Upsilon(\xi)$  for the case of  $v_{DG} \gg 1$ . The simulations were performed for  $\mathcal{K} = 4 \times 10^4$ ,  $\mathcal{M} = 10^8$ ,  $\mathcal{X}/\mathcal{S} = 10^{20}$ : 1)  $\mathcal{S} = 10^9$ ,  $\Lambda = 187$ ; 2)  $\mathcal{S} = 3.3 \times 10^6$ ,  $\Lambda = 207.5$ ; 3)  $\mathcal{S} = 10^6$ ,  $\Lambda = 227$ ; 4)  $\mathcal{S} = 3.3 \times 10^4$ ,  $\Lambda = 318$

provide an explicit expression for the Carter's leak-off coefficient given by (3.93). One more outcome of the chapter is the numerical algorithm for calculation of the transient solution. We have shown that the numerical algorithm agrees well with the asymptotic solutions.

When deriving the governing equations we mentioned that the tip region of a finite fracture can be represented by a semi-infinite fracture only if the diffusion length scale  $\sqrt{ct}$  is small compared to the fracture size  $R$ . This means that in the case of 3D diffusion, when fracture size is small compared to the diffusion length scale,  $R \ll \sqrt{ct}$ , this representation is not valid. Therefore, a new approach of modeling the tip region of a finite fracture is needed.

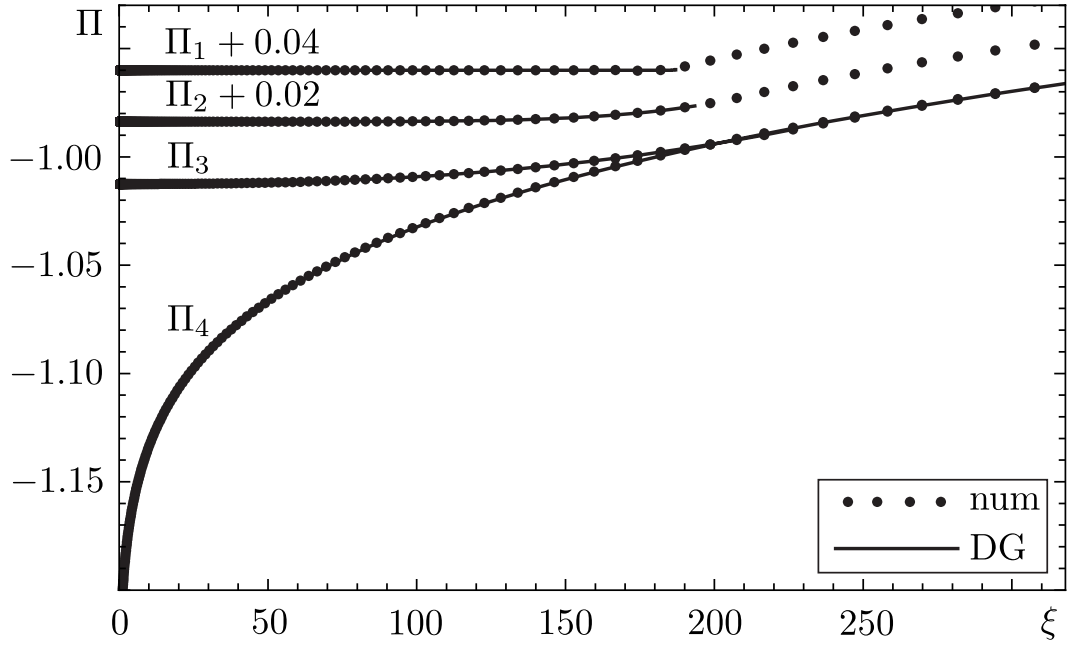


Figure 3.17: Comparison with analytical solution found by Detournay and Garagash (2003): fluid pressure profile  $\Pi(\xi)$  for the case of  $v_{DG} \gg 1$ . The simulations were performed for  $\mathcal{K} = 4 \times 10^4$ ,  $\mathcal{M} = 10^8$ ,  $\mathcal{X}/\mathcal{S} = 10^{20}$ : 1)  $\mathcal{S} = 10^9$ ,  $\Lambda = 187$ ; 2)  $\mathcal{S} = 3.3 \times 10^6$ ,  $\Lambda = 207.5$ ; 3)  $\mathcal{S} = 10^6$ ,  $\Lambda = 227$ ; 4)  $\mathcal{S} = 3.3 \times 10^4$ ,  $\Lambda = 318$

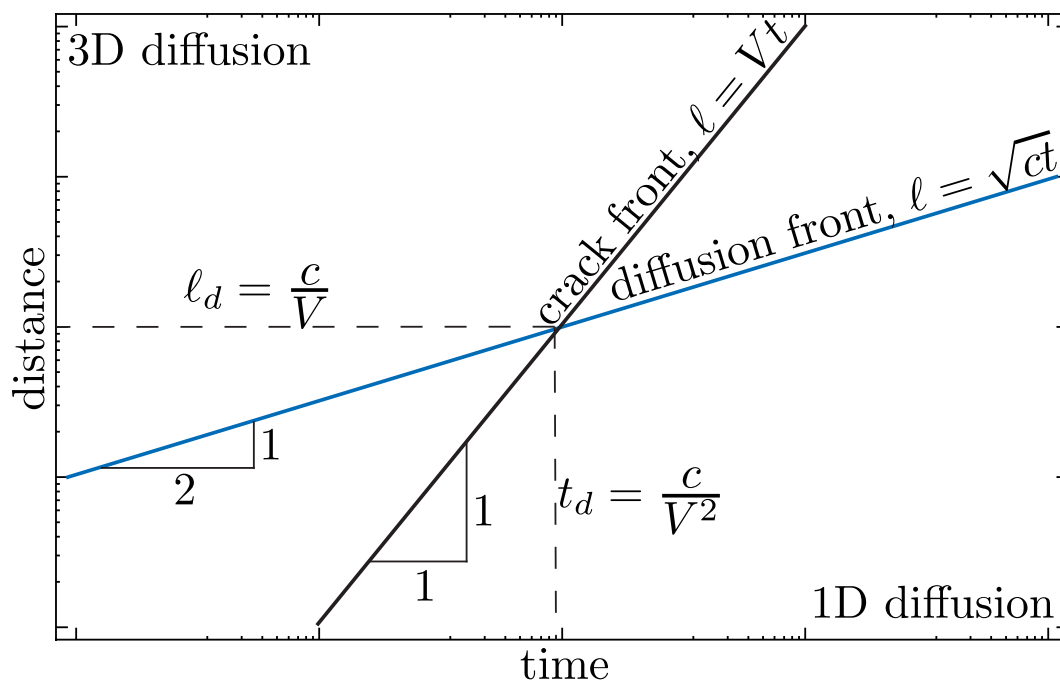


Figure 3.18: Illustration of diffusion length scale

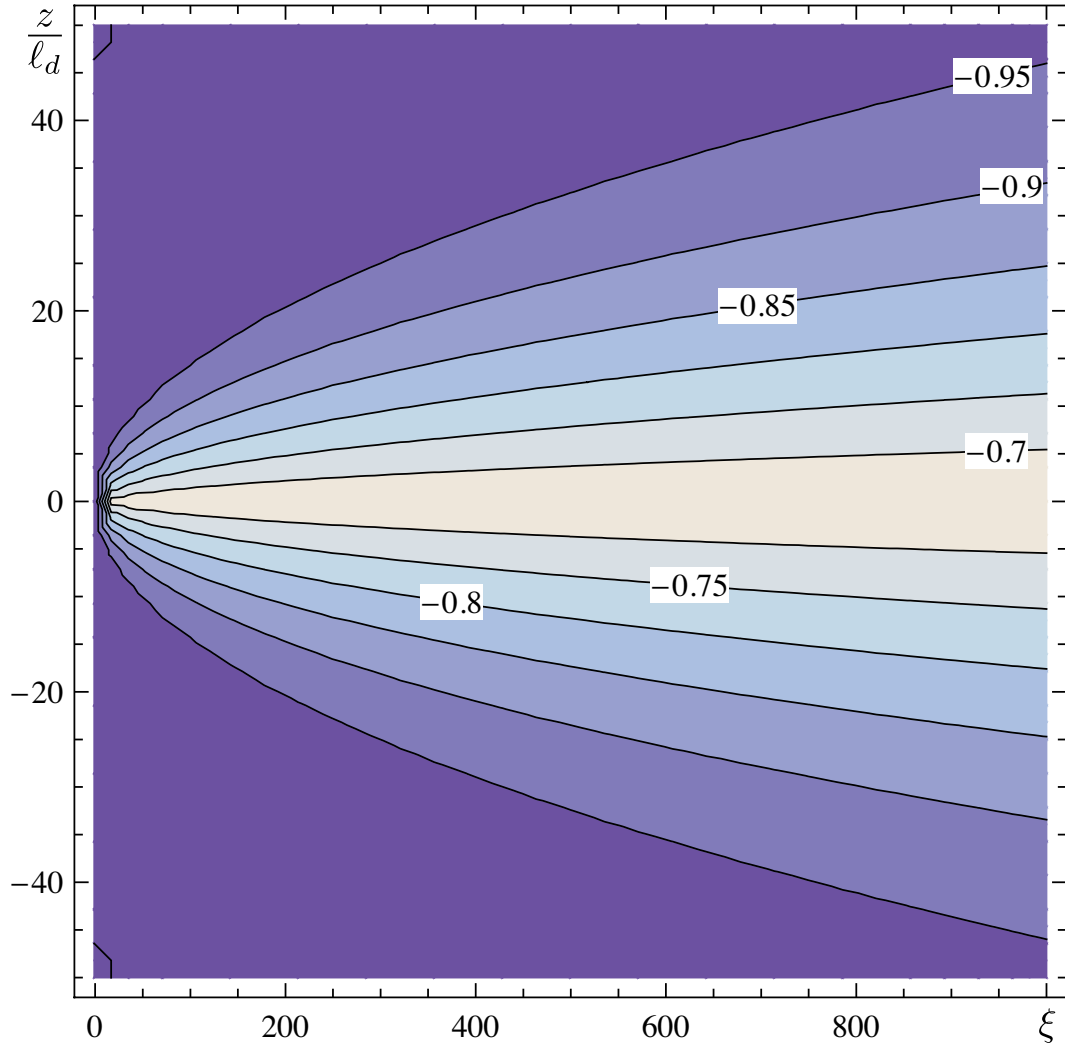


Figure 3.19: Pore pressure distribution  $-1 + \Pi_d(\xi, z/\ell_d)$ ,  $\mathcal{K} = \mathcal{M} = \mathcal{X} = \mathcal{S} = 1$ , and  $\eta = 0.5$

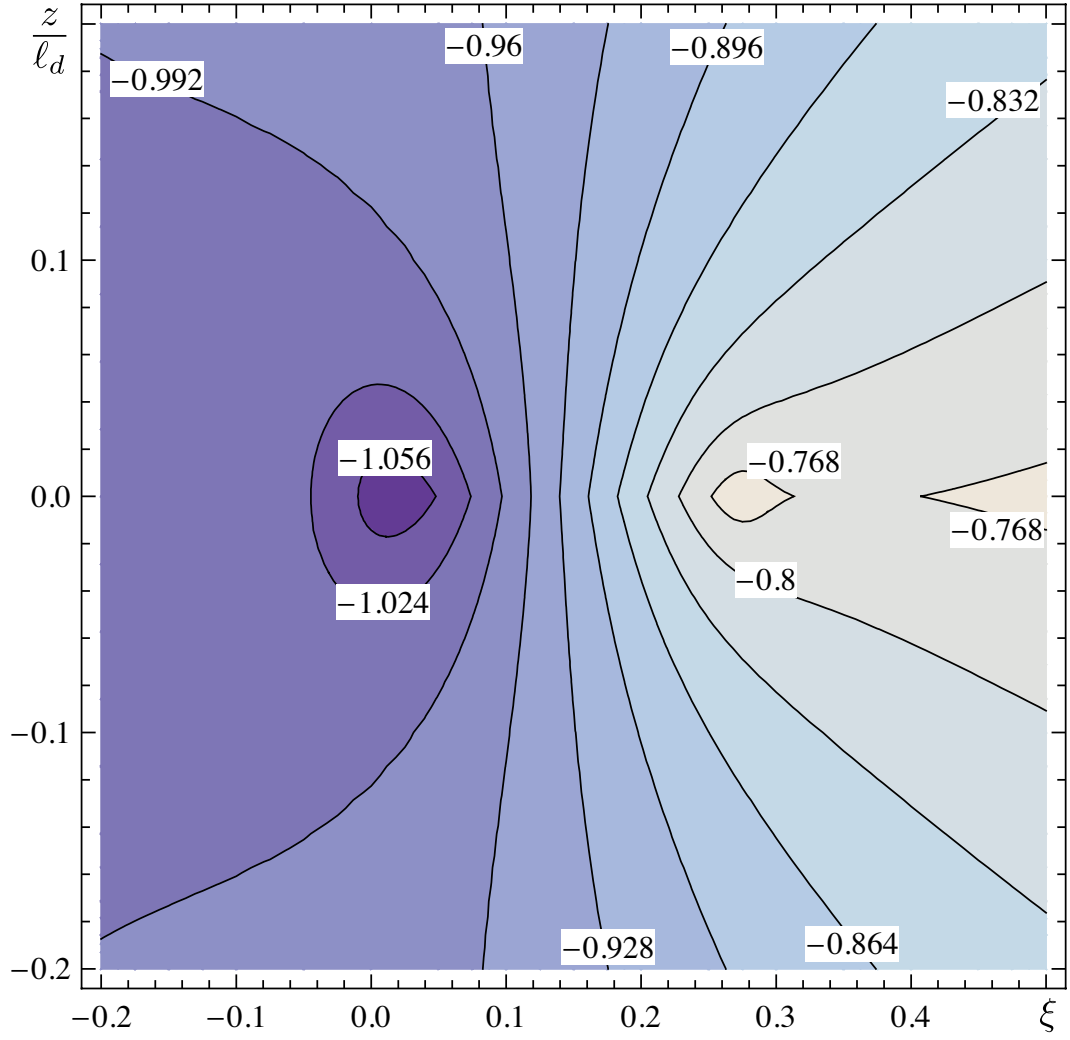


Figure 3.20: Pore pressure distribution  $-1 + \Pi_d(\xi, z/\ell_d)$  (lag region),  $\mathcal{K} = \mathcal{M} = \mathcal{X} = \mathcal{S} = 1$ , and  $\eta = 0.5$

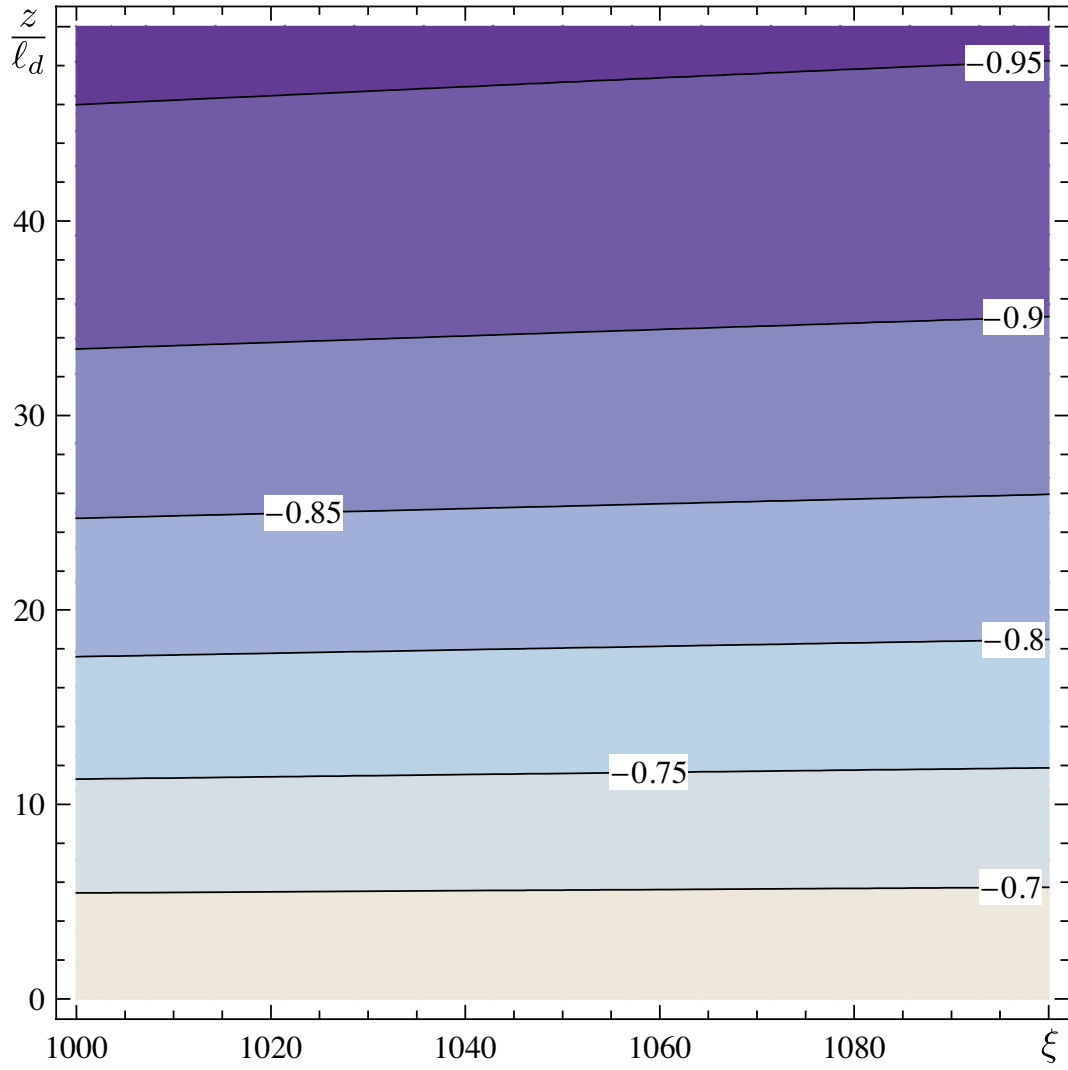


Figure 3.21: Pore pressure distribution  $-1 + \Pi_d(\xi, z/\ell_d)$  (far-field),  $\mathcal{K} = \mathcal{M} = \mathcal{X} = \mathcal{S} = 1$ , and  $\eta = 0.5$



## Chapter 4

# Auxiliary problem

### 4.1 Introduction

In this chapter we study the so-called auxiliary problem, i.e., the poroelastic medium response to a unit pore pressure pulse applied to a disk-shaped surface  $\mathcal{S}$ . The disc of radius  $R$  is located at the origin of a cylindrical coordinate system  $\{r, \varphi, z\}$ ,  $\mathcal{S} = \{r \leq R, z = 0\}$ . We restrict the description of the medium response to  $u(r, t)$ , the component of the fluid displacement, normal to the disc, and to  $\sigma_{zz}(r, t)$ , the normal stress component.

Instead of the fluid displacement function  $u(r, t)$ , one could use the fluid exchange rate  $g(r, t) = \partial u(r, t) / \partial t$  to describe the medium response. Mathematically these two functions are equivalent, whereas from a physical point of view it is easier to operate with the fluid exchange rate  $g(r, t)$ , which is more intuitive. In hydraulic fracturing, however, we are more interested in the total fluid losses than in the instantaneous rates. Thus, the fluid displacement function  $u(r, t)$  is more convenient choice here.

From a diffusion point of view, a hydraulic fracture simply correspond to a planar distribution of fluid sources, which evolves with time. It is conventional to describe this fluid source distribution by the fluid rate distribution  $g$ . As a result the terms “fluid

source distribution” and “fluid rate distribution” are often used as equivalent. In the present research we also use the fluid displacement function distribution  $u$  to characterize the fluid source distribution. We believe that there will not be any confusion.

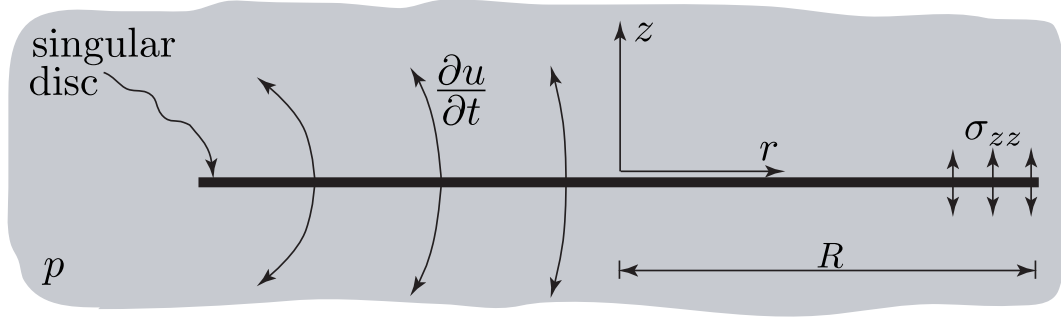


Figure 4.1: Sketch of auxiliary problem

The auxiliary problem is the cornerstone of the present research. First of all, it helps us understand the physics of the leak-off process. Once the solution of the auxiliary problem is known, the problem of a propagating fracture can be simplified significantly. Indeed, if one assumes that the fluid pressure is uniform along the fracture and that there is no low permeability cake build-up, i.e.,  $p_{\text{in}}(r, t) = p_{\text{out}}(r, z = 0, t)$ , then after decomposition of a continuous in time pressure variation into series of pressure pulses (Berchenko et al., 1997),

$$p_{\text{in}}(t) - p_0 = \int_0^t \delta(t - \bar{t}) [p_{\text{in}}(\bar{t}) - p_0] d\bar{t},$$

one can obtain the following expression for the fluid displacement function [cf. (1.11)]

$$v(r, t) = \int_0^t u[R(\bar{t}), r, t - \bar{t}] [p_{\text{in}}(\bar{t}) - p_0] d\bar{t}. \quad (4.1)$$

Similar expression can be written for the backstress

$$\sigma_b(r, t) = \int_0^t \sigma_{zz}[R(\bar{t}), r, t - \bar{t}] [p_{\text{in}}(\bar{t}) - p_0] d\bar{t}. \quad (4.2)$$

The assumption of uniform fluid pressure is valid only if  $p_{\text{in}} - p_0 \gg p_{\text{in}} - \sigma_0$ . Indeed, the fracture propagation is driven by the net fluid pressure, i.e., by the difference between

the fracturing fluid pressure  $p_{\text{in}}$  and the far-field confining stress  $\sigma_0$ , whereas the diffusion process is driven by the difference between the fluid pressure inside the fracture  $p_{\text{in}}$  and the far-field pore pressure  $p_0$ . Thus the criterion  $p_{\text{in}} - p_0 \gg p_{\text{in}} - \sigma_0$  means that from a diffusion point of view the fluid pressure inside the fracture is uniform and can be approximated by the far-field confining stress,  $p_{\text{in}} \approx \sigma_0$ .

Also we have assumed here that the diffusion process does not depend on the stress field, i.e., the solid-to-fluid coupling can be neglected. This simplification was studied by Detournay and Cheng (1991) who have concluded that in the case of hydraulic boundary conditions, when the pore pressure is prescribed, the fluid exchange between the fracture and the medium calculated via poroelastic theory is nearly identical to that computed by uncoupled diffusion equation. This assumption allows us to uncouple the elastic deformation due to hydraulic loading from the pore pressure diffusion leading to the generation of the backstress.

The plane strain analog of our problem was studied by Detournay and Cheng (1991). The authors have analyzed the poroelastic medium response to a unit step of pore pressure rather than to an impulse. Although mathematically the medium response to a unit step loading is just integrated over time medium response to a unit impulse [see (4.1)], sometimes it is easier to think in terms of a step loading. Thus below we will analyze some results in terms of a step loading, whereas all calculations will be done in terms of a unit impulse of the pore pressure. One more useful connection between a unit step and impulse is that the fluid exchange rate between the fracture and the medium in the case of a step loading is equal to the fluid displacement function in the case of a unit impulse.

In contrast to Detournay and Cheng (1991), we perform here a detailed analysis of the region near the stationary tip. In particular we show that solution of the auxiliary problem in this region is singular, and that it strongly depends on the diffusion length

scale  $\ell_d \sim \sqrt{ct}$ , where  $c$  is the diffusion coefficient.

The results of this chapter can also be applied to the equivalent thermal problem.

## 4.2 Problem formulation

### 4.2.1 Starting equations

We assume that the pore pressure  $p$  as well as the stress  $\sigma_{ij}$  in the medium are initially equal to zero,  $p = \sigma_{ij} = 0$ . At time  $t = 0$  a unit pulse of pore pressure is then generated along the disc  $r \leq R$ ,  $z = 0$ .

$$p(r, \varphi, z, t) = \delta(t), \quad r \leq R, \quad z = 0. \quad (4.3)$$

This pulse triggers diffusion of the porous fluid throughout the medium. The pore pressure field is governed by

$$\frac{\partial p}{\partial t} - c \nabla^2 p = \frac{1}{S} \frac{\partial u}{\partial t} \delta(z) H(R - r), \quad (4.4)$$

where  $H(x)$  is the Heaviside step function,  $u$  is the fluid displacement function introduced previously, and  $S = \kappa/c$  is the storage coefficient. The right-hand side of this diffusion equation describes yet unknown fluid sources distributed over the disc  $r \leq R$ ,  $z = 0$ . On the other hand the pore pressure field induced by a known distribution  $u$  along the disk  $\mathcal{S}$  and over the time period  $[0, t]$  can be written as [see discussion related to (2.12), and (2.13)]

$$p(\mathbf{r}, t) = \int_0^t d\bar{t} \int_{\bar{z}=0, \bar{r} < R} u(\bar{\mathbf{r}}, \bar{t}) p^{\text{li}}(\mathbf{r} - \bar{\mathbf{r}}, t - \bar{t}) d\bar{\mathbf{r}}, \quad (4.5)$$

where  $p^{\text{li}}$  is given by (2.16).

The pressure change into the poroelastic medium leads to a generation of stress  $\sigma_{ij}$ . Here we are interested only in the normal stress  $\sigma_{zz}$  acting on the plane  $z = 0$ , which

can be expressed in the same way as the pressure [cf. (2.15)]

$$S_b(r, t) \equiv \sigma_{zz}(r, t) = \int_0^t d\bar{t} \int_{\bar{z}=0, \bar{r} < R} u(\bar{r}, \bar{t}) \sigma_{zz}^{\text{li}}(\mathbf{r} - \bar{\mathbf{r}}, t - \bar{t}) d\bar{\mathbf{r}}, \quad (4.6)$$

where  $\sigma_{zz}^{\text{li}}$  is given by (2.17).

We can now formulate the problem mathematically: we are looking for a fluid source distribution  $u(r, t)$ , such that the pore pressure field given by (4.5) satisfies the boundary condition (4.3). Once the source distribution is known, we calculate the backstress distribution using (4.6).

In some cases, we are more interested in the total fluid volume exchange between the “fracture” and the medium  $U$  rather than in the detailed distribution of  $u$

$$U(R, t) = 2\pi \int_0^R r u(r, t) dr. \quad (4.7)$$

Therefore, we will also compute this total fluid displacement function  $U$ .

## 4.2.2 Scaling

The problem has four parameters  $c$ ,  $\kappa$ ,  $\eta$ , and  $R$ . The explicit dependence of the solution on these parameters can be determined by introducing the following scaling

$$\begin{aligned} (r, z) &= (R\xi, R\zeta), \quad t = T_R\tau, \quad u = \frac{SR}{T_R}\psi, \quad U = \frac{SR^3}{T_R}\Psi, \\ p &= \frac{\Pi}{T_R}, \quad p^{li} = \frac{\Pi^{li}}{SR^3T_R}, \quad S_b = \eta \frac{\Xi}{T_R}, \quad \sigma_{zz}^{li} = \frac{\eta \Xi^{li}}{SR^3T_R}, \end{aligned} \quad (4.8)$$

where  $T_R = R^2/(4c)$  is the diffusion time scale. In this scaling, equations (4.5), (2.16), (4.6), (2.17), and (4.3) yield

$$\Pi(\xi, \tau) = \int_0^\tau d\bar{\tau} \int_{\bar{\zeta}=0, \bar{\xi} < 1} \psi(\bar{\xi}, \bar{\varphi}, \bar{\tau}) \Pi^{li}(\xi - \bar{\xi}, \tau - \bar{\tau}) d\bar{\xi}, \quad (4.9)$$

$$\Pi^{li}(\xi, \tau) = \frac{1}{2\pi^{3/2}|\xi|^5} \left( 2 \frac{|\xi|^2}{\tau} - 3 \right) \left( \frac{|\xi|}{\sqrt{\tau}} \right)^5 \exp\left( -\frac{|\xi|^2}{\tau} \right), \quad (4.10)$$

$$\Xi(\boldsymbol{\xi}, \tau) = \int_0^\tau d\bar{\tau} \int_{\bar{\zeta}=0, \bar{\xi}<1} \psi(\bar{\xi}, \bar{\varphi}, \bar{\tau}) \Xi^{li}(\boldsymbol{\xi} - \bar{\boldsymbol{\xi}}, \tau - \bar{\tau}) d\bar{\boldsymbol{\xi}}, \quad (4.11)$$

$$\Xi^{li}(\boldsymbol{\xi}, \tau) = \frac{1}{2\pi |\boldsymbol{\xi}|^3} \left[ \delta(\tau) + \frac{4}{\sqrt{\pi}} \frac{1}{|\boldsymbol{\xi}|^2} \left( 1 - \frac{|\boldsymbol{\xi}|^2}{\tau} \right) \left( \frac{|\boldsymbol{\xi}|}{\sqrt{\tau}} \right)^5 \exp\left(-\frac{|\boldsymbol{\xi}|^2}{\tau}\right) \right], \quad (4.12)$$

$$\Pi(\boldsymbol{\xi}, \tau) = \delta(\tau), \quad \xi \leq 1, \quad \zeta = 0. \quad (4.13)$$

We also will work in the Laplace transform domain. The Laplace transform of the scaled governing equations (4.9)-(4.13) are given by

$$\tilde{\Pi}(\boldsymbol{\xi}, s) = \int_{\bar{\zeta}=0, \bar{\xi}<1} \tilde{\psi}(\bar{\xi}, \bar{\varphi}, s) \tilde{\Pi}^{li}(\boldsymbol{\xi} - \bar{\boldsymbol{\xi}}, s) d\bar{\boldsymbol{\xi}}, \quad (4.14)$$

$$\tilde{\Pi}^{li}(\boldsymbol{\xi}, s) = \frac{e^{-2\sqrt{s}|\boldsymbol{\xi}|}}{\pi |\boldsymbol{\xi}|} s, \quad (4.15)$$

$$\tilde{\Xi}(\boldsymbol{\xi}, \tau) = \int_{\bar{\zeta}=0, \bar{\xi}<1} \tilde{\psi}(\bar{\xi}, \bar{\varphi}, s) \tilde{\Xi}^{li}(\boldsymbol{\xi} - \bar{\boldsymbol{\xi}}, s) d\bar{\boldsymbol{\xi}}, \quad (4.16)$$

$$\tilde{\Xi}^{li}(\boldsymbol{\xi}, s) = \frac{1}{2\pi |\boldsymbol{\xi}|^3} \left[ 1 - \left( 1 + 2s^{1/2} |\boldsymbol{\xi}| + 4s |\boldsymbol{\xi}|^2 \right) \exp\left(-2s^{1/2} |\boldsymbol{\xi}|\right) \right], \quad (4.17)$$

$$\tilde{\Pi}(\boldsymbol{\xi}, s) = 1, \quad \xi \leq 1, \quad \zeta = 0, \quad (4.18)$$

where  $s$  is the Laplace transform parameter.

### 4.3 Small-time asymptote, $\tau \ll 1$

At small times the problem can be split into two independent parts: the global and the tip region problems. The tip region is such a region near the boundary of the prescribed pressure domain where the geometry of the domain is not important. Furthermore, if the size of the tip region is large compared to the length scales of all physical processes under consideration, the solution of the tip region problem is autonomous.

In general, the geometry can be described by two length scales: the size of the domain and the radius of the boundary curvature. In our case of a unit disc, these two length scales are the same and equal to 1. Therefore the tip region is defined by  $|1 - \xi| \ll 1$ .

The physical processes are represented only by diffusion with a length scale of the order of  $\sqrt{\tau}$ . Thus the solution of the tip region problem is autonomous only if  $\sqrt{\tau} \ll 1$ . We see that this criterion is time dependent, and it is valid only for small times. Physically, it means that at early times the tip region does not “know” anything about the finiteness of the prescribed pressure domain. As time elapses the diffusion explores a larger domain bringing information about the finiteness of the prescribed pressure domain to the tip. This makes the separation of the problem into the tip region problem and the global one impossible.

Below, we find the solution for both the tip region and the global problem. We show that these solutions match each other.

#### 4.3.1 Tip region, $|1 - \xi| \ll 1$

In the tip region equations (4.9), (4.12), and (4.18) written for  $z = 0$  yield (see Appendix B.1 for the details of the derivation)

$$\tilde{\Pi} = \frac{1}{\pi} \int_0^{2\sqrt{s}} \phi(\bar{\zeta}) K_0(|\zeta - \bar{\zeta}|) d\bar{\zeta}, \quad (4.19)$$

$$\frac{1}{2} \begin{Bmatrix} \tilde{\Xi}_{xx} \\ \tilde{\Xi}_{zz} \end{Bmatrix} = \mp \frac{1}{\pi} \int_0^{2\sqrt{s}} \phi(\bar{\zeta}) \left[ \frac{1}{(\zeta - \bar{\zeta})^2} - \frac{K_1(|\zeta - \bar{\zeta}|)}{|\zeta - \bar{\zeta}|} \right] d\bar{\zeta} - \begin{Bmatrix} 0 \\ \tilde{\Pi} \end{Bmatrix}, \quad (4.20)$$

$$\tilde{\Pi} = 1, \quad 0 < \zeta < 2\sqrt{s}, \quad (4.21)$$

where  $\phi \equiv \sqrt{s}\tilde{\psi}$ ,  $\zeta \equiv 2\sqrt{s}(1 - \xi)$ ,  $K_\nu(x)$  is the modified Bessel function of the second kind, and by  $\tilde{\Xi}_{xx}$  we denote the normal stress parallel to the disc (the problem under consideration has only two dimensions). The  $\sqrt{s}$  in these equations reflects the fact that we still do not do any assumptions about the relative size of the diffusion length scale and the size of the prescribed pressure domain, but we do assume that the curvature of the domain boundary is large compared to the diffusion length scale. This helps us

to estimate the error of the assumption  $\sqrt{\tau} \ll 1$  in the case of finite small times (recall that both geometry related length scales are of the same order, and  $\tau \sim 1/s$ ).

It is interesting to note the following properties of the poroelastic stress

$$\tilde{\Xi}_{xx} + \tilde{\Xi}_{zz} = -2\tilde{\Pi}, \quad \int_{-\infty}^{+\infty} \tilde{\Xi}_{zz}(\zeta) d\zeta = 0. \quad (4.22)$$

Here the first equation can be linked to the irrotationality of the displacement field (Cheng and Detournay, 1998), while the second equation follows from equilibrium consideration.

#### 4.3.1.1 Near-field asymptote, $|\zeta| \ll 1$

Let us consider the near-tip region when it is small compared to the diffusion length,  $\zeta \ll 1$ . On these scales the diffusion is so fast that it flattens the pressure distribution  $\tilde{\Pi}$ . In other words the pressure is uniform near the very tip (inside and outside the domain of the prescribed pressure). At the same time due to the logarithmic singularity of the kernel in (4.19), the flux function  $\phi$  should have a square root singularity,  $\phi \sim 1/\sqrt{\zeta}$  (Polyanin and Manzhirov, 2008). To prove this property we rewrite the governing equation (4.19) in the following way

$$\pi = \int_0^\Delta \phi(\bar{\zeta}) K_0(|\zeta - \bar{\zeta}|) d\bar{\zeta} + \int_\Delta^\infty \phi(\bar{\zeta}) K_0(|\zeta - \bar{\zeta}|) d\bar{\zeta}, \quad |\zeta| \ll 1. \quad (4.23)$$

Let  $0 < \zeta \ll \Delta \ll 1$  such that in the first integral we can use the small-argument asymptote of the kernel,  $K_0(|\zeta - \bar{\zeta}|) \simeq -\ln(|\zeta - \bar{\zeta}|)$ , and in the second one we can omit the  $\zeta$ , hence

$$\pi = - \int_0^\Delta \phi(\bar{\zeta}) \ln(|\zeta - \bar{\zeta}|) d\bar{\zeta} + \int_\Delta^\infty \phi(\bar{\zeta}) K_0(|\bar{\zeta}|) d\bar{\zeta}, \quad \zeta \geq 0. \quad (4.24)$$

Here only the first integral depends on  $\zeta$ . Therefore for  $\zeta \ll 1$  the flux distribution function  $\phi$  should be such that the first integral does not depend on  $\zeta$ . Let us check a



solution of the form  $\phi \sim 1/\sqrt{\zeta}$

$$\int_0^\Delta \frac{\ln(|\zeta - \bar{\zeta}|)}{\sqrt{\bar{\zeta}}} d\bar{\zeta} = 2\sqrt{\Delta} \left[ \ln(\Delta - \zeta) - 2 + \sqrt{\frac{\zeta}{\Delta}} \ln \left( \frac{\sqrt{\Delta} + \sqrt{\zeta}}{\sqrt{\Delta} - \sqrt{\zeta}} \right) \right],$$

$$\int_0^\Delta \frac{\ln(|\zeta - \bar{\zeta}|)}{\sqrt{\bar{\zeta}}} d\bar{\zeta} \stackrel{\zeta \ll \Delta}{\simeq} 2\Delta^{1/2} \ln \Delta. \quad (4.25)$$

#### 4.3.1.2 Far-field asymptotes, $2\sqrt{s} \gg |\zeta| \gg 1$

One more change of variable,  $x = \bar{\zeta} - \zeta$ , moves the lower limit of integration of (4.19) to the minus infinity. Then equations (4.19) and (4.21) have the following solution

$$\phi_\infty = 1. \quad (4.26)$$

In time domain this solution corresponds to  $\psi_\infty = 1/\sqrt{\pi t}$ .

The divergence of this asymptote from the exact solution of (4.19), (4.21) is given by

$$\varepsilon_\infty \sim \frac{1}{\pi} \int_{\min(\zeta, 2\sqrt{s}-\zeta)}^\infty K_0(x) dx \approx \frac{e^{-\min(\zeta, 2\sqrt{s}-\zeta)}}{\sqrt{2\pi \min(\zeta, 2\sqrt{s}-\zeta)}}. \quad (4.27)$$

Substitution of (4.26) into (4.19) and (4.20) yields

$$\tilde{\Pi} = 0, \quad \zeta \ll -1, \quad (4.28)$$

$$\frac{1}{2} \begin{Bmatrix} \tilde{\Xi}_{xx} \\ \tilde{\Xi}_{zz} \end{Bmatrix} = \pm \frac{1}{\pi\zeta} - \begin{Bmatrix} 1 \\ 0 \end{Bmatrix}, \quad \zeta \gg 1, \quad (4.29)$$

$$\frac{1}{2} \begin{Bmatrix} \tilde{\Xi}_{xx} \\ \tilde{\Xi}_{zz} \end{Bmatrix} = \pm \frac{1}{\pi\zeta}, \quad \zeta \ll -1. \quad (4.30)$$

#### 4.3.1.3 Transient solution

The explicit form of the near-field solution as well as the transient solution that connects the near- and far-field asymptotes are computed numerically. A detailed description of

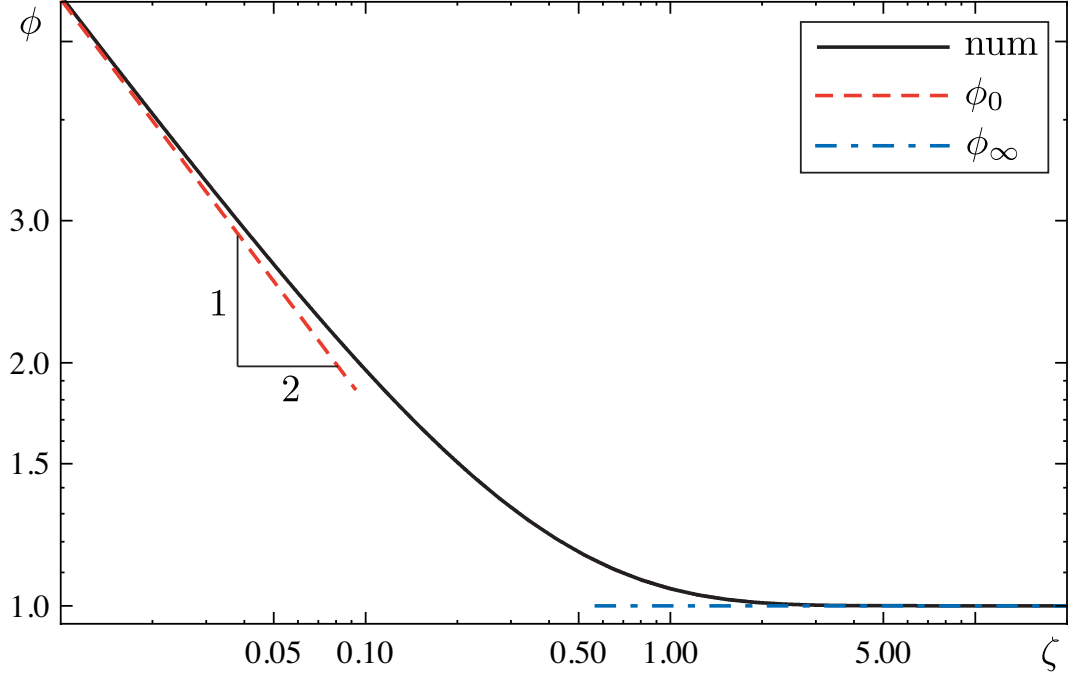


Figure 4.2: Stationary tip: flux distribution function  $\phi \equiv \sqrt{s}\tilde{\psi}$  vs  $\zeta$

the algorithm can be found in Appendix B.2. The results of the numerical simulations are shown in Figs 4.2-4.6. We see that the transient solution converges to the asymptotes studied above. In particular in Fig. 4.6 we show the backstress distribution in the tip region. One can see that although in the far-field the backstress behaviour is singular,  $\tilde{\Xi}_{zz} \sim 1/\zeta$ , it is finite in the near-field. Below we will show that the far-field asymptote of the tip solution corresponds to the near-field asymptote of the global solution.

An interesting illustration of the diffusion process is presented in Fig. 4.7 where we show the fluid displacement function distribution in the time domain for different times. We normalize the fluid displacement function on its value at the center of the disc. One can see, that for small times the fluid displacement function distribution is not uniform only in a very small region near the tip. The size of this region is approximately equal to  $2\sqrt{\tau}$ . As time elapses the size of this region increases and the shape of the fluid

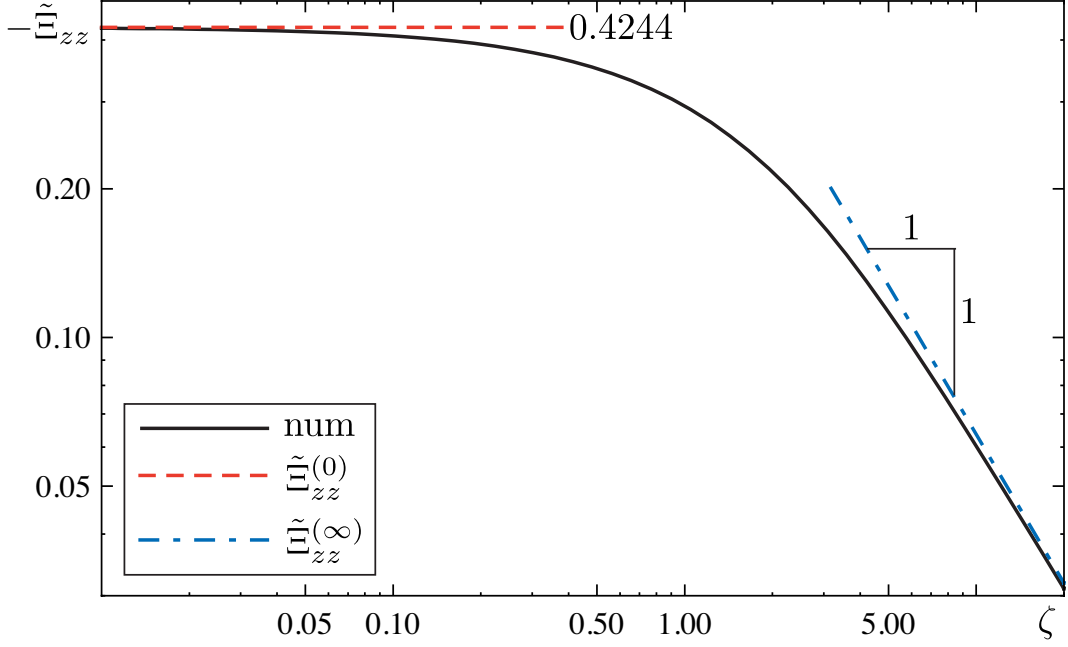


Figure 4.3: Stationary tip: normal component of stress  $\tilde{\Xi}_{zz}$  behind tip,  $\zeta > 0$

displacement function distribution evolves towards the shape of the large-time asymptote given by  $(1 - \xi^2)^{-1/2}$  [see (4.50)].

### 4.3.2 Global solution

Assuming  $\tau \ll 1$  we can reduce the governing equations (4.9)-(4.12) to (see Appendix B.1 for the details of the derivation)

$$\Pi_0 = -\frac{1}{2\sqrt{\pi}} \int_0^\tau \frac{\psi_0(\xi, \bar{\tau}) d\bar{\tau}}{(\tau - \bar{\tau})^{3/2}}, \quad (4.31)$$

$$\Xi_0 = \frac{2}{\pi} \int_0^1 \bar{\xi} \psi_0(\bar{\xi}, \tau) \frac{E\left[\frac{4\xi\bar{\xi}}{(\xi+\bar{\xi})^2}\right]}{(\xi - \bar{\xi})^2 (\xi + \bar{\xi})} d\bar{\xi}, \quad (4.32)$$

where  $E(x)$  is the complete elliptic integral of the second kind (Abramowitz and Stegun, 1972), and subscript “0” stands for small-time. Equation (4.31) with the boundary condition (4.13) can easily be solved using the Laplace transform. As the result we have

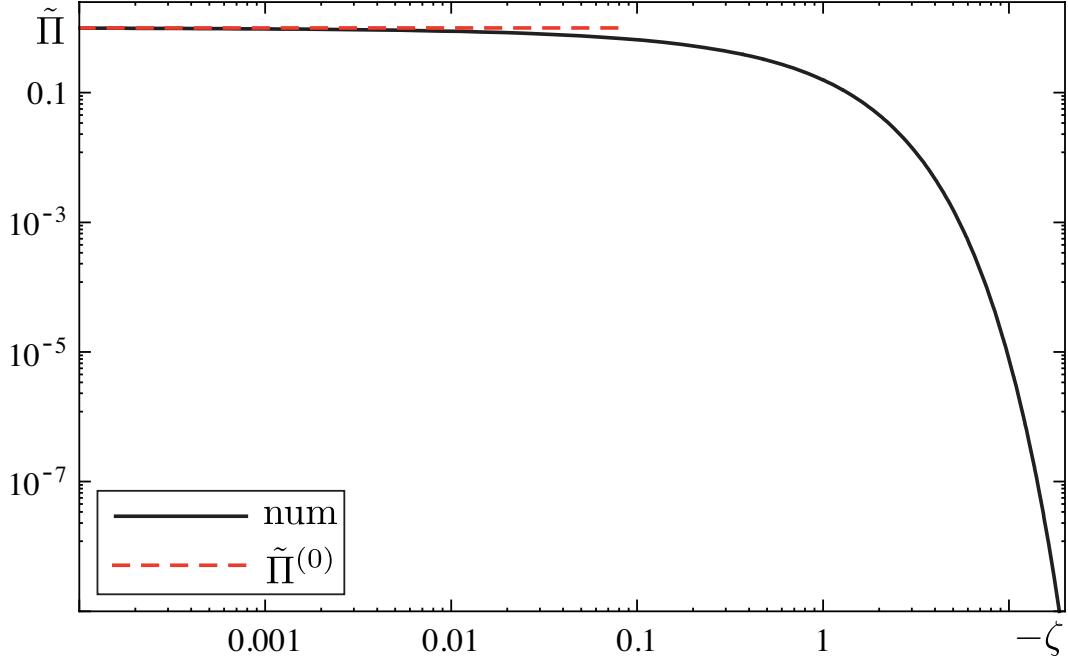


Figure 4.4: Stationary tip: pressure distribution  $\tilde{\Pi}$  ahead of tip,  $\zeta < 0$

the following solution for the source distribution function

$$\psi_0 = \frac{1}{\sqrt{\pi\tau}} \frac{1 + \operatorname{sgn}(1 - \xi)}{2}. \quad (4.33)$$

The fluid exchange function  $\Psi_0$  is equal to

$$\Psi_0 = \sqrt{\frac{\pi}{\tau}}. \quad (4.34)$$

Substitution of the solution (4.33) into (4.32) yields

$$\Xi_0 = -\frac{1}{\pi^{3/2}\tau^{1/2}} \left\{ (1 - \xi)^{-1} E \left[ \frac{4\xi}{(1 + \xi)^2} \right] + (1 + \xi)^{-1} K \left[ \frac{4\xi}{(1 + \xi)^2} \right] \right\}, \quad (4.35)$$

where  $K(x)$  is the complete elliptic integral of the first kind (Abramowitz and Stegun, 1972).

Note that our solution (4.33), (4.35) matches the far-field tip region solution (4.26), (4.28)-(4.30) (see Figs 4.2 and 4.6).

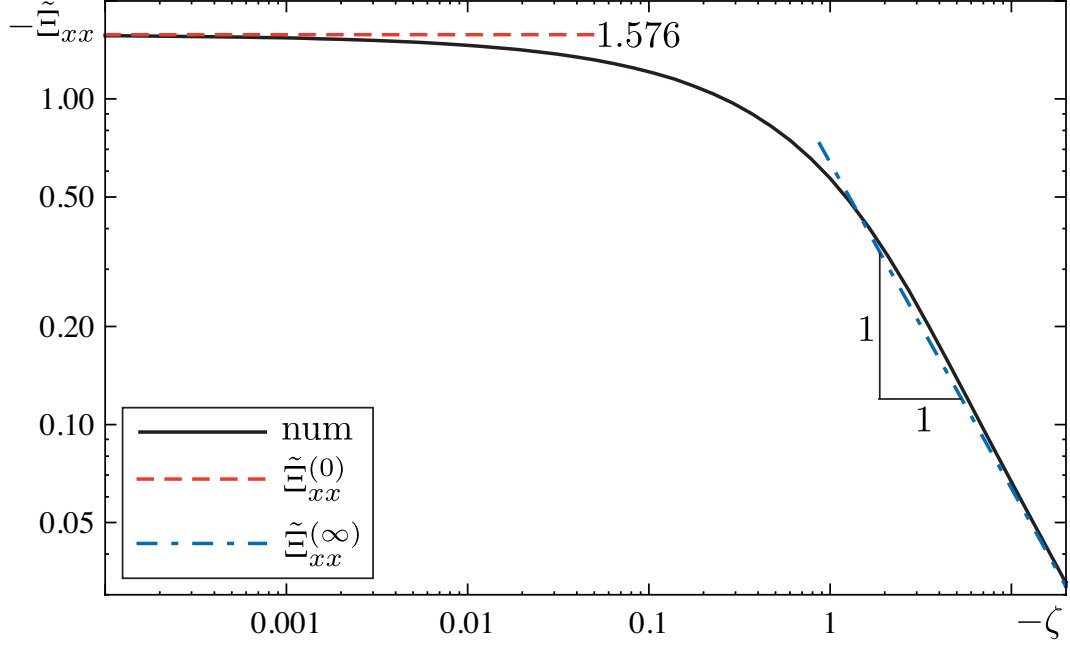


Figure 4.5: Stationary tip: parallel component of stress  $\tilde{\Xi}_{xx}$  ahead of tip,  $\zeta < 0$

#### 4.4 Large-time asymptote, $\tau \gg 1$

To derive the large-time asymptote we work mainly in the Laplace space. In terms of the Laplace transform parameter  $s$ , large times  $\tau \gg 1$  means that  $s \ll 1$ . Therefore, we have a small parameter  $s$ . Asymptotic expansion of the singular fluid dilation solutions (4.15) and (4.17) for small  $s$  yields

$$\tilde{\Pi}^{li}(\boldsymbol{\xi}, s) \simeq \frac{s}{\pi |\boldsymbol{\xi}|} - \frac{2s^{3/2}}{\pi}, \quad (4.36)$$

$$\tilde{\Xi}^{li}(\boldsymbol{\xi}, s) \simeq -\frac{s}{\pi |\boldsymbol{\xi}|} + \frac{8s^{3/2}}{3\pi}. \quad (4.37)$$

Hence, we can seek a solution in the form of series with respect to  $\sqrt{s}$

$$\tilde{A}_{\infty}(\boldsymbol{\xi}, s) = \tilde{A}_{\infty}^{(0)}(\boldsymbol{\xi}, s) + s^{1/2} \tilde{A}_{\infty}^{(1)}(\boldsymbol{\xi}, s) + \dots, \quad (4.38)$$

where  $A = \{\psi, \Pi, \Xi\}$ .

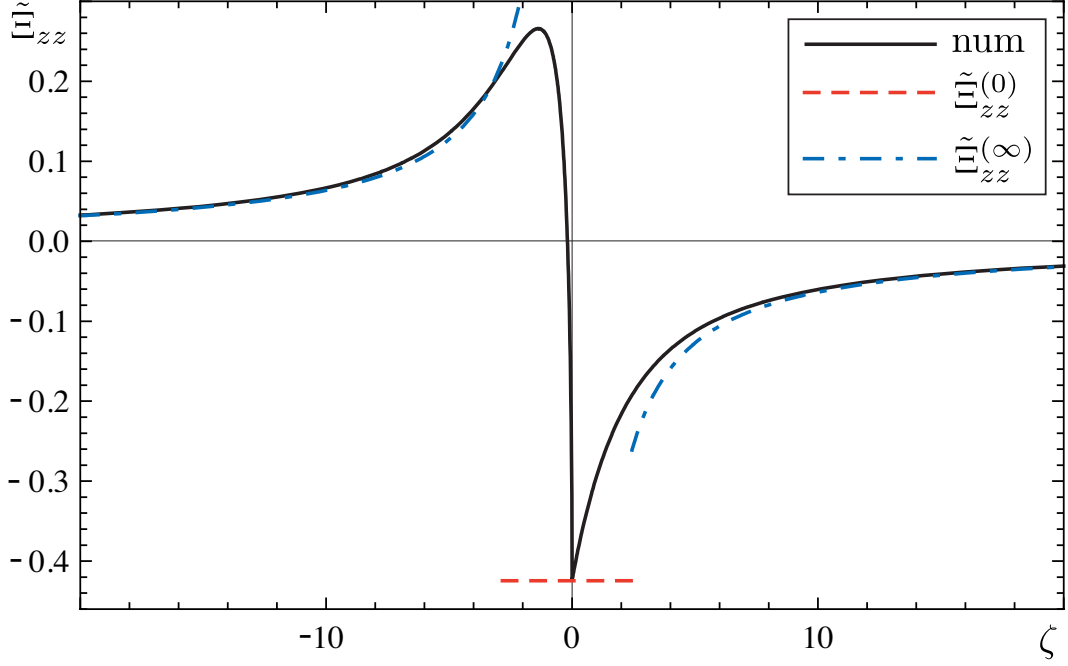


Figure 4.6: Stationary tip: backstress distribution  $\tilde{\Xi}_{zz}$  vs  $\zeta$

After substituting our singular solutions (4.36) and (4.37) into the governing equations (4.14) and (4.16) and collecting  $\mathcal{O}(1)$  and  $\mathcal{O}(s^{1/2})$  terms, we have

$$\mathcal{O}(1): \quad \tilde{\Pi}_{\infty}^{(0)}(\xi, s) = \frac{s}{\pi} \int_{\bar{\zeta}=0, \bar{\xi}<1} \frac{\tilde{\psi}_{\infty}^{(0)}(\bar{\xi}, \bar{\varphi}, s)}{|\xi - \bar{\xi}|} d\bar{\xi}, \quad (4.39)$$

$$\mathcal{O}(s^{1/2}): \quad \tilde{\Pi}_{\infty}^{(1)}(\xi, s) = \frac{s}{\pi} \int_{\bar{\zeta}=0, \bar{\xi}<1} \frac{\tilde{\psi}_{\infty}^{(1)}(\bar{\xi}, \bar{\varphi}, s)}{|\xi - \bar{\xi}|} d\bar{\xi} - \frac{2s}{\pi} \tilde{\Psi}_{\infty}^{(0)}(s), \quad (4.40)$$

$$\mathcal{O}(1): \quad \tilde{\Xi}_{\infty}^{(0)}(\xi, s) = -\frac{s}{\pi} \int_{\bar{\zeta}=0, \bar{\xi}<1} \frac{\tilde{\psi}_{\infty}^{(0)}(\bar{\xi}, \bar{\varphi}, s)}{|\xi - \bar{\xi}|} d\bar{\xi} = -\tilde{\Pi}_{\infty}^{(0)}(\xi, s), \quad (4.41)$$

$$\mathcal{O}(s^{1/2}): \quad \tilde{\Xi}_{\infty}^{(1)}(\xi, s) = -\frac{s}{\pi} \int_{\bar{\zeta}=0, \bar{\xi}<1} \frac{\tilde{\psi}_{\infty}^{(1)}(\bar{\xi}, \bar{\varphi}, s)}{|\xi - \bar{\xi}|} d\bar{\xi} + \frac{8s}{3\pi} \tilde{\Psi}_{\infty}^{(0)}(s). \quad (4.42)$$

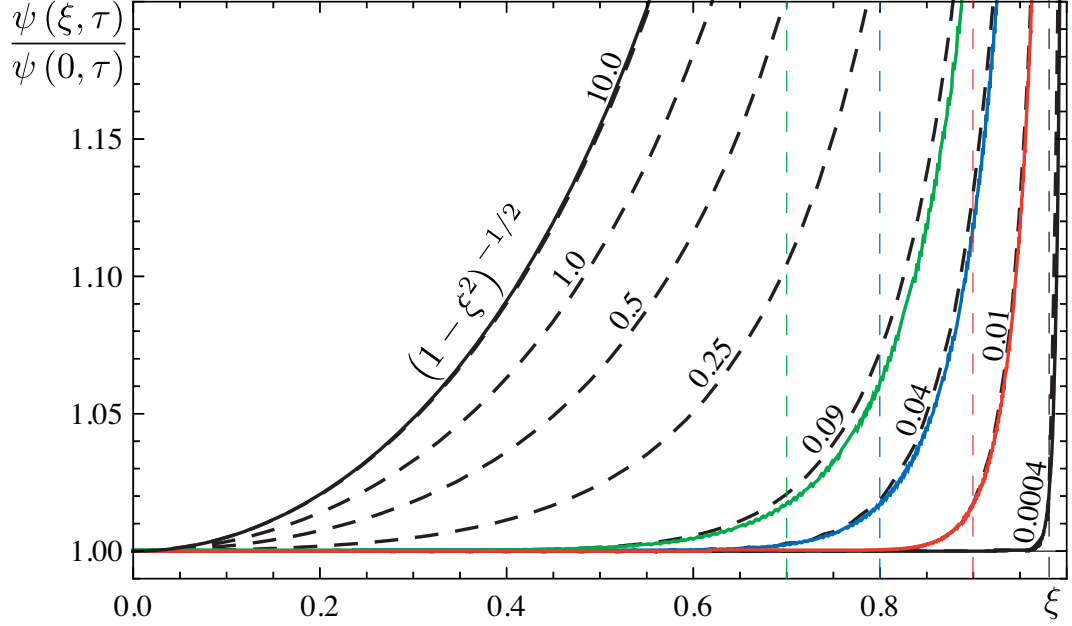


Figure 4.7: Normalized flux distribution function  $\psi(\xi, \tau) / \psi(0, \tau)$  in time domain for different times:  $\tau = 0.0004, 0.01, 0.04, 0.09, 0.25, 0.5, 1.0, 10.0$ . Solid lines for  $\tau = 0.0004, 0.01, 0.04, 0.09$  were obtained from inverse Laplace transform of the tip solution; dashed thick lines are numerical solutions of the global problem; solid line  $(1 - \xi^2)^{-1/2}$  is the large-time asymptote; and dashed thin lines mark diffusion length scale for  $\tau = 0.0004, 0.01, 0.04, 0.09$  and located at  $\xi = 1 - \sqrt{\tau}$ .

#### 4.4.1 $O(1)$ solutions

Integration of (4.39) over the angle leads to

$$\tilde{\Pi}_{\infty}^{(0)}(\xi, \zeta = 0, s) = \frac{4}{\pi} s \int_0^1 \bar{\xi} \tilde{\psi}_{\infty}^{(0)}(\bar{\xi}, s) \frac{K \left[ \frac{4\xi\bar{\xi}}{(\xi+\bar{\xi})^2} \right]}{\xi + \bar{\xi}} d\bar{\xi}. \quad (4.43)$$

The solution of this equation with the boundary condition (4.18) is given by

$$\tilde{\psi}_{\infty}^{(0)}(\xi, s) = \frac{(\pi s)^{-1}}{\sqrt{1 - \xi^2}}. \quad (4.44)$$

Substitution of this solution into (4.43) gives us the pressure distribution outside the domain of the prescribed pressure (domain of the boundary condition)

$$\tilde{\Pi}_{\infty}^{(0)}(\xi, \zeta = 0) = \begin{cases} 1, & \xi \leq 1 \\ \frac{2}{\pi} \arctan\left(\frac{1}{\sqrt{\xi^2 - 1}}\right), & \xi > 1 \end{cases}. \quad (4.45)$$

Here we have used the following formulas for the elliptic integral  $K(x)$  (Gradshteyn and Ryzhik, 1994)

$$K\left[\frac{4x}{(1+x)^2}\right] = (1+x)K(x^2), \quad x \leq 1,$$

$$K(x) = \int_0^1 \frac{1}{\sqrt{1-xt^2}} \frac{dt}{\sqrt{1-t^2}}.$$

The fluid exchange function  $\tilde{\Psi}_{\infty}^{(0)}(s)$  is given by

$$\tilde{\Psi}_{\infty}^{(0)}(s) = 2/s. \quad (4.46)$$

#### 4.4.2 $O(\sqrt{s})$ solutions

Mathematically, equations (4.39) and (4.40) are almost identical. The only difference is that instead of term  $\tilde{\Pi}_{\infty}^{(0)}$  in the left-hand side of (4.39), equation (4.40) has  $\tilde{\Pi}_{\infty}^{(1)} + 2s\tilde{\Psi}_{\infty}^{(0)}(s)/\pi$ . The boundary condition for (4.39) is  $\tilde{\Pi}_{\infty}^{(0)}(\xi \leq 1, \zeta = 0, s) = 1$ , whereas for (4.40) we have  $\tilde{\Pi}_{\infty}^{(1)}(\xi \leq 1, \zeta = 0, s) = 0$ . Therefore we have the following expression for  $\tilde{\psi}_{\infty}^{(1)}(\xi, s)$

$$\tilde{\psi}_{\infty}^{(1)}(\xi, s) = \frac{2s}{\pi} \tilde{\Psi}_{\infty}^{(0)}(s) \tilde{\psi}_{\infty}^{(0)}(\xi, s). \quad (4.47)$$

The fluid exchange function  $\tilde{\Psi}_{\infty}^{(1)}(s)$  is then given by

$$\tilde{\Psi}_{\infty}^{(1)}(s) = \frac{2s}{\pi} \tilde{\Psi}_{\infty}^{(0)2}(s). \quad (4.48)$$

Substitution of the solution (4.47) into (4.42) yields

$$\tilde{\Xi}_{\infty}^{(1)}(\xi, s) = -\frac{2s}{\pi} \tilde{\Psi}_{\infty}^{(0)}(s) \tilde{\Pi}_{\infty}^{(0)}(\xi) + \frac{8s}{3\pi} \tilde{\Psi}_{\infty}^{(0)}(s). \quad (4.49)$$



#### 4.4.2.1 Back to time domain

Combining equations (4.38), (4.44), and (4.47) and applying the inverse Laplace transform, we obtain

$$\psi_{\infty}(\xi, \tau) = \frac{1 + 4\pi^{-3/2}\tau^{-1/2}}{\pi\sqrt{1 - \xi^2}}. \quad (4.50)$$

Doing the same with equations (4.38), (4.46), and (4.48) we get

$$\Psi_{\infty}(\tau) = 2 + \frac{8\tau^{-1/2}}{\pi^{3/2}}. \quad (4.51)$$

And finally, combination of (4.38), (4.41), and (4.49) yields

$$\Xi_{\infty}(\xi, \tau) = -\tilde{\Pi}_{\infty}^{(0)}(\xi) \left[ \delta(\tau) - 2(\pi\tau)^{-3/2} \right] - \frac{8}{3}(\pi\tau)^{-3/2}. \quad (4.52)$$

A reasonable question arises: should we keep the delta function in the above equation? On one hand it seems that for large times this delta function is not important. On the other hand it is clear from the expression for the backstress in the case of a propagating fracture (4.2) that this delta function is important. To understand the meaning of this delta function we write down (4.52) in the case of a unit step loading  $\Pi(\xi \leq 1, \zeta = 0, \tau) = H(\tau)$

$$\Xi_{\infty}^H(\xi, \tau) = -\tilde{\Pi}_{\infty}^{(0)}(\xi) \left[ H(\tau) + \frac{4}{\pi^{3/2}\tau^{1/2}} \right] + \frac{16}{3\pi^{3/2}\tau^{1/2}},$$

where  $H(\tau)$  is the Heaviside step function.

One can see that the Heaviside function corresponds to the large-time equilibrium backstress generated by a unit pressure step loading. This is what one would expect from such a loading. Now if we have a unit impulse of the pore pressure, the backstress at large times is equal to zero and the history of the backstress evolution looks like an impulse. Therefore the delta function in (4.52) is simply a mathematical description of this history.

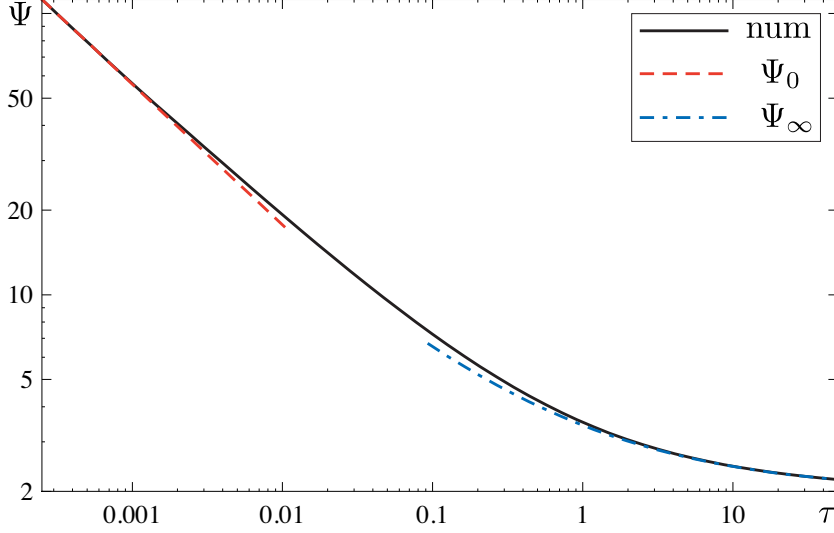


Figure 4.8: Total fluid displacement function  $\Psi$  vs time  $\tau$

## 4.5 Transient solution

The transient solution, which connects the small- and large-time asymptotes, is computed numerically. First, we solve the integral equation (4.14) with the boundary condition (4.18). As a result, we find the flux distribution function in the Laplace domain,  $\tilde{\psi}$ . Then, we use this solution in (4.16) to calculate the Laplace transform of the backstress,  $\tilde{\Xi}$ . We finish our computation with a numerical inversion of the Laplace transform solution, following the technique developed by Lopez-Fernandez and Palencia (2004) (see also Appendix B.4). The details of the computation can be found in Appendix B.3.

The algorithm was implemented in *Mathematica 6.0*. Computation of the backstress was done inside the disc  $\{\xi \leq 10, \zeta = 0\}$ , which was discretized with a spatial step equal to 0.1. The problem was solved for quite a wide range of times:  $10^{-5} < \tau < 10^5$ . Outside this large domain the region of the prescribed pore pressure can be approximated by a point source. Therefore we have the following far-field asymptote

$$\tilde{\Xi}_{ff}(\boldsymbol{\xi}, s) = \tilde{\Psi}(s) \tilde{\Xi}^{li}(\boldsymbol{\xi}, s). \quad (4.53)$$

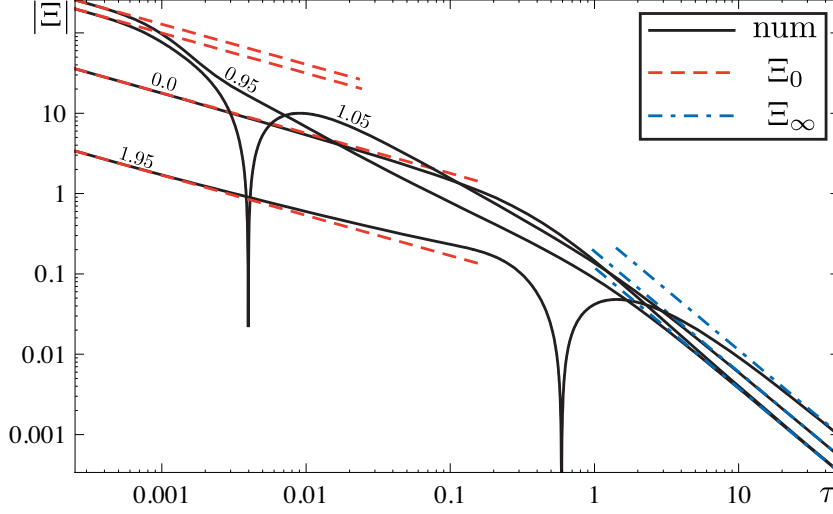


Figure 4.9: Backstress  $\Xi$  vs time  $\tau$  for different spacial points:  $\xi = 0, 0.95, 1.05, 1.95$

The results of the numerical simulation are shown in Figs 4.8-4.12. Fig. 4.8 shows the time dependence of the fluid exchange function  $\Psi$ . Figs 4.9-4.12 illustrate the temporal and spatial behavior of the backstress. One can observe a very good agreement between the numerical transient solution and the asymptotic solutions.

Note that inside the region  $\xi < \xi_{\Xi=0}(\tau)$ , where  $\Xi[\xi_{\Xi=0}(\tau), \tau] = 0$ , the backstress is compressive,  $\Xi < 0$ , whereas outside this region it is tensile,  $\Xi > 0$ , see Fig. 4.9. It is clear that  $\xi_{\Xi=0}(0) = 1$  and  $\xi_{\Xi=0}(\tau \rightarrow \infty) \rightarrow \infty$ . This behavior of the backstress mimics the diffusion process. In fact, when the diffusion is one dimensional (early times) the backstress is mainly concentrated inside the pressurising domain, and as time elapses the compressive backstress occupies a larger region of the medium.

## 4.6 Summary of the chapter results

In this chapter we have solved the auxiliary problem (see the Introduction). Namely, we have found a semi-analytical solution for the response of a poroelastic medium to an

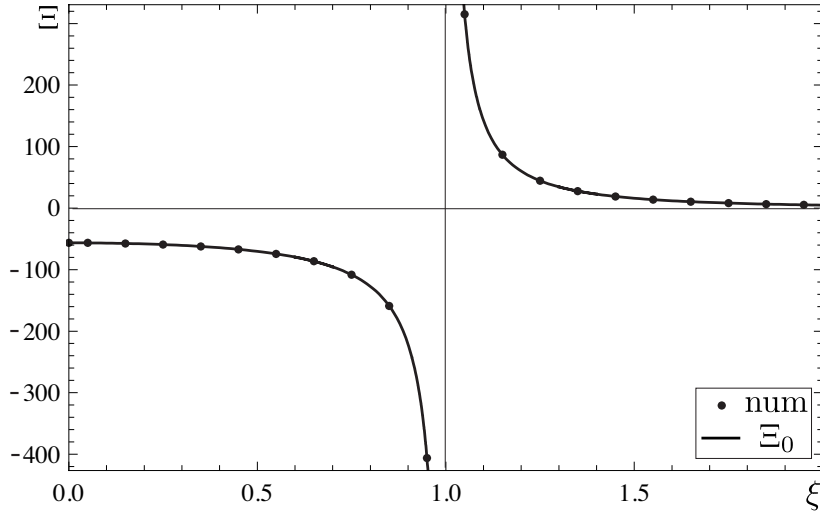


Figure 4.10: Spatial distribution of backstress  $\Xi$  for small time,  $\tau = 10^{-4}$

impulse of pore pressure applied to a penny-shaped domain. This semi-analytical solution includes the analytical small- and large-times asymptotes for the flux distribution around the fracture as well as for the backstress [see (4.34), (4.35), (4.51), (4.52)]. For intermediate times we have built a numerical transient solution (see Section 4.5). Also we have found the semi-analytical far-field asymptote (4.53) for the backstress where the spatial dependence is known analytically and the temporal dependence was obtained by doing a numerical inversion of the Laplace domain using the numerical solution for the fluid exchange function  $\Psi$ .

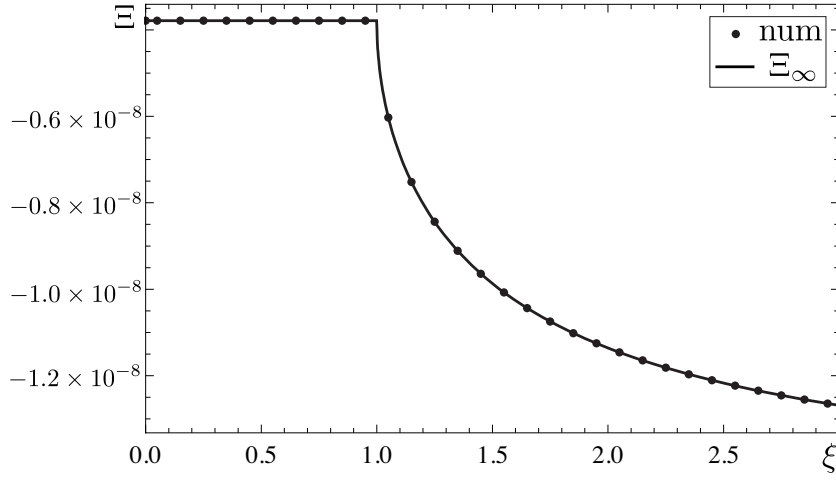


Figure 4.11: Spatial distribution of backstress  $\Xi$  for large time,  $\tau = 10^5$

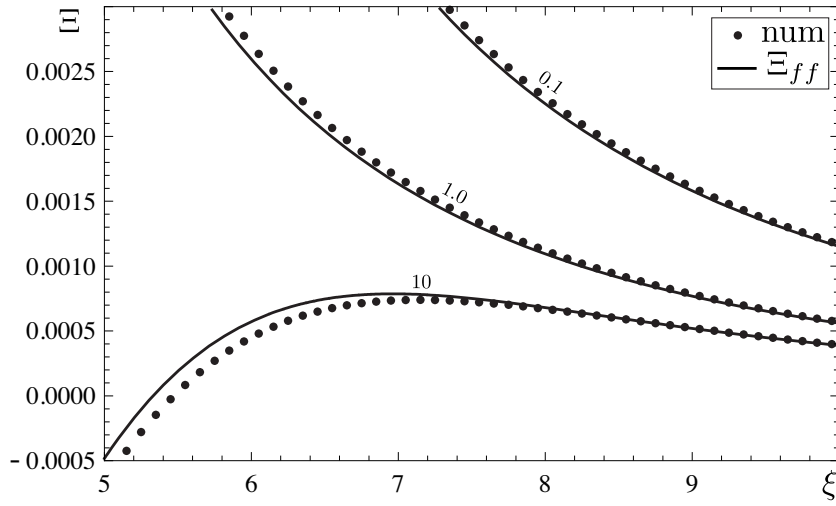


Figure 4.12: Far-field spatial distribution of backstress  $\Xi$  for different times:  $\tau = 0.1, 1.0, 10$

## Chapter 5

# Fracture propagation: zero viscosity

### 5.1 Preamble

Finally, we have arrived to a point when we can study the propagation of a hydraulic fracture through a poroelastic medium. In this chapter we consider the simple case of zero viscosity. The main assumption here is that the most of the energy dissipation is associated with the damage of the solid medium rather than with the viscous flow of the fracturing fluid. In other words the fracturing fluid viscosity is assumed to be equal to zero, with the implication that the fluid pressure inside the fracture is uniform. Savitski and Detournay (2002) have shown that in the case of a penny-shaped fracture propagating through an impermeable medium by injection of a Newtonian fluid, the toughness-dominated regime can be observed only at large times  $t \gtrsim t_{mk}$ , where  $t_{mk}$  is the characteristic transition time between the viscosity- and the toughness-dominated regimes given by

$$t_{mk} = \sqrt{\frac{\mu_{\text{in}}^5 Q_0^3 E'^{13}}{K_{Ic}^{18}}}. \quad (5.1)$$

One more simplification introduced in this chapter is the disregard for the low permeability cake build-up effect. As a result, there is no need to distinguish  $p_{\text{in}}$  and  $p_{\text{out}}$

and, similarly, the viscosities  $\mu_{\text{in}}$  and  $\mu_{\text{out}}$ . Therefore, we shall now omit the subscripts “in” and “out”.

Earlier works on the toughness-dominated regimes with leak-off include studies performed by Bungler et al. (2005) and Mathias and Reeuwijk (2009). Bungler et al. (2005) have conducted a detailed examination of the case of the Carter’s leak-off model by means of scaling and asymptotic analyses. On the other hand, Mathias and Reeuwijk (2009) studied the case of “stationary” 3D leak-off, when the propagation of a fluid-driven fracture is very slow and the pore pressure around the fracture is always in equilibrium. The authors have not provided any estimations of applicability of their pseudo steady-state model.

An interesting work was conducted by Berchenko et al. (1997) who studied propagation of a natural fracture through a porous medium. The authors have introduced an efficient approach to calculation of the fluid exchange volume between the fracture and the medium. Namely they decomposed a continuous in time fluid pressure variation inside the fracture into series of pressure impulses and then represented the fluid exchange volume induced by the continuous pressure variation by the superposition of the fluid exchanges induced by a single impulse (see introduction to Chapter 4). Unfortunately Berchenko et al. (1997) have made some significant algebraic errors. In fact simple scaling analysis shows that the main expression for the fluid exchange volume is incorrect [see equation (7) of Berchenko et al. (1997)]. Nevertheless we should admit that the idea introduced by these authors is the core of our research.

Neither of these papers considered the backstress effect.

In this chapter we build a general model of a hydraulic fracture driven by a zero viscosity fluid through a poroelastic medium. The main restrictive assumptions are i) there is no low permeability cake build-up, and ii) the solid-to-fluid coupling can be neglected (see introduction to Chapter 4). Throughout this chapter we intensively use

scaling and asymptotic analyses. We show that the parametric space is a prism. In this parametric space the case of the Carter's leak-off model studied by Bunger et al. (2005) occupies only one edge, whereas the pseudo steady-state model introduced by Mathias and Reeuwijk (2009) covers only one face.

The main objective of the problem is to define the evolution of the fracture radius  $R(t)$ , the fracturing fluid pressure  $p_{\text{in}}(t)$ , and the efficiency of the hydraulic fracturing  $\mathcal{E}(t) \equiv V_{\text{crack}}/V_{\text{inject}}$ , where  $V_{\text{crack}}$  is the volume of the fracture and  $V_{\text{inject}}$  is the volume of the injected fracturing fluid.

## 5.2 Mathematical model

### 5.2.1 Dimensional formulation

In the case of zero viscosity,  $\mu = 0$ , the fluid pressure along the fracture is uniform,  $p(r < R(t), z = 0, t) = p(t)$ . As a result, Poiseuille's law (2.2), introduced in Chapter 2, degenerates. Therefore, instead of the local volume balance equation (2.1) introduced in Chapter 2, we use the global volume balance

$$V_{\text{inject}}(t) = V_{\text{crack}}(t) + V_{\text{leak}}(t). \quad (5.2)$$

Here  $V_{\text{inject}}(t) = Q_0 t$  is the volume of the injected fracturing fluid and  $V_{\text{crack}}(t)$  is the fracture volume

$$V_{\text{crack}}(t) = 2\pi R^2(t) \int_0^1 w[R(t)s, t] s ds. \quad (5.3)$$

Substitution of the elasticity equation (2.7) into (5.3) yields

$$V_{\text{crack}}(t) = \frac{16}{3} \frac{R^3(t)}{E'} \left\{ p(t) - \sigma_0 + 3 \int_0^1 \sigma_b[R(t)s, t] \sqrt{1-s^2} s ds \right\}, \quad (5.4)$$

where  $E' \equiv E/(1-\nu^2)$  is the plane strain modulus,  $E$  is the Young's modulus,  $\nu$  is the Poisson's ration, and  $\sigma_b(r, t)$  is the backstress.



As indicated earlier [see Chapter 4], we can represent the continuous evolution of the fluid pressure inside the crack by a sum of spatially uniform time impulses of pressure. Then, the leaked-off volume  $V_{\text{leak}}$  and the backstress  $\sigma_b$  can be written in the form

$$V_{\text{leak}}(t) = \int_0^t U[R(s), t-s] [p(s) - p_0] ds, \quad (5.5)$$

$$\sigma_b(r, t) = \int_0^t S_b[R(s), r, t-s] [p(s) - p_0] ds, \quad (5.6)$$

where  $U(R, t)$  is the volume of the fracturing fluid that has escaped from a fracture of radius  $R$  at an elapsed time  $t$  after a uniform unit impulse of pressure has been applied (see Chapter 4), and  $S_b(R, r, t)$  is the generated backstress. In the following we refer to  $U(R, t)$  as the leak-off Green function, and to  $S_b(R, r, t)$  as the backstress Green function.

Recall the following relations between these dimensional Green functions  $U(R, t)$ ,  $S_b(R, r, t)$  and the dimensionless ones  $\Psi(\tau)$ ,  $\Xi(\xi, \tau)$ , obtained in Chapter 4 [see (4.8)]

$$U(R, t) = \frac{SR^3}{T_R} \Psi\left(\frac{t}{T_R}\right), \quad S_b(R, r, t) = \frac{\eta}{T_R} \Xi\left(\frac{r}{R}, \frac{t}{T_R}\right), \quad T_R = \frac{R^2}{4c}, \quad (5.7)$$

where  $S$  is the storage coefficient,  $c$  is the diffusion coefficient, and  $\eta$  is the poroelastic stress coefficient.

We close the formulation of the problem with the propagation criterion [see (2.9) and (2.10)]

$$K_{Ic} = \frac{2}{\sqrt{\pi}} R^{1/2}(t) \int_0^1 \frac{p[sR(t), t] + \sigma_b[sR(t), t] - \sigma_0}{\sqrt{1-s^2}} s ds, \quad (5.8)$$

where  $K_{Ic}$  is the material toughness.

One can see that our model has only two unknowns: the fracturing fluid pressure  $p(t)$  and the fracture radius  $R(t)$ .

### 5.2.2 Dimensionless formulation

The problem depends on seven dimensional parameters:  $K_{Ic}$ ,  $E'$ ,  $Q_0$ ,  $c$ ,  $S$ ,  $\sigma_0$ , and  $p_0$ , and one dimensionless parameter  $\eta$ . It is possible to reduce this set of parameters to five dimensionless quantities. Inspired by earlier works on hydraulic fracture (Detournay, 2004) we introduce the following scaling

$$r = R(t) \xi, \quad R(t) = L(t) \rho(t),$$

$$p(t) - \sigma_0 = \frac{K_{Ic}}{L^{1/2}(t)} \Pi(t), \quad \sigma_b(r, t) = \frac{K_{Ic}}{L^{1/2}(t)} \Sigma(\xi, t). \quad (5.9)$$

where  $\rho(t) \sim 1$  is the dimensionless radius,  $\Pi(t) \sim 1$  is the dimensionless net pressure,  $\Sigma(\xi, t)$  is the dimensionless back stress, and  $L(t) \sim R(t)$  is the characteristic size of the fracture. Note that the introduced above scaling is time-dependent. Moreover we have not defined yet the parameter  $L(t)$ . Below we will show that for different propagation regimes the parameter  $L(t)$  can be defined in such a way that the dimensionless quantities  $\rho$ ,  $\Pi$ , and  $\Sigma$  will not depend on time.

In the scaling (5.9) our governing equations transform to

- Backstress equation (5.6) after substitution of (5.7)

$$\Sigma(\xi, t) = 4\eta \mathcal{G}_d(t) \int_0^1 \frac{L^2(t)}{L^2(ts)} \frac{1}{\rho^2(ts)} \Xi \left[ \xi \frac{L(t) \rho(t)}{L(ts) \rho(ts)}, 4\mathcal{G}_d(t) \frac{L^2(t)}{L^2(ts)} \frac{1-s}{\rho^2(ts)} \right] \times$$

$$\times \left[ \mathcal{G}_\sigma(t) + \sqrt{\frac{L(t)}{L(ts)}} \Pi(ts) \right] ds, \quad (5.10)$$

- Propagation criterion (5.8) combined with the backstress equation (5.10)

$$1 = \frac{2}{\sqrt{\pi}} \rho^{1/2}(t) \Pi(t) + K_{bs}(t), \quad (5.11)$$

- Volume balance equation (5.2) where we substituted (5.4), (5.5), (5.7), and (5.11)

$$1 = \frac{8\sqrt{\pi}}{3} \mathcal{G}_v(t) \rho^{5/2}(t) [1 + V_{bs}(t) - K_{bs}(t)] +$$

$$+ 4\mathcal{G}_c(t) \int_0^1 \frac{L(ts)}{L(t)} \rho(ts) \Psi \left[ 4\mathcal{G}_d(t) \frac{L^2(t)}{L^2(ts)} \frac{1-s}{\rho^2(ts)} \right] \left[ \mathcal{G}_\sigma(t) + \sqrt{\frac{L(t)}{L(ts)}} \Pi(ts) \right] ds. \quad (5.12)$$

Here  $K_{bs}(t)$  is the change of the stress intensity factor due to the backstress

$$K_{bs}(t) = \frac{4\eta\mathcal{G}_d(t)}{\rho^{1/2}(t)} \int_0^1 \frac{L(t)}{L(ts)} \frac{1}{\rho(ts)} k_{bs} \left[ \frac{L(t)\rho(t)}{L(ts)\rho(ts)}, 4\mathcal{G}_d(t) \frac{L^2(t)}{L^2(ts)} \frac{1-s}{\rho^2(ts)} \right] \times \\ \left[ \mathcal{G}_\sigma(t) + \sqrt{\frac{L(t)}{L(ts)}} \Pi(ts) \right] ds, \quad (5.13)$$

and  $V_{bs}(t)$  is the change of the fracture volume due to the backstress

$$V_{bs}(t) = \frac{4\eta\mathcal{G}_d(t)}{\rho^{5/2}(t)} \int_0^1 \rho(ts) \frac{L(ts)}{L(t)} v_{bs} \left[ \frac{L(t)\rho(t)}{L(ts)\rho(ts)}, 4\mathcal{G}_d(t) \frac{L^2(t)}{L^2(ts)} \frac{1-s}{\rho^2(ts)} \right] \times \\ \left[ \mathcal{G}_\sigma(t) + \sqrt{\frac{L(t)}{L(ts)}} \Pi(ts) \right] ds, \quad (5.14)$$

where

$$k_{bs}(\mathcal{R}, \tau) = \frac{2}{\sqrt{\pi}} \int_0^{\mathcal{R}} \frac{\xi \Xi(\xi, \tau)}{\sqrt{\mathcal{R}^2 - \xi^2}} d\xi, \quad (5.15)$$

$$v_{bs}(\mathcal{R}, \tau) = \frac{6}{\sqrt{\pi}} \int_0^{\mathcal{R}} \xi \sqrt{\mathcal{R}^2 - \xi^2} \Xi(\xi, \tau) d\xi. \quad (5.16)$$

One can see that our dimensionless formulation depends on the following four time-dependent dimensionless groups:

- Storage group

$$\mathcal{G}_v(t) = \frac{K_{Ic}}{Q_0 E'} \frac{L^{5/2}(t)}{t}, \quad (5.17)$$

which is proportional to the fraction of the injected fluid volume stored in the fracture;

- Leak-off group

$$\mathcal{G}_c(t) = \frac{cSK_{Ic}}{Q_0} L^{1/2}(t), \quad (5.18)$$

which characterizes the amount of the fluid that has leaked into the formation;

- Diffusion group

$$\mathcal{G}_d = \frac{ct}{L^2(t)}, \quad (5.19)$$

which is related to the diffusion process with  $\sqrt{\mathcal{G}_d}$  proportional to the ratio of the diffusion length scale to the fracture size. Thus this dimensionless group is small,  $\mathcal{G}_d \ll 1$ , in the case of 1D diffusion and large in the case of 3D diffusion,  $\mathcal{G}_d \gg 1$ ;

- Pressure group

$$\mathcal{G}_\sigma(t) = \frac{\sigma_0 - p_0}{K_{Ic}} L^{1/2}(t) \sim \frac{\sigma_0 - p_0}{p - \sigma_0}, \quad (5.20)$$

which describes the effect of the material toughness on the net fluid pressure  $p - \sigma_0$  compared to  $\sigma_0 - p_0$ . Indeed, in the case of small toughness when  $K_{Ic} \rightarrow 0$  and  $\mathcal{G}_\sigma \rightarrow \infty$ , one can assume that from a diffusion point of view the fracturing fluid pressure  $p$  is equal to the confining stress  $\sigma_0$ ,  $p \approx \sigma_0$ ; whereas in the case of large toughness when  $K_{Ic} \rightarrow \infty$  and  $\mathcal{G}_\sigma \rightarrow 0$ , the net fluid pressure  $p - \sigma_0$  is large compared to  $\sigma_0 - p_0$ .

Note that the only unknown here are the dimensionless fracture radius  $\rho(\tau)$  and fracturing fluid pressure  $\Pi(\tau)$ .

### 5.3 Methodology

Incorporation of the diffusion and poroelastic effects into the theory of hydraulic fracturing relies on evaluating the convolution type integrals [see (5.10), (5.12)-(5.14)]. Indeed, evaluation of the fracturing fluid volume which has leaked into the formation requires a “convolution” on  $\Psi(\tau)$  [see (5.12)], whereas evaluation of the backstress  $\Sigma(\xi, t)$  and related fracture volume  $V_{bs}(t)$  and stress intensity factor  $K_{bs}(t)$  changes requires “convolutions” on  $\Xi(\xi, \tau)$ . These “convolutions” involves both arguments of  $\Xi(\xi, \tau)$  and are way more complicated than the “convolution” on the single argument  $\Psi(\tau)$  [see (5.10), (5.13), and (5.14)].

To simplify calculations of  $V_{bs}(t)$  and  $K_{bs}(t)$  we have introduced the two additional functions  $v_{bs}(\mathcal{R}, \tau)$  and  $k_{bs}(\mathcal{R}, \tau)$ , such that “convolutions” on these functions yield  $V_{bs}(t)$  and  $K_{bs}(t)$  [see (5.13)-(5.16)]. Physically the function  $v_{bs}(\mathcal{R}, \tau)$  can be interpreted as the volume change of a fracture of radius  $\mathcal{R} > 1$  at an elapsed time  $\tau$  due to the backstress generated by a unit impulse of the pore pressure applied at time  $\tau = 0$  along the part of the fracture  $\mathcal{R}$  located inside the unit circle  $\xi < 1$  (we assume that the center of the fracture  $\mathcal{R}$  is located at  $\xi = 0$ ). The function  $k_{bs}(\mathcal{R}, \tau)$  is the corresponding change in the stress intensity factor. Note that there is a simple connection between  $k_{bs}(\mathcal{R}, \tau)$  and  $v_{bs}(\mathcal{R}, \tau)$  [see (5.15), (5.16)]

$$k_{bs}(\mathcal{R}, \tau) = \frac{2}{3} \frac{\partial v_{bs}(\mathcal{R}, \tau)}{\partial \mathcal{R}^2}. \quad (5.21)$$

#### Small-time asymptotes of $k_{bs}(\mathcal{R}, \tau)$ and $v_{bs}(\mathcal{R}, \tau)$

Recall the small-time asymptote of  $\Xi(\xi, \tau)$  [see, (4.35)]

$$\Xi_0(\xi, \tau) = -\frac{1}{\pi^{3/2}\tau^{1/2}} \left\{ (1-\xi)^{-1} E \left[ \frac{4\xi}{(1+\xi)^2} \right] + (1+\xi)^{-1} K \left[ \frac{4\xi}{(1+\xi)^2} \right] \right\}, \quad (5.22)$$

where  $K(x)$  and  $E(x)$  are the complete elliptic integrals of the first and second kinds respectively (Abramowitz and Stegun, 1972).

Note that this asymptote has rather strong singularity  $1/(1-\xi)$ , which causes significant problems in numerical simulations. Also one can observe a separation of variables, which simplifies the evaluation of  $k_{bs}(\mathcal{R}, \tau)$  and  $v_{bs}(\mathcal{R}, \tau)$  at small time.

Substitution of this small-time asymptote  $\Xi_0(\xi, \tau)$  into the expression for  $k_{bs}(\mathcal{R}, \tau)$  (5.15) yields

$$k_{bs}(\mathcal{R}, \tau) = 0. \quad (5.23)$$

Therefore,  $v_{bs}(\mathcal{R}, \tau)$  depends only on time [see (5.21)], and in order to define  $v_{bs}(\mathcal{R}, \tau)$  we can evaluate it at any convenient point, e.g.,  $\mathcal{R} = 1$ . The expression for the stress

distribution, given by (5.22), can be simplified by means of (Gradshteyn and Ryzhik, 1994)

$$E \left[ \frac{4x}{(1+x)^2} \right] = (1+x) [2E(x^2) - (1-x^2) K(x^2)], \quad x \leq 1,$$

$$K \left[ \frac{4x}{(1+x)^2} \right] = (1+x) K(x^2), \quad x \leq 1,$$

such that

$$\Xi_0(\xi, \tau) = -\frac{2}{\pi^{3/2}\tau^{1/2}} \frac{E(\xi^2)}{1-\xi^2}, \quad \xi \leq 1. \quad (5.24)$$

Now, using the integral representation of the elliptic integral

$$E(x) = \int_0^1 \sqrt{\frac{1-xt^2}{1-t^2}} dt,$$

one can calculate  $v_{bs}(\mathcal{R}, \tau)$  [see (5.16)]

$$v_{bs}(\mathcal{R}, \tau) = -\frac{3}{2}\tau^{-1/2}. \quad (5.25)$$

### Large-time asymptotes of $k_{bs}(\mathcal{R}, \tau)$ and $v_{bs}(\mathcal{R}, \tau)$

The large-time asymptote of  $\Xi(\xi, \tau)$  is given by [see, (4.52)]

$$\Xi_\infty(\xi, \tau) = -\tilde{\Pi}_\infty^{(0)}(\xi) \left[ \delta(\tau) - 2(\pi\tau)^{-3/2} \right] - \frac{8}{3}(\pi\tau)^{-3/2}, \quad (5.26)$$

where  $\delta(\tau)$  is the Dirac delta function and

$$\tilde{\Pi}_\infty^{(0)}(\xi) = \begin{cases} 1, & \xi \leq 1 \\ \frac{2}{\pi} \arctan\left(\frac{1}{\sqrt{\xi^2-1}}\right), & \xi > 1 \end{cases}.$$

Note that in the leading order we have separation of variables.

Substitution of this large-time asymptote  $\Xi_\infty(\xi, \tau)$  into the definitions of  $k_{bs}(\mathcal{R}, \tau)$  and  $v_{bs}(\mathcal{R}, \tau)$ , given by (5.15) and (5.16), leads to

$$k_{bs}(\mathcal{R}, \tau) = -\frac{2\delta(\tau)}{\sqrt{\pi}} + \mathcal{O}(\tau^{-3/2}), \quad (5.27)$$

$$v_{bs}(\mathcal{R}, \tau) = -\frac{3\mathcal{R}^2-1}{\sqrt{\pi}}\delta(\tau) + \mathcal{O}(\tau^{-3/2}). \quad (5.28)$$

## 5.4 Propagation regimes

The problem under study has six propagation regimes. Therefore it is convenient to represent the fracture propagation by a trajectory line lying inside the prismatic parametric space shown in Fig. 5.4 where

- $K_0$ -vertex represents the storage-dominated regime with 1D diffusion, during which most of the injected fluid is stored inside the fracture;
- $\tilde{K}_{\kappa 0}$ -vertex is related to the leak-off-dominated regime with 1D diffusion, when the net fluid pressure  $p - \sigma_0$  is large compared to  $\sigma_0 - p_0$ ;
- $\tilde{K}_{\sigma 0}$ -vertex is another leak-off-dominated regime with slow 1D diffusion, when from a diffusion point of view the fracturing fluid pressure  $p$  is approximately equal to the confining stress  $\sigma_0$ ;
- $K_\infty$ -vertex is the storage-dominated regime with pseudo steady-state (3D) diffusion;
- $\tilde{K}_{\kappa \infty}$ -vertex is the pseudo steady-state (3D) diffusion version of the  $\tilde{K}_{\kappa 0}$ -vertex;
- $\tilde{K}_{\sigma \infty}$ -vertex is the pseudo steady-state (3D) diffusion version of the  $\tilde{K}_{\sigma 0}$ -vertex.

In the transition from one regime to another, the domination of one physical process is displaced by the domination of another one. Mathematically this means that the transition is controlled by the ratio of the dimensionless groups, representing the physical processes. For example the transition  $K_\infty \tilde{K}_{\kappa \infty}$  is governed by  $\mathcal{G}_c/\mathcal{G}_v$ , such that  $\mathcal{G}_c/\mathcal{G}_v = 0$  for the  $K_\infty$ -vertex, and  $\mathcal{G}_c/\mathcal{G}_v = \infty$  for the  $\tilde{K}_{\kappa \infty}$ -vertex. In another example the transition from 1D to 3D diffusion is governed by  $\mathcal{G}_d$ , such that  $\mathcal{G}_d = 0$  for 1D diffusion, and  $\mathcal{G}_d = \infty$  for 3D diffusion.

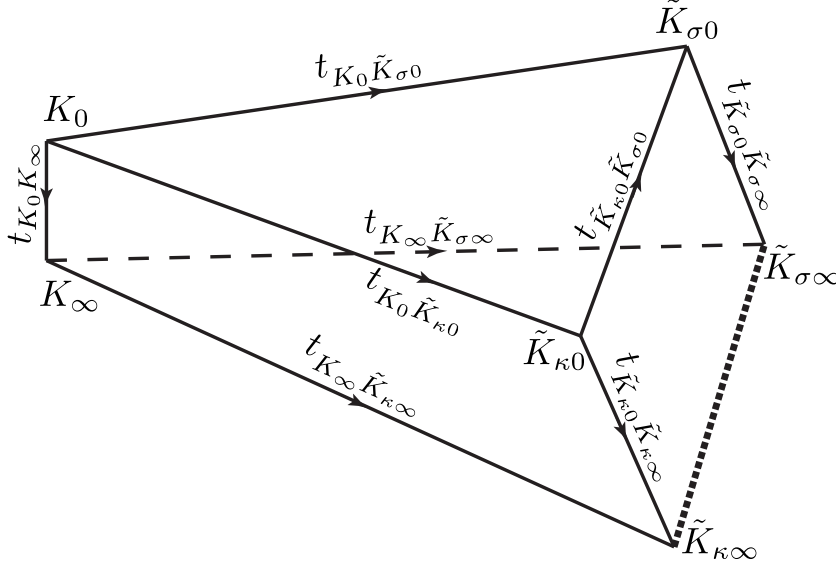


Figure 5.1: Parametric space

Usually, each propagation regime is studied in an inherent time-dependent scaling, such that the propagation of a fracture in a given propagation regime does not depend on time in this scaling. It is convenient to introduce an inherent scaling in such a way that all dimensionless groups which correspond to the dominating physical processes are equal to 1, whereas all the other groups are small compared to 1. Note that these small dimensionless groups are still time-dependent, therefore it is easy to estimate when a given propagation regime is valid. Also using these small time-dependent groups we can easily calculate the characteristic transition times between different propagation regimes. For example in order to calculate the characteristic transition time  $t_{AB}$  between the two propagation regimes  $A$  and  $B$ , one should follow the following procedure: first, introduce an inherent to the propagation regime  $A$  scaling; second, obtain in terms of this inherent scaling an expression for the dimensionless group  $\mathcal{G}_B^{(A)}(t)$ , which is dominant in the regime  $B$ , whereas it is small in the regime  $A$ ; and third, solve the equation  $\mathcal{G}_B^{(A)}(t_{AB}) = 1$  to obtain the characteristic transition time  $t_{AB}$ .



ver- tex	definition			scaling		solution
	$\mathcal{G}_d$	$\mathcal{G}_\sigma$	$\mathcal{G}_v/\mathcal{G}_c$	definition	$L(t)$	
$K_0$	$\ll 1$	–	$\gg \mathcal{G}_d^{-1/2} \max[1, \mathcal{G}_\sigma]$	$\mathcal{G}_v = 1$	$\left(\frac{Q_0 E'}{K_{Ic}} t\right)^{2/5}$	$\left(\frac{3}{8\sqrt{\pi}}\right)^{2/5}$
$\tilde{K}_{\kappa 0}$	$\ll 1$	$\ll 1$	$\ll \mathcal{G}_d^{-1/2}$	$\mathcal{G}_c^{(1D)} = 1$	$\left(\frac{Q_0 \mathcal{I}^{-1} t^{1/2}}{c^{1/2} S K_{Ic}}\right)^{2/3}$	$\frac{2^{2/3}}{\pi^{4/3}}$
$\tilde{K}_{\sigma 0}$	$\ll 1$	$\gg 1$	$\ll \mathcal{G}_d^{-1/2} \mathcal{G}_\sigma$	$\mathcal{G}_c^{(1D)} \mathcal{G}_\sigma = 1$	$\left[\frac{Q_0 \mathcal{I}^{-1} t^{1/2}}{c^{1/2} S (\sigma_0 - p_0)}\right]^{1/2}$	$\pi^{-3/4}$
$K_\infty$	$\gg 1$	–	$\gg \max[1, \mathcal{G}_\sigma]$	$\mathcal{G}_v = 1$	$\left(\frac{Q_0 E'}{K_{Ic}} t\right)^{2/5}$	$\left(\frac{3}{8\sqrt{\pi}}\right)^{2/5}$
$\tilde{K}_{\kappa \infty}$	$\gg 1$	$\ll 1$	$\ll 1$	$\mathcal{G}_c = 1$	$\left(\frac{Q_0}{c S K_{Ic}}\right)^2$	$\frac{(1-\eta)^2}{16\pi}$
$\tilde{K}_{\sigma \infty}$	$\gg 1$	$\gg 1$	$\ll \mathcal{G}_\sigma$	$\mathcal{G}_c \mathcal{G}_\sigma = 1$	$\frac{Q_0}{c S (\sigma_0 - p_0)}$	$\frac{1-\eta}{8}$

Here  $\mathcal{G}_c^{(1D)} \equiv \frac{\mathcal{G}_c}{\mathcal{G}_d^{1/2}} \left(1 - \frac{4\eta}{E'S}\right)$  and  $\mathcal{I} \equiv 1 - \frac{4\eta}{E'S}$

Table 5.1: Propagation regimes and corresponding scalings

In our case we can introduce different scalings by fixing the length scale  $L(t)$  [see (5.20)-(5.17)]. We define different propagation regimes in terms of the dimensionless groups (5.20)-(5.17) in Table 5.1, where we also introduce different scalings which are intrinsic to each of these propagation regimes. The transition times between different propagation regimes are given by

- $K_0 K_\infty$ - edge

$$t_{K_0 K_\infty} = \frac{Q_0^4 E'^4}{c^5 K_{Ic}^4};$$

- $K_0 \tilde{K}_{\kappa 0}$ - edge

$$t_{K_0 \tilde{K}_{\kappa 0}} = \left[ c^{1/2} S \left( \frac{K_{Ic}^2 E'^3}{Q_0^2} \right)^{1/5} \left( 1 - \frac{4\eta}{E'S} \right) \right]^{-10};$$

- $K_0 \tilde{K}_{\sigma 0}$ - edge

$$t_{K_0 \tilde{K}_{\sigma 0}} = \left[ c^{1/2} S (\sigma_0 - p_0) \left( \frac{E'^4}{Q_0 K_{Ic}^4} \right)^{1/5} \left( 1 - \frac{4\eta}{E'S} \right) \right]^{-10/3};$$

- $\tilde{K}_{\kappa 0} \tilde{K}_{\sigma 0}$ - edge

$$t_{\tilde{K}_{\kappa 0} \tilde{K}_{\sigma 0}} = \left[ \frac{c^{1/2} S K_{Ic}^4}{(\sigma_0 - p_0)^3 Q_0} \left( 1 - \frac{4\eta}{E'S} \right) \right]^2;$$

- $\tilde{K}_{\kappa 0} \tilde{K}_{\kappa \infty}$ - edge

$$t_{\tilde{K}_{\kappa 0} \tilde{K}_{\kappa \infty}} = \frac{Q_0^4}{c^5 S^4 K_{Ic}^4};$$

- $\tilde{K}_{\sigma 0} \tilde{K}_{\sigma \infty}$ - edge

$$t_{\tilde{K}_{\sigma 0} \tilde{K}_{\sigma \infty}} = \frac{Q_0^2}{c^3 S^2 (\sigma_0 - p_0)^2};$$

- $K_{\infty} \tilde{K}_{\kappa \infty}$ - edge

$$t_{K_{\infty} \tilde{K}_{\kappa \infty}} = \frac{Q_0^4}{c^5 S^5 E' K_{Ic}^4};$$

- $K_{\infty} \tilde{K}_{\sigma \infty}$ - edge

$$t_{K_{\infty} \tilde{K}_{\sigma \infty}} = \sqrt{\frac{Q_0^3 K_{Ic}^2}{c^5 S^5 E'^2 (\sigma_0 - p_0)^5}}.$$

- $\tilde{K}_{\kappa \infty} \tilde{K}_{\sigma \infty}$ -edge is self-similar, i.e., the transition along this edge is impossible.

Moreover all trajectory lines of the fracture propagation begin at the  $K_0$ -vertex and end at some point of the  $\tilde{K}_{\kappa \infty} \tilde{K}_{\sigma \infty}$ -edge.

Note that the case of the Carter's leak-off model studied by Bungner et al. (2005) corresponds to the  $K_0 \tilde{K}_{\sigma 0}$ -edge, whereas the pseudo steady-state model introduced by Mathias and Reeuwijk (2009) corresponds to the  $K_{\infty} \tilde{K}_{\kappa \infty} \tilde{K}_{\sigma \infty}$ -face with  $\mathcal{G}_\eta = 0$ .

In the rest of this section we give some details of derivation of asymptotic solutions for different propagation regimes.

#### 5.4.1 $K_0 \tilde{K}_{\kappa 0} \tilde{K}_{\sigma 0}$ -face: 1D diffusion, $\mathcal{G}_d \ll 1$

Substitution of the small-time asymptotes of  $k_{bs}(\mathcal{R}, \tau)$  and  $v_{bs}(\mathcal{R}, \tau)$  [see (5.23) and (5.25)] into the expressions for  $K_{bs}(t)$  and  $V_{bs}(t)$  [see (5.13) and (5.14)] leads to

$$K_{bs}(t) = 0, \quad (5.29)$$

and

$$V_{bs}(t) = -\frac{3\eta \mathcal{G}_d^{1/2}(t)}{\rho^{1/2}(t)} \int_0^1 \left( \frac{L(ts) \rho(ts)}{L(t) \rho(t)} \right)^2 \left[ \mathcal{G}_\sigma(t) + \sqrt{\frac{L(t)}{L(ts)}} \Pi(ts) \right] \frac{ds}{\sqrt{1-s}}. \quad (5.30)$$

Combination of the propagation criterion (5.11) and the volume balance equation (5.12) followed by substitution of the obtained above expressions for  $K_{bs}(t)$  and  $V_{bs}(t)$  and the small-time asymptote  $\Psi_0(\tau) = \sqrt{\pi/\tau}$  [see (4.34)] yields

$$1 = \frac{8\sqrt{\pi}}{3} \mathcal{G}_v \rho^{5/2}(t) + 2\sqrt{\pi} \mathcal{G}_c^{(1D)}(t) \rho^2(t) \times \\ \times \int_0^1 \left[ \frac{L(ts) \rho(ts)}{L(t) \rho(t)} \right]^2 \left[ \mathcal{G}_\sigma(t) + \frac{\sqrt{\pi}}{2} \sqrt{\frac{L(t)}{L(ts)}} \rho^{-1/2}(ts) \right] \frac{ds}{\sqrt{1-s}}. \quad (5.31)$$

Here

$$\mathcal{G}_c^{(1D)}(t) \equiv \frac{\mathcal{G}_c(t)}{\mathcal{G}_d^{1/2}(t)} \left( 1 - \frac{4\eta \mathcal{G}_d(t) \mathcal{G}_v(t)}{\mathcal{G}_c(t)} \right) = \frac{c^{1/2} S K_{Ic}}{Q_0 t^{1/2}} L^{3/2}(t) \left( 1 - \frac{4\eta}{E'S} \right), \quad (5.32)$$

where the second term in the brackets corresponds to the fracture volume decrease due to the pore pressure induced dilation of the medium. Obviously, the medium dilation should be less than the amount of fluid it absorbs, therefore

$$\frac{4\eta \mathcal{G}_d(t) \mathcal{G}_v(t)}{\mathcal{G}_c(t)} < 1, \quad \text{or} \quad \frac{4\eta}{E'S} < 1. \quad (5.33)$$

The only unknown in the volume balance equation (5.31) is the fracture radius  $\rho(\tau)$ . Once the fracture radius  $\rho(\tau)$  is known, one can use the propagation criterion (5.11) to obtain the fracturing fluid pressure

$$\Pi(t) = \frac{\sqrt{\pi}}{2} \rho^{-1/2}(t), \quad (5.34)$$

where we have used the fact that  $K_{bs}(t) = 0$  [see (5.29)].

As indicated above, in the case of 1D diffusion we have only three different propagation regimes, namely  $K_0$ ,  $\tilde{K}_{\kappa 0}$ , and  $\tilde{K}_{\sigma 0}$ . It is easy to solve the volume balance equation (5.31) for each of these propagation regimes. One should simply introduce an inherent propagation regime scaling [see Table 5.1], then rewrite the volume balance equation (5.31) in terms of this scaling and solve the resultant equation. The solutions of the volume balance equation for each propagation regime are presented in Table 5.1.

#### 5.4.2 $K_\infty \tilde{K}_{\kappa\infty} \tilde{K}_{\sigma\infty}$ -face: pseudo steady-state diffusion, $\mathcal{G}_d \gg 1$

Substitution of the large-time asymptotes of  $k_{bs}(\mathcal{R}, \tau)$  and  $v_{bs}(\mathcal{R}, \tau)$  [see (5.27) and (5.28)] into the expressions for  $K_{bs}(t)$  and  $V_{bs}(t)$  [see (5.13) and (5.14)] leads to

$$K_{bs}(t) = V_{bs}(t) = -\frac{2}{\sqrt{\pi}} \rho^{1/2}(t) \eta [\mathcal{G}_\sigma(t) + \Pi(t)] \left[ 1 + \mathcal{O}(\mathcal{G}_d^{-1/2}) \right]. \quad (5.35)$$

Thus, the propagation criterion (5.11) gives

$$\Pi(t) = \frac{\sqrt{\pi} \rho^{-1/2}(t)}{2} + \frac{\eta \mathcal{G}_\sigma(t)}{1 - \eta}, \quad (5.36)$$

whereas the volume balance equation (5.12) combined with the above equation (5.36) yields

$$1 = \frac{8\sqrt{\pi}}{3} \mathcal{G}_v(t) \rho^{5/2}(t) + \frac{8\mathcal{G}_c(t) \rho(t)}{1 - \eta} \int_0^1 \frac{L(ts) \rho(ts)}{L(t) \rho(t)} \left[ \mathcal{G}_\sigma(t) + \frac{\sqrt{\pi}}{2} \sqrt{\frac{L(t)}{L(ts)}} \rho^{-1/2}(ts) \right] ds. \quad (5.37)$$

where we have used the large-time asymptote of the leak-off Green function  $\Psi_\infty = 2$  [see (4.51)].

One can see that the volume balance equation (5.37) depends only on the fracture radius  $\rho(t)$ . Following the procedure described at the end of the previous subsection, one can easily solve this volume balance equation for each of the pseudo steady-state diffusion propagation regimes  $K_\infty$ ,  $\tilde{K}_{\kappa\infty}$ , and  $\tilde{K}_{\sigma\infty}$ . The results of the solution are presented in Table 5.1. Below we discuss only some characteristic features of each propagation regimes.

#### $K_\infty$ -vertex: storage-dominated regime

The solutions for the two storage-dominated regimes  $K_0$  (1D diffusion) and  $K_\infty$  (pseudo steady-state diffusion) are the same in terms of the fracture radius  $\rho$ . However in terms of the fracturing fluid pressure  $\Pi$  these solutions are different [see (5.34) and (5.36)].

Indeed the propagation criterion (5.36) yields

$$\Pi_{K_\infty}(t) = \frac{\Pi_{K_\infty}(t)|_{\eta=0}}{1-\eta} + \frac{\eta \mathcal{G}_\sigma(t)}{1-\eta}, \quad \Pi_{K_\infty}(t)|_{\eta=0} = 0.5\sqrt{\pi}\rho_{K_\infty}^{-1/2}(t), \quad (5.38)$$

whereas the 1D diffusion solution is

$$\Pi_{K_0}(t) = \Pi_{K_\infty}(t)|_{\eta=0}. \quad (5.39)$$

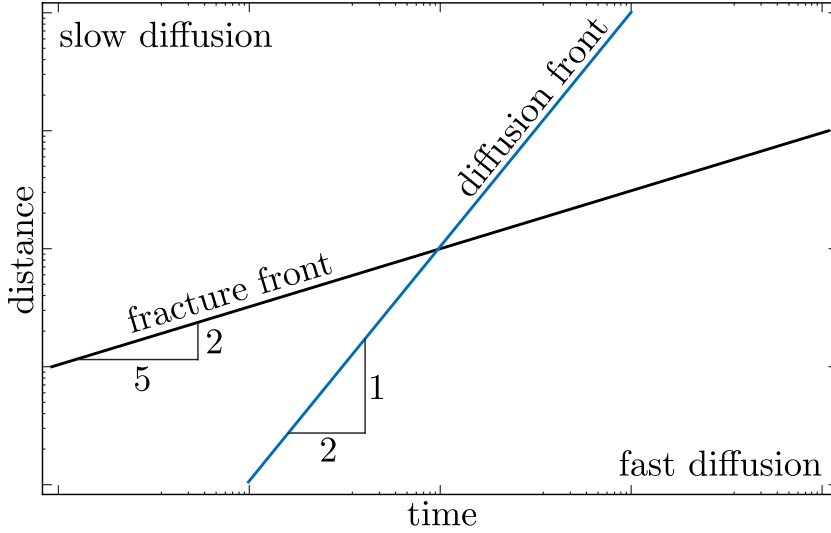


Figure 5.2: Physical interpretation of the difference between  $K_0$ - and  $K_\infty$ -vertices

Therefore the poroelastic effects split the storage dominated regime (known before as the  $K$ -vertex, see Bungler et al. (2005)) into two: the  $K_0$ -vertex (1D diffusion) which is similar to the former  $K$ -vertex, and the  $K_\infty$ -vertex (pseudo steady-state diffusion) characterized by a higher pressure. The essence of the difference between these two regimes is illustrated in Fig. 5.2. Initially the fracture front propagates faster than the diffusion front, therefore the diffusion length scale is small compared to the size of the fracture and the diffusion is one dimensional. As time goes on, the diffusion front catches up and then passes the fracture front, making the diffusion length scale to be larger than the fracture size, and, as a result, switching the propagation regime from the 1D diffusion to the pseudo steady-state (3D) diffusion.

$\tilde{K}_{\kappa\infty}\tilde{K}_{\sigma\infty}$ -edge: leak-off-dominated regime,  $\mathcal{G}_v \ll 1$

In this case the fracture is stationary, and the volume balance equation (5.37) has the following solution

$$R_{\infty}(t) = \left[ \frac{\sqrt{\pi + 2(1-\eta)\mathcal{G}_{\sigma}/\mathcal{G}_c} - \sqrt{\pi}}{4\mathcal{G}_{\sigma}} \right]^2 \bigg|_{L=1}. \quad (5.40)$$

It is interesting to note that the  $\tilde{K}_{\kappa\infty}\tilde{K}_{\sigma\infty}$  edge is self-similar, i.e. a trajectory of the system can not follow this edge. Moreover, all trajectories of the system end at some point on this edge.

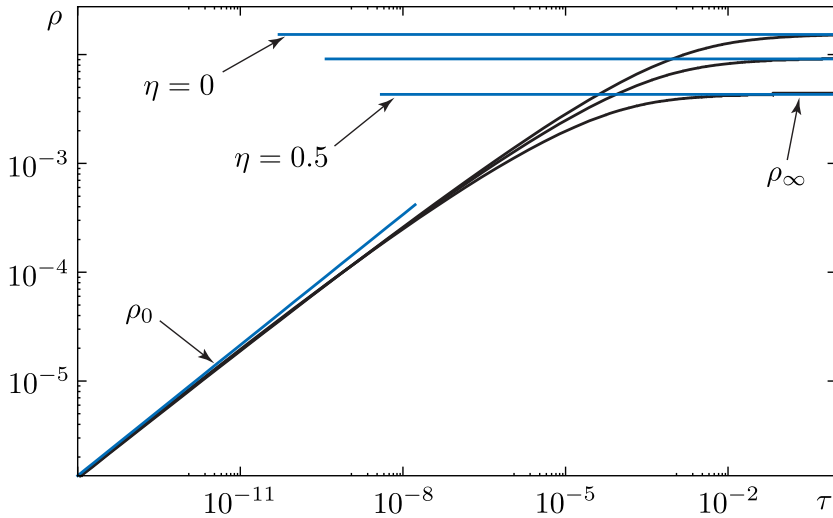


Figure 5.3: Fracture radius  $\rho$  vs time  $\tau$ : general case  $G_v = G_c = 1$ ,  $\eta = 0.0, 0.25, 0.5$

## 5.5 Transient solution

To obtain a general trajectory of the system starting at the  $K_0$ -vertex and ending at the  $\tilde{K}_{\kappa\infty}\tilde{K}_{\sigma\infty}$ -edge, we develop an implicit numerical algorithm solving our set of governing equations (5.11)-(5.16). From a numerical point of view it is convenient to introduce a

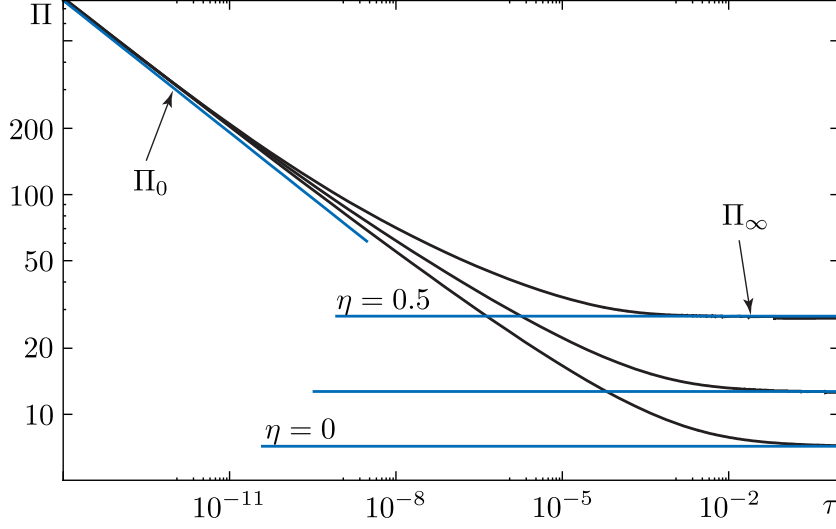


Figure 5.4: Fracturing fluid pressure  $\Pi$  vs time  $\tau$ : general case  $G_v = G_c = 1$ ,  $\eta = 0.0, 0.25, 0.5$

new, time-independent scaling such that  $\mathcal{G}_\sigma = 1$

$$\rho(\tau) = \frac{R(t)}{L_{\text{tr}}}, \quad \tau = \frac{t}{T}, \quad (5.41)$$

where

$$L_{\text{tr}} = \left( \frac{K_{Ic}}{\sigma_0 - p_0} \right)^2, \quad T = \frac{L_{\text{tr}}^2}{4c}. \quad (5.42)$$

Now the governing equations (5.11)-(5.16) transform to

- Propagation criterion

$$1 = \frac{2}{\sqrt{\pi}} \rho^{1/2}(\tau) \Pi(\tau) + K_{bs}(\tau), \quad (5.43)$$

- Volume balance equation

$$\begin{aligned} \tau = & \frac{8\sqrt{\pi}}{3} G_v \rho^{5/2}(\tau) [1 + V_{bs}(\tau) - K_{bs}(\tau)] + \\ & + 4G_c \int_0^\tau \rho(\bar{\tau}) \Psi \left[ \frac{\tau - \bar{\tau}}{\rho^2(\bar{\tau})} \right] [1 + \Pi(\bar{\tau})] d\bar{\tau}, \end{aligned} \quad (5.44)$$

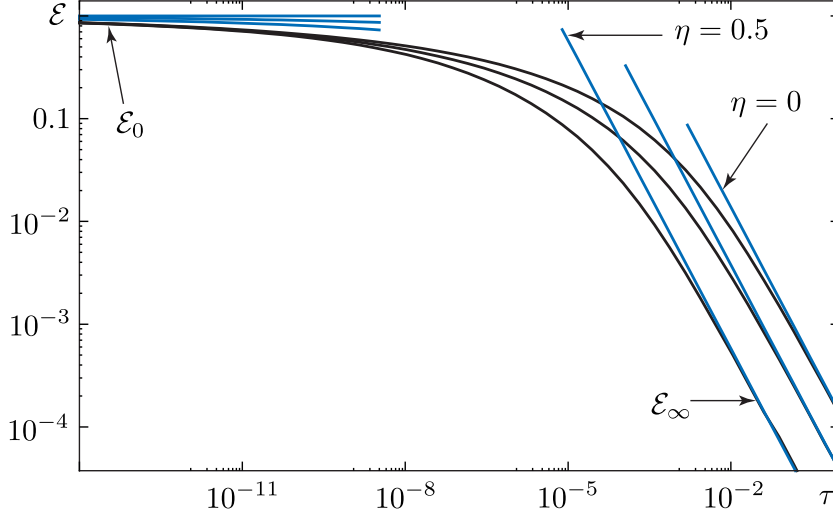


Figure 5.5: Hydraulic fracturing efficiency  $\mathcal{E}$  vs time  $\tau$ : general case  $G_v = G_c = 1$ ,  $\eta = 0.0, 0.25, 0.5$

where  $G_i = \mathcal{G}_i(t = T, L = L_{\text{tr}})$  and

$$K_{bs}(\tau) = \frac{\eta}{\rho^{1/2}(\tau)} \int_0^\tau \frac{1 + \Pi(\bar{\tau})}{\rho(\bar{\tau})} k_{bs} \left[ \frac{\rho(\tau)}{\rho(\bar{\tau})}, \frac{\tau - \bar{\tau}}{\rho^2(\bar{\tau})} \right] d\bar{\tau}, \quad (5.45)$$

$$V_{bs}(\tau) = \frac{\eta}{\rho^{5/2}(\tau)} \int_0^\tau \rho(\bar{\tau}) v_{bs} \left[ \frac{\rho(\tau)}{\rho(\bar{\tau})}, \frac{\tau - \bar{\tau}}{\rho^2(\bar{\tau})} \right] [1 + \Pi(\bar{\tau})] d\bar{\tau}, \quad (5.46)$$

In this scaling the found above asymptotes have the following form:

- $K_0$ -vertex

$$\begin{aligned} \rho_0(\tau) &= \left( \frac{3}{8\sqrt{\pi}G_v} \right)^{2/5} \tau^{2/5}, \quad K_{bs0}(\tau) = 0, \\ V_{bs0}(\tau) &= -\frac{3}{2} \eta \frac{\pi^{1/2} \tau^{1/2}}{\rho_0^{1/2}(\tau)} \left[ \frac{\Gamma(9/5)}{\Gamma(23/10)} + \frac{\pi^{1/2}}{2\rho_0^{1/2}(\tau)} \frac{\Gamma(8/5)}{\Gamma(21/10)} \right], \\ \Pi_0(\tau) &= \frac{\pi^{1/2}}{2} \rho_0^{-1/2}(\tau), \quad \mathcal{E}_0(\tau) = \frac{8\sqrt{\pi}}{3} G_v \frac{\rho_0^{5/2}(\tau) [1 + V_{bs0}(\tau)]}{\tau}; \end{aligned}$$

- $\tilde{K}_{\kappa 0}$ -vertex

$$\rho_\kappa(\tau) = \pi^{-4/3} G_c^{-2/3} \left( 1 - \frac{\eta G_v}{G_c} \right)^{-2/3} \tau^{1/3}, \quad K_{bs\kappa}(\tau) = 0,$$



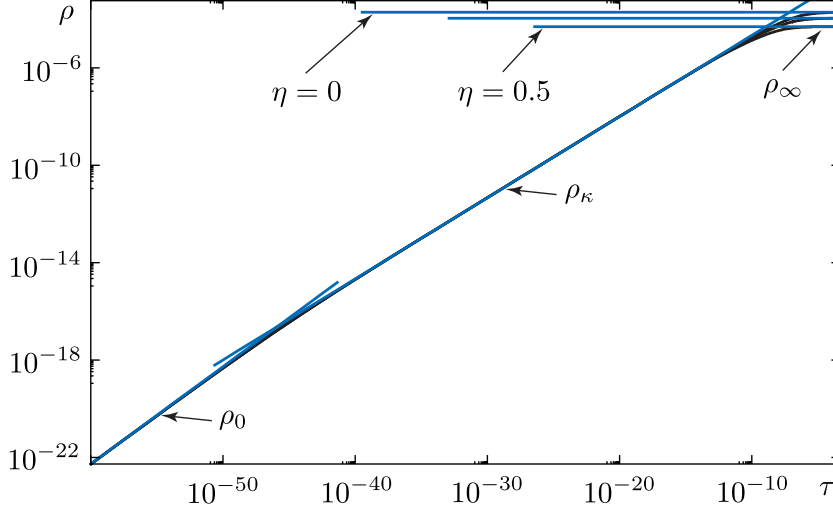


Figure 5.6: Fracture radius  $\rho$  vs time  $\tau$ :  $G_v = 10^{-5}$ ,  $G_c = 10$ ,  $\eta = 0.0, 0.25, 0.5$ . Here fracture goes through  $\tilde{K}_{\kappa 0}$ -vertex

$$V_{bs\kappa}(\tau) = -\frac{3}{2}\eta \frac{\pi^{1/2}\tau^{1/2}}{\rho_{\kappa}^{1/2}(\tau)} \left[ \frac{\Gamma(5/3)}{\Gamma(13/6)} + \frac{\pi}{4\rho_{\kappa}^{1/2}(\tau)} \right],$$

$$\Pi_{\kappa}(\tau) = \frac{\pi^{1/2}}{2}\rho_{\kappa}^{-1/2}(\tau), \quad \mathcal{E}_{\kappa}(\tau) = \frac{8\sqrt{\pi}}{3}G_v \frac{\rho_{\kappa}^{5/2}(\tau)[1 + V_{bs\kappa}(\tau)]}{\tau};$$

- $\tilde{K}_{\sigma 0}$ -vertex

$$\rho_{\sigma}(\tau) = 2^{-1/2}\pi^{-3/4}G_c^{-1/2} \left( 1 - \frac{\eta G_v}{G_c} \right)^{-1/2} \tau^{1/4}, \quad K_{bs\sigma}(\tau) = 0,$$

$$V_{bs\sigma}(\tau) = -\frac{3}{4}\eta \frac{\pi\tau^{1/2}}{\rho_{\sigma}^{1/2}(\tau)} \left[ 1 + \frac{1}{\rho_{\sigma}^{1/2}(\tau)} \frac{\Gamma(11/8)}{\Gamma(15/8)} \right],$$

$$\Pi_{\sigma}(\tau) = \frac{\pi^{1/2}}{2}\rho_{\sigma}^{-1/2}(\tau), \quad \mathcal{E}_{\sigma}(\tau) = \frac{8\sqrt{\pi}}{3}G_v \frac{\rho_{\sigma}^{5/2}(\tau)[1 + V_{bs\sigma}(\tau)]}{\tau};$$

- $\tilde{K}_{\kappa\infty}\tilde{K}_{\sigma\infty}$ -edge

$$\rho_{\infty}(\tau) = \left[ \frac{\sqrt{\pi + 2(1-\eta)/G_c} - \sqrt{\pi}}{4} \right]^2, \quad \Pi_{\infty}(\tau) = \frac{\pi^{1/2}}{2} \frac{\rho_{\infty}^{-1/2}(\tau)}{1-\eta} + \frac{\eta}{1-\eta},$$

$$V_{bs\infty}(\tau) = K_{bs\infty}(\tau) = -\frac{2}{\sqrt{\pi}}\eta\rho_{\infty}^{1/2}(\tau)[1 + \Pi_{\infty}(\tau)], \quad \mathcal{E}_{\infty}(\tau) = \frac{8\sqrt{\pi}}{3}G_v \frac{\rho_{\infty}^{5/2}(\tau)}{\tau}.$$

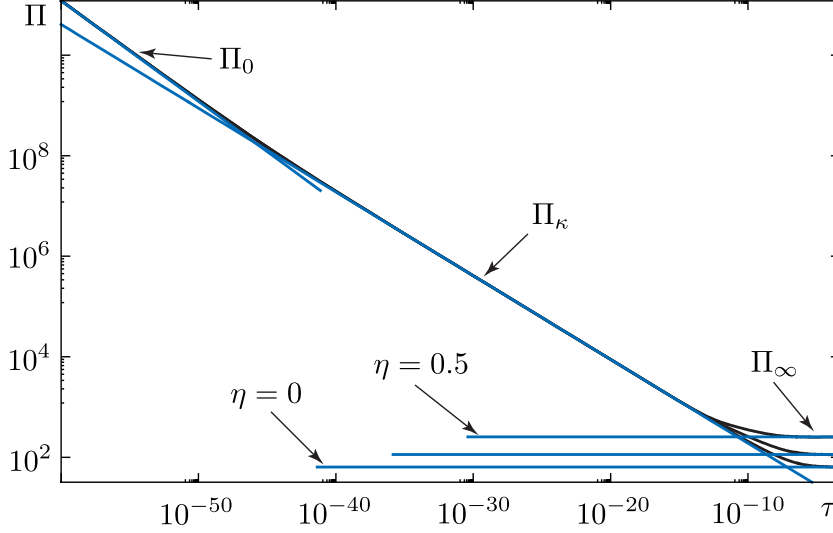


Figure 5.7: Fracturing fluid pressure  $\Pi$  vs time  $\tau$ :  $G_v = 10^{-5}$ ,  $G_c = 10$ ,  $\eta = 0.0, 0.25, 0.5$ . Here fracture goes through  $\tilde{K}_{\kappa 0}$ -vertex

Here we have introduced the hydraulic fracturing efficiency  $\mathcal{E}$  defined by  $\mathcal{E} \equiv V_{\text{crack}}/V_{\text{inject}}$ .

During the development of the numerical solution we encounter the following difficulties: i) the problem is history dependent and ii) the leak-off and the backstress Green function are numerical and singular. As a result, it is difficult to perform the spatial integration of the backstress Green function in (5.15) and (5.16) as well as the temporal integration (convolution) in (5.45), (5.46) and (5.44). To overcome these difficulties we use remeshing and numerical decomposition of the backstress Green function into “physically meaningful” analytical functions. The implementation of these ideas is described in Appendix C.

The results of the numerical simulations for different values of the parameters  $G_i$  are presented in Figs 5.3-5.14. We show that, depending on the values of the parameters  $G_i$ , the system can travel through different vertices, although the journey always has to start at the  $K_0$ -vertex and terminate at the  $\tilde{K}_{\kappa\infty}\tilde{K}_{\sigma\infty}$ -edge.

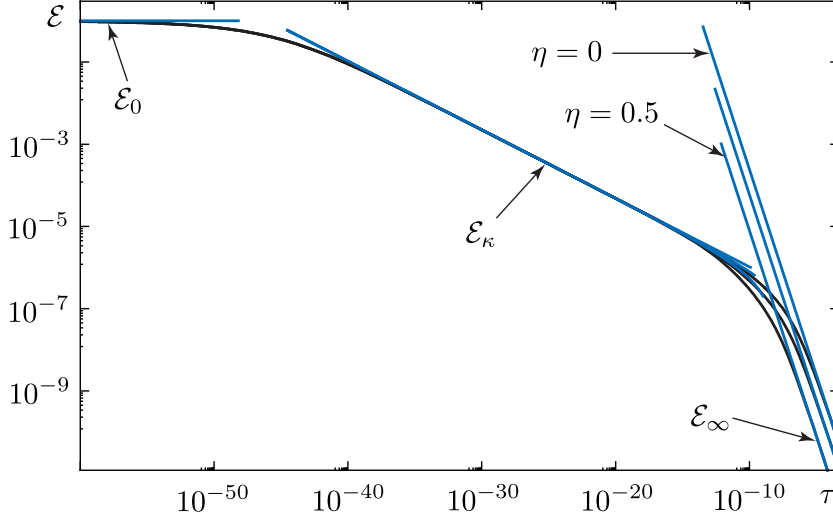


Figure 5.8: Hydraulic fracturing efficiency  $\mathcal{E}$  vs time  $\tau$ :  $G_v = 10^{-5}$ ,  $G_c = 10$ ,  $\eta = 0.0, 0.25, 0.5$ . Here fracture goes through  $\tilde{K}_{\kappa 0}$ -vertex

In some cases the propagation of the fracture terminates before it arrives to the  $\tilde{K}_{\kappa\infty}\tilde{K}_{\sigma\infty}$ -edge (see Figs 5.9-5.14). In these cases, the system, going through a diffusion-dominated vertices, arrives to a point when the dilation of the poroelastic medium  $\sim V_{bs}$  is very large, such that the volume of the fracture becomes equal to zero. Substituting the obtained above analytical expressions for  $V_{bs}$  and  $K_{bs}$  into  $V_{\text{crack}}(\tau) \sim 1 + V_{bs}(\tau) - K_{bs}(\tau) = 0$  and solving it with respect to time  $\tau$  one can easily estimate the fracture closure time. Note the this estimate is based only on the total volume of fracture and it does not say where the fracture will close. In reality though the fracture will rather switch to a viscosity-dominated propagation regime then close. Indeed, from a point of view of the lubrication theory, the fracture is just a channel for the fracturing fluid. Therefore the decrease of the fracture opening leads to an increase of the pressure gradient of the viscous fracturing fluid, which in turn leads to an increase of energy dissipation associated with the fluid viscosity. This leads to the violation of the assumption of zero fracturing fluid viscosity. Moreover the pressure profile of the fracturing fluid inside the

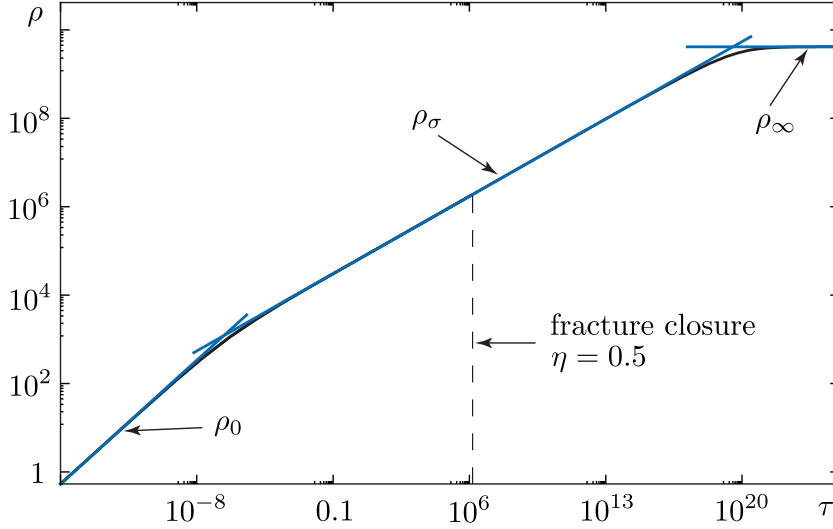


Figure 5.9: Fracture radius  $\rho$  vs time  $\tau$ :  $G_v = 10^{-15}$ ,  $G_c = 3 \times 10^{-11}$ ,  $\eta = 0.0, 0.5$ . Here fracture goes through  $\tilde{K}_{\sigma 0}$ -vertex

fracture becomes to be strongly nonuniform, thus one can not use the results of the auxiliary problem to model the poroelastic effects. As a result one has to use more sophisticated models to study this situation.

## 5.6 Discussion

In the present chapter we have performed a detailed study of a penny-shaped fracture driven by a zero viscosity fluid through a poroelastic medium. The main contribution of this study is the incorporation of large scale 3D diffusion and related poroelastic effect (backstress) into the theory of hydraulic fracturing. The study relies on scaling and asymptotic analyses. In fact, we have shown that the problem under consideration has six self-similar propagation regimes (see Section 5.4). In particular we have demonstrated the existence of a stationary solution ( $\tilde{K}_{\kappa\infty}\tilde{K}_{\sigma\infty}$ -edge) when the fracture propagation arrests. In this case the fracturing fluid injection is balanced by the 3D fluid leak-off. This stationary solution in the case of zero backstress,  $\eta = 0$ , was originally obtained by

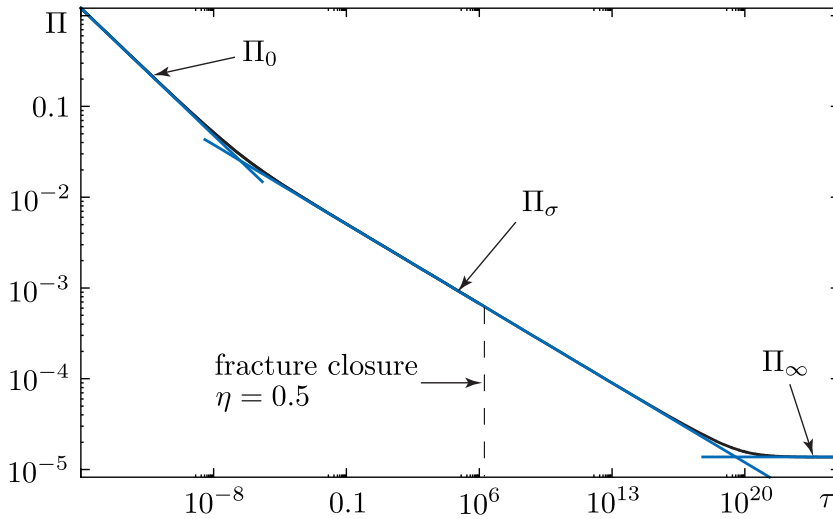


Figure 5.10: Fracturing fluid pressure  $\Pi$  vs time  $\tau$ :  $G_v = 10^{-15}$ ,  $G_c = 3 \times 10^{-11}$ ,  $\eta = 0.0, 0.5$ . Here fracture goes through  $\tilde{K}_{\sigma 0}$ -vertex

Mathias and Reeuwijk (2009).

Numerical simulations illustrate that poroelastic effects represented by the backstress have significant influence on the propagation of a hydraulic fracture. Namely in the case of 3D diffusion the backstress effect leads to a decrease of the fracture radius (see Figs 5.3 and 5.6) accompanied by an increase of the fracturing fluid pressure (see Figs 5.4 and 5.7). Moreover, the poroelastic effects can lead to premature closure of a fracture propagating in a leak-off dominating regime with 1D diffusion (see the discussion at the end of the previous section).

Let us perform some simple numerical estimates of the influence of the poroelastic effects. Using data of typical high permeable reservoirs (see Chapter 7) one can conclude that the fracture arrives into the  $\tilde{K}_{\sigma\infty}$ -vertex in just a few minutes which is very fast compared to the treatment time. In the  $\tilde{K}_{\sigma\infty}$ -vertex the fracture radius is equal to  $R \approx 3.4$  m and the net pressure is  $p - \sigma_0 \approx 7.4$  MPa in the case of the low porosity reservoir (LPR), whereas for the mean porosity reservoir (MPR)  $R \approx 0.35$  m and  $p - \sigma_0 \approx 7.2$  MPa (see Table 7.1). If one does not take into account the poroelastic effect he would

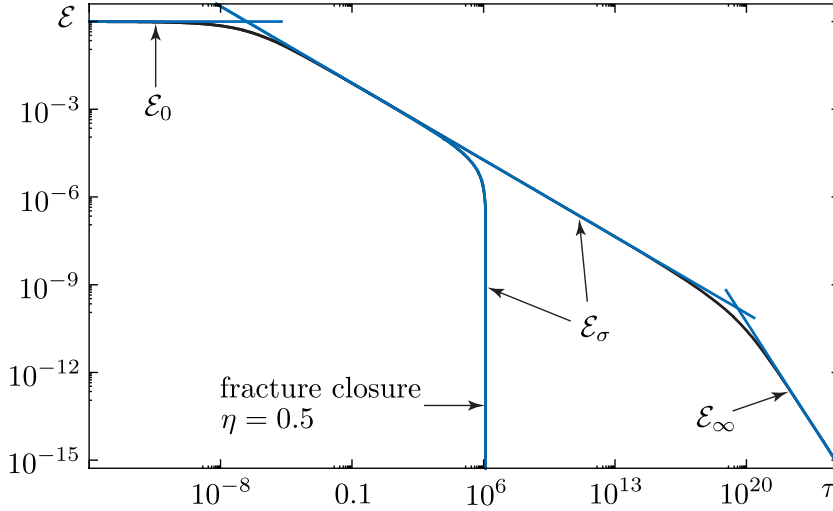


Figure 5.11: Hydraulic fracturing efficiency  $\mathcal{E}$  vs time  $\tau$ :  $G_v = 10^{-15}$ ,  $G_c = 3 \times 10^{-11}$ ,  $\eta = 0.0, 0.5$ . Here fracture goes through  $\tilde{K}_{\sigma 0}$ -vertex

arrive to  $R \approx 4.4$  m and  $p - \sigma_0 \approx 0.071$  MPa in the LPR case, and  $R \approx 0.44$  m and  $p - \sigma_0 \approx 0.71$  MPa in the MPR case. One can see that the fracture radius decrease due to the poroelastic effects is not so significant. At the same time the net pressure increase is huge (100 times in the LPR case and 10 times in the MPR case).

In all our examples, the numerical simulation sweeps huge time ranges. Is it reasonable from a practical point of view? Well, if one wants to get accurate solution one has to have good, from a physical point of view, initial condition. In this research we use the small-time asymptote ( $K_0$ -vertex) as the initial condition. This force us to go to very small initial times. This is one more inconvenient feature of the problem of hydraulic fracturing. In practice though assessment of the part of the parametric space of the fracture propagation can dramatically simplify the situation. Knowing this information one can use the analytical vertex asymptotes for preliminary estimation, and then optimize a numerical algorithm. For example Figs 5.6-5.14 illustrate that one can use the asymptotic solution of an intermediate vertex as the initial condition provided that the transition time from the  $K_0$ -vertex into this vertex is small compared to the treatment

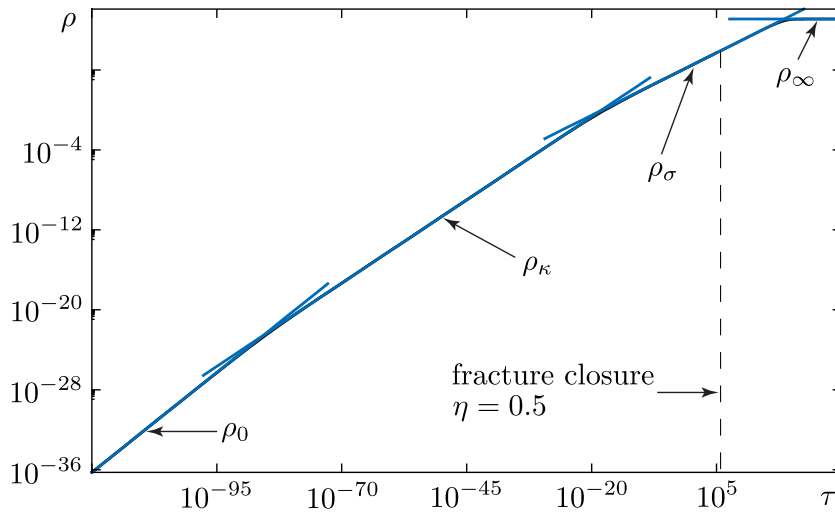


Figure 5.12: Fracture radius  $\rho$  vs time  $\tau$ :  $G_v = 10^{-30}$ ,  $G_c = 10^{-10}$ ,  $\eta = 0.0, 0.5$ . Here fracture goes through  $\tilde{K}_{\kappa 0}$ - and  $\tilde{K}_{\sigma 0}$ -vertices

time. In Chapter 7 we consider in details an example of production water reinjection. We show there that the fracture propagation arrests within just a few minutes, whereas the characteristic treatment time is of order of hundred days. Thus from a practical point of view in this case one can simply use the analytical large-time asymptote to design the treatment.

The technique developed in this chapter could be also applied to the problem of in situ stress determination by hydraulic fracture (Detournay et al., 1989). In this application the in situ stress determination relies on the interpretation of the fracture breakdown and reopening fluid pressure as well as of the fracture closure pressure during the shut-in phase of experiment. It is obvious that the poroelastic effects could lead to a significant corrections into the stress measurements.

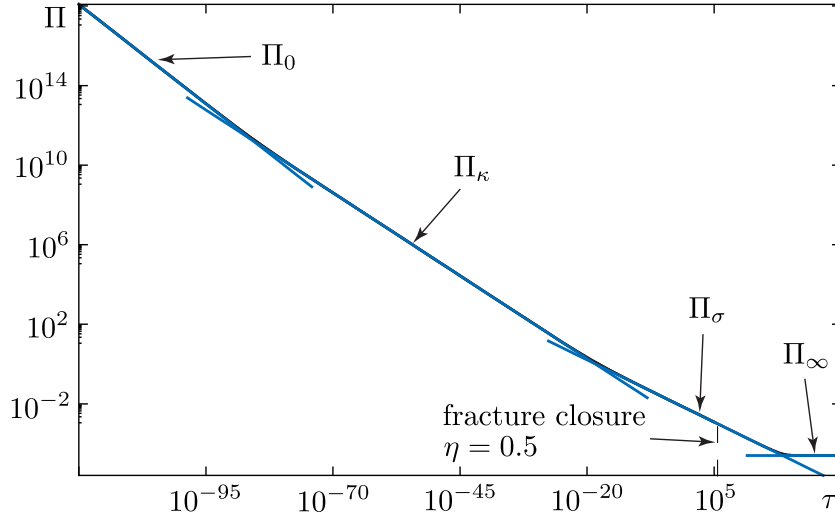


Figure 5.13: Fracturing fluid pressure  $\Pi$  vs time  $\tau$ :  $G_v = 10^{-30}$ ,  $G_c = 10^{-10}$ ,  $\eta = 0.0, 0.5$ . Here fracture goes through  $\tilde{K}_{\kappa 0}$ - and  $\tilde{K}_{\sigma 0}$ -vertices

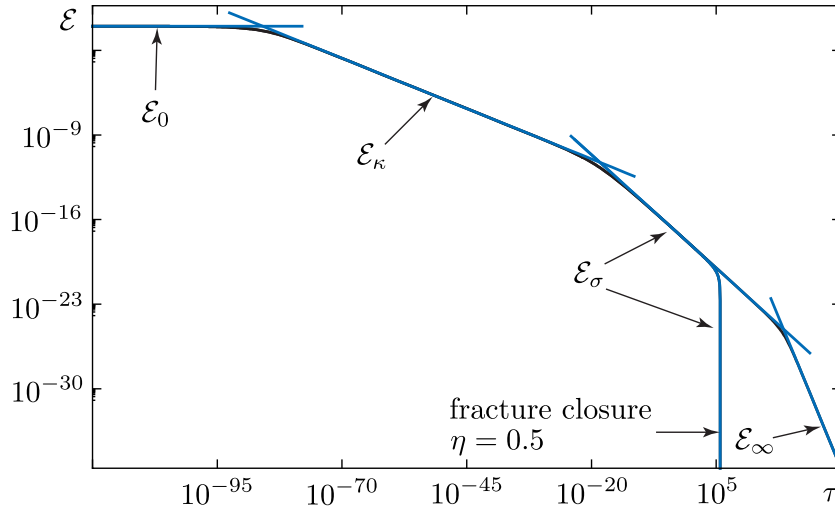


Figure 5.14: Hydraulic fracturing efficiency  $\mathcal{E}$  vs time  $\tau$ :  $G_v = 10^{-30}$ ,  $G_c = 10^{-10}$ ,  $\eta = 0.0, 0.5$ . Here fracture goes through  $\tilde{K}_{\kappa 0}$ - and  $\tilde{K}_{\sigma 0}$ -vertices



## Chapter 6

# Fracture propagation: zero toughness

### 6.1 Preamble

In this chapter, we study the propagation of a hydraulic fracture driven by a viscous Newtonian fluid through a poroelastic medium with zero material toughness. In contrast to the case analyzed in the previous chapter, we assume here that energy dissipation associated with the cracking of the rock material is small compared to energy dissipation associated with the viscous flow of the fracturing fluid. Similarly to the previous chapter we neglect the low permeability cake build-up effect. One more restrictive assumption of this chapter is that the net pressure  $p - \sigma_0$  is small compared to  $\sigma_0 - p_0$ . Thus, from a diffusion point of view the fluid pressure  $p$  inside the fracture is uniform and approximately equal to the confining stress,  $p \approx \sigma_0$ . As a result, the fluid leak-off process and the associated backstress effect can be studied in terms of the decompositions introduced in the previous chapters [see Chapters 4 and 5].

Some particular cases of our problem were studied by Savitski and Detournay (2002)

and Madyarova and Detournay (2008). The former work dealt with the impermeable case, whereas the latter one adopted the Carter's leak-off model to study the permeable case. The main contribution of this chapter is the introduction of 3D leak-off and the backstress effect into the theory of hydraulic fracturing. The main objective of the problem is to define the evolution of the fracture radius  $R(t)$ , fracture opening profile  $w(r, t)$ , fluid displacement function profile  $v(r, t)$ , and fracturing fluid pressure profile  $p(r, t)$ .

Although, we include the backstress effect into the analytical consideration, we are not able to incorporate this effect into the numerical simulations. This is due to the strong singularities of the backstress Green function  $\Xi(\xi, \tau)$  with respect to space and time (see Chapter 4).

## 6.2 Mathematical model

### 6.2.1 Dimensional formulation

Substitution of (2.2) into (2.1) yields

$$\frac{\partial(w + v)}{\partial t} = \frac{1}{\mu' r} \frac{\partial}{\partial r} \left( r w^3 \frac{\partial p}{\partial r} \right), \quad (6.1)$$

where  $\mu' \equiv 12\mu$ . The boundary conditions are given by [see (2.3)]

$$\begin{aligned} w(R(t), t) = v(R(t), t) &= \lim_{r \rightarrow R(t)} w^3(r, t) \frac{\partial p(r, t)}{\partial r} = 0, \\ -\frac{2\pi}{\mu'} \lim_{r \rightarrow 0} r w^3(r, t) \frac{\partial p(r, t)}{\partial r} &= Q_0, \end{aligned} \quad (6.2)$$

where  $Q_0$  is the fracturing fluid injection rate.

It is also useful to write down the global volume balance equation, which can be obtained by the integration of the lubrication equation (6.1) over space and time

$$Q_0 t = 2\pi \int_0^{R(t)} w(r, t) r dr + 2\pi \int_0^{R(t)} v(r, t) r dr, \quad (6.3)$$

where we have used our boundary conditions (6.2).

The connection between the fracture opening  $w$  and the fracturing fluid pressure  $p$  is given by the elasticity equation (2.7)

$$w(r, t) = \frac{8}{\pi} \frac{R(t)}{E'} \int_0^1 \{p[sR(t), t] + \sigma_b[sR(t), t] - \sigma_0\} G\left[\frac{r}{R(t)}, s\right] s ds, \quad (6.4)$$

where  $E' \equiv E/(1 - \nu^2)$  is the plane strain modulus,  $E$  is the Young's modulus,  $\nu$  is the Poisson's ration,  $\sigma_b(r, t)$  is the backstress due to the leak-off, and  $G(\xi, s)$  is the elasticity kernel,

$$G(\xi, s) = \begin{cases} \frac{1}{\xi} F\left(\arcsin \sqrt{\frac{1-\xi^2}{1-s^2}}, \frac{s^2}{\xi^2}\right), & \xi > s \\ \frac{1}{s} F\left(\arcsin \sqrt{\frac{1-s^2}{1-\xi^2}}, \frac{\xi^2}{s^2}\right), & \xi < s \end{cases}, \quad (6.5)$$

$F(\phi, m)$  is the incomplete elliptic integral of the first kind (Abramowitz and Stegun, 1972).

The leak-off displacement function  $v$  and the backstress  $\sigma_b$  are given by [cf. (5.5), (5.6)]

$$v(r, t) = (\sigma_0 - p_0) \int_0^t u[R(s), r, t - s] ds, \quad (6.6)$$

$$\sigma_b(r, t) = (\sigma_0 - p_0) \int_0^t S_b[R(s), r, t - s] ds, \quad (6.7)$$

where  $u(R, r, t)$  is the volume of the fracturing fluid that has escaped through a unit area around a point  $r$  from a fracture of size  $R$  at an elapsed time  $t$  after a uniform unit impulse of pressure has been applied (see Chapter 4), and  $S_b(R, r, t)$  is the generated backstress.

Simple scaling analysis reveals (see Chapter 4)

$$u(R, r, t) = \frac{SR}{T_R} \psi\left(\frac{r}{R}, \frac{t}{T_R}\right), \quad S_b(R, r, t) = \frac{\eta}{T_R} \Xi\left(\frac{r}{R}, \frac{t}{T_R}\right), \quad T_R = \frac{R^2}{4c}, \quad (6.8)$$

where  $S$  is the storage coefficient,  $c$  is the diffusion coefficient, and  $\eta$  is the poroelastic stress modulus.

### 6.2.2 Dimensionless formulation

Here we introduce the following scaling [cf. (5.9)]

$$\begin{aligned} r &= R(t) \xi, \quad R(t) = L(t) \gamma(t), \quad v(r, t) = U(t) \Upsilon(\xi, t), \quad \sigma_b(r, t) = \varepsilon(t) E' \Sigma(\xi, t), \\ p(r, t) - \sigma_0 &= \varepsilon(t) E' \Pi(\xi, t), \quad w(r, t) = \varepsilon(t) L(t) \Omega(\xi, t). \end{aligned} \quad (6.9)$$

where  $\gamma(t) \sim 1$  is the dimensionless radius,  $\Pi(\xi, t) \sim 1$  is the dimensionless net pressure,  $\Omega(\xi, t) \sim 1$  is the dimensionless opening,  $\Upsilon(\xi, t) \sim 1$  is the dimensionless leak-off displacement function,  $\Sigma(\xi, t)$  is the dimensionless backstress,  $L(t) \sim R(t)$  is the characteristic size of the fracture,  $U(t) \sim v(r, t)$  is the characteristic value of the fluid displacement function, and  $\varepsilon(t)$  is a small time-dependent parameter. Note that in contrast to the previous chapter here we have three undefined time-dependent parameters  $L(t)$ ,  $U(t)$ , and  $\varepsilon(t)$ , which we will use to adjust our scaling to a given propagation regime (see Chapter 5).

In terms of the introduced above scaling (6.9) our governing equations read

- Lubrication equation (6.1)

$$\begin{aligned} \mathcal{G}_v \left[ \dot{\Omega} t + \left( \frac{\dot{\varepsilon} t}{\varepsilon} + \frac{\dot{L} t}{L} \right) \Omega - \left( \frac{\dot{L} t}{L} + \frac{\dot{\gamma} t}{\gamma} \right) \xi \frac{\partial \Omega}{\partial \xi} \right] + \\ + \mathcal{G}_c \left[ \dot{\Upsilon} t + \frac{\dot{U} t}{U} \Upsilon - \left( \frac{\dot{L} t}{L} + \frac{\dot{\gamma} t}{\gamma} \right) \xi \frac{\partial \Upsilon}{\partial \xi} \right] = \frac{\mathcal{G}_\mu^{-1}}{\gamma^2 \xi} \frac{\partial}{\partial \xi} \left( \xi \Omega^3 \frac{\partial \Pi}{\partial \xi} \right), \end{aligned} \quad (6.10)$$

- Boundary condition (6.2)

$$-2\pi \lim_{\xi \rightarrow 0} \xi \Omega^3 \frac{\partial \Pi}{\partial \xi} = \mathcal{G}_\mu, \quad (6.11)$$

- Global volume balance equation (6.3)

$$1 = \mathcal{G}_v 2\pi \gamma^2 \int_0^1 \Omega(\xi, t) \xi d\xi + \mathcal{G}_c 2\pi \gamma^2 \int_0^1 \Upsilon(\xi, t) \xi d\xi, \quad (6.12)$$

- Elasticity equation (6.4)

$$\Omega(\xi, t) = \frac{8\gamma}{\pi} \int_0^1 [\Pi(\zeta, t) + \Sigma(\zeta, t)] G(\xi, \zeta) \zeta d\zeta. \quad (6.13)$$

- Leak-off displacement equation (6.6)

$$\Upsilon(\xi, t) = \frac{\mathcal{G}_d \mathcal{G}_S}{\gamma(t)} \int_0^1 \frac{L(t) \gamma(t)}{L(ts) \gamma(ts)} \psi \left[ \frac{L(t) \gamma(t)}{L(ts) \gamma(ts)} \xi, \mathcal{G}_d(t) \frac{L^2(t)}{L^2(ts)} \frac{1-s}{\gamma^2(ts)} \right] ds, \quad (6.14)$$

- Backstress equation (6.7)

$$\begin{aligned} \Sigma(\xi, t) &= \frac{\mathcal{G}_\eta}{\gamma^2(t)} \frac{\mathcal{G}_c \mathcal{G}_d \mathcal{G}_S}{\mathcal{G}_v} \int_0^1 \left[ \frac{L(t) \gamma(t)}{L(ts) \gamma(ts)} \right]^2 \times \\ &\times \Xi \left[ \frac{L(t) \gamma(t)}{L(ts) \gamma(ts)} \xi, \mathcal{G}_d(t) \frac{L^2(t)}{L^2(ts)} \frac{1-s}{\gamma^2(ts)} \right] ds, \end{aligned} \quad (6.15)$$

One can see that our dimensionless formulation depends on the following six time-dependent dimensionless groups:

- Viscosity group

$$\mathcal{G}_\mu(t) = \frac{\mu' Q_0}{\varepsilon^4(t) E' L^3(t)}, \quad (6.16)$$

which characterizes energy dissipation associated with the viscosity of the fracturing fluid. In the present chapter viscosity is the only dissipation mechanism therefore it is reasonable to put this dimensionless group to be equal to 1,  $\mathcal{G}_\mu(t) = 1$ .

As a result

$$\varepsilon(t) = \left( \frac{\mu' Q_0}{E'} \right)^{1/4} L^{-3/4}(t); \quad (6.17)$$

- Storage group

$$\mathcal{G}_v(t) = \frac{\varepsilon(t) L^3(t)}{Q_0 t} = \left( \frac{\mu'}{Q_0^3 E'} \right)^{1/4} \frac{L^{9/4}(t)}{t}, \quad (6.18)$$

which is proportional to the fraction of the injected fluid volume stored in the fracture;

- Leak-off group

$$\mathcal{G}_c(t) = \frac{U(t) L^2(t)}{Q_0 t}, \quad (6.19)$$

which characterize the amount of the fluid that has leaked into the formation;

- Diffusion group

$$\mathcal{G}_d(t) = \frac{c' t}{L^2(t)}, \quad c' \equiv 4c, \quad (6.20)$$

which is related to the diffusion process with  $\sqrt{\mathcal{G}_d}$  proportional to the ratio of the diffusion length scale to the fracture size. Thus this dimensionless group is small,  $\mathcal{G}_d \ll 1$ , in the case of 1D diffusion and large in the case of 3D diffusion,  $\mathcal{G}_d \gg 1$ ;

- Filtrate storage group

$$\mathcal{G}_S(t) = \frac{S(\sigma_0 - p_0) L(t)}{U(t)}, \quad (6.21)$$

which characterizes storage of the filtrate inside the poroelastic medium;

- Backstress group

$$\mathcal{G}_\eta = \frac{\eta}{S E'}, \quad (6.22)$$

which represents the poroelastic effect. In the previous chapter (see Section 5.4)

we have shown that this group is smaller than 1/4,  $\mathcal{G}_\eta < 1/4$ .

The aim of our study is to define the dimensionless fracture radius  $\gamma(t)$ , fracture opening profile  $\Omega(\xi, t)$ , fluid displacement function profile  $\Upsilon(\xi, t)$ , and fracturing fluid pressure profile  $\Pi(\xi, t)$ .

### 6.3 Propagation regimes

The problem under study has three propagation regimes. Therefore it is convenient to represent the fracture propagation by a trajectory curve lying inside the triangle shown in Fig. 6.1 where

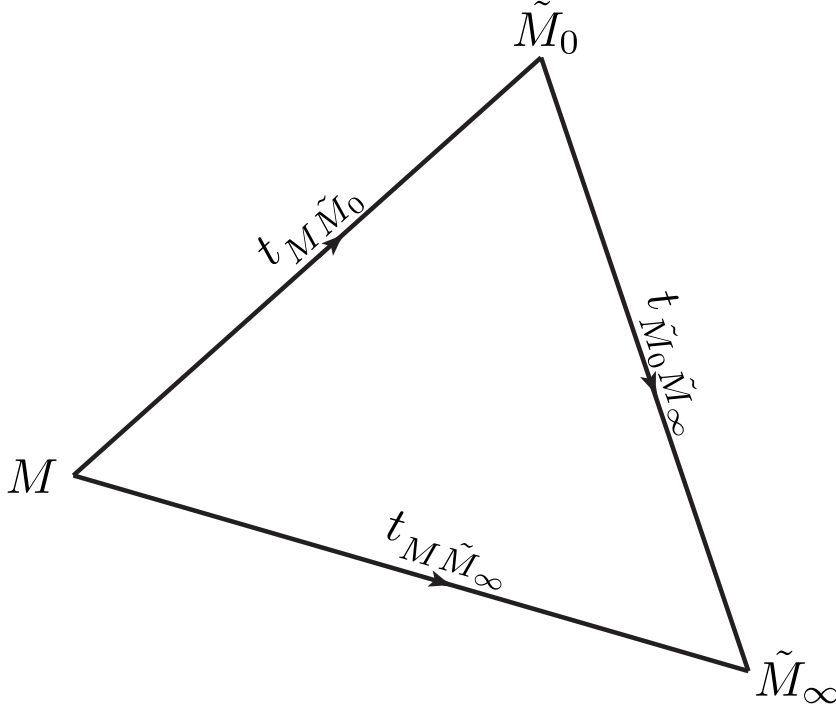


Figure 6.1: Parametric space

- $M$ -vertex represents the storage-dominated regime during which most of the injected fluid is stored inside the fracture;
- $\tilde{M}_0$ -vertex is related to the leak-off-dominated regime with 1D diffusion;
- $\tilde{M}_\infty$ -vertex is the pseudo steady-state (3D) diffusion version of the  $\tilde{M}_0$ -vertex.

We summarize the definitions of different propagation regimes in terms of the dimensionless groups (6.18)-(6.22) in Table 6.1, where we also introduce the scalings that are inherent to each of these propagation regimes [see Chapter 5]. Here the different scalings can be introduced by fixing the length scale  $L(t)$  and the fluid displacement scaling parameter  $U(t)$ . The transition times between different propagation regimes are given by

ver- tex	definition			scaling		
	$\mathcal{G}_d$	$\mathcal{G}_\eta$	$\mathcal{G}_v/\mathcal{G}_c$	definition	$L(t)$	$U(t)$
$M_0$	–	–	$\gg \frac{\mathcal{G}_S \mathcal{G}_d}{\min[\mathcal{G}_d^{1/2}, 1]}$	$\mathcal{G}_v = 1$	$\left(\frac{Q_0^3 E'}{\mu'} t^4\right)^{1/9}$	–
$\tilde{M}_0$	$\ll 1$	0	$\ll \mathcal{G}_S \mathcal{G}_d^{1/2}$	$\mathcal{G}_c = 1,$ $\mathcal{G}_S \mathcal{G}_d^{1/2} = 1$	$\left[\frac{Q_0 t^{1/2}}{\sqrt{c'} S(\sigma_0 - p_0)}\right]^{1/2}$	$\sqrt{c'} S(\sigma_0 - p_0) t^{1/2}$
$\tilde{M}_\infty$	$\gg 1$	–	$\ll \mathcal{G}_S \mathcal{G}_d$	$\mathcal{G}_c = 1,$ $\mathcal{G}_S \mathcal{G}_d = 1$	$\frac{Q_0}{c' S(\sigma_0 - p_0)}$	$\frac{[c' S(\sigma_0 - p_0)]^2}{Q_0} t$

Table 6.1: Propagation regimes and corresponding scalings

- $M\tilde{M}_0$ -edge

$$t_{M\tilde{M}_0} = \left[\sqrt{c'} S(\sigma_0 - p_0)\right]^{-18/7} \left(\frac{\mu'^2 Q_0^3}{E'^2}\right)^{2/7};$$

- $M\tilde{M}_\infty$ -edge

$$t_{M\tilde{M}_\infty} = [c' S(\sigma_0 - p_0)]^{-9/4} \left(\frac{\mu' Q_0^6}{E'}\right)^{1/4};$$

- $\tilde{M}_0\tilde{M}_\infty$ -edge

$$t_{\tilde{M}_0\tilde{M}_\infty} = c'^{-3} \left[\frac{Q_0}{S(\sigma_0 - p_0)}\right]^2.$$

The case of an impermeable medium studied by Savitski and Detournay (2002) corresponds to our  $M$ -vertex, whereas the case of the Carter's leak-off model studied by Madyarova and Detournay (2008) corresponds to the  $M\tilde{M}_0$ -edge.

The rest of the chapter is dedicated to a detailed study of the propagation regimes and the development of an numerical scheme for a transient solution.

### 6.3.1 $M$ -vertex: storage-dominated regime

In this case in terms of the intrinsic scaling [see Table 6.1] the lubrication equation (6.23) reads

$$\frac{1}{9}\Omega - \frac{4}{9}\xi \frac{\partial \Omega}{\partial \xi} + \mathcal{O}\left(\mathcal{G}_c \mathcal{G}_S \mathcal{G}_d \max\left[\mathcal{G}_d^{-1/2}, 1\right]\right) = \frac{1}{\gamma^2 \xi} \frac{\partial}{\partial \xi} \left(\xi \Omega^3 \frac{\partial \Pi}{\partial \xi}\right). \quad (6.23)$$



Since  $\Sigma \sim \mathcal{G}_\eta \mathcal{O} \left( \mathcal{G}_c \mathcal{G}_S \mathcal{G}_d \max \left[ \mathcal{G}_d^{-1/2}, 1 \right] \right) \ll 1 \sim \Pi$ , the backstress effect is negligible, and the elasticity equation (6.13) then reads

$$\Omega(\xi, t) = \frac{8\gamma}{\pi} \int_0^1 \Pi(\zeta, t) G(\xi, \zeta) \zeta d\zeta. \quad (6.24)$$

Equations (6.23), (6.24) together with the boundary condition (6.11) were solved by Savitski and Detournay (2002). Below we present only the final result

$$\begin{aligned} \Pi_M(\xi) &= \sum_{i=1}^{\infty} A_{Mi} \Pi_{Mi}^*(\xi) + B_M \Pi^{**}(\xi), \\ \Omega_M(\xi) &= \gamma_M \left[ \sum_{i=1}^{\infty} C_{Mi} \Omega_{Mi}^*(\xi) + B_M \Omega^{**}(\xi) \right]. \end{aligned} \quad (6.25)$$

Here

$$\begin{aligned} \Pi^{**}(\xi) &= -\ln \xi + \ln 2 - 1, \quad \Omega^{**}(\xi) = \frac{8}{\pi} (1 - \xi^2)^{1/2} - \frac{8}{\pi} \xi \arccos \xi, \\ \Pi_{Mi}^*(\xi) &= -\bar{\Pi}_{Mi}^*(\xi) + \int_0^1 \frac{\bar{\Pi}_{Mi}^*(\zeta)}{\sqrt{1 - \zeta^2}} \zeta d\zeta, \\ \bar{\Pi}_{Mi}^*(\xi) &= \frac{(1 - \xi)^{-1/3}}{h_{i-1}^{1/2}(4/3, 2)} G_{i-1} \left( \frac{4}{3}, 2, \xi \right), \quad \Omega_{Mi}^*(\xi) = \frac{(1 - \xi)^{2/3}}{h_{i-1}^{1/2}(10/3, 2)} G_{i-1} \left( \frac{10}{3}, 2, \xi \right), \end{aligned}$$

where  $G_i(p, k, \xi)$  is the Jacobi polynomial (Abramowitz and Stegun, 1972)

$$\begin{aligned} G_i(p, k, \xi) &= \frac{\Gamma(q+i)}{\Gamma(p+2i)} \sum_{j=0}^i (-1)^j \frac{i!}{j!(i-j)!} \frac{\Gamma(p+2i-j)}{\Gamma(q+i-j)} \xi^{i-j}, \\ h_i(p, q) &= \frac{i! \Gamma(i+q) \Gamma(i+p) \Gamma(i+p-q+1)}{(2i+p) \Gamma^2(2i+p)}. \end{aligned}$$

The coefficients  $A_{Mi}$ ,  $B_M$ , and  $C_{Mi}$  as well as the dimensionless fracture radius  $\gamma_M$  were computed numerically. In the case of truncated sums in (6.25) (four terms for the pressure and five terms for the opening) Savitski and Detournay (2002) found the following numbers

$$\begin{aligned} \gamma_M &= 0.697572, \quad A_{M1} = 0.338609, \quad A_{M2} = 0.011333, \quad A_{M3} = 0.00235756, \\ A_{M4} &= 0.000164632, \quad B_M = 0.0932001, \quad C_{M1} = 0.678295, \quad C_{M2} = 0.0686402, \\ C_{M3} &= 0.00019302, \quad C_{M4} = 0.000886672, \quad C_{M5} = 0.000221234. \end{aligned}$$

### 6.3.2 $\tilde{M}_0$ -vertex: leak-off-dominated regime with 1D diffusion, $\mathcal{G}_d \ll 1$

Substitution of the small-time asymptote of the leak-off Green function  $\psi$ , given by (4.33)

$$\psi_0(\xi, \tau) = \frac{1}{\sqrt{\pi\tau}} \frac{1 + \operatorname{sgn}(1 - \xi)}{2}, \quad (6.26)$$

into the expression for the dimensionless fluid displacement function  $\Upsilon$  (6.14) yields

$$\Upsilon(\xi, t) = \frac{2}{\sqrt{\pi}} \mathcal{G}_s \mathcal{G}_d^{1/2} \sqrt{1 - \theta(\xi, t)}, \quad (6.27)$$

where  $\theta(\xi, t) = t_0 [L(t) \gamma(t) \xi] / t$ , and  $t_0(r)$  is the time at which the crack has reached point  $r$ .

In the  $\tilde{M}_0$ -scaling [see Table 6.1] the backstress stress equation (6.15) reads

$$\Sigma(\xi, t) = \frac{\mathcal{G}_\eta}{\gamma^2(t) \mathcal{G}_v} \int_0^1 \frac{L(t) \gamma(t)}{L(ts) \gamma(ts)} \Xi_\xi^{(0)} \left[ \frac{L(t) \gamma(t)}{L(ts) \gamma(ts)} \xi \right] ds. \quad (6.28)$$

Here  $\Xi_\xi^{(0)}(\xi) \equiv \tau^{1/2} \Xi_0(\xi, \tau)$  [see (4.35)]

$$\Xi_\xi^{(0)}(\xi) = -\frac{1}{\pi^{3/2}} \left\{ (1 - \xi)^{-1} E \left[ \frac{4\xi}{(1 + \xi)^2} \right] + (1 + \xi)^{-1} K \left[ \frac{4\xi}{(1 + \xi)^2} \right] \right\}, \quad (6.29)$$

where  $K(x)$  and  $E(x)$  are the complete elliptic integrals of the first and second kind respectively (Abramowitz and Stegun, 1972).

We see that  $\Sigma \sim \mathcal{G}_\eta / \mathcal{G}_v$ , whereas by the scaling definition  $\mathcal{G}_v \ll 1$  [see Table 6.1]. According to the previous chapter the fracture volume change due to the poroelastic material dilation  $V_{\text{crack}}^{bs}$  is related to the leak-off volume  $V_{\text{leak}}$  by  $V_{\text{crack}}^{bs} / V_{\text{leak}} = -4\mathcal{G}_\eta$ . At the same time the fracture volume should be positive,  $V_{\text{crack}} > 0$  (recall that  $(V_{\text{crack}} - V_{\text{crack}}^{bs}) / V_{\text{leak}} \sim \mathcal{G}_v$ ). This means that in the case of leak-off-domination with 1D diffusion when  $\mathcal{G}_v \ll 1$ , a self-similar solution exists only if  $\mathcal{G}_\eta = 0$ . Hereafter in this subsection we assume that  $\mathcal{G}_\eta = 0$ , in other words the backstress is equal to zero,  $\Sigma(\xi, t) = 0$ .

Since in the inherent scaling the dimensionless fracture radius  $\gamma$  does not depend on time, then  $\theta = \xi^4$ , and the global volume balance equation (6.12) yields,

$$\gamma_{\tilde{M}_0} = \frac{2^{1/2}}{\pi^{3/4}}. \quad (6.30)$$

The lubrication equation (6.35) transforms to

$$\arccos(\xi^2) + \mathcal{O}(\mathcal{G}_v) = -\pi^2 \xi \Omega^3 \frac{\partial \Pi}{\partial \xi}, \quad (6.31)$$

This equation together with the boundary condition (6.11) and the elasticity equation (6.13) (where we assume  $\Sigma = 0$ ) gives the full set of the governing equations for the leak-off-dominated regime with 1D diffusion. Similarly to the storage-dominated regime we solve this set of the governing equations using the procedure developed by Savitski and Detournay (2002)

$$\begin{aligned} \Pi_{\tilde{M}_0}(\xi) &= \sum_{i=1}^{\infty} A_{\tilde{M}_0 i} \Pi_{\tilde{M}_0 i}^*(\xi) + B_{\tilde{M}_0} \Pi^{**}(\xi), \\ \Omega_{\tilde{M}_0}(\xi) &= \sum_{i=1}^{\infty} C_{\tilde{M}_0 i} \Omega_{\tilde{M}_0 i}^*(\xi) + B_{\tilde{M}_0} \gamma_{\tilde{M}_0} \Omega^{**}(\xi). \end{aligned} \quad (6.32)$$

Here

$$\begin{aligned} \Pi_{\tilde{M}_0 i}^*(\xi) &= -\bar{\Pi}_{\tilde{M}_0 i}^*(\xi) + \int_0^1 \frac{\bar{\Pi}_{\tilde{M}_0 i}^*(\zeta)}{\sqrt{1-\zeta^2}} \zeta d\zeta, \\ \bar{\Pi}_{\tilde{M}_0 i}^*(\xi) &= \frac{(1-\xi)^{-3/8}}{h_{i-1}^{1/2}(5/4, 2)} G_{i-1}\left(\frac{5}{4}, 2, \xi\right), \quad \Omega_{\tilde{M}_0 i}^*(\xi) = \frac{(1-\xi)^{5/8}}{h_{i-1}^{1/2}(13/4, 2)} G_{i-1}\left(\frac{13}{4}, 2, \xi\right), \\ A_{\tilde{M}_0 1} &= 0.273806, \quad A_{\tilde{M}_0 2} = 0.0231315, \quad A_{\tilde{M}_0 3} = 0.00216872, \\ A_{\tilde{M}_0 4} &= 0.000211575, \quad B_{\tilde{M}_0} = 0.107441, \quad C_{\tilde{M}_0 1} = 0.454113, \quad C_{\tilde{M}_0 2} = 0.0409774, \\ C_{\tilde{M}_0 3} &= -0.0009154, \quad C_{\tilde{M}_0 4} = 0.00036471, \quad C_{\tilde{M}_0 5} = 0.000052578. \end{aligned}$$

### 6.3.3 $\tilde{M}_\infty$ -vertex: leak-off-dominated regime with pseudo steady-state (3D) diffusion, $\mathcal{G}_d \gg 1$

Substitution of the large-time asymptote of the leak-off Green function  $\psi$ , given by (4.50)

$$\psi_\infty(\xi, \tau) = \frac{1}{\pi\sqrt{1-\xi^2}} \frac{1 + \operatorname{sgn}(1-\xi)}{2},$$

into the expression for the dimensionless fluid displacement function  $\Upsilon$  (6.14) yields

$$\Upsilon_{\tilde{M}_\infty} = \frac{1}{\pi\gamma_{\tilde{M}_\infty}} \frac{1}{\sqrt{1-\xi^2}}, \quad (6.33)$$

where we have used the inherent scaling [see Table 6.1].

Substitution of this equation into the global volume balance equation (6.12) and into the lubrication equation (6.10) yields

$$\gamma_{\tilde{M}_\infty} = 1/2, \quad (6.34)$$

$$\sqrt{1-\xi^2} + \mathcal{O}(\mathcal{G}_v) = -2\pi\xi\Omega^3 \frac{\partial\Pi}{\partial\xi}. \quad (6.35)$$

The backstress equation (6.15) reads

$$\Sigma_{\tilde{M}_\infty} = -\frac{\mathcal{G}_\eta}{\mathcal{G}_d\mathcal{G}_v}, \quad (6.36)$$

where we have used the large-time asymptote of the backstress Green function  $\Xi$ , given by (4.52)

$$\Xi_\infty(\xi, \tau) = -\delta(\tau) \begin{cases} 1, & \xi \leq 1 \\ \frac{2}{\pi} \arctan\left(\frac{1}{\sqrt{\xi^2-1}}\right), & \xi > 1 \end{cases}. \quad (6.37)$$

The solution of (6.35), (6.11), (6.13) is given by

$$\begin{aligned} \Pi_{\tilde{M}_\infty}(\xi) &= \sum_{i=1}^{\infty} A_{\tilde{M}_\infty i} \Pi_{\tilde{M}_0 i}^*(\xi) + B_{\tilde{M}_\infty} \Pi^{**}(\xi) - \Sigma_{\tilde{M}_\infty}, \\ \Omega_{\tilde{M}_\infty}(\xi) &= \sum_{i=1}^{\infty} C_{\tilde{M}_\infty i} \Omega_{\tilde{M}_0 i}^*(\xi) + B_{\tilde{M}_\infty} \gamma_{\tilde{M}_\infty} \Omega^{**}(\xi). \end{aligned} \quad (6.38)$$

Here

$$\begin{aligned}\Pi_{\tilde{M}_{\infty}i}^*(\xi) &= -\bar{\Pi}_{\tilde{M}_{\infty}i}^*(\xi) + \int_0^1 \frac{\bar{\Pi}_{\tilde{M}_{\infty}i}^*(\zeta)}{\sqrt{1-\zeta^2}} \zeta d\zeta, \\ \bar{\Pi}_{\tilde{M}_{\infty}i}^*(\xi) &= \frac{(1-\xi)^{-3/8}}{h_{i-1}^{1/2}(5/4, 2)} G_{i-1}\left(\frac{5}{4}, 2, \xi\right), \quad \Omega_{\tilde{M}_{\infty}i}^*(\xi) = \frac{(1-\xi)^{5/8}}{h_{i-1}^{1/2}(13/4, 2)} G_{i-1}\left(\frac{13}{4}, 2, \xi\right), \\ A_{\tilde{M}_{\infty}1} &= 0.323853, \quad A_{\tilde{M}_{\infty}2} = 0.0242777, \quad A_{\tilde{M}_{\infty}3} = 0.00271007, \\ A_{\tilde{M}_{\infty}4} &= 0.000219905, \quad B_{\tilde{M}_{\infty}} = 0.118428, \quad C_{\tilde{M}_{\infty}1} = 0.444079, \quad C_{\tilde{M}_{\infty}2} = 0.0405383, \\ C_{\tilde{M}_{\infty}3} &= -0.000785927, \quad C_{\tilde{M}_{\infty}4} = 0.000366025, \quad C_{\tilde{M}_{\infty}5} = 0.0000601663.\end{aligned}$$

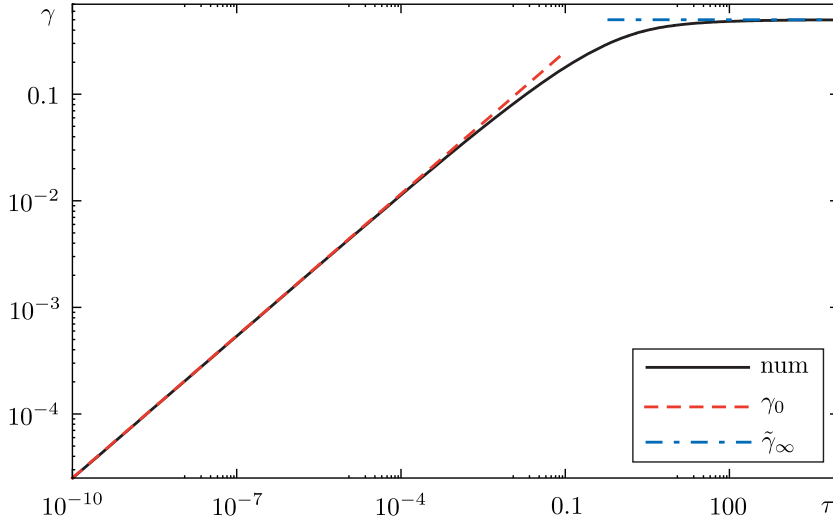


Figure 6.2: Fracture radius  $\gamma$  vs time  $\tau$ :  $G_v = 1$

## 6.4 Transient solution

To obtain a general trajectory of the system starting at the  $M$ -vertex and ending at the  $\tilde{M}_{\infty}$ -vertex, we developed an implicit numerical algorithm which solves our set of governing equations (6.10)-(6.15). From a numerical point of view it is convenient to introduce a new, time-independent scaling which is based on the leak-off-dominated,

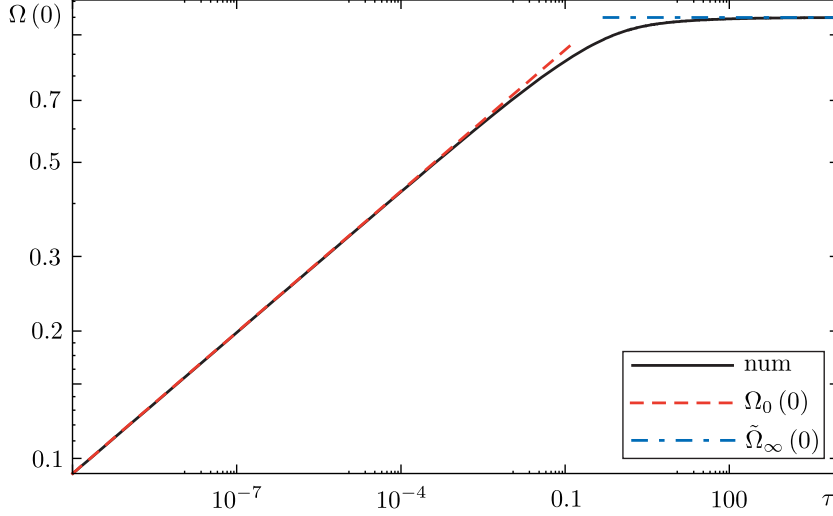


Figure 6.3: Fracture opening at the injection point  $\Omega(0)$  vs time  $\tau$ :  $G_v = 1$

pseudo steady-state diffusion scaling

$$\gamma(\tau) = \frac{R(t)}{L_{\tilde{M}_\infty}}, \quad \tau = \frac{t}{T}, \quad U = S(\sigma_0 - p_0)L_{\tilde{M}_\infty}, \quad T = \frac{L_{\tilde{M}_\infty}^2}{c'}. \quad (6.39)$$

The governing equations (6.10)-(6.15) transform to

- Lubrication equation (6.10)

$$G_v \left( \dot{\Omega} - \frac{\dot{\gamma}}{\gamma} \xi \frac{\partial \Omega}{\partial \xi} \right) + \left( \dot{\Upsilon} - \frac{\dot{\gamma}}{\gamma} \xi \frac{\partial \Upsilon}{\partial \xi} \right) = \frac{1}{\gamma^2 \xi} \frac{\partial}{\partial \xi} \left( \xi \Omega^3 \frac{\partial \Pi}{\partial \xi} \right), \quad (6.40)$$

- Boundary condition (6.11)

$$-2\pi \lim_{\xi \rightarrow 0} \xi \Omega^3 \frac{\partial \Pi}{\partial \xi} = 1, \quad (6.41)$$

- Global volume balance equation (6.12)

$$\tau = G_v 2\pi \gamma^2 \int_0^1 \Omega(\xi, \tau) \xi d\xi + 2\pi \gamma^2 \int_0^1 \Upsilon(\xi, \tau) \xi d\xi, \quad (6.42)$$

- Elasticity equation (6.13)

$$\Omega(\xi, \tau) = \frac{8\gamma}{\pi} \int_0^1 [\Pi(\zeta, \tau) + \Sigma(\zeta, \tau)] G(\xi, \zeta) \zeta d\zeta. \quad (6.43)$$

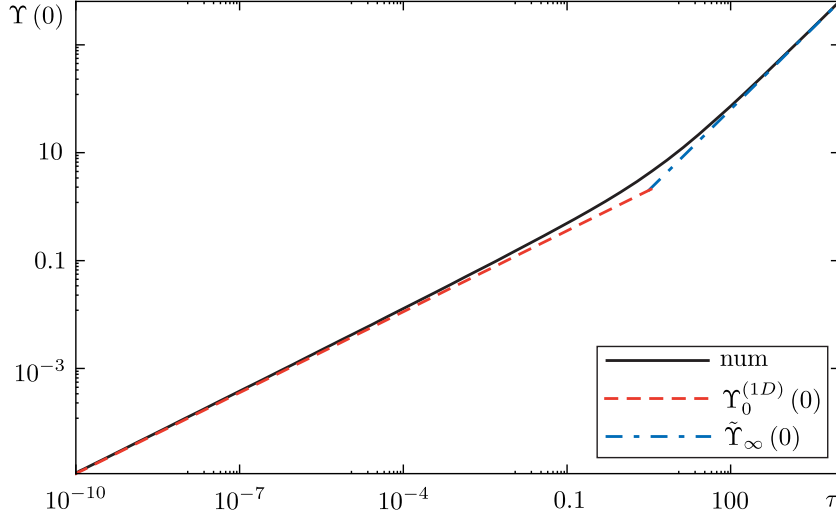


Figure 6.4: Fracturing fluid displacement function at the injection point  $\Upsilon(0)$  vs time  $\tau$ :  $G_v = 1$

- Leak-off displacement equation (6.28)

$$\Upsilon(\xi, \tau) = \int_0^\tau \gamma^{-1}(\bar{\tau}) \psi \left[ \frac{\gamma(\tau)}{\gamma(\bar{\tau})} \xi, \frac{\tau - \bar{\tau}}{\gamma^2(\bar{\tau})} \right] d\bar{\tau}, \quad (6.44)$$

- Backstress equation (6.15)

$$\Sigma(\xi, \tau) = \frac{\mathcal{G}_\eta}{G_v} \int_0^\tau \gamma^{-2}(\bar{\tau}) \Xi \left[ \frac{\gamma(\tau)}{\gamma(\bar{\tau})} \xi, \frac{\tau - \bar{\tau}}{\gamma^2(\bar{\tau})} \right] d\bar{\tau}, \quad (6.45)$$

where  $G_v = \mathcal{G}_v(t = T, L = L_{\tilde{M}_\infty})$ .

In this scaling the found above asymptotes have the following form:

- $M$ -vertex:

$$\begin{aligned} \gamma_0 &= G_v^{-4/9} \tau^{4/9} \gamma_M, & \Omega_0 &= G_v^{-1/9} \tau^{1/9} \Omega_M, \\ \Pi_0 &= G_v^{1/3} \tau^{-1/3} \Pi_M, & \Upsilon_0^{(1D)} &= \frac{2\tau^{1/2}}{\pi^{1/2}} \sqrt{1 - \xi^{9/4}}, \\ \Upsilon_0^{(3D)} &= \frac{9G_v^{4/9}}{8\pi\gamma_M} \tau^{5/9} \xi^{5/4} \left[ \frac{\pi^{1/2} \Gamma(-5/8)}{\Gamma(-1/8)} - B(\xi^2, -5/8, 1/2) \right], \end{aligned}$$

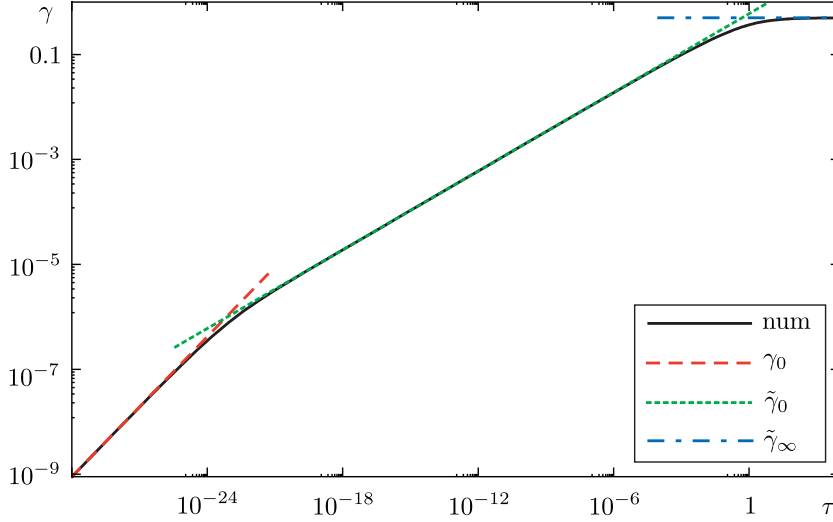


Figure 6.5: Fracture radius  $\gamma$  vs time  $\tau$ :  $G_v = 10^{-10}$

- $\tilde{M}_0$ -vertex:

$$\begin{aligned}\tilde{\gamma}_0 &= \tau^{1/4} \gamma_{\tilde{M}_0}, & \tilde{\Omega}_0 &= \tau^{1/16} \Omega_{\tilde{M}_0}, \\ \tilde{\Pi}_0 &= \tau^{-3/16} \Pi_{\tilde{M}_0}, & \tilde{\Upsilon}_0 &= \frac{2\tau^{1/2}}{\pi^{1/2}} \sqrt{1 - \xi^4},\end{aligned}$$

- $\tilde{M}_\infty$ -vertex:

$$\tilde{\gamma}_\infty = \gamma_{\tilde{M}_\infty}, \quad \tilde{\Omega}_\infty = \Omega_{\tilde{M}_\infty}, \quad \tilde{\Pi}_\infty = \Pi_{\tilde{M}_\infty}, \quad \tilde{\Upsilon}_\infty = \frac{2\tau}{\pi} \frac{1}{\sqrt{1 - \xi^2}}.$$

Here  $B(x, p, q)$  is the incomplete Euler beta function.

As indicated earlier at the beginning of this chapter we are not able to incorporate the backstress effect into the numerical scheme. This is the result of very complicated structure of the backstress Green function  $\Xi(\xi, \tau)$ . In fact, this Green function has very strong singularity at small times,  $\Xi_0(\xi, \tau) \sim \tau^{-1/2} / (1 - \xi)$  [see (6.29)], whereas at large times it behaves as the Dirac delta function,  $\Xi_\infty(\xi, \tau) \sim \delta(\tau)$  [see (6.37)]. During the numerical simulations we assume that  $\mathcal{G}_\eta = 0$ . As a result the backstress is equal to zero,  $\Sigma(\xi, \tau) = 0$ .



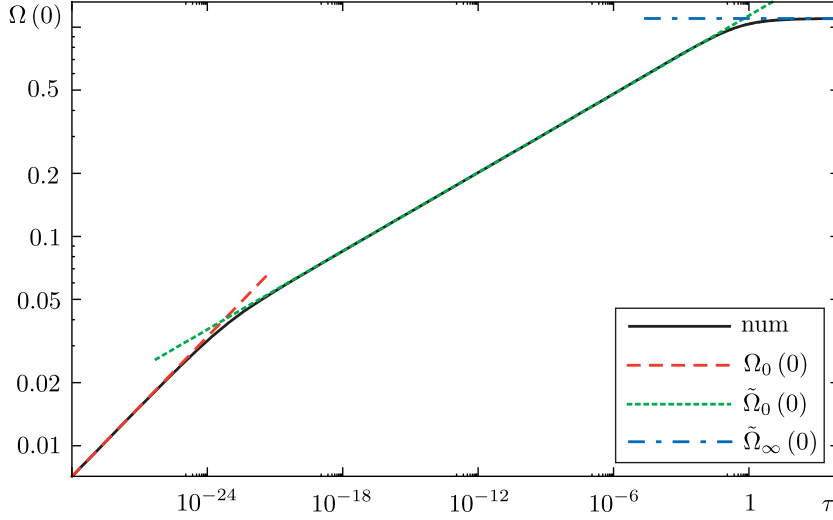


Figure 6.6: Fracture opening at the injection point  $\Omega(0)$  vs time  $\tau$ :  $G_v = 10^{-10}$

In contrast to the backstress Green function  $\Xi(\xi, \tau)$ , the leak-off Green function  $u(\xi, \tau)$  has slightly weaker singularities [see (6.26) and (6.33)]. This fact allows us to perform numerical integration of the leak-off displacement equation (6.44).

One more challenge here is the absence of a tip asymptote. As it was shown in Chapter 3, where we have studied the propagation of a semi-infinite fracture, the standard approach to model the tip region by a semi-infinite fracture is not applicable to the case of large scale 3D diffusion. In fact this approach can be used only at early times when the diffusion length scale is small compared to the fracture size, i.e.,  $\sqrt{ct}/R(t) \ll 1$ . At the same time, the solution of the problem in the tip region is always singular whether the diffusion length scale is small or large. This means that in order to develop an efficient numerical scheme one has to have an appropriate tip asymptote.

Looking at the reduced lubrication equation in different scaling (6.23), (6.31), and (6.35) one can observe that all these equations have the same structure in the tip region. Moreover, this structure is similar to the one of the classical Carter's leak-off model.

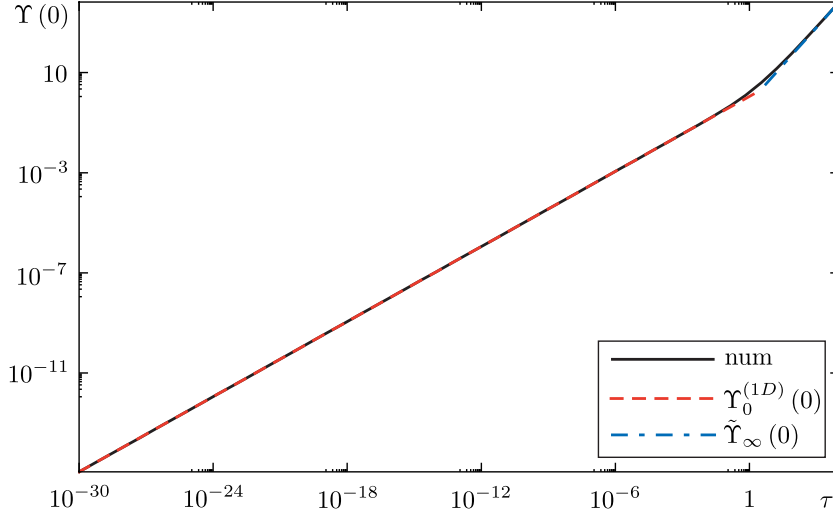


Figure 6.7: Fracturing fluid displacement function at the injection point  $\Upsilon(0)$  vs time  $\tau$ :  $G_v = 10^{-10}$

During the numerical simulations we assume that the structure of the lubrication equation in the tip region is always of this simple form. The implementation of this idea is described in Appendix D.3.

The numerical algorithm itself is based on the control volume method adopted to the fracture propagation problem by Kovalyshen and Detournay (2009). The details of the algorithm are described in Appendix D.

The results of the numerical simulations are shown in Figs 6.2-6.19. The simulations were conducted for different values of the dimensionless parameter  $G_v$ . We see that in all these cases the trajectory of the system starts at the  $M$ -vertex and arrives to the  $\tilde{M}_\infty$ -vertex. Sometimes the system can go through the third vertex  $\tilde{M}_0$  (see Figs 6.5-6.16). We would like to note here that, strictly speaking, the  $M$ -vertex can be split into two limiting cases: i) the case of 1D diffusion, and ii) the case of pseudo steady-state (3D) diffusion in which the fracture growth is so slow that the pore pressure around it is always in equilibrium. The difference between these two cases can be observed in the fracturing fluid displacement functions' time dependence and spacial distribution (see

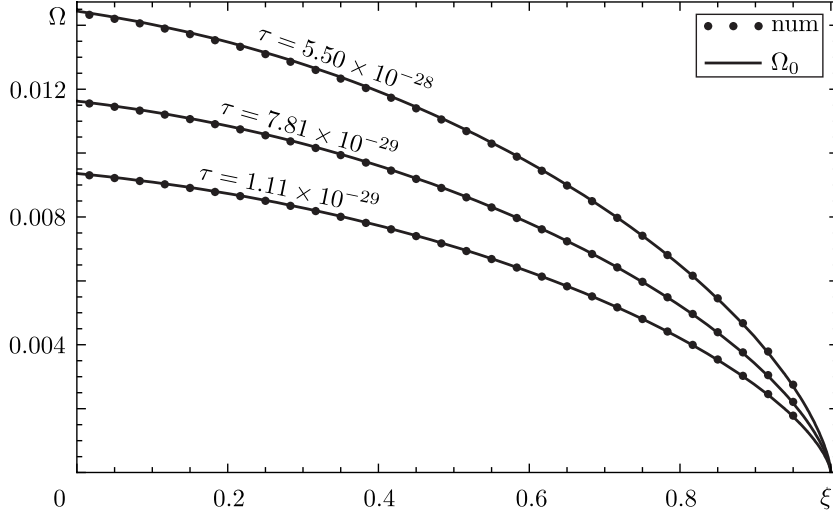


Figure 6.8: Fracture opening profile:  $M$ -vertex,  $G_v = 10^{-10}$

Figs 6.7, 6.10, 6.18, 6.19).

## 6.5 Summary of the chapter results

In this chapter we have performed a detailed study of the propagation of a penny-shaped hydraulic fracture driven by a viscous Newtonian fluid through a poroelastic medium with zero toughness. The study relies on scaling and asymptotic analyses. In fact, we have shown that the problem has three self-similar propagation regimes (see Section 6.3). We have found semi-analytical solutions for each of these propagation regimes. Also we have developed a numerical algorithm, which is able to build a transient solution connecting these asymptotes.

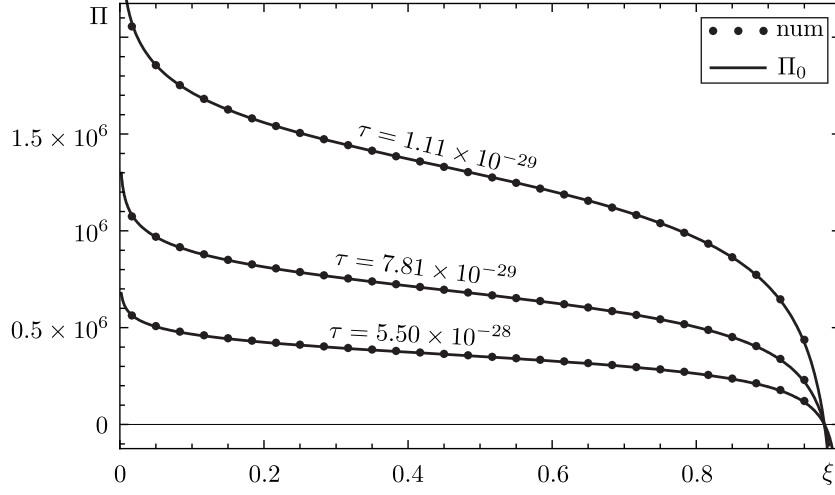


Figure 6.9: Fracturing fluid pressure profile:  $M$ -vertex,  $G_v = 10^{-10}$

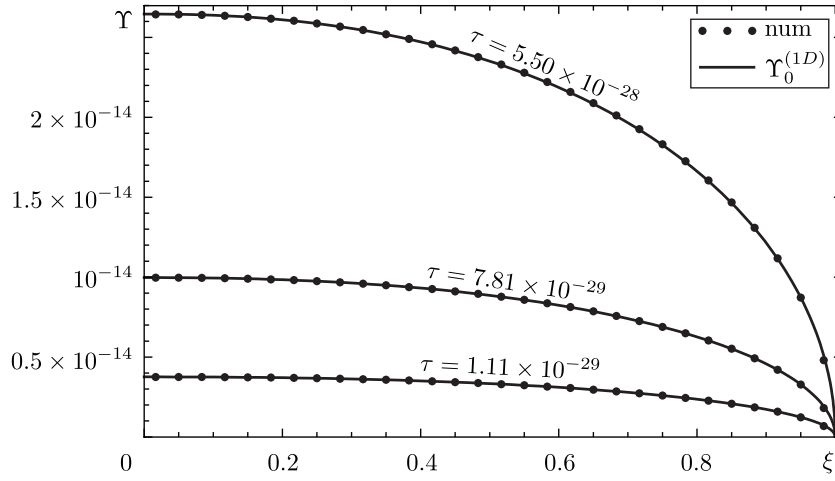


Figure 6.10: Fracturing fluid displacement function profile:  $M$ -vertex, 1D diffusion,  $G_v = 10^{-10}$

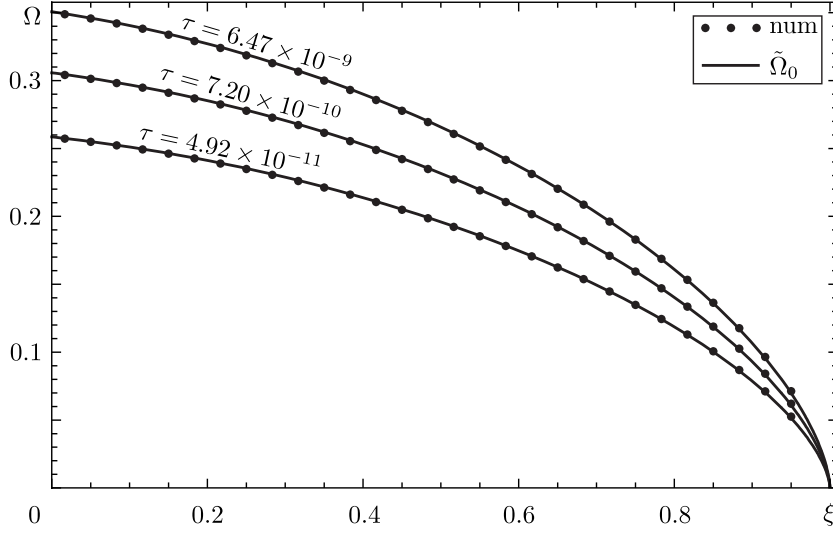


Figure 6.11: Fracture opening profile:  $\tilde{M}_0$ -vertex,  $G_v = 10^{-10}$

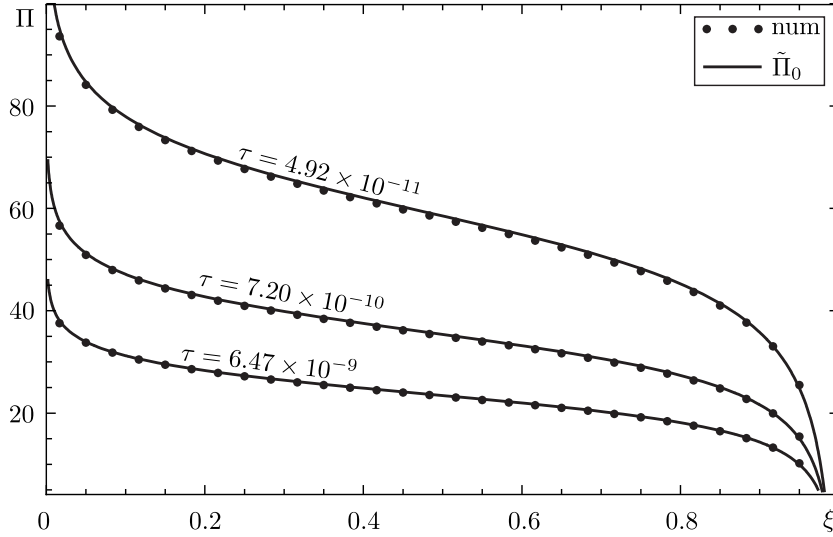


Figure 6.12: Fracturing fluid pressure profile:  $\tilde{M}_0$ -vertex,  $G_v = 10^{-10}$

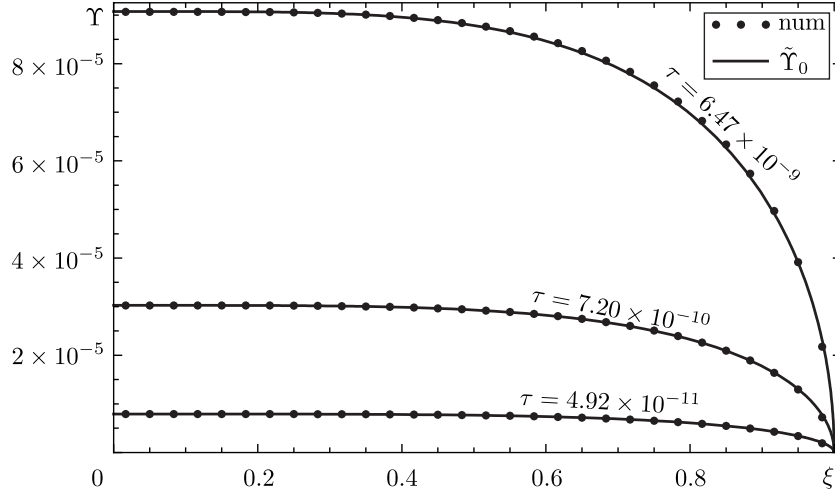


Figure 6.13: Fracturing fluid displacement function profile:  $\tilde{M}_0$ -vertex,  $G_v = 10^{-10}$

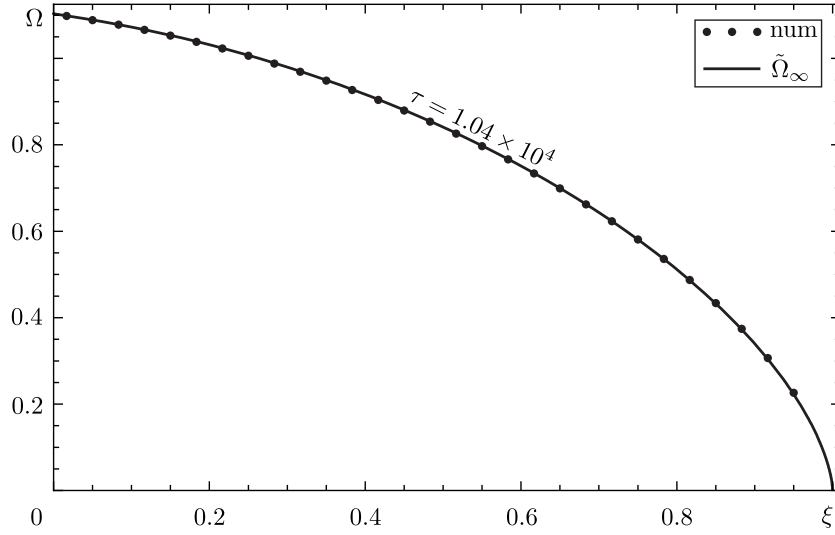


Figure 6.14: Fracture opening profile:  $\tilde{M}_\infty$ -vertex,  $G_v = 10^{-10}$

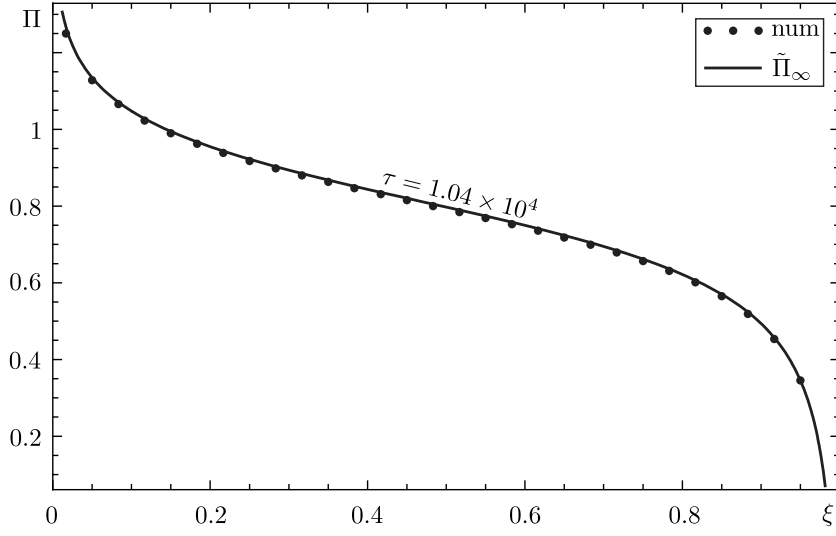


Figure 6.15: Fracturing fluid pressure profile:  $\tilde{M}_\infty$ -vertex,  $G_v = 10^{-10}$

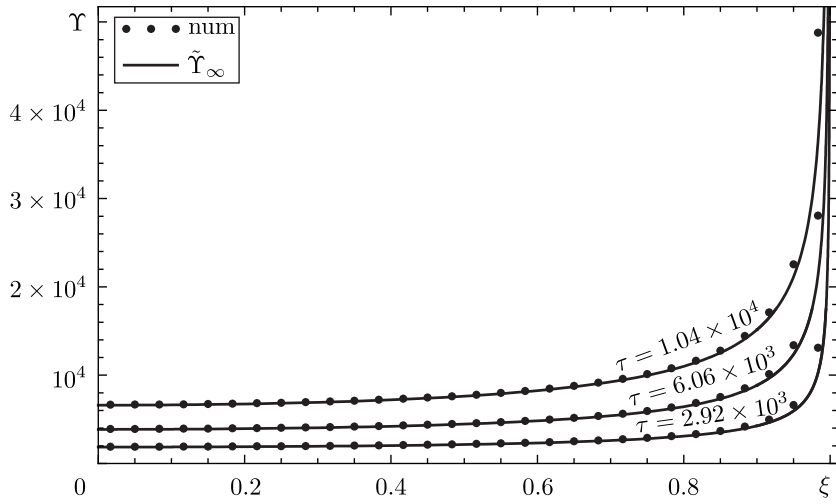


Figure 6.16: Fracturing fluid displacement function profile:  $\tilde{M}_\infty$ -vertex,  $G_v = 10^{-10}$

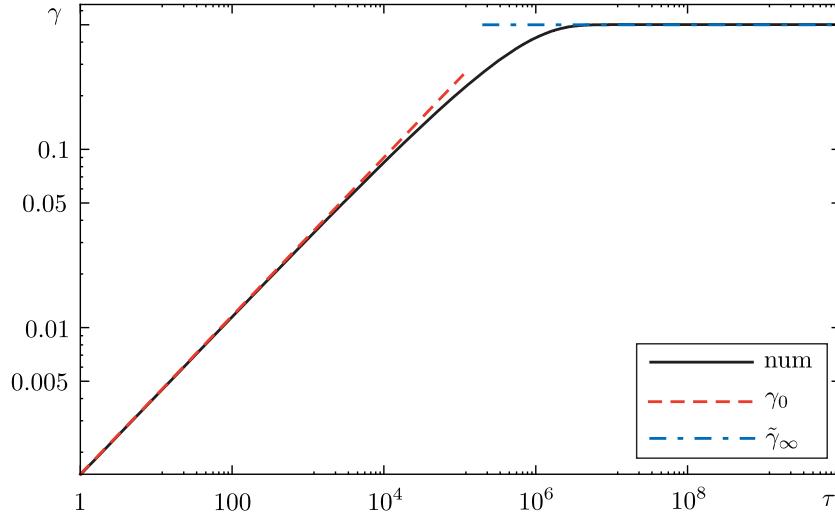


Figure 6.17: Fracture radius  $\gamma$  vs time  $\tau$ :  $G_v = 10^6$

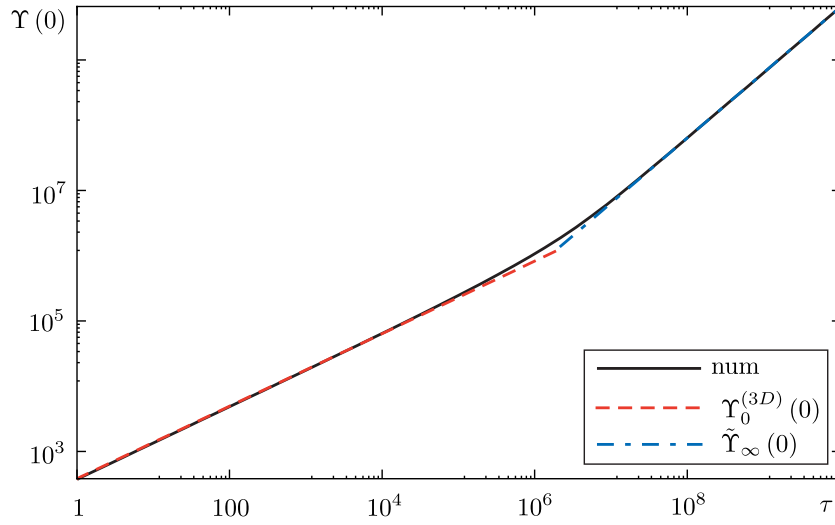


Figure 6.18: Fracturing fluid displacement function at the injection point  $\Upsilon(0)$  vs time  $\tau$ :  $G_v = 10^6$



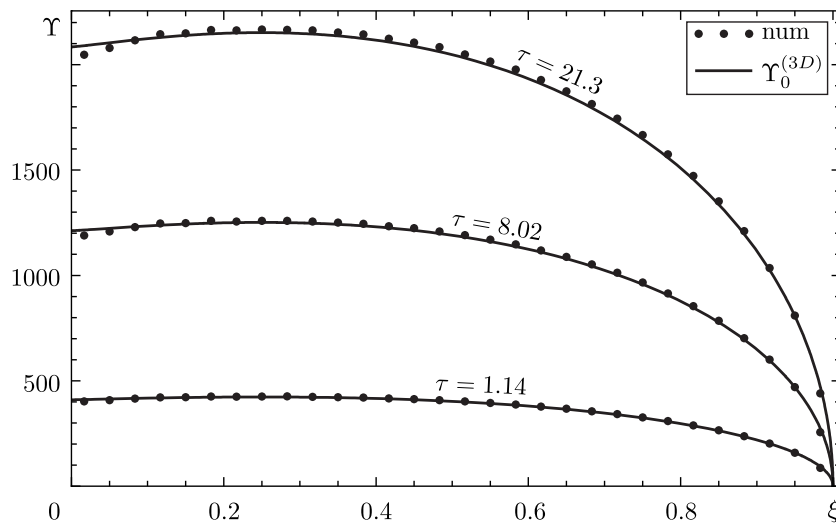


Figure 6.19: Fracturing fluid displacement function profile:  $M$ -vertex, 3D diffusion,  $G_v = 10^6$

## Chapter 7

# Conclusions

### 7.1 Main results

During the course of this research we have studied the propagation of a penny-shaped hydraulic fracture within a poroelastic medium. We put the emphasis on the investigation of the 3D diffusion and related poroelastic effects. Instead of developing a straightforward numerical solution of the general problem as was done for example by Boone and Ingraffea (1990) and Boone et al. (1991), we aimed at grasping a physical understanding of the processes under consideration using simplified models. In this study, we used scaling and asymptotic analyses adopted to the hydraulic fracturing problem by Detournay (2004).

We believe that the present research is the first rigorous study on the influence of large scale diffusion together with the associated poroelastic effects on the propagation of a hydraulic fracture.

The problem of the fluid fracture propagation is challenging, in particular due to the singular behaviour of the solution at the moving front. Usually in order to understand this behaviour, the tip region is modeled by a semi-infinite fracture propagating at

a constant velocity [see Desroches et al. (1994); Lenoach (1995); Carter et al. (2000); Detournay et al. (2002); Garagash and Detournay (2005), and Garagash et al. (2009)]. As a result, the terms “tip region” and “semi-infinite fracture” are often used interchangeably, nowadays.

We started our research by studying the propagation of a semi-infinite fracture. We have shown that the semi-infinite model and the tip region are equivalent only at early times  $R \gg \sqrt{ct}$ , when the characteristic diffusion length scale  $\sqrt{ct}$  is small compared to the fracture size  $R$ . Assuming that this criterion is satisfied, we have found a semi-analytical solution for this problem (see Section 3). In particular we have shown that the far-field solution can be described by the classical Carter’s leak-off model. Additionally we have shown that if the confining stress  $\sigma_0$  is large compared to the far-field pore pressure  $p_0$ ,  $\sigma_0 \gg p_0$ , then the solution of the problem is of the same form as in the Carter’s leak-off model. We would like to stress that in this case the diffusion is not necessarily one dimensional.

In Chapter 4 we have studied the so-called auxiliary problem, which consists in the determination of a poroelastic medium response to a unit impulse of pressure applied from inside of a stationary penny-shaped fracture of radius  $R$ . As a result we have defined the fluid exchange rates between the fracture and the medium as well as the generated backstress, which embodies the response of the poroelastic medium to the change in the pore pressure field caused by the pressure pulse in the fracture. The solution to the auxiliary problem is a key element of this research as it helps significantly simplify the formulation and treatment of the hydraulic fracture propagation problem.

We then developed the solution of the propagation problem. We restricted ourselves to the cases of toughness-dominated regimes (Chapter 5) and viscosity-dominated regimes with  $\sigma_0 \gg p_0$  (Chapter 6). We have shown that compared to the classical

case with the Carter's leak-off (Adachi and Detournay, 2008; Madyarova and Detournay, 2008), the problem under consideration has a series of stationary vertices when the fracture does not propagate. These vertices exist only due to well developed 3D diffusion.

## 7.2 Practical applications

Let us consider the results from an application point of view. In the Table 7.1 we list parameters of a production water re-injection (Longuemare et al., 2001).

	low porosity reservoir (LPR)	mean porosity reservoir (MPR)
porosity $\phi$ (%)	10	20
permeability $k$ (md)	10	100
Young's modulus $E$ (GPa)	30	15
Poisson's ratio $\nu$	0.2	0.25
rock toughness $K_{Ic}$ (MPa $\cdot$ m <sup>1/2</sup> )	1.0	
water bulk modulus $K_f$ (GPa)	2.2	
water viscosity $\mu$ (mPa $\cdot$ s)	1.0	
Biot coefficient $\alpha$	0.6	
diffusion coefficient $c$ (m <sup>2</sup> /s)	0.212	1.04
storage coefficient $S$ (Pa <sup>-1</sup> )	$4.65 \times 10^{-11}$	$9.49 \times 10^{-11}$
poroelastic stress modulus $\eta$	0.225	0.2
reservoir thickness $H$ (m)	50	5
confining stress $\sigma_0$ (MPa)	55	
initial pore pressure $p_0$ (MPa)	30	
injection rate $Q_0$ (m <sup>3</sup> /day)	750	
treatment time $T$ (days)	100	

Table 7.1: Characteristic parameters during production water re-injection (Longuemare et al., 2001)

Here, in order to calculate values for  $S$  and  $c$ , we have assumed that  $K_f/E \ll 1$  and have used equations provided by Detournay and Cheng (1993).

To characterize the propagation of a fracture we compute the transition times, found

current vertex	possible transitions				vertex choice
	vertex	transition time	LPR, sec	MPR, sec	
$M_\mu$	$K_0$	$t_{M_\mu K_0} = \sqrt{\frac{\mu'^5 Q_0^3 E'^{13}}{K_{Ic}^{18}}}$	$2.1 \times 10^6$	$2.7 \times 10^4$	$M$
	$M$	$t_{M_\mu M} = \frac{\mu' E'^2}{(\sigma_0 - p_0)^3}$	$7.5 \times 10^{-4}$	$2.0 \times 10^{-4}$	
	$\tilde{M}_{\mu 0}$	$t_{M_\mu \tilde{M}_{\mu 0}} = \frac{Q_0^6}{c'^9 S^{18} \mu'^2 E'^{16}}$	$1.5 \times 10^{10}$	$1.1 \times 10^3$	
	$\tilde{M}_{\mu \infty}$	$t_{M_\mu \tilde{M}_{\mu \infty}} = \frac{Q_0^6}{c'^9 S^9 \mu'^2 E'^7}$	$4.4 \times 10^{11}$	$4.7 \times 10^4$	
$M$	$K_0$	$t_{MK_0} = \sqrt{\frac{\mu'^5 Q_0^3 E'^{13}}{K_{Ic}^{18}}}$	$2.1 \times 10^6$	$2.7 \times 10^4$	$\tilde{M}_0$
	$\tilde{M}_0$	$t_{M\tilde{M}_0} = \frac{1}{[\sqrt{c'} S(\sigma_0 - p_0)]^{18/7}} \left( \frac{\mu'^2 Q_0^3}{E'^2} \right)^{2/7}$	$5.9 \times 10^{-2}$	$1.8 \times 10^{-3}$	
	$\tilde{M}_\infty$	$t_{M\tilde{M}_\infty} = \frac{1}{[c' S(\sigma_0 - p_0)]^{9/4}} \left( \frac{\mu' Q_0^6}{E'} \right)^{1/4}$	3.7	$2.4 \times 10^{-2}$	
$\tilde{M}_0$	$\tilde{K}_{\sigma 0}$	$t_{M\tilde{K}_{\sigma 0}} = \frac{c' S^2(\sigma_0 - p_0)^2 \mu'^4 Q_0^2 E'^{12}}{K_{Ic}^{16}}$	$1.2 \times 10^{12}$	$10^{10}$	$\tilde{M}_\infty$
	$\tilde{M}_\infty$	$t_{\tilde{M}_0 \tilde{M}_\infty} = c'^{-3} \left[ \frac{Q_0}{S(\sigma_0 - p_0)} \right]^2$	91.1	0.19	

Table 7.2: Crack propagation

in the present research. To describe the transitions between the viscosity- and toughness-dominated regimes we introduce the following dimensionless group [known as the dimensionless viscosity (Savitski and Detournay, 2002)]

$$\mathcal{G}_m(t) = \frac{\mu' Q_0 E'^3}{K_{Ic}^4 L(t)}, \quad (7.1)$$

where  $L(t)$  is the characteristic fracture size. If the fracture propagates in a viscosity-dominated regime, then  $\mathcal{G}_m(t) \gg 1$ . In the case of toughness domination we have  $\mathcal{G}_m(t) \ll 1$ . Using this property, one can easily estimate transition times between different viscosity- and toughness-dominated regimes. For the storage-dominated regimes, for example, the transition time from the  $M$ -vertex into the  $K_0$ -vertex can be estimated after one substitutes  $L(t)$  for the  $M$ -vertex, see Table 6.1, into (7.1).

Also, during the examination of the fracture propagation through a rock with zero toughness (see Chapter 6), we assumed that  $p - \sigma_0 \ll \sigma_0 - p_0$ . In general, one can have

a situation when this assumption is not applicable. In order to study validity of this assumption we introduce the following dimensionless group

$$\mathcal{G}_\mu(t) \cong \frac{p(t) - \sigma_0}{\sigma_0 - p_0} \sim \frac{E'}{\sigma_0 - p_0} \left( \frac{\mu' Q_0}{E'} \right)^{1/4} L^{-3/4}(t), \quad (7.2)$$

where the subscript  $\mu$  indicates that the difference  $p - \sigma_0$  occurs due to the viscous flow of the fracturing fluid. [We believe that there should not be any confusion with the dimensionless group  $\mathcal{G}_\mu$  introduced by (6.16).] To derive (7.2) we used the definition of the viscosity-dominated scaling (6.9), (6.18)-(6.22). It is clear that if  $\mathcal{G}_\mu(t) \ll 1$  then the assumption  $p - \sigma_0 \ll \sigma_0 - p_0$  is quite accurate.

The results of the analysis of the fracture propagation are presented in Table 7.2. Obviously, at the beginning of the fracture propagation, when the aperture is very small, the viscous flow of the fracturing fluid leads to large fluid pressure  $p$ ,  $p - \sigma_0 \gtrsim \sigma_0 - p_0$ . We denote this storage-dominated regime by  $M_\mu$ . We see that the fluid pressure decreases quite rapidly and the system moves to the  $M$ -vertex. Note that the vertices  $\tilde{M}_{\mu 0}$  and  $\tilde{M}_{\mu \infty}$  are analogous to  $\tilde{K}_{\kappa 0}$  and  $\tilde{K}_{\kappa \infty}$  in the sense that these are leak-off-dominated regimes in the case of 1D and 3D diffusion respectively with high fracturing fluid pressure  $p$ ,  $p - \sigma_0 \gg \sigma_0 - p_0$ , generated by the viscous flow. Recall that in the case of the  $\tilde{K}_{\kappa 0}$ - and  $\tilde{K}_{\kappa \infty}$ -vertices this high pressure is due to the rock toughness. To calculate the transition times  $t_{M_\mu \tilde{M}_{\mu 0}}$  and  $t_{M_\mu \tilde{M}_{\mu \infty}}$  we follow the general procedure of calculating the transition times (see Section 5.4). Namely, we introduce the scalings  $\mathcal{G}_\mu \mathcal{G}_S \mathcal{G}_d^{1/2} = 1$  and  $\mathcal{G}_c = 1$  for the  $\tilde{M}_{\mu 0}$ -vertex and  $\mathcal{G}_\mu \mathcal{G}_S \mathcal{G}_d = 1$  and  $\mathcal{G}_c = 1$  for the  $\tilde{M}_{\mu \infty}$ -vertex (cf. Table 6.1). Then, for each scaling we define the length scale  $L(t)$  and estimate the transition times using the inequality  $\mathcal{G}_v \ll 1$ .

We would like to stress that in the present example all time scales are well separated. As a result, the fracture follows the edges with the shortest transition time passing through the  $\tilde{M}_0$ -vertex and ending up at the  $\tilde{M}_\infty$ -vertex. Note that at the  $\tilde{M}_\infty$ -vertex the dimensionless groups  $\mathcal{G}_m$  and  $\mathcal{G}_\mu$  are equal to  $\mathcal{G}_m = 3.6 \times 10^2$  and  $\mathcal{G}_\mu = 5.9 \times 10^{-2}$

in the case of the low porosity reservoir, and  $\mathcal{G}_m = 4.9 \times 10^2$  and  $\mathcal{G}_\mu = 0.2$  for the mean porosity reservoir. Therefore our model is still applicable there.

We see that the fracture almost immediately reaches its steady state. This occurs within a few minutes compared to the 100 day length of the total treatment time. From a modeling point of view this means that in order to build a more general (e.g. case of general fracture geometry) model of the described above treatment, one can study only a stationary fracture. Note that during the analysis performed above we used only general results of the scaling analysis, without involving explicit asymptotic solutions.

At the  $\tilde{M}_\infty$ -vertex the poroelastic effects do not have any influence on the fracture radius  $R$ . In the case of LPR  $R = 4.4$  m whereas in the case of MPR  $R = 0.44$  m. It is also interesting to see what is the influence of the poroelastic effects on the net fluid pressure. At the  $\tilde{M}_\infty$ -vertex in the case of LPR with  $\eta = 0$  the net pressure is of order  $p - \sigma_0 \sim \varepsilon E' = 1.5$  MPa whereas in the case of MPR  $p - \sigma_0 = 5.0$  MPa ( $\eta = 0$ ). The poroelastic effects lead to an increase of the net pressure by  $\Delta p = -\varepsilon E' \Sigma_{\tilde{M}_\infty}$ , which in the case of LPR is equal to  $\Delta p = 5.6$  MPa, whereas in the case of MPR,  $\Delta p = 5.0$  MPa.

### 7.3 Further development

We see that as we add more and more physical processes into consideration the parametric space of the problem grows quite fast. Therefore we believe that it is inefficient to build a general solution, which takes into account everything. It seems more reasonable to take a particular case (as it was done in the previous section), define which part of the parametric space corresponds to this case and then adopt/develop a solution only for this particular case.

Another direction of research could be the incorporation of large scale diffusion into 2D models of fluid-driven fracture, e.g., into the KGD and PKN models which are very important in practical applications (Economides and Nolte, 2000). A significant

difference between a penny-shaped and 2D fractures is in the propagation speeds. Indeed, we have shown that the size of a penny-shaped fracture depends on time as  $R(t) \sim t^{\alpha(t)}$ , where  $\alpha(t) < 1/2$  and  $d\alpha/dt < 0$ . As a result at early times when  $R(t) \gg \ell_d(t) \sim \sqrt{ct}$  the diffusion process is one dimensional, whereas at large times when  $R(t) \lesssim \ell_d(t)$  it is three dimensional. In contrast, in the 2D case  $\ell(t) \sim t^{\beta(t)}$ , where  $\ell(t)$  is the length of the fracture,  $1/2 \leq \beta(t) < 1$ , and  $d\beta/dt < 0$  (Adachi and Detournay, 2008; Bunger et al., 2005; Kovalyshen and Detournay, 2009). Moreover  $\beta = 1/2$  in the leak-off-dominating regime (the Carter's leak-off model). As a result diffusion is two dimensional at early times but not necessarily one dimensional for large times. Preliminary scaling analysis shows that at large times when the leak-off dominates over the storage, the fracture length evolves as a square root of time, thus  $\ell(t)/\ell_d(t) = \text{const}$ . Therefore the diffusion process can be either one or two dimensional. Moreover, the problem does not have a stationary solution.

Let us consider an example of the PKN model with the Carter's leak-off model. In the leak-off-dominating regime the fracture length is given by  $\ell = Q_0 t^{1/2} / (\pi C H)$ , where  $C$  is the Carter's coefficient and  $H$  is the fracture height which is equal to the thickness of the reservoir (Kovalyshen and Detournay, 2009). Using 1D solution of the fluid displacement function (6.27) one can find the following expression for the Carter's coefficient:  $C = 2\pi^{-1/2} \sqrt{c} S (\sigma_0 - p_0)$ . Substitution of the data from the previous section into these expressions yields  $\ell(t)/\ell_d(t) \sim 0.25$  for both LPR and MPR. Therefore the Carter's leak-off model is not applicable to these cases. In similar way one can check applicability of the Carter's leak-off to 2D models. If  $\ell(t)/\ell_d(t) \gg 1$  then the Carter's leak-off model is an appropriate choice (note that in the case of low permeability cake build-up one should use the results of Chapter 3 to calculate the Carter's coefficient  $C$ ).



# Bibliography

- Abé, H., Mura, T., and Keer, L. (1976). Growth rate of a penny-shaped crack in hydraulic fracturing of rocks. *J. Geophys. Res.*, 81:5335–5340. pdf.
- Abramowitz, M. and Stegun, I., editors (1972). *Handbook of Mathematical Functions with Formulas, Graphs, and Mathematical Tables*. Dover Publications Inc., New York NY.
- Adachi, J. and Detournay, E. (2008). Plane strain propagation of a hydraulic fracture in a permeable rock. *Engineering Fracture Mechanics*, 75(16):4666–4694.
- Adachi, J., Detournay, E., and Garagash, D. I. (2002). Propagation of a fluid-driven KGD fracture in a permeable elastic medium. Personal discussions.
- Adachi, J., Siebrits, E. ., Peirce, A. P., and Desroches, J. (2007). Computer simulation of hydraulic fractures. *Int. J. Rock Mech. Min. Sci.*, 44(5):739–757.
- Adachi, J. I. (2001). *Fluid-Driven Fracture in Permeable Rock*. PhD thesis, University of Minnesota, Minneapolis.
- Advani, S., Torok, J., Lee, J., and Choudhry, S. (1987). Explicit time-dependent solutions and numerical evaluations for penny-shaped hydraulic fracture models. *J. Geophys. Res.*, 92(B8):8049–8055.

- Arin, K. and Erdogan, F. (1971). Penny-shaped crack in an elastic layer bonded to dissimilar half space. *Int. J. Eng. Sci.*, 9:231–232.
- Atkinson, C. and Craster, R. (1991). Plane-strain fracture in poroelastic medium. *Proc. Roy. Soc. London Ser. A*, 434(1892):605–633.
- Atkinson, C. and Craster, R. (1992). Fracture in fully coupled dynamic thermoelasticity. *J. Mech. Phys. Solids*, 40(7):1415–1432.
- Barr, D. (1991). *Leading-Edge Analysis for Correct Simulation of Interface Separation and Hydraulic Fracturing*. PhD thesis, Massachusetts Institute of Technology, Cambridge MA.
- Berchenko, I., Detournay, E., and Chandler, N. (1997). Propagation of natural hydraulic fractures. *Int. J. Rock Mech. Min. Sci.*, 34(3-4).
- Biot, M. (1941). General theory of three-dimensional consolidation. *jap*, 12:155–164.
- Biot, M., Massé, L., and Medlin, W. (1986). A two-dimensional theory of fracture propagation. *spepe*, 1(1):17–30. (SPE 11067).
- Boone, T. and Ingraffea, A. (1990). A numerical procedure for simulation of hydraulically-driven fracture propagation in poroelastic media. *Int. J. Numer. Anal. Methods Geomech.*, 14(1):27–47.
- Boone, T., Ingraffea, A., and Roegiers, J. (1991). Simulation of hydraulic fracture propagation in poroelastic rock with application to stress measurement techniques. *ijrmms*, 28(1):1–14.
- Bunger, A., Detournay, E., and Garagash, D. (2005). Toughness-dominated hydraulic fracture with leak-off. *Int. J. Fracture*, 134(2):175–190.

- Bunger, A. P. and Detournay, E. (2008). The tip region in fluid-driven fracture experiments. *J. Mech. Phys. Solids*. in preparation.
- Carbonell, R., Desroches, J., and Detournay, E. (1999). A comparison between a semi-analytical and a numerical solution of a two-dimensional hydraulic fracture. *ijss*, 36(31–32):4869–4888.
- Carslaw, H. and Jaeger, J. (1950). *Heat Conduction in Solids*. Oxford Clarendon Press.
- Carter, B., Desroches, J., Ingraffea, A., and Wawrzynek, P. (2000). Simulating fully 3D hydraulic fracturing. In Zaman, M., Gioda, G., and Booker, J., editors, *Modeling in Geomechanics*. John Wiley & Sons., New York NY.
- Carter, E. (1957). Optimum fluid characteristics for fracture extension. In Howard, G. and Fast, C., editors, *Drilling and Production Practices*, pages 261–270. American Petroleum Institute, Tulsa OK.
- Cheng, A. H.-D. and Detournay, E. (1998). On singular integral equations and fundamental solutions of poroelasticity. *Int. J. Solids Structures*, 35:4521–4555.
- Cleary, M. (1978). Moving singularities in elasto-diffusive solids with applications to fracture propagation. *Int. J. Solids Structures*, 14:81–97.
- Cleary, M. and Wong, S. (1985). Numerical simulation of unsteady fluid flow and propagation of a circular hydraulic fracture. *ijnamg*, 9:1–14.
- Craig, F. (1971). *The Reservoir Engineering Aspects of Waterflooding*. Society of Mining Engineers of AIME.
- Craster, R. and Atkinson, C. (1994). Crack problems in a poroelastic medium: an asymptotic approach. *Phil. Trans. R. Soc. London. A*, 346:387–428.

- Craster, R. and Atkinson, C. (1996). On finite-length cracks and inclusions in poroelasticity. *Mech. appl. Math.*, 49:311–335.
- Desroches, J., Detournay, E., Lenoach, B., Papanastasiou, P., Pearson, J., Thiercelin, M., and Cheng, A.-D. (1994). The crack tip region in hydraulic fracturing. *Proc. Roy. Soc. London, Ser. A*, 447:39–48.
- Detournay, E. (2004). Propagation regimes of fluid-driven fractures in impermeable rocks. *Int. J. Geomechanics*, 4(1):1–11.
- Detournay, E., Adachi, J., and Garagash, D. (2002). Asymptotic and intermediate asymptotic behavior near the tip of a fluid-driven fracture propagating in a permeable elastic medium. In Dyskin, A., Hu, X., and Sahouryeh, E., editors, *Structural Integrity and Fracture*, pages 9–18, Lisse, The Netherlands. Swets & Zeitlinger.
- Detournay, E. and Cheng, A.-D. (1991). Plane strain analysis of a stationary hydraulic fracture in a poroelastic medium. *Int. J. Solids Structures*, 27(13):1645–1662.
- Detournay, E. and Cheng, A.-D. (1993). *Comprehensive Rock Engineering*, volume 2, chapter 5: Fundamentals of Poroelasticity, pages 113–171. Pergamon, New York NY.
- Detournay, E., Cheng, A. H.-D., Roegiers, J. C., and McLennan, J. D. (1989). Poroelasticity considerations in in situ stress determination by hydraulic fracturing. *Int. J. Rock Mech. Min. Sci.*, 26(6):507–513.
- Detournay, E. and Garagash, D. (2003). The near-tip region of a fluid-driven fracture propagating in a permeable elastic solid. *J. Fluid Mech.*, 494:1–32.
- Economides, M. and Nolte, K., editors (2000). *Reservoir Stimulation*. John Wiley & Sons, Chichester UK, 3rd edition.

- Entov, V. M., Chekhonin, E. M., Detournay, E., and Thiercelin, M. (2007). Fracture Propagation in High-Permeability Rocks: The Key Influence of Fracture Tip Behavior. In *Proc. 2007 SPE Hydraulic Fracturing Technology Conference*. SPE 106225.
- Garagash, D. (2006). Plane-strain propagation of a fluid-driven fracture during injection and shut-in: Asymptotics of large toughness. *Eng. Fract. Mec.*, 73(4):456–481.
- Garagash, D. and Detournay, E. (2000). The tip region of a fluid-driven fracture in an elastic medium. *ASME J. Appl. Mech.*, 67(1):183–192.
- Garagash, D. and Detournay, E. (2005). Plane-strain propagation of a fluid-driven fracture: Small toughness solution. *ASME J. Appl. Mech.*, 72:916–928.
- Garagash, D. I., Detournay, E., and Adachi, J. (2009). The tip region of a fluid-driven fracture in a permeable elastic medium. *J. Mech. Phys. Solids*. In preparation.
- Geertsma, J. and de Klerk, F. (1969). A rapid method of predicting width and extent of hydraulic induced fractures. *J. Pet. Tech.*, 246:1571–1581. (SPE 2458).
- Gordeyev, Y. (1993). Growth of a crack produced by hydraulic fracture in a poroelastic medium. *ijrm*, 30(3):233–238. pdf.
- Gordeyev, Y. N. and Entov, V. M. (1997). The pressure distribution around a growing crack. *J. Appl. Maths Mech.*, 61(6):1025–1029.
- Gradshteyn, I. and Ryzhik, I. (1994). *Table of Integrals, Series and Products*. Academic Press, San Diego CA, 5th edition.
- Hagoort, J., Weatherill, B. D., and Settari, A. (1980). Modeling the propagation of waterflood-induced hydraulic fractures. *Soc. Pet. Eng. J.*, pages 293–301.

- Khristianovic, S. and Zheltov, Y. (1955). Formation of vertical fractures by means of highly viscous fluids. In *Proc. 4th World Petroleum Congress, Rome*, volume II, pages 579–586.
- Kovalyshen, Y. and Detournay, E. (2009). A reexamination of the classical pkn model of hydraulic fracture. *Transport in Porous Media*.
- Lenoach, B. (1995). The crack tip solution for hydraulic fracturing in a permeable solid. *jmps*, 43(7):1025–1043.
- Lister, J. (1990). Buoyancy-driven fluid fracture: The effects of material toughness and of low-viscosity precursors. *J. Fluid Mech.*, 210:263–280.
- Lister, J. and Kerr, R. (1991). Fluid-mechanical models of crack propagation and their application to magma transport in dykes. *J. Geophys. Res.*, pages 10,049–10,077.
- Longuemare, P., Detienne, J.-L., Lemonnier, P., Bouteau, M., and Onaisi, A. (2001). Numerical modeling of fracture propagation induced by water injection/re-injection. *SPE European Formation Damage, The Hague, The Netherlands*. (SPE 68974).
- Lopez-Fernandez, M. and Palencia, C. (2004). On the numerical inversion of the laplace transform of certain holomorphic mapping. *Appl. Numer. Math.*, 51:289–303.
- Madyarova, M. (2003). Propagation of a fluid-driven penny-shaped fracture in a permeable elastic medium. Master’s thesis, University of Minnesota.
- Madyarova, M. and Detournay, E. (2008). Fluid-driven penny-shaped fracture in permeable rock. *Int. J. Numer. Anal. Methods Geomech.* Submitted.
- Mathias, S. A. and Reeuwijk, M. (2009). Hydraulic fracture propagation with 3-d leak-off. *Transport in Porous Media*.

- Murdoch, L. C. and Germanovich, L. N. (2006). Analysis of a deformable fracture in permeable material. *Int. J. Numer. Anal. Methods Geomech.*, 30:529–561.
- Nordgren, R. (1972). Propagation of vertical hydraulic fractures. *J. Pet. Tech.*, 253:306–314. (SPE 3009).
- Perkins, T. and Kern, L. (1961). Widths of hydraulic fractures. *J. Pet. Tech., Trans. AIME*, 222:937–949.
- Polyanin, A. D. and Manzhirov, A. V. (2008). *Handbook of integral equations*. Boca Raton : Chapman & Hall/CRC.
- Rice, J. (1968). Mathematical analysis in the mechanics of fracture. In Liebowitz, H., editor, *Fracture, an Advanced Treatise*, volume II, chapter 3, pages 191–311. Academic Press, New York NY.
- Savitski, A. and Detournay, E. (2002). Propagation of a fluid-driven penny-shaped fracture in an impermeable rock: Asymptotic solutions. *Int. J. Solids Structures*, 39(26):6311–6337.
- Sneddon, I. (1951). *Fourier Transforms*. McGraw-Hill, New York NY.
- Sneddon, I. and Lowengrub, M. (1969). *Crack Problems in the Classical Theory of Elasticity*. John Wiley & Sons, New York NY.
- Spence, D. A. and Sharp, P. W. (1985). Self-similar solution for elastohydrodynamic cavity flow. *Proc. Roy. Soc. London, Ser. A*, 400:289–313.
- Thakur, G., Cobb, B., Satter, A., Stiles, L., Wiggins, M., and Willhite, P. (2003). *Water-flooding*. SPE reprint series; no. 56. Richardson TX: Society of Petroleum Engineers.

## Appendix A

### Semi-infinite fracture

#### A.1 Approach of Entov et al. (2007)

Here we would like to make clear distinguish between our model and the one developed by Entov et al. (2007), who have examined the tip behavior of a fluid-driven fracture propagating in a high-permeability rock. In their approach a finite fracture was divided into two parts: the tip region and the channel. The tip region was modeled by a finite fracture propagating through a permeable medium. The analysis of the tip region was based on the assumptions: i) the cavity is fully filled with the pore fluid, ii) the tip region is stationary, i.e., the size of the tip region, the tip velocity, and the fluid lag length are constant, iii) both the infiltration of the fracturing fluid and reinjection of the pore fluid from the cavity region into the porous medium lead to a low permeability cake build up on the fracture walls, iv) all fluids have the same viscosity, v) the walls of the channel are impermeable, vi) the fluid pressure in the channel is uniform and small compared to the fluid pressure in the tip, and vii) the fluid pressure in the channel and the length of the tip region are input parameters.



The third assumption leads to the following cake build-up equation [cf. (3.12)]

$$p_{\text{in}} - p_{\text{out}}|_{z=0} = \frac{1 + \text{sign}(g)}{2} \frac{\beta v}{\kappa_c} g. \quad (\text{A.1})$$

The fifth assumption yields the following pore pressure field [cf. (3.10)]

$$p_{\text{out}} - p_0 = \int_0^{L_{\text{tip}}} g(s) p^{(V)}(x-s) ds, \quad (\text{A.2})$$

where  $L_{\text{tip}}$  is the length of the tip region.

To derive the elasticity equation used by Entov et al. (2007) we first write the elasticity equation for a finite plane strain fracture of length  $2\ell$  and then use the sixth assumption. Thus, we have the following chain of transformations

$$\begin{aligned} w(X) &= \frac{4}{\pi E'} \int_0^\ell B(X, s) [p_{\text{in}}(s) - \sigma_0] ds, \\ w(X) &= \frac{4}{\pi E'} \int_{\ell-L_{\text{tip}}}^\ell B(X, s) [p_{\text{in}}(s) - p_{\text{ch}} - \sigma_0] ds + \frac{4}{\pi E'} \int_0^\ell B(X, s) (p_{\text{ch}} - \sigma_0) ds, \end{aligned} \quad (\text{A.3})$$

where  $X$  is the axis which originates at the fracture center and runs along the fracture,  $p_{\text{ch}}$  is the fluid pressure in the channel which is uniform,  $B(X, s)$  is the elasticity kernel given by

$$B(X, s) = \ln \left| \frac{\sqrt{\ell^2 - X^2} + \sqrt{\ell^2 - s^2}}{\sqrt{\ell^2 - X^2} - \sqrt{\ell^2 - s^2}} \right|.$$

The last step consist of the evaluation of the second integral in (A.3), the evaluation of the limits  $X, s \rightarrow \ell$ ,  $p_{\text{in}} \gg p_{\text{ch}}$  in the first integral, and the change of coordinate  $x = X - \ell$

$$w(x) = \frac{4}{\pi E'} \int_0^{L_{\text{tip}}} \ln \left| \frac{x^{1/2} + s^{1/2}}{x^{1/2} - s^{1/2}} \right| [p_{\text{in}}(s) - \sigma_0] ds + C_\infty \sqrt{x}, \quad (\text{A.4})$$

where

$$C_\infty = 2^{5/2} \ell^{1/2} \frac{p_{\text{ch}} - \sigma_0}{E'}.$$

However, Entov et al. (2007) did not use the last expression. Instead,  $C_\infty$  was one more input parameter.

Finally Entov et al. (2007) arrive to the following set of equations: (3.2), (3.3), (3.4), (3.9), (A.1), (A.2), and (A.4). Then the authors perform one more change of variable  $u \sim x^{1/2}$  and solve the resultant set of equations numerically using an uniform discretization mesh. We would like to stress here that the set of governing equation derived by Entov et al. (2007) does not contain a propagation criterion.

## A.2 Uniform pressure

Here we show that

$$\Pi_d(\xi) = \frac{A_{\Upsilon}^{const} \theta}{4\pi} \int_0^\infty \bar{\xi}^{-1/2} e^{\xi - \bar{\xi}} K_0(|\xi - \bar{\xi}|) d\bar{\xi} = \frac{\pi^{1/2}}{2^{5/2}} A_{\Upsilon}^{const} \theta = const. \quad (A.5)$$

To do this we use the following representation of the Bessel function (Cleary, 1978)

$$K_0(z) = \int_1^\infty \frac{\exp(-zt)}{\sqrt{t^2 - 1}} dt. \quad (A.6)$$

Substitution of this representation into (A.5) yields

$$\Pi_d(\xi) \sim \int_1^\infty \frac{dt}{\sqrt{t^2 - 1}} \left[ \int_0^\xi \bar{\xi}^{-1/2} e^{(\bar{\xi} - \xi)(t-1)} d\bar{\xi} + \int_\xi^\infty \bar{\xi}^{-1/2} e^{-(\bar{\xi} - \xi)(t+1)} d\bar{\xi} \right], \quad (A.7)$$

$$\frac{d\Pi_d}{d\xi} \sim \int_1^\infty \left[ -\sqrt{\frac{t-1}{t+1}} \int_0^\xi \bar{\xi}^{-1/2} e^{(\bar{\xi} - \xi)(t-1)} d\bar{\xi} + \sqrt{\frac{t+1}{t-1}} \int_\xi^\infty \bar{\xi}^{-1/2} e^{-(\bar{\xi} - \xi)(t+1)} d\bar{\xi} \right] dt, \quad (A.8)$$

$$\frac{d\Pi_d}{d\xi} \sim \int_1^\infty \left\{ -\frac{e^{-\xi(t-1)} \operatorname{erfi} \left[ \sqrt{\xi(t-1)} \right]}{\sqrt{t+1}} + \frac{e^{\xi(t+1)} \operatorname{erfc} \left[ \sqrt{\xi(t+1)} \right]}{\sqrt{t-1}} \right\} dt, \quad (A.9)$$

where  $\operatorname{erfc}(z) = 1 - \operatorname{erf}(z)$  and  $\operatorname{erfi}(z) = \operatorname{erf}(iz)/i$ ,  $\operatorname{erf}(z)$  are the error functions.

Integration by parts of the first term yields

$$\int_1^\infty \frac{e^{-\xi(t-1)} \operatorname{erfi} \left[ \sqrt{\xi(t-1)} \right]}{\sqrt{t+1}} dt = \pi^{1/2} \frac{e^{2\xi}}{\sqrt{\xi}} \operatorname{erf} \left[ \sqrt{\xi(t+1)} \right] \operatorname{erfi} \left[ \sqrt{\xi(t-1)} \right] \Big|_{t=1}^\infty -$$

$$- \int_1^\infty \frac{e^{\xi(t+1)} \operatorname{erf} \left[ \sqrt{\xi(t+1)} \right]}{\sqrt{t-1}} dt. \quad (\text{A.10})$$

Substitution of this equation into (A.9) followed by the evaluation of the integral in the left-hand side of the resultant equation leads to

$$\frac{d\Pi_d}{d\xi} \sim \operatorname{erfc} \left[ \sqrt{\xi(t+1)} \right] \operatorname{erfi} \left[ \sqrt{\xi(t-1)} \right] \Big|_{t=1}^\infty. \quad (\text{A.11})$$

Simple investigation shows that  $\operatorname{erfc}(z) \operatorname{erfi}(z) \rightarrow \pi^{-1} z^{-2}$  as  $z \rightarrow \infty$ , thus  $d\Pi_d/d\xi = 0$ . Therefore, we have that  $\Pi_d$  is uniform. In order to find the exact value of it, one can simply evaluate the integral in (A.5) at  $\xi = 0$ .

### A.3 Far-field asymptote

Here we evaluate the diffusion part of the pressure  $\Pi_d$  [see (3.26)] in the case  $\Upsilon_\infty(\xi) = A_\Upsilon^\infty \xi^{a_\Upsilon}$ ,  $0 < a_\Upsilon < 1$ , and  $\xi \rightarrow \infty$

$$\Pi_d(\xi) = \frac{\theta}{2\pi} A_\Upsilon^\infty a_\Upsilon \int_0^\infty \bar{\xi}^{a_\Upsilon-1} e^{\xi-\bar{\xi}} K_0(|\xi-\bar{\xi}|) d\bar{\xi}. \quad (\text{A.12})$$

Let us rewrite this equation in the following form

$$\frac{2\Pi_d}{\theta A_\Upsilon^\infty a_\Upsilon} \equiv I = I_1 + I_2, \quad (\text{A.13})$$

where

$$I_1 = \frac{1}{\pi} \int_0^\xi \bar{\xi}^{a_\Upsilon-1} e^{\xi-\bar{\xi}} K_0(|\xi-\bar{\xi}|) d\bar{\xi}, \quad (\text{A.14})$$

$$I_2 = \frac{1}{\pi} \int_\xi^\infty \bar{\xi}^{a_\Upsilon-1} e^{\xi-\bar{\xi}} K_0(|\xi-\bar{\xi}|) d\bar{\xi}. \quad (\text{A.15})$$

Assuming that the far-field asymptote,  $\sqrt{\pi/(2x)}$ , of the diffusion kernel,  $e^x K_0(|x|)$ , is accurate enough for  $x > \Delta$  ( $\Delta \sim 1$  for the accuracy within 10%, and  $\Delta \sim 10$  for the accuracy within 1%) we can split  $I_1$  into  $I_{11}$  and  $I_{12}$  given by

$$I_{11} = \frac{1}{\pi} \int_0^{\xi-\Delta} \bar{\xi}^{a_\Upsilon-1} e^{\xi-\bar{\xi}} K_0(|\xi-\bar{\xi}|) d\bar{\xi}, \quad (\text{A.16})$$

$$I_{12} = \frac{1}{\pi} \int_{\xi-\Delta}^{\xi} \bar{\xi}^{a_{\Upsilon}-1} e^{\xi-\bar{\xi}} K_0(|\xi-\bar{\xi}|) d\bar{\xi}. \quad (\text{A.17})$$

The first integral  $I_{11}$  can be evaluated using the far-field asymptote of the kernel

$$I_{11} = \frac{1}{\sqrt{2\pi}} \int_0^{\xi-\Delta} \frac{\bar{\xi}^{a_{\Upsilon}-1} d\bar{\xi}}{\sqrt{\xi-\bar{\xi}}} = -\sqrt{\frac{2}{\pi}} \xi^{a_{\Upsilon}-1} \sqrt{\xi-\bar{\xi}} {}_2F_1\left(\frac{1}{2}, 1-a_{\Upsilon}; \frac{3}{2}; 1-\frac{\bar{\xi}}{\xi}\right) \Big|_{\bar{\xi}=0}^{\xi-\Delta},$$

$$I_{11} = \frac{\xi^{a_{\Upsilon}-1/2}}{\sqrt{2}} \frac{\Gamma(a_{\Upsilon})}{\Gamma(a_{\Upsilon}+1/2)} \left[1 + \mathcal{O}\left(\sqrt{\frac{\Delta}{\xi}}\right)\right], \quad (\text{A.18})$$

where  ${}_2F_1(a, b; c; x)$  is the hypergeometric function and  $\Gamma(x)$  is the Euler gamma function (Abramowitz and Stegun, 1972). We assume here that  $\Delta \ll \xi$ .

To estimate  $I_{12}$  we use the fact that  $\sqrt{\pi/(2x)} > e^x K_0(|x|)$

$$I_{12} < \frac{1}{\sqrt{2\pi}} \int_{\xi-\Delta}^{\xi} \frac{\bar{\xi}^{a_{\Upsilon}-1} d\bar{\xi}}{\sqrt{\xi-\bar{\xi}}} < \frac{(\xi-\Delta)^{a_{\Upsilon}-1}}{\sqrt{2\pi}} \int_{\xi-\Delta}^{\xi} \frac{d\bar{\xi}}{\sqrt{\xi-\bar{\xi}}} = \sqrt{\frac{2\Delta}{\pi}} (\xi-\Delta)^{a_{\Upsilon}-1},$$

$$I_{12} < \xi^{a_{\Upsilon}-1/2} \mathcal{O}\left(\sqrt{\frac{\Delta}{\xi}}\right) = I_{11} \mathcal{O}\left(\sqrt{\frac{\Delta}{\xi}}\right). \quad (\text{A.19})$$

Similarly, one can estimate  $I_2$

$$I_2 < \frac{1}{\sqrt{2\pi}} \int_{\xi}^{\infty} \frac{\bar{\xi}^{a_{\Upsilon}-1} e^{2(\xi-\bar{\xi})}}{\sqrt{\bar{\xi}-\xi}} d\bar{\xi} < \frac{\xi^{a_{\Upsilon}-1}}{\sqrt{2\pi}} \int_{\xi}^{\infty} \frac{e^{2(\xi-\bar{\xi})} d\bar{\xi}}{\sqrt{\bar{\xi}-\xi}} =$$

$$= \frac{\xi^{a_{\Upsilon}-1}}{\sqrt{2\pi}} \left( \int_{\xi}^{\xi+1} + \int_{\xi+1}^{\infty} \right) \frac{e^{2(\xi-\bar{\xi})} d\bar{\xi}}{\sqrt{\bar{\xi}-\xi}} < \frac{\xi^{a_{\Upsilon}-1}}{\sqrt{2\pi}} \left( \int_{\xi}^{\xi+1} \frac{d\bar{\xi}}{\sqrt{\bar{\xi}-\xi}} + \int_{\xi+1}^{\infty} e^{2(\xi-\bar{\xi})} d\bar{\xi} \right) =$$

$$= \frac{\xi^{a_{\Upsilon}-1}}{\sqrt{2\pi}} \left( 2 + \frac{1}{2e} \right),$$

$$I_2 < \xi^{a_{\Upsilon}-1/2} \mathcal{O}\left(\xi^{-1/2}\right) = I_{11} \mathcal{O}\left(\xi^{-1/2}\right). \quad (\text{A.20})$$

Compilation of (A.13), (A.18), (A.19), and (A.20) yields

$$\Pi_d = \frac{\xi^{a_{\Upsilon}-1/2}}{2^{3/2}} \frac{\Gamma(a_{\Upsilon})}{\Gamma(a_{\Upsilon}+1/2)} \theta A_{\Upsilon}^{\infty} \xi^{a_{\Upsilon}} \left[1 + \mathcal{O}\left(\sqrt{\frac{\Delta}{\xi}}\right)\right], \quad (\text{A.21})$$

where we have assumed that  $\Delta > 1$ .

## A.4 Numerical scheme

Inspired by Garagash and Detournay (2000), we introduce a so-called interpolation mesh  $\xi_i$ ,  $i = 0, 1, \dots, n$ , such that for  $\xi \leq \xi_0$  the solution has the shape of the near-field asymptote, and for  $\xi \geq \xi_n$  the solution has the shape of the far-field asymptote, i.e.,  $\Pi(\xi \leq \xi_0) = \text{const}$ ,  $\Pi(\xi \leq \xi_0) + \Sigma(\xi \leq \xi_0) = \text{const}$ ,  $\Sigma(\xi \leq \xi_0) = \text{const}$ ,  $\Upsilon(\xi \leq \xi_0) \sim \xi^{1/2}$  and  $\Pi(\xi \geq \xi_n) \sim \xi^{-1/3}$ ,  $\Pi(\xi \geq \xi_n) + \Sigma(\xi \geq \xi_n) \sim \xi^{-1/3}$ ,  $\Sigma(\xi \geq \xi_n) \sim \xi^{-5/6}$ ,  $\Upsilon(\xi \geq \xi_n) \sim \xi^{1/2}$ . Also, we introduce two adjacent meshes  $\xi_i^{(0)}$ ,  $i = 0, 1, \dots, n^{(0)}$ , and  $\xi_i^{(\infty)}$ ,  $i = 0, 1, \dots, n^{(\infty)}$ , such that,  $\xi_0^{(0)} = 0$ ,  $\xi_{n^{(0)}}^{(0)} = \xi_0$ , and  $\xi_0^{(\infty)} = \xi_n$ . During the simulations we also use  $\xi_{n^{(\infty)}}^{(\infty)} \approx 2\xi_n$ . The general philosophy of this scheme is the following: the fluid pressure  $\Pi$ , the backstress  $\Sigma$ , and the fluid displacement function  $\Upsilon$  are discretized on the interpolation mesh. Then, by means of using the shapes of the near- and far-field asymptotes, these parameters are extrapolated onto the adjacent meshes. At the same time, all governing equations are discretized on the joint mesh (the two adjacent meshes and the interpolation mesh). The resultant set of algebraic equations, which has more equations than unknowns, is solved using the least-squares minimization.

### A.4.1 Elasticity equation

Following Garagash and Detournay (2000) we use the following inversion of the elasticity equation (3.25)

$$\Omega = k\xi^{1/2} + \frac{4}{\pi} \int_0^\infty K(\xi, \bar{\xi}) [\Pi(\bar{\xi}) + \Sigma(\bar{\xi})] d\bar{\xi}, \quad (\text{A.22})$$

where

$$K(\xi, \bar{\xi}) = \ln \left| \frac{\xi^{1/2} + \bar{\xi}^{1/2}}{\xi^{1/2} - \bar{\xi}^{1/2}} \right| - 2 \left( \frac{\xi}{\bar{\xi}} \right)^{1/2}.$$

The fluid pressure and the backstress distributions are approximated by

$$\Pi(\xi) + \Sigma(\xi) = \begin{cases} \Pi_0 + \Sigma_0, & \xi \leq \xi_0 \\ a_i + b_i \xi^{-1/3}, & \xi \in [\xi_i, \xi_{i+1}] \\ b_\infty \xi^{-1/3}, & \xi \geq \xi_n \end{cases}, \quad (\text{A.23})$$

where

$$a_i = \frac{(\Pi_i + \Sigma_i) \xi_{i+1}^{-1/3} - (\Pi_{i+1} + \Sigma_{i+1}) \xi_i^{-1/3}}{\xi_{i+1}^{-1/3} - \xi_i^{-1/3}}, \quad b_i = \frac{\Pi_{i+1} + \Sigma_{i+1} - \Pi_i - \Sigma_i}{\xi_{i+1}^{-1/3} - \xi_i^{-1/3}},$$

$$b_\infty = \frac{\Pi_n + \Sigma_n}{\xi_n^{-1/3}}, \quad \Pi_i + \Sigma_i \equiv \Pi(\xi_i) + \Sigma(\xi_i).$$

Substitution of (A.23) into (A.22) yields the following discretization of the elasticity equation

$$\begin{aligned} \Omega(\xi) = & k\xi^{1/2} + \frac{4}{\pi} (\Pi_0 + \Sigma_0) F_a(\xi, \bar{\xi}) \Big|_{\bar{\xi}=0}^{\xi_0} + \frac{4}{\pi} b_\infty F_b(\xi, \bar{\xi}) \Big|_{\bar{\xi}=\xi_n}^{\infty} + \\ & + \frac{4}{\pi} \sum_{i=0}^{i=n-1} [a_i F_a(\xi, \bar{\xi}) + b_i F_b(\xi, \bar{\xi})] \Big|_{\bar{\xi}=\xi_i}^{\xi_{i+1}}, \end{aligned} \quad (\text{A.24})$$

where the functions  $F_a(\xi, \bar{\xi})$  and  $F_b(\xi, \bar{\xi})$  are defined by

$$F_a(\xi, \bar{\xi}) = \int_0^{\bar{\xi}} K(\xi, \zeta) d\zeta, \quad F_b(\xi, \bar{\xi}) = \int_0^{\bar{\xi}} \zeta^{-1/3} K(\xi, \zeta) d\zeta.$$

Substitution of the elasticity kernel  $K(\xi, \bar{\xi})$  into these definitions leads to

$$\begin{aligned} F_a(\xi, \bar{\xi}) = & -\xi \left[ 2\zeta + (1 - \zeta^2) \ln \left| \frac{1 + \zeta}{1 - \zeta} \right| \right], \quad \zeta = \sqrt{\frac{\bar{\xi}}{\xi}}, \\ F_b(\xi, \bar{\xi}) = & -\frac{3}{4} \xi^{2/3} \left[ 4\zeta + 2\sqrt{3} \arctan \left( \frac{1 + 2\zeta}{\sqrt{3}} \right) - 2\sqrt{3} \arctan \left( \frac{1 - 2\zeta}{\sqrt{3}} \right) + \right. \\ & \left. + \ln \left[ \frac{1 - \zeta^3}{1 + \zeta^3} \left( \frac{1 + \zeta}{1 - \zeta} \right)^3 \right] - 2\zeta^4 \ln \left| \frac{1 + \zeta^3}{1 - \zeta^3} \right| \right], \quad \zeta = \left( \frac{\bar{\xi}}{\xi} \right)^{1/6}. \end{aligned}$$

### A.4.2 Leak-off equation

Integration of the leak-off equation (3.26) over  $\xi$  leads to

$$\int_0^\zeta \Pi(\xi) d\xi + \zeta = \frac{\chi\theta}{2} \frac{1 + \text{sign}(\Upsilon)}{2} \Upsilon^2 + \frac{\theta}{2\pi} \int_0^\infty \Upsilon(\bar{\xi}) e^{\xi - \bar{\xi}} K_0(|\xi - \bar{\xi}|) d\bar{\xi} \Big|_{\xi=0}^\zeta. \quad (\text{A.25})$$

During the numerical simulations we evaluate this equation only at the midpoints of our joint mesh, i.e., at  $\xi_{i+1/2}^{(0)}$ ,  $\xi_{i+1/2}$ , and  $\xi_{i+1/2}^{(\infty)}$ .

To calculate the first term in the left-hand side of (A.25) we use similar to (A.23) representation of the fluid pressure

$$\Pi(\xi) = \begin{cases} \Pi_0, & \xi \leq \xi_0 \\ a_i + b_i \xi^{-1/3}, & \xi \in [\xi_i, \xi_{i+1}] \\ b_\infty \xi^{-1/3}, & \xi \geq \xi_n \end{cases}, \quad (\text{A.26})$$

where

$$a_i = \frac{\Pi_i \xi_{i+1}^{-1/3} - \Pi_{i+1} \xi_i^{-1/3}}{\xi_{i+1}^{-1/3} - \xi_i^{-1/3}}, \quad b_i = \frac{\Pi_{i+1} - \Pi_i}{\xi_{i+1}^{-1/3} - \xi_i^{-1/3}}, \quad b_\infty = \frac{\Pi_n}{\xi_n^{-1/3}}.$$

To compute the integral in the right-hand side of (A.25), we approximate the fluid leak-off function by

$$\Upsilon(\xi) = v_0 \xi^{1/2} + \Upsilon^{(r)}(\xi), \quad (\text{A.27})$$

where

$$\Upsilon^{(r)}(\xi) = \begin{cases} 0, & \xi \leq \xi_0 \\ \Upsilon_{i+1/2}^{(r)}, & \xi \in [\xi_i, \xi_{i+1}] \\ (v_\infty - v_0) \xi^{1/2}, & \xi \geq \xi_n \end{cases},$$

and  $\Upsilon_{i+1/2}^{(r)} \equiv \Upsilon(\xi_{i+1/2}) - v_0 \xi_{i+1/2}^{1/2}$ . Substitution of this expansion into the integral yields

$$\begin{aligned} \int_0^\infty \Upsilon(\bar{\xi}) e^{\xi - \bar{\xi}} K_0(|\xi - \bar{\xi}|) d\bar{\xi} \Big|_{\xi=0}^\zeta &= \left[ v_0 \int_0^\infty \bar{\xi}^{1/2} e^{\xi - \bar{\xi}} K_0(|\xi - \bar{\xi}|) d\bar{\xi} + \right. \\ &\left. + (v_\infty - v_0) \int_{\xi_n^{(\infty)}}^\infty \bar{\xi}^{1/2} e^{\xi - \bar{\xi}} K_0(|\xi - \bar{\xi}|) d\bar{\xi} + \int_{\xi_0}^{\xi_n^{(\infty)}} \Upsilon^{(r)}(\bar{\xi}) e^{\xi - \bar{\xi}} K_0(|\xi - \bar{\xi}|) d\bar{\xi} \right] \Big|_{\xi=0}^\zeta. \end{aligned}$$

The first term of the right-hand side is equal to

$$\int_0^\infty \bar{\xi}^{1/2} e^{\xi - \bar{\xi}} K_0(|\xi - \bar{\xi}|) d\bar{\xi} = \left(\frac{\pi}{2}\right)^{3/2} \left(\xi + \frac{1}{4}\right);$$

the second term is of order of  $e^{-2\xi_n^{(\infty)}} \ll 1$ , thus it can be dismissed; and the third term can be calculated using

$$\begin{aligned} \int_{\xi_i}^{\xi_{i+1}} \Upsilon^{(r)}(\bar{\xi}) e^{\xi - \bar{\xi}} K_0(|\xi - \bar{\xi}|) d\bar{\xi} &\approx \Upsilon^{(r)}(\xi_{i+1/2}) \int_{\xi_i}^{\xi_{i+1}} e^{\xi - \bar{\xi}} K_0(|\xi - \bar{\xi}|) d\bar{\xi}, \\ \int_{\xi_i}^{\xi_{i+1}} e^{\xi - \bar{\xi}} K_0(|\xi - \bar{\xi}|) d\bar{\xi} &= e^{\xi} [\xi K_0(|\xi|) + |\xi| K_1(|\xi|)]. \end{aligned}$$

The last two formulae are used to perform the integration over  $\xi_i$  and  $\xi_i^{(\infty)}$  meshes.

#### A.4.3 Backstress equation

Here we follow the procedure as we did for the leak-off equation. Thus, the integration of the backstress equation (3.27) leads to

$$\int_0^\zeta \Sigma(\xi) d\xi = \frac{\eta\theta}{2\pi} \int_0^\infty \Upsilon(\bar{\xi}) \frac{\partial}{\partial \bar{\xi}} \left[ \ln(|\xi - \bar{\xi}|) + e^{\xi - \bar{\xi}} K_0(|\xi - \bar{\xi}|) \right] d\bar{\xi} \Big|_{\xi=0}^\zeta. \quad (\text{A.28})$$

We evaluate this equation numerically only at  $\xi_{i+1/2}^{(0)}$ ,  $\xi_{i+1/2}$ , and  $\xi_{i+1/2}^{(\infty)}$ .

To calculate the left-hand side of (A.28) we approximate the backstress by

$$\Sigma(\xi) = \begin{cases} \Sigma_0, & \xi \leq \xi_0 \\ a_i + b_i \xi^{-5/6}, & \xi \in [\xi_i, \xi_{i+1}] \\ b_\infty \xi^{-5/6}, & \xi \geq \xi_n \end{cases}, \quad (\text{A.29})$$

where

$$a_i = \frac{\Sigma_i \xi_{i+1}^{-5/6} - \Sigma_{i+1} \xi_i^{-5/6}}{\xi_{i+1}^{-5/6} - \xi_i^{-5/6}}, \quad b_i = \frac{\Sigma_{i+1} - \Sigma_i}{\xi_{i+1}^{-5/6} - \xi_i^{-5/6}}, \quad b_\infty = \frac{\Sigma_n}{\xi_n^{-5/3}}.$$

To calculate the right-hand side of (A.28) we use (A.27) to approximate the fluid displacement function  $\Upsilon$ . Substitution of this approximation into the backstress equation



yields

$$\begin{aligned} \int_0^\infty \Upsilon(\bar{\xi}) \frac{\partial}{\partial \bar{\xi}} \left[ \ln(|\xi - \bar{\xi}|) + e^{\xi - \bar{\xi}} K_0(|\xi - \bar{\xi}|) \right] d\bar{\xi} \Big|_{\xi=0}^\zeta &= \left[ (v_\infty - v_0) \int_{\xi_n^{(\infty)}}^\infty \frac{\bar{\xi}^{1/2} d\bar{\xi}}{\bar{\xi} - \xi} + \right. \\ &\quad \left. + \int_{\xi_0}^{\xi_n^{(\infty)}} \Upsilon^{(r)}(\bar{\xi}) \frac{\partial}{\partial \bar{\xi}} \left[ \ln(|\xi - \bar{\xi}|) + e^{\xi - \bar{\xi}} K_0(|\xi - \bar{\xi}|) \right] d\bar{\xi} \right]_{\xi=0}^\zeta, \end{aligned} \quad (\text{A.30})$$

where we have used the fact that a square root fluid displacement function does not generate any backstress (see Subsection 3.5.1.2). Also, in the first term of the right-hand side, we have neglected the Bessel function term which is of order of  $e^{-2\xi_n^{(\infty)}} \ll 1$ .

To evaluate the right-hand side of (A.30) we use the following formulae

$$\begin{aligned} \int_{\xi_n^{(\infty)}}^\infty \frac{\bar{\xi}^{1/2} d\bar{\xi}}{\bar{\xi} - \xi} \Big|_{\xi=0}^\zeta &= -\sqrt{\zeta} \ln \left| \frac{\sqrt{\xi_n^{(\infty)}} - \sqrt{\zeta}}{\sqrt{\xi_n^{(\infty)}} + \sqrt{\zeta}} \right|, \\ \int_{\xi_i}^{\xi_{i+1}} \Upsilon^{(r)}(\bar{\xi}) \frac{\partial}{\partial \bar{\xi}} \left[ \ln(|\xi - \bar{\xi}|) + e^{\xi - \bar{\xi}} K_0(|\xi - \bar{\xi}|) \right] d\bar{\xi} &\approx \\ \approx \Upsilon^{(r)}(\xi_{i+1/2}) \left[ \ln(|\xi - \bar{\xi}|) + e^{\xi - \bar{\xi}} K_0(|\xi - \bar{\xi}|) \right] \Big|_{\bar{\xi}=\xi_i}^{\xi_{i+1}}. \end{aligned}$$

#### A.4.4 Lubrication equation

The lubrication equation (3.23) is discretized in a standard way [cf. Garagash and Detournay (2000)]

$$\Omega_{i+1/2} + \Upsilon_{i+1/2} = \frac{1}{m\mathcal{M}} \Omega_{i+1/2}^3 \frac{\Pi_{i+1} - \Pi_i}{\xi_{i+1} - \xi_i}, \quad m = \begin{cases} \mu_{out}/\mu_{in}, & \Upsilon_{i+1/2} < 0 \\ 1, & \Upsilon_{i+1/2} > 0 \end{cases}. \quad (\text{A.31})$$

#### A.4.5 Closing remarks

After the discretization we get a set of nonlinear algebraic equations

$$\mathcal{F}(\Pi_0, \Pi_1, \dots, \Pi_n; v_0, \Upsilon_{1/2}, \Upsilon_{3/2}, \dots, \Upsilon_{n-1/2}, v_\infty) = 0.$$

Note that there are more equations than unknowns.

To solve this set of equations we use a Newton-method-like linearization of the equations around the input guess. The resultant set of linear equations is then solved using the least-squares minimization. The main difference between the numerical scheme presented here and the one which was developed by Garagash and Detournay (2000) is that the former scheme “knows” only the shapes of the asymptotic solutions, whereas the latter scheme uses the exact asymptotes. In this respect, our scheme is more flexible and, as a result, more stable.

The algorithm was implemented in *Mathematica 6.0*. We used a logarithmic interpolation mesh and homogeneous adjacent meshes.

## Appendix B

# Auxiliary problem

### B.1 Small-time and tip asymptotes

Here we give the details of the derivation of (4.19), (4.20), (4.31), and (4.32).

Substitution of the singular solutions (4.10) and (4.12) into (4.9) and (4.11) yields

$$\begin{aligned} \Pi = & \frac{1}{\sqrt{\pi}} \int_0^\tau \frac{d\bar{\tau}}{(\tau - \bar{\tau})^{5/2}} \int_0^1 \bar{\xi} \psi(\bar{\xi}, \bar{\tau}) \exp\left(-\frac{\xi^2 + \bar{\xi}^2}{\tau - \bar{\tau}}\right) \times \\ & \times \left\{ \frac{2}{\tau - \bar{\tau}} \left[ (\xi^2 + \bar{\xi}^2) I_0\left(\frac{2\xi\bar{\xi}}{\tau - \bar{\tau}}\right) - 2\xi\bar{\xi} I_1\left(\frac{2\xi\bar{\xi}}{\tau - \bar{\tau}}\right) \right] - 3I_0\left(\frac{2\xi\bar{\xi}}{\tau - \bar{\tau}}\right) \right\} d\bar{\xi}, \end{aligned} \quad (\text{B.1})$$

$$\begin{aligned} \Xi = & \frac{2}{\pi} \int_0^1 \bar{\xi} \psi(\bar{\xi}, \tau) \frac{E\left[\frac{4\xi\bar{\xi}}{(\xi + \bar{\xi})^2}\right]}{(\xi - \bar{\xi})^2 (\xi + \bar{\xi})} d\bar{\xi} + \\ & + \frac{4}{\sqrt{\pi}} \int_0^\tau \frac{d\bar{\tau}}{(\tau - \bar{\tau})^{5/2}} \int_0^1 \bar{\xi} \psi(\bar{\xi}, \bar{\tau}) \exp\left(-\frac{\xi^2 + \bar{\xi}^2}{\tau - \bar{\tau}}\right) \times \\ & \times \left\{ I_0\left(\frac{2\xi\bar{\xi}}{\tau - \bar{\tau}}\right) - \frac{1}{\tau - \bar{\tau}} \left[ (\xi^2 + \bar{\xi}^2) I_0\left(\frac{2\xi\bar{\xi}}{\tau - \bar{\tau}}\right) - 2\xi\bar{\xi} I_1\left(\frac{2\xi\bar{\xi}}{\tau - \bar{\tau}}\right) \right] \right\} d\bar{\xi}, \end{aligned} \quad (\text{B.2})$$

where  $E(x)$  is the complete elliptic integral of the second kind and  $I_\nu(x)$  is the modified Bessel function of the first kind (Abramowitz and Stegun, 1972). The Bessel function

has the following large argument asymptote

$$I_\nu(x) \simeq \frac{\exp(x)}{\sqrt{2\pi x}} \left(1 + \frac{1 - 4\nu^2}{8x}\right). \quad (\text{B.3})$$

In the case of small times the argument of the Bessel functions in (B.1), (B.2) is large.

Therefore we can write

$$\begin{aligned} \Pi_0 = & \frac{1}{2\pi} \int_0^\tau \frac{d\bar{\tau}}{(\tau - \bar{\tau})^2} \int_0^1 \sqrt{\frac{\bar{\xi}}{\xi}} \psi_0(\bar{\xi}, \bar{\tau}) \exp\left[-\frac{(\xi - \bar{\xi})^2}{\tau - \bar{\tau}}\right] \times \\ & \times \left[2\frac{(\xi - \bar{\xi})^2}{\tau - \bar{\tau}} + \frac{\xi^2 + \bar{\xi}^2 - 18\xi\bar{\xi}}{8\xi\bar{\xi}}\right] d\bar{\xi}, \end{aligned} \quad (\text{B.4})$$

$$\begin{aligned} \Xi_0 = & \frac{2}{\pi} \int_0^1 \bar{\xi} \psi(\bar{\xi}, \tau) \frac{E\left[\frac{4\xi\bar{\xi}}{(\xi + \bar{\xi})^2}\right]}{(\xi - \bar{\xi})^2(\xi + \bar{\xi})} d\bar{\xi} + \\ & + \frac{2}{\pi} \int_0^\tau \frac{d\bar{\tau}}{(\tau - \bar{\tau})^2} \int_0^1 \sqrt{\frac{\bar{\xi}}{\xi}} \psi_0(\bar{\xi}, \bar{\tau}) \exp\left[-\frac{(\xi - \bar{\xi})^2}{\tau - \bar{\tau}}\right] \left[\frac{10\xi\bar{\xi} - \xi^2 - \bar{\xi}^2}{16\xi\bar{\xi}} - \frac{(\xi - \bar{\xi})^2}{\tau - \bar{\tau}}\right] d\bar{\xi}. \end{aligned} \quad (\text{B.5})$$

The exponents in the above equations are non-vanishing only in a very narrow neighborhood  $\bar{\xi} \simeq \xi$ , therefore we can move the integration limits to infinity. Evaluation of the integrals in (B.4) and (B.5) leads to (4.31) and (4.32).

To obtain the tip region equations (4.19) and (4.20), we eliminate the curvature effect in (B.4) and (B.5), assuming  $\bar{\xi} \simeq \xi \simeq 1$  everywhere except in the terms that include  $\xi - \bar{\xi}$ . From here we apply the Laplace transform.

## B.2 Numerical solution of the tip region problem (4.19),

$$(4.21)$$

The numerical algorithm is similar to the one we used in Chapter 3 (see Appendix A.4).

Similarly, we introduce an interpolation mesh  $\zeta_i$ ,  $i = 0, 1, \dots, N$ , such that  $\phi(\zeta < \zeta_0) \sim$

$\zeta^{-1/2}$  (the shape of the near-field asymptote) and  $\phi(\zeta > \zeta_N) = \text{const}$  (the shape of the far-field asymptote). Then we approximate the flux distribution function  $\phi$  by

$$\phi(\zeta_i \leq \zeta \leq \zeta_{i+1}) \simeq \hat{\phi}_i(\zeta) \equiv \frac{a_i}{\sqrt{\zeta}} + b_i, \quad (\text{B.6})$$

where  $a_i$  and  $b_i$  are unknown constants which can be related to the values of the flux distribution function in the nodes of the interpolation mesh  $\phi_i \equiv \phi(\zeta_i)$

$$a_i = \frac{\phi_{i+1} - \phi_i}{\zeta_{i+1}^{-1/2} - \zeta_i^{-1/2}}, \quad b_i = \frac{\phi_{i+1}\zeta_{i+1}^{1/2} - \phi_i\zeta_i^{1/2}}{\zeta_{i+1}^{1/2} - \zeta_i^{1/2}}. \quad (\text{B.7})$$

Substitution of the interpolation (B.6) into the governing equation (4.19) yields the following linear algebraic equation

$$\begin{aligned} \pi = & \phi_0 \sqrt{\zeta_0} \int_0^{\zeta_0} \frac{K_0(|\zeta - \bar{\zeta}|)}{\sqrt{\bar{\zeta}}} d\bar{\zeta} + \phi_N \int_{\zeta_i}^{\zeta_{i+1}} K_0(|\zeta - \bar{\zeta}|) d\bar{\zeta} + \\ & + \sum_{i=0}^{N-1} \left[ a_i \int_{\zeta_i}^{\zeta_{i+1}} \frac{K_0(|\zeta - \bar{\zeta}|)}{\sqrt{\bar{\zeta}}} d\bar{\zeta} + b_i \int_{\zeta_i}^{\zeta_{i+1}} K_0(|\zeta - \bar{\zeta}|) d\bar{\zeta} \right]. \end{aligned} \quad (\text{B.8})$$

Here the unknowns are the values of the flux distribution function in the nodes of the interpolation mesh  $\phi_i$ . This equation can be solved using a fitting procedure. Note that the only assumptions we make here are  $\phi(\zeta < \zeta_0) \sim \zeta^{-1/2}$  and  $\phi(\zeta > \zeta_N) = \text{const}$ , i.e., we assume only the general shapes of the asymptotes and do not force the numerical algorithm to follow any exact asymptotic solutions.

During this study we developed the following fitting procedure. First we enrich the interpolation mesh  $\zeta_i$  by i) an interval  $[0, \zeta_0)$  discretized with an uniform step equal to  $\zeta_1 - \zeta_0$ , and ii) an interval  $(\zeta_N, 2\zeta_N]$  discretized with an uniform step equal to  $\zeta_N - \zeta_{N-1}$ . We denote the resulting mesh by  $\check{\zeta}_i$ . Here we use a logarithmic interpolation mesh. For collocation we use the geometric mean  $\sqrt{\check{\zeta}_i \check{\zeta}_{i+1}}$ , and for fitting we use the least-squares minimization.

The algorithm was implemented in *Mathematica 6.0*. Although we used standard *Mathematica* functions to evaluate the integrals in (B.8), we treated all singularities analytically by means of an analytical series expansion and integration of the corresponding

expansions. The results shown in this paper were obtained using the following set of parameters:  $\zeta_0 = 10^{-8}$ ,  $\zeta_N = 20$ , and  $N = 100$ .

### B.3 Numerical algorithm for the transient solution

First we introduce a homogeneous spatial mesh  $\xi_i$ ,  $i = 0, 1, \dots, N$ , where  $\xi_0 = 0$  and  $\xi_N = 1$ . Then we approximate the flux distribution function  $\tilde{\psi}$  by

$$\tilde{\psi}(\xi_i \leq \xi \leq \xi_{i+1}) \simeq \hat{\psi}_i(\xi) \equiv \frac{a_i}{\sqrt{1-\xi^2}} + b_i, \quad (\text{B.9})$$

where  $a_i$  and  $b_i$  are unknown constants which can be related to the values of the flux distribution function in the nodes of the mesh  $\tilde{\psi}_i \equiv \tilde{\psi}(\xi_i)$

$$a_i = \frac{\tilde{\psi}_{i+1} - \tilde{\psi}_i}{(1 - \xi_{i+1}^2)^{-1/2} - (1 - \xi_i^2)^{-1/2}}, \quad b_i = \frac{\tilde{\psi}_{i+1}\sqrt{1 - \xi_{i+1}^2} - \tilde{\psi}_i\sqrt{1 - \xi_i^2}}{\sqrt{1 - \xi_{i+1}^2} - \sqrt{1 - \xi_i^2}}. \quad (\text{B.10})$$

In other words, we use a linear combination of the small- and large-time asymptotes to approximate the flux distribution function  $\tilde{\psi}$  at each interval  $[\xi_i, \xi_{i+1}]$ . To describe our flux distribution function  $\tilde{\psi}$  at the interval  $[\xi_{N-1}, \xi_N]$ , instead of  $\tilde{\psi}_N$ , which is equal to infinity, we use the singularity strength,  $\varrho_\psi \equiv \lim_{\xi \rightarrow 1} \tilde{\psi}(\xi) \sqrt{1 - \xi^2}$ . In other words instead of (B.10) we have

$$a_{N-1} = \varrho_\psi, \quad b_{N-1} = \tilde{\psi}_{N-1} - \frac{\varrho_\psi}{\sqrt{1 - \xi_{N-1}^2}}. \quad (\text{B.11})$$

Using the approximation (B.9) the problem (4.14), (4.15), (4.18) can be reduced to

$$1 = \frac{2}{\pi} \sum_{i=0}^{N-1} \int_{\xi_i}^{\xi_{i+1}} \bar{\xi} \left( \frac{a_i}{\sqrt{1 - \bar{\xi}^2}} + b_i \right) \int_0^\pi \frac{\exp \left[ -2s^{1/2} \sqrt{\xi^2 + \bar{\xi}^2 - 2\xi\bar{\xi} \cos(\varphi)} \right]}{\sqrt{\xi^2 + \bar{\xi}^2 - 2\xi\bar{\xi} \cos(\varphi)}} d\varphi d\bar{\xi}, \quad (\text{B.12})$$

where  $0 \leq \xi \leq 1$ . This equation represents the discretized analog of (4.14). Writing this equation for  $N$  different  $\xi$  and solving the resultant set of equations we can find

the unknowns  $\tilde{\psi}_i$ ,  $i \in [0, N - 1]$ , and  $\varrho_\psi$ . During this study we evaluated (B.12) at the midpoints of  $\xi_i$  and at  $\xi = 0$ . The only problem here is the computation of the integrals in the right-hand side of (B.12). Let us consider the following integral

$$I = \int_{\xi_1}^{\xi_2} \bar{\xi} f(\bar{\xi}) \int_0^\pi \frac{\exp \left[ -2s^{1/2} \sqrt{\xi^2 + \bar{\xi}^2 - 2\xi\bar{\xi} \cos(\varphi)} \right]}{\sqrt{\xi^2 + \bar{\xi}^2 - 2\xi\bar{\xi} \cos(\varphi)}} d\varphi d\bar{\xi}, \quad (\text{B.13})$$

where  $f(\xi)$  is a non-singular function, and  $0 < \xi_1 < \xi < \xi_2 < 1$ . The standard approach in calculating this integral is through the regularization procedure

$$I = I_r + I_s, \quad (\text{B.14})$$

where  $I_r(\xi)$  is the regular part of the integral

$$I_r = \int_{\xi_1}^{\xi_2} \bar{\xi} f(\bar{\xi}) \int_0^\pi \frac{\exp \left[ -2s^{1/2} \sqrt{\xi^2 + \bar{\xi}^2 - 2\xi\bar{\xi} \cos(\varphi)} \right] - 1}{\sqrt{\xi^2 + \bar{\xi}^2 - 2\xi\bar{\xi} \cos(\varphi)}} d\varphi d\bar{\xi}, \quad (\text{B.15})$$

and  $I_s(\xi)$  is the singular part, which can be simplified analytically

$$I_s = \int_{\xi_1}^{\xi_2} \int_0^\pi \frac{\bar{\xi} f(\bar{\xi}) d\varphi d\bar{\xi}}{\sqrt{\xi^2 + \bar{\xi}^2 - 2\xi\bar{\xi} \cos(\varphi)}} = 2 \int_{\xi_1}^{\xi_2} \frac{\bar{\xi} f(\bar{\xi})}{\xi + \bar{\xi}} K \left[ \frac{4\xi\bar{\xi}}{(\xi + \bar{\xi})^2} \right] d\bar{\xi}. \quad (\text{B.16})$$

The problem here is that when the Laplace transform parameter  $s$  is large,  $s \gg 1$ , the integral (B.13) is small compared to both integrals (B.15) and (B.16). As a result, the usage of the regularization (B.14) leads to a significant error. Indeed, the left-hand side of (B.14) contains a subtraction of two large numbers. To avoid this problem we divide the entire integration domain,  $\{\xi_1 < \xi < \xi_2, 0 < \varphi < \pi\}$ , into three regions (see Fig. B.1): i) the near-field domain  $\sqrt{\xi^2 + \bar{\xi}^2 - 2\xi\bar{\xi} \cos(\varphi)} < \rho_0$  where we can use the regularization technique (B.14); ii) the far-field domain  $\sqrt{\xi^2 + \bar{\xi}^2 - 2\xi\bar{\xi} \cos(\varphi)} > \rho_\infty \cap \xi_1 < \xi < \xi_2$  where the under integral function is vanishingly small, thus the integration over this domain is also vanishingly small; and iii) the transient region  $\rho_0 < \sqrt{\xi^2 + \bar{\xi}^2 - 2\xi\bar{\xi} \cos(\varphi)} < \rho_\infty$  where the integral is not singular anymore and can be calculated straightforwardly. From a numerical point of view the shapes of the near-

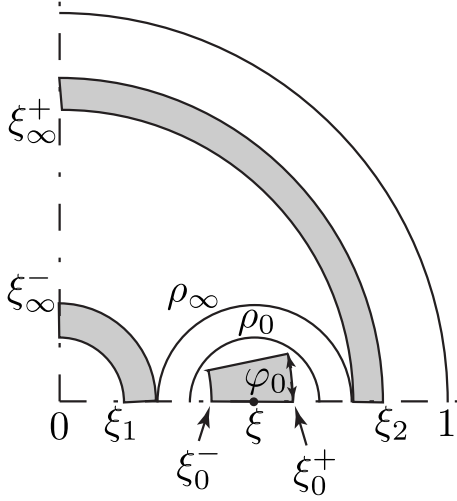


Figure B.1: Sketch of numerical integration

and far-field domains are quite inconvenient. In their place, we introduce the following simple ones (see Fig.B.1):  $\{\xi_0^- < \xi < \xi_0^+, 0 < \varphi < \varphi_0\}$  as the near-field domain, and  $\{\xi_1 < \xi < \xi_\infty^-, 0 < \varphi < \pi\} \cup \{\xi_\infty^+ < \xi < \xi_2, 0 < \varphi < \pi\}$  as the far-field domain. Here  $\xi_0^\pm = \xi \pm \rho_0/\sqrt{2}$ ,  $\varphi_0 = \rho_0/(\sqrt{2}\xi_0^+)$ , and  $\xi_\infty^\pm = \xi \pm \rho_\infty$ . Therefore we compute the integral (B.13) by means of the following representation (see Fig. B.1)

$$\begin{aligned}
 I &= \int_{\xi_1}^{\xi_2} \int_0^\pi (\dots) d\varphi d\bar{\xi} = \int_{\xi_0^-}^{\xi_0^+} \int_0^{\varphi_0} (\dots) d\varphi d\bar{\xi} + \\
 &+ \left[ \int_{\xi_0^-}^{\xi_0^+} \int_{\varphi_0}^\pi (\dots) d\varphi d\bar{\xi} + \int_{\xi_0^+}^{\xi_\infty^+} \int_0^\pi (\dots) d\varphi d\bar{\xi} + \int_{\xi_\infty^-}^{\xi_0^-} \int_0^\pi (\dots) d\varphi d\bar{\xi} \right] + \\
 &+ \left[ \int_{\xi_1}^{\xi_\infty^-} \int_0^\pi (\dots) d\varphi d\bar{\xi} + \int_{\xi_\infty^+}^{\xi_2} \int_0^\pi (\dots) d\varphi d\bar{\xi} \right], \tag{B.17}
 \end{aligned}$$

where the first integral we calculate using the regularization technique (B.14). The integrals in the first square brackets are not singular and we calculate them straightforwardly. The last square brackets are equal to zero. Note that this simplification of the integration domains significantly increases the efficiency of the scheme.

We conclude this Appendix with simple estimations for the near- and far-field domain



sizes  $\rho_0$  and  $\rho_\infty$ . To estimate  $\rho_0$  we impose an acceptable smallness of the ratio  $I^{(0)}$  to  $\min [I_r^{(0)}, I_s^{(0)}]$  equal to  $\epsilon_0$ , i.e.,  $I^{(0)}/\min [I_r^{(0)}, I_s^{(0)}] \gtrsim \epsilon_0$ . Here superscript (0) means that we integrate over the near-field domain,  $\sqrt{\xi^2 + \bar{\xi}^2 - 2\xi\bar{\xi}\cos(\varphi)} < \rho_0$ . Now it is easy to estimate the size  $\rho_0$

$$e^{-2\sqrt{s}\rho_0} \gtrsim \epsilon_0 \Rightarrow \rho_0 = -\frac{\ln \epsilon_0}{2\sqrt{s}}. \quad (\text{B.18})$$

To estimate  $\rho_\infty$  we impose the truncation error  $\epsilon_\infty$  defined by  $I^{(\infty)}/I_{01} \lesssim \epsilon_\infty$ , where  $I^{(\infty)}$  is the integration over the far-field domain,  $\sqrt{\xi^2 + \bar{\xi}^2 - 2\xi\bar{\xi}\cos(\varphi)} > \rho_\infty \cap 0 < \xi < 1$ , and  $I_{01}$  is the integration over the whole disc,  $0 < \xi < 1$ . The far-field integration domain is non-empty only for large values of the Laplace transform parameter  $s$ , therefore we can substitute  $I_{01}$  by  $I_\infty$ , where  $I_\infty$  is the integration over the infinite plane,  $0 < \xi < \infty$ . The estimation of the size  $\rho_\infty$  thus can be done as it follows

$$\begin{aligned} I_{01} \sim I_\infty &\sim 2 \int_0^\infty \int_0^\pi e^{-2\sqrt{s}\bar{\xi}} d\varphi d\bar{\xi} = \frac{\pi}{\sqrt{s}}, \\ I^{(\infty)} &\lesssim 2\pi e^{-2\sqrt{s}\rho_\infty}, \\ \rho_\infty &= \frac{1}{2\sqrt{s}} \ln \left( \frac{2\sqrt{s}}{\epsilon_\infty} \right). \end{aligned} \quad (\text{B.19})$$

## B.4 On numerical inversion of the Laplace transform

The Laplace transform is introduced by (Sneddon, 1951)

$$\tilde{f}(s) = \int_0^\infty f(t) \exp(-st) dt. \quad (\text{B.20})$$

The inverse Laplace transform is given by

$$f(t) = \frac{1}{2\pi i} \int_{\nu-i\infty}^{\nu+i\infty} \tilde{f}(s) \exp(st) ds, \quad (\text{B.21})$$

where  $\nu > 0$ , such that all singularities of  $\tilde{f}(s)$  are to the left of the line  $\text{Re}(s) = \nu$ .

Lopez-Fernandez and Palencia (2004) have shown that in the case when all singularities of  $\tilde{f}$  are inside a sector  $\arg(-s) < \delta < \pi/2$  the inversion formula (B.21) for  $t_0 < t < t_1$  can be approximated by

$$f_n(t) = \frac{1}{2\pi i} \frac{\ln(n)}{n} \sum_{k=-n}^n \exp[tT(x_k)] \tilde{f}[T(x_k)] T'(x_k). \quad (\text{B.22})$$

Here  $x_k = k \ln(n)/n$ ,

$$T(x) = \lambda [1 - \sin(\alpha - ix)], \quad \alpha + d + \delta < \pi/2, \quad d < \min(\alpha, \pi/2 - \alpha), \quad (\text{B.23})$$

$\alpha$ ,  $d$ , and  $\lambda$  are numerical constants.

It was shown that the error of this approximation is

$$\|f(t) - f_n(t)\| \leq \frac{2M}{\pi} F_n(x, \alpha, d), \quad (\text{B.24})$$

where  $x = \lambda t_0$ ,  $M$  is a constant such that  $\|\tilde{f}(s)\| \leq M/|s|$ , and

$$\begin{aligned} F_n(x, \alpha, \lambda) &= \sqrt{\frac{1 + \sin(\alpha + d)}{1 - \sin(\alpha + d)}} \left[ 1 + \left| \ln \left( 1 - e^{-x \sin(\alpha - d)} \right) \right| \right] \times \\ &\times e^{\Lambda x} \left( \frac{1}{e^{2\pi d n / \ln n} - 1} + \frac{1}{e^{\sin \alpha x n / 2}} \right), \end{aligned} \quad (\text{B.25})$$

where  $\Lambda = t_1/t_0$ .

The parameters  $\alpha$ ,  $d$ , and  $\lambda$  can be found by the error minimization

$$\min \{F_n(x, \alpha, \lambda) \mid x, \alpha d > 0, d < \min(\alpha, \pi/2 - \alpha), \alpha + d + \delta < \pi/2\}. \quad (\text{B.26})$$

In our case  $\delta = 0$ , and we take  $\Lambda = 10$ . Thus  $\alpha = 0.79$ , and  $x = 3.27$ .

## Appendix C

# Zero viscosity case: numerical scheme

### C.1 Temporal integration

Here we consider in detail only the backstress intensity factor equation (5.45). Let us introduce two times,  $\tau_0$  and  $\tau_\infty$ , such that for  $\tau < \tau_0$  the backstress intensity factor is given by the small-time asymptote (5.29), and for  $\tau > \tau_\infty$  the backstress stress intensity factor is given by the large-time asymptote (5.35). Let us also assume that we know the solution of our governing equation on mesh  $\tau_i^{(g)}$ , where  $i = 1, \dots, N$ ,  $\tau_1^{(g)} = \tau_0$ ,  $\tau_N^{(g)} = \tau_\infty$ , and the superscript  $(g)$  stands for “global”. The backstress intensity factor at moment  $\tau_i^{(g)}$ ,  $K_{bs}(\tau_i^{(g)})$ , is given by

$$K_{bs}(\tau_i^{(g)}) = \frac{\eta}{\rho^{1/2}(\tau_i^{(g)})} \int_0^{\tau_i^{(g)}} \frac{1 + \Pi(\bar{\tau})}{\rho(\bar{\tau})} k_{bs} \left[ \frac{\rho(\tau_i^{(g)})}{\rho(\bar{\tau})}, \frac{\tau_i^{(g)} - \bar{\tau}}{\rho^2(\bar{\tau})} \right] d\bar{\tau}, \quad (\text{C.1})$$

To evaluate the integral in the right-hand side of (C.1) we introduce the convolution mesh  $\tau_j^{(c)}$ ,  $j = 1, \dots, n$ ,  $\tau_1^{(c)} = 0$ , and  $\tau_n^{(c)} = \tau_i^{(g)}$ . Hence we can write

$$K_{bs} \left( \tau_i^{(g)} \right) = \frac{\eta}{\rho^{1/2} \left( \tau_i^{(g)} \right)} \sum_{j=1}^{n-1} \int_{\tau_j^{(c)}}^{\tau_{j+1}^{(c)}} \frac{1 + \Pi(\bar{\tau})}{\rho(\bar{\tau})} k_{bs} \left[ \frac{\rho \left( \tau_i^{(g)} \right)}{\rho(\bar{\tau})}, \frac{\tau_i^{(g)} - \bar{\tau}}{\rho^2(\bar{\tau})} \right] d\bar{\tau}, \quad (\text{C.2})$$

The problem with the evaluation of the integrals in the last equation is related to the small time singularity of the backstress Green function [see (4.35)]. Therefore we introduce the following function  $k_{bs}^I(\mathcal{R}, \tau)$  which is regular with respect to time

$$k_{bs}^I(\mathcal{R}, \tau) \equiv \int_0^\tau k_{bs}(\mathcal{R}, \bar{\tau}) d\bar{\tau}. \quad (\text{C.3})$$

Simple transformations lead to

$$\begin{aligned} \frac{d}{d\bar{\tau}} \left\{ \left[ \frac{\rho(\bar{\tau})}{\rho(\tau)} \right]^\alpha k_{bs}^I \left[ \frac{\rho(\tau)}{\rho(\bar{\tau})}, \frac{\tau - \bar{\tau}}{\rho^2(\bar{\tau})} \right] \right\} &= \alpha \frac{\dot{\rho}(\bar{\tau})}{\rho(\bar{\tau})} \left[ \frac{\rho(\bar{\tau})}{\rho(\tau)} \right]^\alpha k_{bs}^I - \\ &- \frac{\dot{\rho}(\bar{\tau})}{\rho(\bar{\tau})} \left[ \frac{\rho(\bar{\tau})}{\rho(\tau)} \right]^{\alpha-1} \frac{\partial k_{bs}^I}{\partial \mathcal{R}} - \left[ \frac{\rho(\bar{\tau})}{\rho(\tau)} \right]^\alpha \frac{1}{\rho^2(\bar{\tau})} \left[ 1 + 2 \frac{\dot{\rho}(\bar{\tau})}{\rho(\bar{\tau})} (\tau - \bar{\tau}) \right] k_{bs}, \\ k_{bs} \left[ \frac{\rho(\tau)}{\rho(\bar{\tau})}, \frac{\tau - \bar{\tau}}{\rho^2(\bar{\tau})} \right] &= \frac{\alpha \rho^2(\bar{\tau}) u(\bar{\tau})}{\bar{\tau} + 2u(\bar{\tau})(\tau - \bar{\tau})} k_{bs}^I - \frac{\rho(\tau) \rho(\bar{\tau}) u(\bar{\tau})}{\bar{\tau} + 2u(\bar{\tau})(\tau - \bar{\tau})} \frac{\partial k_{bs}^I}{\partial \mathcal{R}} - \\ &- \frac{\rho^2(\bar{\tau}) \bar{\tau}}{\bar{\tau} + 2u(\bar{\tau})(\tau - \bar{\tau})} \left[ \frac{\rho(\tau)}{\rho(\bar{\tau})} \right]^\alpha \frac{d}{d\bar{\tau}} \left\{ \left[ \frac{\rho(\bar{\tau})}{\rho(\tau)} \right]^\alpha k_{bs}^I \left[ \frac{\rho(\tau)}{\rho(\bar{\tau})}, \frac{\tau - \bar{\tau}}{\rho^2(\bar{\tau})} \right] \right\}, \end{aligned} \quad (\text{C.4})$$

where  $u(\tau) \equiv \tau \dot{\rho}(\tau) / \rho(\tau)$ , and  $\alpha$  is a number yet to be defined. The spatial derivative  $\partial k_{bs}^I(\mathcal{R}, \tau) / \partial \mathcal{R}$  can be found using

$$\begin{aligned} \frac{\partial}{\partial \mathcal{R}} \int_0^\mathcal{R} \frac{\xi \Xi^I(\xi, \tau)}{\sqrt{\mathcal{R}^2 - \xi^2}} d\xi &= \mathcal{R} \left[ \frac{\Xi^I(\mathcal{R}, \tau)}{\sqrt{\mathcal{R}^2 - \xi^2}} \Big|_{\xi=\mathcal{R}} - \int_0^\mathcal{R} \frac{\xi \Xi^I(\xi, \tau)}{(\mathcal{R}^2 - \xi^2)^{3/2}} d\xi \right] = \\ &= \mathcal{R} \left\{ - \int_0^{\xi_1} \frac{\xi \Xi^I(\xi, \tau)}{(\mathcal{R}^2 - \xi^2)^{3/2}} d\xi - \int_{\xi_1}^\mathcal{R} \frac{\xi [\Xi^I(\xi, \tau) - \Xi^I(\mathcal{R}, \tau)]}{(\mathcal{R}^2 - \xi^2)^{3/2}} d\xi + \frac{\Xi^I(\mathcal{R}, \tau)}{\sqrt{\mathcal{R}^2 - \xi_1^2}} \right\}, \end{aligned} \quad (\text{C.5})$$

where  $\xi_1 \in [0, \mathcal{R})$ , and

$$\Xi^I(\xi, \tau) \equiv \int_0^\tau \Xi(\xi, \bar{\tau}) d\bar{\tau}. \quad (\text{C.6})$$

Substitution of (C.4) into the integral of (C.2) yields

$$\begin{aligned}
& \frac{1}{\rho^{1/2}(\tau)} \int_{\tau_j}^{\tau_{j+1}} \frac{1 + \Pi(\bar{\tau})}{\rho(\bar{\tau})} k_{bs} \left[ \frac{\rho(\tau)}{\rho(\bar{\tau})}, \frac{\tau - \bar{\tau}}{\rho^2(\bar{\tau})} \right] d\bar{\tau} = \\
& = \frac{\alpha}{\rho^{1/2}(\tau)} \int_{\tau_j}^{\tau_{j+1}} \frac{\rho(\bar{\tau}) u(\bar{\tau}) [1 + \Pi(\bar{\tau})]}{\bar{\tau} + 2u(\bar{\tau})(\tau - \bar{\tau})} k_{bs}^I \left[ \frac{\rho(\tau)}{\rho(\bar{\tau})}, \frac{\tau - \bar{\tau}}{\rho^2(\bar{\tau})} \right] d\bar{\tau} - \\
& - \rho^{1/2}(\tau) \int_{\tau_j}^{\tau_{j+1}} \frac{\rho(\tau) u(\bar{\tau}) [1 + \Pi(\bar{\tau})]}{\bar{\tau} + 2u(\bar{\tau})(\tau - \bar{\tau})} \frac{\partial}{\partial \mathcal{R}} k_{bs}^I \left[ \frac{\rho(\tau)}{\rho(\bar{\tau})}, \frac{\tau - \bar{\tau}}{\rho^2(\bar{\tau})} \right] d\bar{\tau} - \\
& - \int_{\tau_j}^{\tau_{j+1}} \frac{\bar{\tau} \rho^{1/2}(\bar{\tau}) [1 + \Pi(\bar{\tau})]}{\bar{\tau} + 2u(\bar{\tau})(\tau - \bar{\tau})} \left[ \frac{\rho(\tau)}{\rho(\bar{\tau})} \right]^{\alpha-1/2} \frac{d}{d\bar{\tau}} \left\{ \left[ \frac{\rho(\bar{\tau})}{\rho(\tau)} \right]^\alpha k_{bs}^I \left[ \frac{\rho(\tau)}{\rho(\bar{\tau})}, \frac{\tau - \bar{\tau}}{\rho^2(\bar{\tau})} \right] \right\} d\bar{\tau}. \quad (C.7)
\end{aligned}$$

We introduce the parameter  $\alpha$  in order to have a finite limit as  $\bar{\tau} \rightarrow 0$  of the expression in the curved brackets in the last integral of (C.7). In order to have a finite limit as  $\bar{\tau} \rightarrow 0$  of  $\rho^{1-\alpha}(\bar{\tau}) [1 + \Pi(\bar{\tau})]$  we set  $\alpha = 1/2$ . Now it is natural to introduce the following discretization of the integral (C.7)

$$\begin{aligned}
& \frac{1}{\rho^{1/2}(\tau)} \int_{\tau_j}^{\tau_{j+1}} \frac{1 + \Pi(\bar{\tau})}{\rho(\bar{\tau})} k_{bs} \left[ \frac{\rho(\tau)}{\rho(\bar{\tau})}, \frac{\tau - \bar{\tau}}{\rho^2(\bar{\tau})} \right] d\bar{\tau} \approx \\
& = \frac{\Delta\tau_j}{2\rho^{1/2}(\tau)} \left\{ \frac{\rho(\bar{\tau}) u(\bar{\tau}) [1 + \Pi(\bar{\tau})]}{\bar{\tau} + 2u(\bar{\tau})(\tau - \bar{\tau})} k_{bs}^I \left[ \frac{\rho(\tau)}{\rho(\bar{\tau})}, \frac{\tau - \bar{\tau}}{\rho^2(\bar{\tau})} \right] \right\}_{\bar{\tau}=\tau_{j+1/2}} - \\
& - \rho^{1/2}(\tau) \Delta\tau_j \left\{ \frac{\rho(\tau) u(\bar{\tau}) [1 + \Pi(\bar{\tau})]}{\bar{\tau} + 2u(\bar{\tau})(\tau - \bar{\tau})} \frac{\partial}{\partial \mathcal{R}} k_{bs}^I \left[ \frac{\rho(\tau)}{\rho(\bar{\tau})}, \frac{\tau - \bar{\tau}}{\rho^2(\bar{\tau})} \right] \right\}_{\bar{\tau}=\tau_{j+1/2}} - \\
& - \left\{ \frac{\bar{\tau} \rho^{1/2}(\bar{\tau}) [1 + \Pi(\bar{\tau})]}{\bar{\tau} + 2u(\bar{\tau})(\tau - \bar{\tau})} \right\}_{\bar{\tau}=\tau_{j+1/2}} \left\{ \sqrt{\frac{\rho(\bar{\tau})}{\rho(\tau)}} k_{bs}^I \left[ \frac{\rho(\tau)}{\rho(\bar{\tau})}, \frac{\tau - \bar{\tau}}{\rho^2(\bar{\tau})} \right] \right\}_{\bar{\tau}=\tau_j}^{\bar{\tau}=\tau_{j+1}}, \quad (C.8)
\end{aligned}$$

where  $\Delta\tau_j \equiv \tau_{j+1} - \tau_j$  and  $\tau_{j+1/2} \equiv (\tau_j + \tau_{j+1})/2$ .

To evaluate  $\rho(\tau)$  and  $\Pi(\tau)$  we use piece-wise linear interpolation in log-log space.

To calculate  $u(\tau_{j+1/2})$  we use

$$u(\tau_{j+1}) = \frac{\rho(\tau_{j+1}) - \rho(\tau_j)}{\tau_{j+1} - \tau_j} \frac{\tau_{j+1/2}}{\rho(\tau_{j+1/2})}.$$

## C.2 Spatial integration

Here we consider integrals of the following form

$$I(\mathcal{R}, \tau) \equiv \int_0^{\mathcal{R}} f(\mathcal{R}, \xi) \Xi^I(\xi, \tau) d\xi, \quad (\text{C.9})$$

where  $\Xi^I(\xi, \tau)$  is a numerical function, defined by (C.6), known on mesh  $\xi_i < \mathcal{R}$ , and continuous with respect to time, and  $f(\mathcal{R}, \xi) = \xi (\mathcal{R}^2 - \xi^2)^h$ ,  $h = \{1/2, -1/2, -3/2\}$ .

The small- and large-time asymptotes of  $\Xi^I(\xi, \tau)$  are given by [see (4.35), (4.52)]

$$\begin{aligned} \Xi_0^I(\xi, \tau \ll 1) &= -\frac{2\tau^{1/2}}{\pi^{3/2}} \Sigma_0(\xi), \\ \Xi_\infty^I(\xi, \tau \gg 1) &= -\Sigma_\infty(\xi), \end{aligned} \quad (\text{C.10})$$

where

$$\begin{aligned} \Sigma_0(\xi) &\equiv (1 - \xi)^{-1} E \left[ \frac{4\xi}{(1 + \xi)^2} \right] + (1 + \xi)^{-1} K \left[ \frac{4\xi}{(1 + \xi)^2} \right], \\ \Sigma_\infty(\xi) &\equiv \begin{cases} 1, & \xi \leq 1 \\ \frac{2}{\pi} \arctan \left( \frac{1}{\sqrt{\xi^2 - 1}} \right), & \xi > 1 \end{cases}. \end{aligned} \quad (\text{C.11})$$

One can see that the small-time asymptote is singular at  $\xi = 1$ ,

$$\Sigma_0(\xi) \approx \frac{1}{1 - \xi} + \frac{1}{2} \ln \left( \frac{8}{|1 - \xi|} \right). \quad (\text{C.12})$$

Therefore in order to avoid difficulties during the numerical integration we decompose our numerical  $\Xi^I(\xi, \tau)$  into  $\Sigma_0(\xi)$  and  $\Sigma_\infty(\xi)$

$$\Xi^I(\xi, \tau) = a_i(\tau) \Sigma_0(\xi) + b_i(\tau) \Sigma_\infty(\xi), \quad \xi \in [\xi_i, \xi_{i+1}], \quad (\text{C.13})$$

$$\begin{aligned} a_i(\tau) &= \frac{\Xi^I(\xi_i, \tau) \Sigma_\infty(\xi_{i+1}) - \Xi^I(\xi_{i+1}, \tau) \Sigma_\infty(\xi_i)}{\Sigma_0(\xi_i) \Sigma_\infty(\xi_{i+1}) - \Sigma_0(\xi_{i+1}) \Sigma_\infty(\xi_i)}, \\ b_i(\tau) &= \frac{\Xi^I(\xi_i, \tau) \Sigma_0(\xi_{i+1}) - \Xi^I(\xi_{i+1}, \tau) \Sigma_0(\xi_i)}{\Sigma_\infty(\xi_i) \Sigma_0(\xi_{i+1}) - \Sigma_\infty(\xi_{i+1}) \Sigma_0(\xi_i)}. \end{aligned} \quad (\text{C.14})$$

Substitution of this decomposition into the integral (C.9) yields

$$I_i(\mathcal{R}, \tau) \equiv \int_{\xi_i}^{\min[\xi_{i+1}, \mathcal{R}]} f(\mathcal{R}, \xi) \Xi^I(\xi, \tau) d\xi = a_i(\tau) I_i^{(0)}(\mathcal{R}) + b_i(\tau) I_i^{(\infty)}(\mathcal{R}), \quad (\text{C.15})$$

where

$$I_i^{(j)}(\mathcal{R}) \equiv \int_{\xi_i}^{\min[\xi_{i+1}, \mathcal{R}]} f(\mathcal{R}, \xi) \Sigma_j(\xi) d\xi. \quad (\text{C.16})$$

The decomposition (C.15) takes into account the singularity and gives correct small- and large-time asymptotes of the left-hand side integral. The integral  $I_i^{(\infty)}(\mathcal{R})$  can be calculated analytically. We do not give here the explicit expression of this integral because of its expansive size. At the same time the integral  $I_i^{(0)}(\mathcal{R})$  can be evaluated only numerically, which is expensive from a computational point of view. To save some computational time we adopt one more decomposition of (C.7)

$$I(\mathcal{R}, \tau) \equiv \left( \int_0^{\min[2, \mathcal{R}]} + \int_{\min[2, \mathcal{R}]}^{\mathcal{R}} \right) f(\mathcal{R}, \xi) \Xi^I(\xi, \tau) d\xi, \quad (\text{C.17})$$

where the first integral is evaluated using the decomposition described above (C.15), and the second integral is calculated via linear interpolation of  $\Xi^I(\xi_i, \tau)$ , i.e.,  $\Sigma_0(\xi) = 1$  and  $\Sigma_\infty(\xi) = \xi$ . Further improvement can be achieved by replacing  $\Sigma_0(\xi)$  during the evaluation of the first integral by

$$\Sigma_0^*(\xi) \equiv \frac{1}{1-\xi} + \frac{1}{2} \ln \left( \frac{16}{|1-\xi^2|} \right), \quad (\text{C.18})$$

which has the same singularity as  $\Sigma_0(\xi)$ , but allows an analytical evaluation of  $I_i^{(0)}$ .

### C.3 The end of the story

Using the integration algorithms described above we can reduce our set of governing equations (5.42)-(5.44) to a set of two nonlinear equations

$$\mathcal{F}_i(\rho_1, \rho_2, \dots, \rho_i; \Pi_1, \Pi_2, \dots, \Pi_i) = 0, \quad (\text{C.19})$$

where  $\rho_k \equiv \rho(\tau_k^{(g)})$ ,  $\Pi_k \equiv \Pi(\tau_k^{(g)})$ . The unknowns are the radius  $\rho_i$  and the pressure  $\Pi_i$  at the current time  $\tau_i^{(g)}$ . To solve this set of equations we use the following algorithm:

- Using an input guess for  $\rho_i$  we solve the part of (C.19) related to the propagation criterion (5.43) employing the standard Newton method. As a result, we get

$$\Pi_i = \Pi_i(\rho_1, \rho_2, \dots, \rho_i; \Pi_1, \Pi_2, \dots, \Pi_{i-1});$$

- Substituting this equation into the volume balance part of (C.19) we obtain a nonlinear equation of the form

$$\tilde{\mathcal{F}}_i(\rho_1, \rho_2, \dots, \rho_i; \Pi_1, \Pi_2, \dots, \Pi_{i-1}) = 0,$$

where the only unknown is  $\rho_i$ . We solve this equation using the secant method.

The results presented in this work were obtained using a homogeneous convolution mesh with  $n = 50$  nodes for the cases of  $\eta = 0$  and  $\eta = 0.25$ , and with  $n = 100$  nodes for the case of  $\eta = 0.5$ , and a logarithmic global mesh such that  $\tau_{i+1}^{(g)} - \tau_i^{(g)} = (n-1)^{-1} \tau_i^{(g)}$ . The algorithm was implemented in *Mathematica 6.0*.



## Appendix D

# Zero toughness case: numerical scheme

We divide the fracture into  $n$  control volumes of equal length. The center of a volume is denoted by  $\xi_i$ ,  $i = 1, \dots, n$ . Note that  $\xi_{1/2} = 0$ , and  $\xi_{n+1/2} = 1$ . All governing quantities are evaluated at the centers of these volumes. In other words, our discretized governing quantities are  $\Omega_i \equiv \Omega(\xi_i)$ ,  $\Pi_i \equiv \Pi(\xi_i)$ . Also we assume that the opening into the last two control volumes  $\Omega_{n-1}$  and  $\Omega_n$  is governed by the tip asymptote (see Appendix D.3).

### D.1 Elasticity equation

Here instead of the elasticity equation (6.43) we use the inverted version of it given by (2.5). In the numerical scaling (6.39) this elasticity equation has the following form

$$\Pi(\xi, \tau) = -\frac{1}{\gamma} \int_0^1 M(\xi, \zeta) \frac{\partial \Omega(\zeta, \tau)}{\partial \zeta} d\zeta. \quad (\text{D.1})$$

Integration by parts yields

$$\Pi(\xi, \tau) = \frac{1}{\gamma} \int_0^1 \frac{\partial M(\xi, \zeta)}{\partial \zeta} \Omega(\zeta, \tau) d\zeta. \quad (\text{D.2})$$

Now we discretize this equation as follows

$$\Pi_i = \frac{1}{\gamma} A_{ij} \Omega_j, \quad (\text{D.3})$$

where

$$A_{ij} = M(\xi_i, \xi_{j+1/2}) - M(\xi_i, \xi_{j-1/2}). \quad (\text{D.4})$$

## D.2 Lubrication equation

### D.2.1 Channel

Here we integrate the lubrication equation (6.40) over space from  $\xi_{i-1/2}$  to  $\xi_{i+1/2}$

$$\begin{aligned} \int_{\xi_{i-1/2}}^{\xi_{i+1/2}} \left( \dot{\Omega} - \frac{\dot{\gamma}}{\gamma} \xi \frac{\partial \Omega}{\partial \xi} \right) \xi d\xi &= \int_{\xi_{i-1/2}}^{\xi_{i+1/2}} \dot{\Omega} \xi d\xi - \frac{\dot{\gamma}}{\gamma} \left( \xi^2 \Omega \Big|_{\xi_{i-1/2}}^{\xi_{i+1/2}} - 2 \int_{\xi_{i-1/2}}^{\xi_{i+1/2}} \Omega \xi d\xi \right) \approx \\ &\approx \xi_i \frac{\Omega_i - \Omega_i^{(old)}}{\Delta \tau} \Delta \xi_i - \frac{\dot{\gamma}}{\gamma} \left( \xi^2 \Omega \Big|_{\xi_{i-1/2}}^{\xi_{i+1/2}} - 2 \Omega_i \xi_i \Delta \xi_i \right) \approx \\ &\approx \xi_i \frac{\Omega_i - \Omega_i^{(old)}}{\Delta \tau} \Delta \xi_i - \frac{\dot{\gamma}}{\gamma} \frac{\xi_{i+1/2}^2 \Omega_{i+1} - 2 \xi_i \Omega_i \Delta \xi_i - \xi_{i-1/2}^2 \Omega_{i-1}}{2}. \end{aligned}$$

We apply the same discretization to the leak-off term. The right hand side of the lubrication equation (6.40) is discretized as follows

$$\begin{aligned} \frac{1}{\gamma^2} \int_{\xi_{i-1/2}}^{\xi_{i+1/2}} \frac{\partial}{\partial \xi} \left( \xi \Omega^3 \frac{\partial \Pi}{\partial \xi} \right) d\xi &\approx \\ \approx \frac{\xi_{i+1/2}}{\gamma^2} \left( \frac{\Omega_{i+1} + \Omega_i}{2} \right)^3 \frac{\Pi_{i+1} - \Pi_i}{\Delta \xi_{i+1/2}} - \frac{\xi_{i-1/2}}{\gamma^2} \left( \frac{\Omega_i + \Omega_{i-1}}{2} \right)^3 \frac{\Pi_i - \Pi_{i-1}}{\Delta \xi_{i-1/2}}. \end{aligned}$$

Here we use the following approximations

$$\Omega_{i+1/2} \approx \frac{\Omega_i + \Omega_{i+1}}{2}, \quad \Upsilon_i \approx \frac{\int_{\xi_{i-1/2}}^{\xi_{i+1/2}} \Upsilon \xi d\xi}{\xi_i \Delta \xi_i}, \quad \dot{\gamma} \approx \frac{\gamma - \gamma^{(old)}}{\Delta \tau}.$$

## D.2.2 Tip

Instead of writing a discretized lubrication equation into the tip region we use the global volume balance equation (6.42). As a result we have the following expression for the dimensionless fracture length  $\gamma$

$$\gamma = \left\{ \frac{2\pi}{\tau} \left[ \left( \sum_{i=1}^{n-1} \Omega_i \xi_i \Delta \xi_i + v_{\text{tip}} \right) + V_{\text{leak}} \right] \right\}^{-1/2}, \quad (\text{D.5})$$

where  $v_{\text{tip}}$  is the volume of the last control volume calculated from the tip solution, and

$$V_{\text{leak}} = \int_0^1 \Upsilon(\xi, \tau) \xi d\xi.$$

## D.3 Tip solution

The scaled lubrication equations (6.31) and (6.35) indicate that in the tip region we can use the approximation

$$\int_{\xi}^1 \left( \dot{\Upsilon} - \frac{\dot{\gamma}}{\gamma} \xi \frac{\partial \Upsilon}{\partial \xi} \right) \xi d\xi \approx C_{\Upsilon} \sqrt{1 - \xi^2}. \quad (\text{D.6})$$

In practice, in order to find the coefficient  $C_{\Upsilon}$ , we evaluate the left-hand side of this equation at  $\xi_{n-1}$  using

$$\int_{\xi_{n-1}}^1 \left( \dot{\Upsilon} - \frac{\dot{\gamma}}{\gamma} \xi \frac{\partial \Upsilon}{\partial \xi} \right) \xi d\xi = \int_{\xi_{n-1}}^1 \xi \dot{\Upsilon} d\xi + \frac{\dot{\gamma}}{\gamma} \left( \xi_{n-1}^2 \Upsilon_{n-1} + 2 \int_{\xi_{n-1}}^1 \xi \Upsilon d\xi \right),$$

and then we divide the result by  $\sqrt{1 - \xi_{n-1}^2}$ .

Under the assumption that  $\xi \rightarrow 1$ , substitution of the approximation (D.6) into the lubrication equation (6.40) yields

$$G_v \frac{\dot{\gamma}}{\gamma} \Omega + 2^{1/2} G_c C_{\Upsilon} \sqrt{1 - \xi} = -\frac{1}{\gamma^2} \Omega^3 \frac{\partial \Pi}{\partial \xi}. \quad (\text{D.7})$$

At the same time, the elasticity equation (D.1) transforms to

$$\Pi(\xi, \tau) = \frac{1}{4\pi\gamma} \int_0^{\infty} \frac{\partial \Omega(\zeta, \tau)}{\partial \zeta} \frac{d\zeta}{\xi - \zeta}. \quad (\text{D.8})$$

Now we introduce the following scaling

$$1 - \xi = \hat{\ell}\hat{\xi}, \quad \Omega = \hat{W}\hat{\Omega}, \quad \Pi = \hat{P}\hat{\Pi}, \quad (\text{D.9})$$

where

$$\hat{\ell} = \frac{8\gamma^2}{\dot{\gamma}^8} \frac{G_c^6 C_\Gamma^6}{G_v^8}, \quad \hat{W} = \frac{4\gamma^2}{\dot{\gamma}^5} \frac{G_c^4 C_\Gamma^4}{G_v^5}, \quad \hat{P} = \frac{\dot{\gamma}^3}{2\gamma} \frac{G_v^3}{G_c^2 C_\Gamma^2}. \quad (\text{D.10})$$

The governing equations (D.11) and (D.12) transform to

$$\hat{\Omega} + \hat{\xi}^{1/2} = \hat{\Omega}^3 \frac{d\hat{\Pi}}{d\hat{\xi}}, \quad (\text{D.11})$$

$$\hat{\Pi}(\hat{\xi}) = \frac{1}{4\pi} \int_0^\infty \frac{\partial \hat{\Omega}(\zeta)}{\partial \zeta} \frac{d\zeta}{\hat{\xi} - \zeta}. \quad (\text{D.12})$$

These equations have been well studied [e.g. see (Adachi and Detournay, 2008)]. Note that these equations do not depend on any parameters, therefore one can solve them only once and then tabulate the solution. Throughout this research we use the simplified version of our algorithm developed in Chapter 3.

## D.4 Evaluation of leak-off displacement function (6.44)

### D.4.1 Temporal integration

Let us introduce two times,  $\tau_0$  and  $\tau_\infty$ , such that for  $\tau < \tau_0$  the leak-off displacement function is given by the small-time asymptote  $\Upsilon_M$ , and for  $\tau > \tau_\infty$  the leak-off displacement function is given by the large-time asymptote  $\Upsilon_{\tilde{M}_\infty}$  (for the asymptotes see Section 6.3). Also let us assume that we know the solution of our governing equations on mesh  $\tau_i^{(g)}$ , where  $i = 1, \dots, n_g$ ,  $\tau_1^{(g)} = \tau_0$ ,  $\tau_{n_g}^{(g)} = \tau_\infty$ , and the superscript  $(g)$  stands for “global”. The leak-off displacement function at moment  $\tau_i^{(g)}$ ,  $\Upsilon(\xi, \tau_i^{(g)})$ , is given by

$$\Upsilon(\xi, \tau_i^{(g)}) = \int_0^\tau \gamma^{-1}(\bar{\tau}) \psi \left[ \frac{\gamma(\tau_i^{(g)})}{\gamma(\bar{\tau})} \xi, \frac{\tau_i^{(g)} - \bar{\tau}}{\gamma^2(\bar{\tau})} \right] d\bar{\tau}, \quad (\text{D.13})$$

To evaluate the integral in the right-hand side of (D.13) we introduce the convolution mesh  $\tau_j^{(c)}$ ,  $j = 1, \dots, n_c$ ,  $\tau_1^{(c)} = 0$ , and  $\tau_{n_c}^{(c)} = \tau_i^{(g)}$ . Hence we can write

$$\Upsilon\left(\tau_i^{(g)}\right) = \sum_{j=1}^{n_c-1} \int_{\tau_j^{(c)}}^{\tau_{j+1}^{(c)}} \gamma^{-1}(\bar{\tau}) \psi\left[\frac{\gamma\left(\tau_i^{(g)}\right)}{\gamma(\bar{\tau})} \xi, \frac{\tau_i^{(g)} - \bar{\tau}}{\gamma^2(\bar{\tau})}\right] d\bar{\tau}, \quad (\text{D.14})$$

The problem with the evaluation of the integrals in the last equation is related to the square root singularity of the leak-off Green function [see (4.33)]. Therefore we perform the following transformations

$$\gamma^{-1}(\bar{\tau}) \psi\left[\frac{\gamma\left(\tau_i^{(g)}\right)}{\gamma(\bar{\tau})} \xi, \frac{\tau_i^{(g)} - \bar{\tau}}{\gamma^2(\bar{\tau})}\right] = \frac{1}{\sqrt{\tau_i^{(g)} - \bar{\tau}}} \left\{ \frac{\sqrt{\tau_i^{(g)} - \bar{\tau}}}{\gamma(\bar{\tau})} \psi\left[\frac{\gamma\left(\tau_i^{(g)}\right)}{\gamma(\bar{\tau})} \xi, \frac{\tau_i^{(g)} - \bar{\tau}}{\gamma^2(\bar{\tau})}\right] \right\} \quad (\text{D.15})$$

Now we can approximate the expression in the curly brackets by a polynomial and perform an analytical integration. In this research we used the first order polynomial.

#### D.4.2 Spatial integration

Here we consider integrals of the following form

$$I(\xi_1, \xi_2, \tau) \equiv \int_{\xi_1}^{\xi_2} \xi \psi(\xi, \tau) d\xi, \quad (\text{D.16})$$

where  $\psi(\xi, \tau)$  is a numerical function known on mesh  $\tilde{\xi}_i < 1$ . The small- and large-time asymptotes of  $\psi(\xi, \tau)$  are given by (4.33) and (4.50) respectively. As in the auxiliary problem, here we approximate  $\psi(\xi, \tau)$  by

$$\psi\left(\tilde{\xi}_i \leq \xi \leq \tilde{\xi}_{i+1}\right) \simeq \psi_i(\xi) \equiv \frac{a_i}{\sqrt{1 - \xi^2}} + b_i, \quad (\text{D.17})$$

where  $a_i$  and  $b_i$  are unknown constants which can be related to the values of the flux distribution function in the nodes of the mesh  $\psi_i \equiv \psi(\tilde{\xi}_i)$

$$a_i = \frac{\psi_{i+1} - \psi_i}{\left(1 - \tilde{\xi}_{i+1}^2\right)^{-1/2} - \left(1 - \tilde{\xi}_i^2\right)^{-1/2}}, \quad b_i = \frac{\psi_{i+1} \sqrt{1 - \tilde{\xi}_{i+1}^2} - \psi_i \sqrt{1 - \tilde{\xi}_i^2}}{\sqrt{1 - \tilde{\xi}_{i+1}^2} - \sqrt{1 - \tilde{\xi}_i^2}}. \quad (\text{D.18})$$

In other words, we use a linear combination of the small- and large-time asymptotes to approximate the flux distribution function  $\psi$  at each interval  $[\tilde{\xi}_i, \tilde{\xi}_{i+1}]$ . We then substitute this decomposition into the integral (D.16) and evaluate it.

## D.5 The end of the story

As a result of the discretization described above we get a set of non-linear algebraic equations

$$\mathcal{F}_j(\gamma_1, \gamma_2, \dots, \gamma_j; \mathbf{\Omega}_{j-1}, \mathbf{\Omega}_j; \mathbf{\Upsilon}_{j-1}, \mathbf{\Upsilon}_j; \mathbf{\Pi}_j) = 0, \quad (\text{D.19})$$

where  $\mathbf{A}_j \equiv \{A_1(\tau_j), A_2(\tau_j), \dots, A_n(\tau_j)\}$ . Note that  $\mathbf{\Pi}_j$  and  $\mathbf{\Omega}_j$  are connected through the discretized elasticity equation (D.3), and that  $\mathbf{\Upsilon}_j$  depends only on the dimensionless fracture length  $\{\gamma_1, \gamma_2, \dots, \gamma_j\}$ . Therefore the set of equations (D.19) can be reduced to

$$\bar{\mathcal{F}}_j(\gamma_1, \gamma_2, \dots, \gamma_j; \mathbf{\Omega}_{j-1}, \mathbf{\Omega}_j) = 0. \quad (\text{D.20})$$

The unknowns here are  $\{\gamma_j, \mathbf{\Omega}_j\}$ .

To solve this set of equations we use an algorithm which is similar to the one we have developed for the toughness-dominated case:

- Using an input guess for  $\gamma_j$  we solve the part of (D.20) related to the lubrication equation discretized in the channel by employing the standard Newton method.

As a result, we get

$$\mathbf{\Omega}_j = \mathbf{\Omega}_j(\gamma_1, \gamma_2, \dots, \gamma_j; \mathbf{\Omega}_{j-1});$$

- Substituting this equation into the discretized global volume balance equation (D.5) we obtain the following nonlinear equation

$$\tilde{\mathcal{F}}_j(\gamma_1, \gamma_2, \dots, \gamma_j; \mathbf{\Omega}_{j-1}) = 0,$$

where the only unknown is  $\gamma_j$ . We solve this equation using the secant method.

The results presented in this work were obtained using a homogeneous convolution mesh with 300 nodes, and a logarithmic global mesh such that  $\tau_{i+1}^{(g)} - \tau_i^{(g)} = 0.05\tau_i^{(g)}$ . The algorithm was implemented in *Mathematica 6.0*.